AN ABSTRACT OF THE DISSERTATION OF

Erin C. Rooney for the degree of Doctor of Philosophy in Soil Science presented on April 15, 2022.

Title: The Impact of Freeze-Thaw Cycles to the Physical and Biogeochemical Properties of Alaskan Permafrost Soils.

Abstract approved: ____
Rebecca Lybrand

Abstract approved: ____
Vanessa Bailey

Abstract approved: ____
Markus Kleber

Arctic warming is exposing thawing permafrost to repeated freeze-thaw, a disruptive process that can alter soil biogeochemistry and physical structure. To investigate the impact of permafrost exposure to freeze-thaw, soil response was tested across three scales: 2.5 cm^3 aggregates, a forested hillslope, and two sites at contrasting latitudes. XCT imaging was employed to investigate pore deformation while FT-ICR-MS informed comparisons of carbon chemistry at the soil horizon, hillslope, and site levels. The initial stages of pore-scale freeze-thaw deformation following permafrost thaw resulted in decreasing connectivity and both expansion and collapse of pore throats with potential ramifications for spatial access to carbon and water holding capacity. At the hillslope scale, canopy-driven differences in soil temperature and carbon decomposition were more prevalent in conditions with lower moisture and thinner organic mats compared with high-moisture downslope soils. Across sites with differing freeze-thaw histories, there was greater oxidation of carbon molecules and loss of aliphatics following experimental freeze-thaw at the lower latitude site. Our findings indicate that factors such as freeze-thaw history, moisture, and organic mat thickness may influence carbon response to warming in permafrost soils, resulting in a heterogeneous response to freeze-thaw at both the site and hillslope scale.

The Impact of Freeze-Thaw Cycles to the Physical and Biogeochemical Properties of Alaskan Permafrost Soils.

by

Erin C. Rooney

A DISSERTATION

submitted to

Oregon State University

in partial fulfillment of
the requirements for the
degree of

Doctor of Philosophy

Presented April 15, 2022
Commencement June 2022

Doctor of Philosophy dissertation of Erin C. Rooney presented on April 15, 2022

APPROVED:

Major Professor, representing Soil Science

Major Professor, representing Soil Science

Major Professor, representing Soil Science

Head of the Department of Crop and Soil Science

Dean of the Graduate School

I understand that my dissertation will become part of the permanent collection of Oregon State University libraries. My signature below authorizes release of my dissertation to any reader upon request.

Erin C. Rooney, Author

ACKNOWLEDGEMENTS

I would like to thank my advisors, Rebecca Lybrand and Vanessa Bailey, for their stellar mentorship, excellent leadership, and constant support throughout my doctoral degree. I would also like to thank Kaizad Patel, Angela Possinger, Maria Dragila, Odeta Qafoku, and David Myrold for their guidance and expertise across multiple experiments. I would like to thank my committee members: Dominique Bachelet, Maria Dragila, Jeff Hatten, and Robert Kennedy for the time and energy they generously gave throughout my Ph.D. program. I would also like to express my sincere thanks to Michele Freppaz, Nicola Colombo, Francesca Poratelli, Christian Hauck, and Christin Hilbich for their expertise and mentorship.

I would like to acknowledge the OSU-PNNL Distinguished Graduate Research Program, Oregon State University Department of Crop and Soil Science, Department of Energy, National Ecological Observatory Network, Arctic Institute of North America, Critical Zone Observatory Network, Geological Society of America, and Environmental Molecular Sciences Laboratory at Pacific Northwest National Laboratory for financial support for my training and degree.

My thanks to Maya Bergmann, Holly Golightly, Alex Buchko, Adrian Gallo, Ashley Waggoner, and Ruben Aleman for their assistance in the lab. I would like to express thanks to the OSU Soil Health Laboratory for their support, including Adam Fund and Kristin McAdow.

I would like to thank Jennifer Fedenko for her kinship and encouragement. I would like to thank my family for their support, guidance, and enthusiasm. I would like to acknowledge Austin Bramwell, Norman Bramwell, and Charlie Rooney for their patience and continuing support.

Lastly, I would like to thank my M.S. advisor, Jay Norton, for his kindness, his encouragement, his humor, his thoughtful mentorship, and his inspiring career and life. He will be missed.

CONTRIBUTION OF AUTHORS

Rebecca A. Lybrand, Vanessa L. Bailey, Maria Dragila, Kaizad F. Patel, and Angela R. Possinger assisted with data interpretation and analysis. Michael SanClements, Jeffery Hatten, Alexander Kholodov, and Adrian C. Gallo conducted and provided assistance with soil core collection and sampling. Odeta Qafoku, Tamas Varga, Alexander C. Buchko, Anil K. Battu, Loren Reno, Maya Bergmann, and Holly Golightly assisted with data collection and experimental analysis.

TABLE OF CONTENTS

Page

Chapter 1 Introduction 1

- Soil physical properties under freeze-thaw 5
- Biogeochemical response to freeze-thaw 7

Chapter 2 Soil Pore Network Response to Freeze-thaw Cycles in Permafrost Aggregates 11

- Abstract 11
- 1. Introduction 12
- 2. Materials and Methods 15
  - 2.1. Field setting selection 15
  - 2.2 Sample preparation 17
  - 2.3 Freeze-thaw incubation 18
  - 2.4 XCT scanning and image segmentation 18
  - 2.5 XCT Data Processing 19
    - 2.5.1. Pore connectivity 20
    - 2.5.2. Pore coordination numbers 20
    - 2.5.3. Pore throat diameter distributions 20
    - 2.5.4. Pore Shape Factor 21
  - 2.6 Post processing and filtering 22
  - 2.7 Data analysis 23
- 3. Results 23
  - 3.1. Pore morphology 23
  - 3.2 Pore connectivity and volumetric fractions 24
  - 3.3 Pore throat diameter 27
- 4. Discussion 28
  - 4.1. Pore morphology 28
  - 4.2 Pore connectivity and volumetric fractions 31
  - 4.3 Pore throat diameter 34
- 5. Conclusions 35
- Acknowledgments 36
- Data Availability 36

TABLE OF CONTENTS (continued)

Page

Author Contributions 37
References Cited 37

Chapter 3 The role of canopy in soil function across a Fairbanks hillslope in discontinuous permafrost 41

Abstract 41
1. Introduction 42
2. Materials and Methods 45
    2.1 Site description 45
    2.2 Sampling 45
    2.3 Temperature dynamics 46
    2.4 Soil morphology, texture, SOM, and pH 47
    2.5 Fourier transform ion cyclotron resonance mass spectrometry 48
    2.6 X-ray diffraction, total carbon, and total nitrogen 50
    2.7 Total C and N 51
    2.8 Statistics 51
3. Results 53
    3.1 Soil properties 53
    3.2 Carbon Chemistry 56
4. Discussion 61
    4.1 Organic mat thickness and soil temperature 61
    4.2 Vegetation and soil moisture 62
    4.3 Hillslope processes 63
5. Conclusion 64
Acknowledgments 65
Data availability statement 65
References Cited 65

Chapter 4 The impact of freeze-thaw history on soil carbon response to experimental freeze-thaw cycles 70

Abstract 70

TABLE OF CONTENTS (continued)

Page

Plain Language Summary 70
1. Introduction 72
2. Materials and Methods 77
  2.1 Site description and soil sampling 77
    2.1.1 Calculating in situ freeze-thaw cycles 78
  2.2 Freeze-thaw incubation.. 79
  2.3 Fourier transform ion cyclotron resonance mass spectrometry...................... 81
  2.4 Soil properties and characterization 83
  2.5 X-ray diffraction 85
  2.6 NEON biogeochemical data for soil characterization 85
  2.7 Supplemental respiration experiment 86
  2.8 Statistics... 86
3. Results 88
  3.1 Characterization of control soils.. 88
  3.2 SOM composition of control soils... 90
  3.3 SOM composition following experimental freeze-thaw 92
4. Discussion 98
  4.1 Freeze-thaw history and SOM composition 98
  4.2 SOM response to experimental freeze-thaw.. 99
  4.3 The role of mineralogy and moisture conditions in freeze-thaw response of SOM in lower mineral soils.. 102
5. Conclusions 107
Acknowledgments.. 108
Data Availability 108
References Cited 108

Chapter 5 Conclusion... 114

References.. 118

APPENDICES 128

LIST OF FIGURES

Figure Page

Figure 1.1 Data from the NRCS soil temperature monitoring station in Toolik, Alaska. The years represented are 1999 through 2016. Freeze-thaw cycles determined via the FTCQuant package (Boswell, Thompson, et al., 2020). 3

Figure 1.2 (A) Mean annual precipitation (cm), (B) Mean annual temperature (Celsius), and (C) freeze-thaw cycle counts across four Alaskan permafrost sites spanning the discontinuous to continuous permafrost zones. All data from NEON. Freeze-thaw cycles determined via the *FTCQuant* package (Boswell, Thompson, et al., 2020). 4

Figure 1.3 Two XCT-derived cross sections from the same 2.5 cm^3 soil aggregate from Toolik, Alaska. Here, water (blue) and air (black) spaces are shown prior to freeze-thaw (light brown denotes high density coarse fragments and darker brown denotes low density soil). Deformation or changes in connectivity can alter pore network characteristics as well as the soil's ability to retain moisture. 6

Figure 2.1 (A) Map of Alaska with Toolik Field Station indicated by yellow star. (B) 67 cm soil core collected from the NEON site at Toolik, AK and sampled for XCT analysis. 16

Figure 2.2: Experimental Design. Three cores were sampled from Toolik, AK. Two aggregates per core were sampled from upper mineral permafrost horizons. Aggregates underwent five freeze-thaw cycles with XCT scans performed at the beginning and end of the freeze-thaw incubation. 19

Figure 2.3 Rendering of the connected pore network from Aggregate $C_{28\%}$. Example of (left) the unseparated pore network and (right) separating objects as connected objects, representing individual pores in our analysis. 22

Figure 2.4 XCT images of aggregates before and after freeze-thaw with connectivity and type indicated by color. Connected water-filled pores are blue, connected air-filled pores are red, unconnected water-filled pores are light blue, and unconnected-air filled pores are tan/pink. The volumetric fractions (in percent) of connected and unconnected air and water-filled pores (measured through XCT) across the six experimental aggregates before and after freeze-thaw. Dashed lines provided for ease of viewing. Change in the connected water volumetric fraction was significant (LME, F = 9.1977, P = 0.0142). No changes in any other volumetric fraction were significant. 26

Figure 2.5 Pore coordination number frequency before and after freeze-thaw. Higher frequencies indicate an increase in the occurrence of a pore coordination number. Frequency was calculated as the count/total count. The effect of freeze/thaw differed by pore coordination number (LME, F = 5.84007, P < 0.0001). 27

LIST OF FIGURES (continued)

Figure Page

Figure 2.6 Connected pore network with individual pore regions highlighted by color and pore throat diameter distribution frequencies (bin size = 5 microns) before and after freeze-thaw for each aggregate. Frequency was calculated as the count/total count. Arrows represent regions with the largest changes in frequency following freeze-thaw. 29

Figure 3.1 A) Photograph, sampling plot under closed cover (low backslope); B) Sampling plot under open cover (footslope); C) Diagram, hillslope positions (footslope, low backslope, and backslope). Mineral soil horizons from open (n = 3) and closed cover (n = 3) plots were sampled at each hillslope position. 46

Figure 3.2 Temperature fluctuations at 5 cm (upper panel) and 75 cm (lower panel). Temperature measured from open cover (tan) and closed cover (green) at the research area from 2017 to 2021. Temperature data missing for open cover during summer 2018 and 2019. 47

Figure 3.3 van Krevelen regions of carbon compound classes based on H/C to O/C ratios. Points show the distribution of all assigned peaks for the full data set. 50

Figure 3.4 X-ray diffraction, mineral abundances with comparisons between hillslope positions within cover types. Statistical comparisons are within cover types between slope positions (backslope, low backslope, and footslope). All values are percentages (%). 55

Figure 3.5 Principal Components Analysis biplot of FT-ICR-MS data showing separation by hillslope position for both closed (circles) and open (triangle). Ellipses represent 95% confidence intervals. 56

Figure 3.6 Van Krevelen plots showing organic compounds by slope position and cover type. Molecules are plotted as functions of their H-to-C and O-to-C ratios. 57

Figure 3.7 Relative abundances of carbon compound classes with comparisons between slope positions. Differences were determined at significance 0.05. Statistical comparisons are between slope positions within cover types. All values are percentages (%). 58

Figure 3.8 Backslope soils under open cover had higher NOSC, with lignin-like, condensed aromatic, and aromatic molecules showing greater oxidation. Low backslope soils under open had lower NOSC under open. (A) NOSC of compounds unique to each cover type by slope position. (B) Van Krevelen plot showing organic compounds unique to each cover type by slope position. Molecules are plotted as functions of their H-to-C and O-to-C ratios. Ellipses represent 95% confidence intervals. 60

Figure 4.1 Visual hypothesis: Left soil profile is a high freeze-thaw frequency site (Healy), and the right profile is a low freeze-thaw frequency site (Toolik). Freeze-thaw cycles across both sites were measured via the *FTCQuant* package in R (Boswell, Thompson, et al., 2020) using temperature data from the National Ecological Observatory Network (National Ecological Observatory Network, 2021d). 76

LIST OF FIGURES (continued)

Figure Page

Figure 4.2 Short duration freeze-thaw cycles (four hours < -1.5°C and a minimum of four hours > 1.5°C) measured by site and depth using NEON temperature data from 2018-2020 and calculated using the *FTCQuant* Package (Boswell, Thompson, et al., 2020; National Ecological Observatory Network, 2021d). 89

Figure 4.3 Crystalline and poorly crystalline iron and aluminum, reported as percent weight of soil. Toolik had a higher proportion of crystalline iron and aluminum compared with Healy, which was dominated by poorly crystalline compounds (ANOVA, $P < 0.001$). Data from NEON distributed plot soil chemistry data, 2021 release (National Ecological Observatory Network, 2021b). 90

Figure 4.4 (A) Principal Components Analysis biplot of FT-ICR-MS data showing separation by site for control samples. (B) Euclidean distances between sites for each soil depth (controls only). Black stars indicate intra-depth variability at each site whereas the black circles represent the Euclidean distance between sites at each depth. (C) Principal Components Analysis biplot of FT-ICR-MS data showing separation by site for all samples. Solid points = control (freeze-only) samples, open points = FTC treated samples. Ellipses represent 95% confidence intervals. 91

Figure 4.5 Relative abundances (percentage) of carbon compound classes within each material grouping in control and freeze-thaw soils from Healy and Toolik. Asterisks denote significant differences between control and freeze-thaw, at $\alpha = 0.05$. 92

Figure 4.6 Van Krevelen plots showing organic compounds gained (newly identified) and lost following freeze-thaw, by site and depth. Molecules are plotted as functions of their H-to-C and O-to-C ratios. Ellipses represent 95% confidence intervals. See Appendix Figure C3 for illustration of van Krevelen diagram interpretation. 95

Figure 4.7 Nominal oxidation state of carbon (NOSC) for molecules lost or gained (newly identified) following freeze-thaw, by site and depth. Asterisks denote statistically significant differences between treatments at $\alpha = 0.05$. For Healy soils, NOSC of newly identified compounds was greater than NOSC of compounds lost, for all depths. For Toolik organic soils, NOSC of gained > lost, whereas for Toolik upper mineral soils, NOSC of lost > gained following freeze-thaw. 96

Figure 4.8 Nominal oxidation state of carbon (NOSC) for compounds lost or gained (newly identified) following freeze-thaw, by site and compound class (all depths). Statistical significance was determined at $\alpha = 0.05$. There were significant increases in the NOSC of gained compounds (compared to lost compounds) in lignin-like compounds in Healy soils and aliphatic compounds in Toolik. There were significant decreases in the NOSC of gained compounds (compared to lost compounds) in Healy aliphatics as well as Toolik aromatics and condensed aromatics. 97

LIST OF TABLES

Table Page

Table 3.1 Particle size class as determined by hydrometer method. All values reported in percentages with standard error. 53

Table 3.2 Soil properties including soil moisture, total carbon and nitrogen, carbon to nitrogen ratio, SOM % as determined by loss on ignition, organic mat (OM) thickness, and pH. Data was pooled across all depths within each replicate and then averaged across each cover type and slope position combination. Standard error is reported. 55

Table 3.3 Total FT-ICR-MS resolved peaks by treatment. Peaks calculated across all replicates. 57

Table 4.1 Healy and Toolik soil morphology with depth (cm), horizon designation, and material type (organic, upper mineral, and lower mineral).......... 81

Table 4.2 Soil characterization properties for Healy and Toolik soil depths, reported as mean +/- standard error. Moisture is reported as gravimetric moisture content. Particle size classes were determined only for upper and lower mineral soil depths, via sieve and pipette method............. 84

LIST OF APPENDICES

Appendix Page

Appendix A. Soil Pore Network Response to Freeze-thaw Cycles in Permafrost Aggregates .. 129

Appendix B. The role of canopy in soil function across a Fairbanks hillslope in discontinuous permafrost 142

Appendix C. The impact of freeze-thaw history on soil carbon response to experimental freeze-thaw cycles 157

LIST OF APPENDIX FIGURES

Figure Page

Figure A1. Freeze-thaw count across Toolik cores based on NEON instrumentation data and analyzed using the FTCQuant Package (Boswell, 2020). The active layer is indicated by a horizontal black dashed line at 10 cm. Core A aggregates sampled between 28-38 cm, Core B aggregates sampled between 40-50 cm, and Core C aggregates sampled between 41-50 cm. The figure represents three years (2018-2020) of data collection at six distinct 60-cm temperature profiles by NEON at the Toolik Field Station. Temperature data was collected at six depths (every ~10 cm) except for the first two horizons which were collected at 2 cm and 6 cm. Figure A2. Flowchart demonstrating the XCT data processing method, from image acquisition to the three main result outputs (pore throat diameters, pore coordination numbers, and pore volumes). 130

Figure A3. Grayscale scans of the outer aggregate for all six samples prior to freeze-thaw...... 132

Figure A4. Aggregate scans for each of the six samples with before and after scans segmented into high density soil (green), low density soil (red), water (dark blue), and air (light blue). All aggregates have before/after scans from the same region of the aggregate except for Core A, 28% which has scans from two different regions of the core. 133

Figure A5. Examples of grayscale and segmented scans (Core A, 28-38 cm (before freeze-thaw). The grayscale scan was segmented into four components: high density soil (73.6 to 344.5 grayscale range), low density soil (25.6 to 73.6 grayscale range), water (13.1 to 25.6 grayscale range) and air (-5.9 to 13.1 grayscale range). 134

Figure A6. Pore coordination number examples indicated within a ball and stick pore network structure. The model was not used to indicate pore or pore throat geometry and is only provided for connectivity analysis. 135

Figure A7. Comparing line of best fit equations and R-squared values for breadth (A) and width (B), we determined that breadth was highly correlated with manually calculated pore throat diameter. Breadth was used as the proxy for pore throat diameter throughout the experiment. 136

Figure A8. (A) Pore throat diameter distribution using breadth as a proxy for diameter, (B) pore throat diameter distribution using eq radius as a proxy for diameter. 137

Figure A9. Pore shape factor vs. pore throat diameter, before and after freeze-thaw compared within each aggregate. 138

Figure B1. Tree trunk diameters (diameter at breast height). Statistical comparisons are between slope positions (backslope, low backslope, and footslope), $P < 0.05$. All values are in centimeters. 151

Figure B2. Soil morphological descriptions across hillslope positions and within closed vs. open, including horizon designation, munsell color, and depth. 152

LIST OF APPENDIX FIGURES (continued)

Figure Page

Figure B3. Diffractogram patterns from the x-ray diffraction analysis of the mineral soils at the backslope position under (A) closed and (B) open cover. 153

Figure B4. Diffractogram patterns from the x-ray diffraction analysis of the mineral soils at the low backslope position under (A) closed and (B) open cover. 154

Figure B5. Diffractogram patterns from the x-ray diffraction analysis of the mineral soils at the footslope position under (A) closed and (B) open cover. 155

Figure B6. Nominal oxidation state of unique compounds (NOSC) under open and closed cover by slope position and compound class. Statistical significance was determined at α = 0.05. NOSC was higher in aromatic and lignin-like compounds under open cover on the backslope (compared with closed). NOSC was lower in aliphatic and lignin-like compounds under open on the low backslope (compared with closed). NOSC was lower in aliphatics and higher in aromatics under open on the footslope position. 156

Figure C1. Site map for location of extracted soil cores (red points) at NEON study sites in Healy and Toolik, Alaska. Map displays topography at ~ 1 km resolution as well as contrasting latitude along a longitudinal transect across Alaska at ~ 100 km resolution. (*Source: State of Alaska, Esri, HERE, Garmin, SafeGraph, METI/NASA, USGS, EPA, NPS, USDA, FAO, NOAA, and the GIS User Community*). 161

Figure C2. Experimental Design. 162

Figure C3. van Krevelen regions of carbon compound classes based on H/C to O/C ratios...... 163

Figure C4. Mineralogical composition of mineral soils at Toolik and Healy (N = 3). Abundance is in percentage (%). Site had a significant effect on every mineral (ANOVA, P < 0.05). 164

Figure C5. Diffractogram patterns from the x-ray diffraction analysis of mineral soils at (A) Healy and (B) Toolik. Analysis and plotting done using the *powdR* package. 165

Figure C6. Euclidean distances between treatments for each soil depth within each site. Black squares indicate intra-depth variability in control samples, yellow squares indicate intra-depth variability in freeze-thaw samples, and the black circles represent the Euclidean distance between treatments at each depth. 166

Figure C7. Nominal oxidation state of compounds (NOSC) in control soils by site and depth. Asterisks denote statistically significant differences among treatments at α = 0.05. NOSC was higher in all depths of Healy compared with Toolik. 167

LIST OF APPENDIX FIGURES (continued)

Figure Page

Figure C8. CO^2-C measured by the Picarro at day 1, 4, 7, and 14 of a two-week room temperature incubation on the mineral depths of both control and freeze-thaw soils. Only one sample per point (no replication). Gain of ug measures the change in respiration at each sampling time. 168

LIST OF APPENDIX TABLES

Table Page

Table A1: Manual test for determining which parameter best serves as a proxy for pore throat diameters and the impact to capillarity (all measurements are in µm). Based on this data we determined width and breadth to be the only measurements not statistically different from the manually calculated pore throat diameters. 139

Table A2: Pore coordination number tables with difference in frequency (%) calculated as after frequency – before frequency. Negative values indicate decreases in frequency following freeze-thaw. 140

Table A3: Means (µm), medians (µm), and counts for pore throats in all aggregates before and after freeze-thaw. 141

Table B1: Mineralogy abundances as determined by x-ray diffraction. All values are in percent (%), standard error. 142

Table B2. Total carbon and nitrogen by horizon for the backslope position. Standard error for instrument/analytical replicates. No statistical differences between open and closed cover. All values in %. 143

Table B3. Total carbon and nitrogen by horizon for the low backslope position. No statistical differences between open and closed cover. All values in %. 144

Table B4. Total carbon and nitrogen by horizon for the footslope position. No statistical differences between open and closed cover. All values in %. 145

Table B5. Relative abundances of carbon compound classes with comparisons between slope positions. Differences were determined at significance 0.05 via ANOVA and HSD tests. Statistical comparisons are between slope positions within cover types. All values are percentages (%). 146

LIST OF APPENDIX TABLES (continued)

Table Page

Table B6. Relative abundances of carbon compound classes with comparisons between cover type at each slope position. Differences were determined at significance 0.05 via ANOVA tests. Statistical comparisons are between slope positions. All values are percentages (%). 147

Table B7. Relative abundances of carbon compound classes by horizon for all plots at the backslope position. Statistical comparison between grand means of open vs closed. All values are percentages (%). 148

Table B8. Relative abundances of carbon compound classes by horizon for all plots at the low backslope position. All values are percentages (%)... 149

Table B9. Relative abundances of carbon compound classes by horizon for all plots at the footslope position. All values are percentages (%)... 150

Table C1. Site characteristics for Toolik and Healy (NEON, 2022). 169

Table C2. Particle size classes for Healy and Toolik... 170

Table C3: Relative abundances of carbon compound classes within each material grouping before and after freeze-thaw in Healy and Toolik soils, significance 0.05. Statistical comparisons are within site and class between control and freeze-thaw. All values are percentages (%)...... 171

Table C4: Abundances of minerals within each material grouping (measured in the freeze-only control) Healy and Toolik samples. Values are percentages (%). 172

DEDICATION

For Austin, Charlie, and Norman.

Chapter 1 Introduction

Arctic permafrost is in transition. Soils that underwent freezing, organic matter deposition, and permafrost formation over the past millennia are adapting to a new, warmer climate (Anthony et al., 2014; Schuur et al., 2015; Treat et al., 2016; Turetsky et al., 2020). In past eras, such as the early Holocene, permafrost thaw was not unusual. The combined occurrence of permafrost thaw and regrowth (or aggradation) in the Arctic has been characterized as a pattern of cyclical permafrost formation often associated with rapid thaw events or shifts in vegetation (Anthony et al., 2014; Treat et al., 2016; Turetsky et al., 2020). The permafrost thaw currently occurring in high latitudes as climate change progresses is unlike the cyclical patterns of the past. Modern gradual and rapid thaw are occurring in much warmer conditions, and with far larger potential for emissions of methane (CH_4), carbon dioxide (CO_2), and nitrous oxide (N_2O) given that > 50 % of the world's soil organic carbon occurs in permafrost (Biskaborn et al., 2019; McGuire et al., 2018; Schuur et al., 2015; Turetsky et al., 2020).

Recent work by Turetsky et al. (2020) emphasized the high carbon release possible under abrupt thaw alone, reporting simulation-derived net accumulations of 80 ± 19 peta-grams of carbon (PgC) by 2300. Another modeling study by McGuire et al. (2018) investigated gradual thaw and reported possible losses of 208 PgC by 2300, with these losses in addition to the abrupt thaw projections from Turetsky et al. (2020). Predicting how permafrost will respond to continued warming is pivotal to conceptualizing the future of greenhouse gas emissions. But understanding how permafrost will behave in a solely thawed state is not the same as understanding the behavior of thawing permafrost. Permafrost thaw is characterized by the exposure of previously frozen soils to daily and seasonal freeze-thaw, a process that can deform soil physical structure and trigger changes to pore architecture and connectivity (B. Liu, Fan, et al., 2021; Ma et al., 2021; Oztas & Fayetorbay, 2003; Rooney et al., 2022), alter microbial activity through cell lysis and nutrient influxes (Blackwell et al., 2010; Freppaz et al., 2007; Storey & Storey, 2005), and even promote mineral-organic matter interactions depending on soil characteristics (Joss et al., 2022). The challenge in predicting soil function in thawing permafrost is accounting for the highly dynamic and variable effects of freeze-thaw in the heterogeneous landscapes that contain Arctic permafrost.

Our ability to predict, prepare for, and quantify Arctic permafrost thaw is directly related to our understanding of what exposure to continuous freeze-thaw means for a soil previously frozen for tens to thousands of years (Larsen et al., 2002; Manies et al., 2021; Song et al., 2017). A freeze-thaw cycle is herein defined as the soil temperature fluctuating above and below 0 °C. Increasing freeze-thaw cycles were observed at a long-term monitoring site on the Qinghai-Tibetan Plateau where the total number of frozen days decreased between 1988 and 2007 at a rate of 16.8 days per decade (Li et al., 2012). The warmer air temperatures were most influential in discontinuous permafrost and surface soils, while continuous permafrost soils showed less change in freeze-thaw cycle frequency (Li et al., 2012). In Alaska, increasing freeze-thaw cycle frequency has been observed in continuous permafrost sites as shown by data from the Natural Resource Conservation Service (NRCS) soil temperature monitoring station in Toolik, Alaska (Fig. 1.1). Here, despite annual variability in freeze-thaw by depth, we see an increasing frequency of freeze-thaw cycles penetrating deeper into the soil profile for the past two decades.

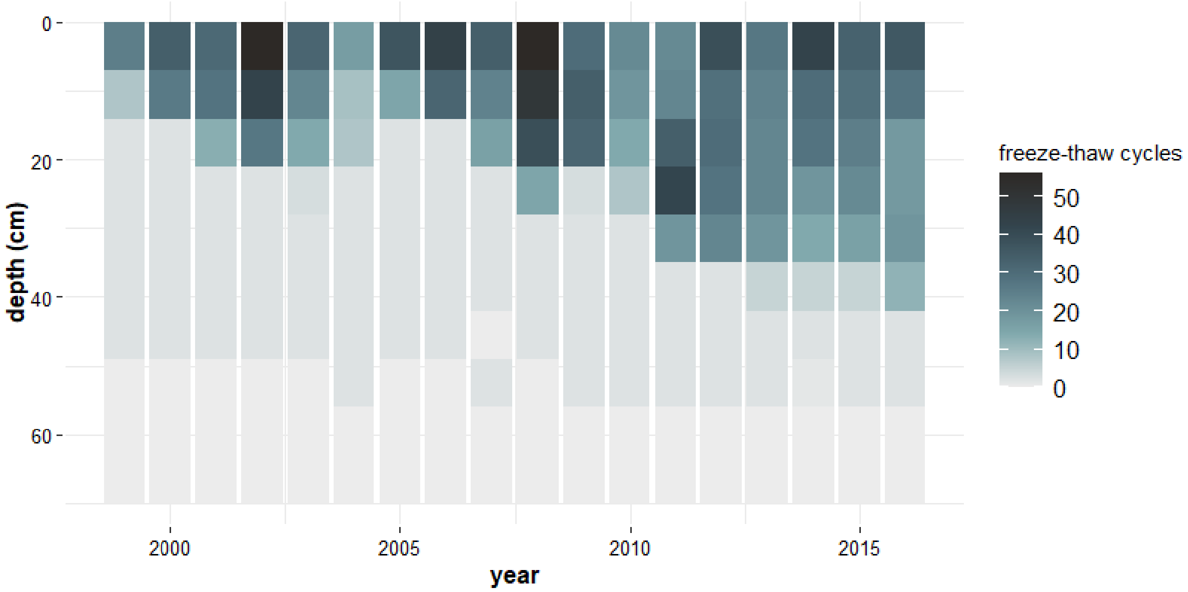

Figure 1.1 Data from the NRCS soil temperature monitoring station in Toolik, Alaska. The years represented are 1999 through 2016. Freeze-thaw cycles determined via the FTCQuant package (Boswell, Thompson, et al., 2020).

Freeze-thaw cycle frequency has been shown to vary with site characteristics across both permafrost and non-permafrost sites, (Fu et al., 2017; Li et al., 2012; Jingyuan Wang et al., 2019). A study in northern China found differences in the depth of freeze-thaw as a function of snow cover thickness and type (compacted vs. natural), with snow cover slowing the rate of soil freezing (Fu et al., 2017). The authors also found differences in surface and subsurface freeze-thaw cycles as well as deeper penetration of warmer soil temperatures under thick snow cover, which echoed previous findings that associated warmer soil and thickening active layers with snow accumulation (Johnson et al., 2013; Shur & Jorgenson, 2007). The effect of snow accumulation on permafrost has highlighted the importance of canopy cover on ground temperatures in permafrost landscapes. A boreal forest study in eastern Siberia found that forest cover reduced solar radiation exposure of the ground surface by 90%, altering snow cover and soil insulation during winter (Stuenzi et al., 2021). In permafrost landscapes dominated by Black spruce and White spruce trees, the impact of canopy can vary depending on hillslope position, with wetter downslope positions favoring smaller Black spruce trees while drier upslope positions favor larger White spruce trees with increased canopy (J. R. Brooks et al., 1998). Despite a clear link between tree canopy and soil temperature, the role of canopy in temperature-driven differences at the hillslope scale in forested permafrost regions is unresolved (Chasmer et al., 2011; Kobayashi et al., 2014).

Data from the National Ecological Observatory Network shows the variation in seasonal freeze-thaw cycles by depth across a latitudinal permafrost transect in Alaska at the site level (Fig. 1.2). Here, the warmest and wettest sites show the most freeze-thaw compared with the colder and drier high latitude sites (Fig. 1.2c). The impact of climate change on freeze-thaw cycle frequency and depth at individual permafrost sites remains understudied, as do the effects of freeze-thaw cycles on the physical and biogeochemical state of these carbon-rich soils. This dissertation seeks to investigate the role of freeze-thaw as a key component of permafrost thaw, examining soil function across permafrost landscapes through the lens of this disruptive, temperature-driven process.

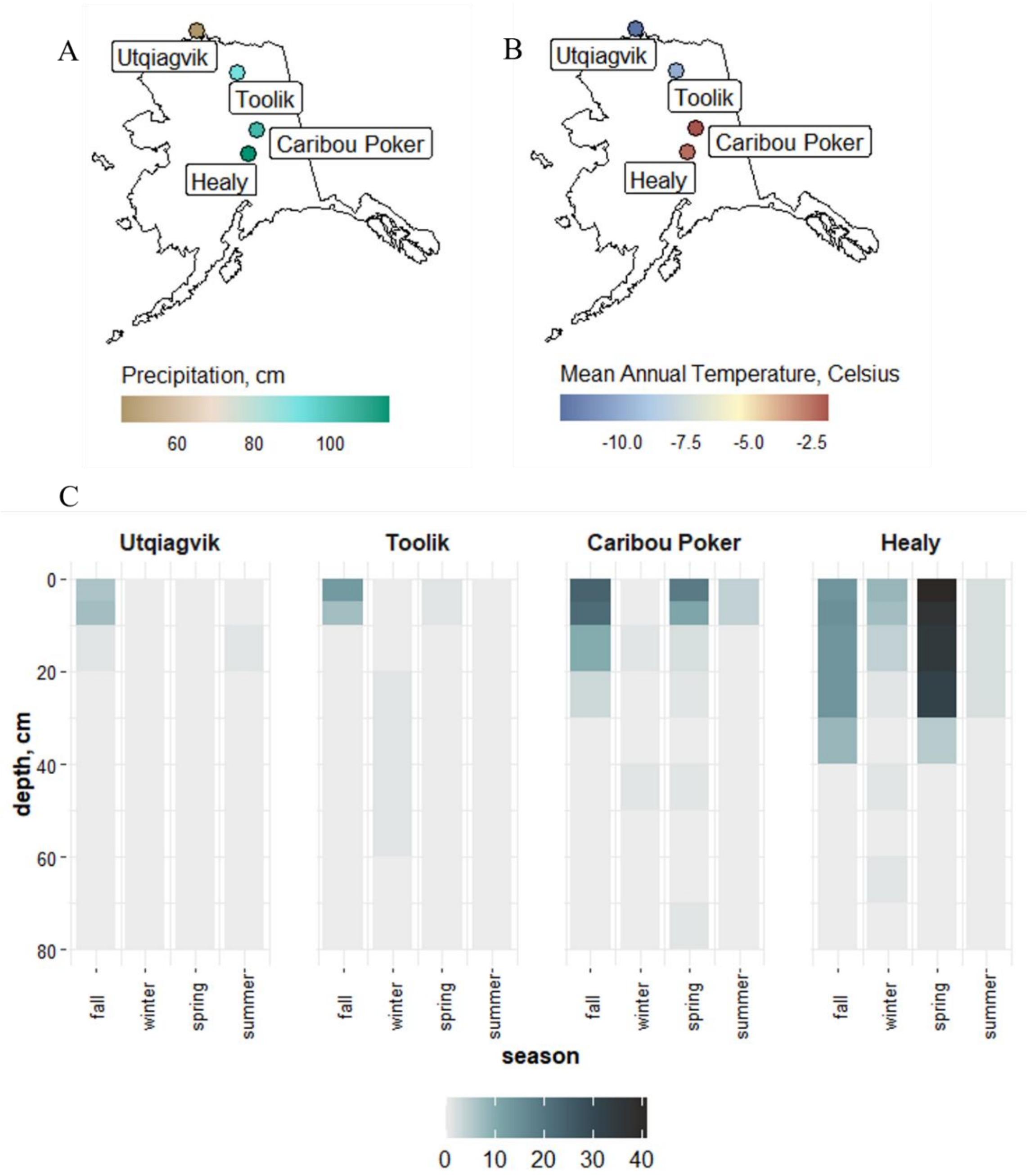

Figure 1.2 (A) Mean annual precipitation (cm), (B) Mean annual temperature (Celsius), and (C) freeze-thaw cycle counts across four Alaskan permafrost sites spanning the discontinuous to continuous permafrost zones. All data from NEON. Freeze-thaw cycles determined via the *FTCQuant* package (Boswell, Thompson, et al., 2020).

Soil physical properties under freeze-thaw

Freeze-thaw impacts can manifest from the micro to macro-scale. The microscale mechanisms influenced by freeze-thaw cycles remain an ongoing topic of research that focuses on particle reorganization, ice lens development, and frost heave (Rempel, 2010; O'Neill & Miller, 1985) with more information needed to understand and predict soil pore deformation (Starkloff et al., 2017; Deprez et al., 2020; Seto & Konrad, 1993). The current understanding of water transport and soil deformation during freezing in an unsaturated, porous media centers around the cryogenic suction of unfrozen water driven by a temperature-derived fluid pressure gradient in which water is drawn from capillary stores through unfrozen water films, feeding ice crystal growth and increasing pressure on surrounding pore walls (Fukuda, 1983; Wettlaufer et al., 1996; Rempel, 2010). Freezing water at the colder end of the fluid pressure gradient has been found to accumulate ice crystals in the most frost-susceptible pore and pore throat sizes (Rempel, 2010). The expansion of water into ice deforms the soil pore structure as demonstrated by increases in macropore size (Starkloff et al., 2017; Liu et al., 2021b) and crystallization pressure measured within pores (Deprez et al., 2020; Seto and Konrad; 1994).

Water transport during the freezing portion of the freeze-thaw cycle is a function of temperature distribution and ice crystal formation as shown by a micrograph freezing experiment which used a water-fed membrane to demonstrate that flow occurs from areas of high fluid energy (warm) to low fluid energy (cold) independent of capillary forces (Wilen & Dash, 1995). Subsequent findings suggested the need for delineations in freeze-thaw disturbance potential by recognizing that the amount of flow and crystal growth reflected the ratio of frozen to unfrozen soil, soil chemical and physical properties, and the steepness of the temperature gradient (Wilen & Dash, 1995; Wettlaufer et al., 1996; and Fukuda, 1983). We have yet to identify a definitive threshold under which crystallization pressure is guaranteed to result in deformation, although pore size and surface tension across the pore-crystal interface are contributing stressors on pore walls (Scherer, 1998). Little information exists for how pore throat size distribution and pore connectivity may be impacted by freeze-thaw deformations to individual pores, or how these responses may vary across multiple aggregates. Understanding the impacts of freeze-thaw on soil function and whether those impacts persist evenly over continued freeze-thaw cycles is crucial to predicting hydrologic changes in permafrost regions (Liu et al., 2021b), especially in soils with no recent history of freeze-thaw. Technological advances in cutting edge capabilities, such as X-ray computed tomography (XCT), enable microscale investigations of permafrost soils and the ability to perform non-destructive, microscale analyses of materials in freeze-thaw incubation experiments (Fig. 1.3). As freeze-thaw cycles alter the pore network within the deepening active layer of permafrost soils, additional work is needed to determine if soils lose the physical properties that enabled ice-richness that would compromise permafrost retention with warming.

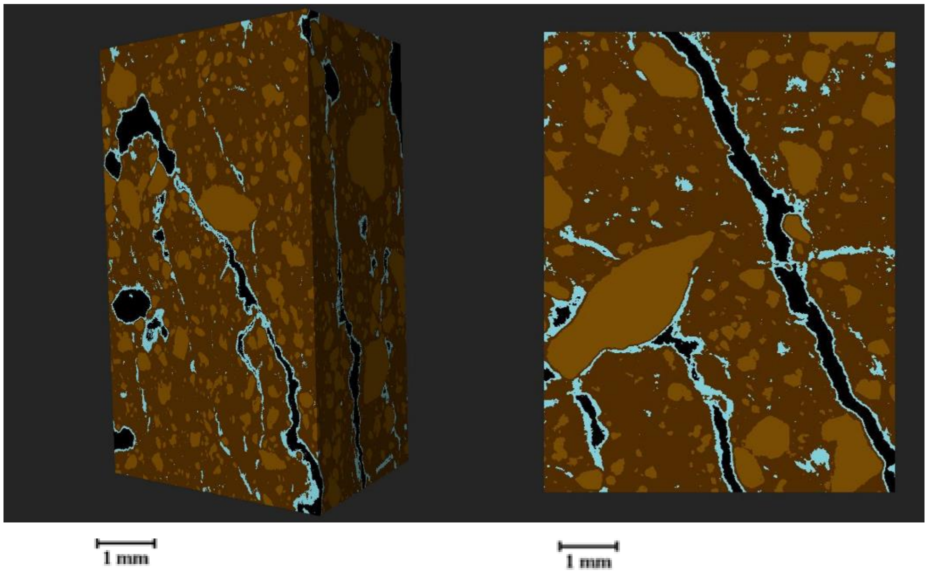

Figure 1.3 Two XCT-derived cross sections from the same 2.5 cm^3 soil aggregate from Toolik, Alaska. Here, water (blue) and air (black) spaces are shown prior to freeze-thaw (light brown denotes high density coarse fragments and darker brown denotes low density soil). Deformation or changes in connectivity can alter pore network characteristics as well as the soil's ability to retain moisture.

Deformation from freeze-thaw assumes two main forms, expansion or contraction of the pore or pore throat (Deprez et al., 2020). Expansion can result in a loss of capillary tension at field capacity if pore throat diameters exceed 30 µm, resulting in the soil favoring drainage in accordance with the Laplace equation (J. Q. Wang et al., 2015). Contraction of pore throats can impact pore connectivity, potentially isolating large swaths of the pore network and result in a larger volume of “inactive” or unconnected pores. Generally, “inactive” pores disconnected from the pore network are excluded from storing and transporting water and gases, leading to a simplification of the pore network and decrease in water storage and transport (Menon et al., 2020). The potential for freeze-thaw to deform and restructure the soil pore network could alter how water and air move through Arctic landscapes. The cross-scale influences of freeze-thaw necessitate the determination of how significant these effects may be and if they should be incorporated in current groundwater models for permafrost conditions.

Biogeochemical response to freeze-thaw

Beyond physical deformation and reorganization, freeze-thaw cycles can disrupt soil biogeochemistry by altering solute concentrations and salt distribution during freezing (Bing et al., 2015); exposing or isolating organic compounds (Gao et al., 2017; Song et al., 2017) which leads to increases in soluble C and N losses in runoff (Freppaz et al., 2019); and shifting microbial community composition and dynamics (Wu et al., 2019). When discussing biogeochemical impacts, the importance of multiple freeze-thaw cycles compared with the initial freeze-thaw cycle depends on the focus of the freeze-thaw experiment. The initial freeze-thaw cycle has been well established as a driver of microbial cell lysis. A decrease in microbial nitrogen and increase in available nitrogen was identified following the first simulated freeze-thaw cycle in sandy, high alpine soils from Northwest Italy (Freppaz et al., 2007). A meta-analysis by Song et al. (2017) reported findings from multiple studies in which over half of total microbial death during freeze-thaw occurred during the initial freeze-thaw cycle (Koponen et al., 2006; Sawicka et al., 2010; Skogland et al., 1988; Song et al., 2017). One study examined repeated freezing and thawing on Arctic sediment from an intertidal flat on Svalbard, Norway. Following initial freeze-thaw (with the thawed state at 4 °C) researchers reported a steep decline in microbial activity of 95.75 % compared with activity prior to freeze-thaw. However, the initial decline was followed by an equally steep incline as activity resumed to 60 % of pre-freeze-thaw levels (Sawicka et al., 2010). Other studies found a lessened impact of multiple freeze-thaw cycles following initial freeze-thaw, with Patel et al. (2021) reporting no influence of multiple freeze-thaw cycles (with comparisons of one, two, and six freeze-thaw cycles of -10 ˚C and + 5 ˚C) on ammonium concentrations in soils from a coniferous forest in Maine.

Other findings have reported significant differences between a single and multiple freeze-thaw cycles. Microbial community composition has been found to shift in favor of bacteria following multiple freeze-thaw cycles (Song et al., 2017) while the Italian freeze-thaw study mentioned above (Freppaz et al., 2007) noted changes in available and organic phosphorus as freeze-thaw cycles continued in one of four soils studied. Notably, while the microbial response may be strongest following the first freeze-thaw cycle, other biogeochemical changes may be cumulative over continuous freeze-thaw (i.e., mineral and pore deformation, aggregate disruption). A wetland experiment investigating dissolved organic carbon (DOC) sorption in soils from the Sanjiang Plain in Northeast China found that sorption capacity increased across five freeze-thaw cycles (Yu et al., 2010). The authors posited that reactive iron minerals increased across the five freeze-thaw cycles. Similarly, the team concluded that clay minerals (such as hydrous mica) may become more reactive during freeze-thaw as a result of aggregate breakage and exposure of available mineral surfaces (Yu et al., 2010).

While experimental freeze-thaw has captured changes in cumulative biogeochemical effects, longer freeze-thaw history, such as examined indirectly through cryoturbation and permafrost formation, may also impact the vulnerability of carbon to mineralization and loss during thaw. A recent paper examining the role of permafrost formation and type on carbon decomposability found that soils with epigenetic permafrost, or soils in which peat formed prior to rather than in combination with permafrost) resulted in less carbon bioavailability and losses following thaw compared with sites containing syngenetic permafrost (peat and permafrost formed in combination) (Manies et al., 2021). Interestingly, the likely decomposition that occurred prior to permafrost formation in epigenetic permafrost soils may have encouraged protective mineral-organic matter associations as observed in an Arctic permafrost experiment in the Lower Kolyma Region of Russia (Gentsch et al., 2015). Using findings obtained via x-ray photoelectron spectroscopy and nuclear magnetic resonance, researchers proposed that the lower bioavailability of carbon in frozen permafrost soils to be a function of mineral-associations such as aluminum and iron oxide and clay mineral sorption or co-precipitation of dissolved organic carbon (Gentsch et al., 2015). Reactive iron associations with organic carbon were recently reported in cryoturbated soil horizons at concentrations ~7 % higher than in non-cryoturbated organic and mineral horizons (Joss et al., 2022). Cryoturbation is driven by seasonal freeze-thaw processes (Mackay, 1980), further highlighting the gap in our understanding of how freeze-thaw may influence carbon availability and protection as permafrost soils become more exposed to and susceptible to freeze-thaw.

This dissertation investigates freeze-thaw processes in permafrost soils across three scales: (1) impacts of freeze-thaw to physical properties of the pore network at the micron-scale, (2) the effect of canopy-driven differences in ground temperature on carbon dynamics at the hillslope scale, and (3) the role of previous freeze-thaw history on carbon response to experimental freeze-thaw across two permafrost tundra sites in Alaska. The overarching goal of this work is to identify the physical and biogeochemical responses of thawing permafrost soils to freeze-thaw, and to understand how heterogeneous that response will be both within and across multiple scales of study.

SOIL PORE NETWORK RESPONSE TO FREEZE-THAW CYCLES IN PERMAFROST AGGREGATES

Erin C. Rooney, Vanessa L. Bailey, Kaizad F. Patel, Maria Dragila, Anil K. Battu, Alexander C. Buchko, Adrian C. Gallo, Jeffery Hatten, Angela R. Possinger, Odeta Qafoku, Loren. R. Reno, Michael SanClements , Tamas Varga, Rebecca A. Lybrand

Geoderma
Netherlands
Issue 411

Chapter 2 Soil Pore Network Response to Freeze-thaw Cycles in Permafrost Aggregates

Abstract

Climate change in Arctic landscapes may increase freeze-thaw frequency within the active layer as well as newly thawed permafrost. A highly disruptive process, freeze-thaw can deform soil pores and alter the architecture of the soil pore network with varied impacts to water transport and retention, redox conditions, and microbial activity. Our objective was to investigate how freeze-thaw cycles impacted the pore network of newly thawed permafrost aggregates to improve understanding of what type of transformations can be expected from warming Arctic landscapes. We measured the impact of freeze-thaw on pore morphology, pore throat diameter distribution, and pore connectivity with X-ray computed tomography (XCT) using six permafrost aggregates with sizes of 2.5 cm^3 from a mineral soil horizon (Bw; 28-50 cm depths) in Toolik, Alaska. Freeze-thaw cycles were performed using a laboratory incubation consisting of five freeze-thaw cycles (-10˚C to 20˚C) over five weeks. Our findings indicated decreasing spatial connectivity of the pore network across all aggregates with higher frequencies of singly connected pores following freeze-thaw. Water-filled pores that were connected to the pore network decreased in volume while the overall connected pore volumetric fraction was not affected. Shifts in the pore throat diameter distribution were mostly observed in pore throats ranges of 100 microns or less with no corresponding changes to the pore shape factor of pore throats. Responses of the pore network to freeze-thaw varied with aggregate, suggesting that initial pore morphology may play a role in driving freeze-thaw response. Our research suggests that freeze-thaw alters the microenvironment of permafrost aggregates during the incipient stage of deformation following permafrost thaw, impacting soil properties and function in Arctic landscapes undergoing transition.

Key words: pore morphology, pore connectivity, freeze thaw, microscale, permafrost thaw, Arctic, aggregates.

1. Introduction

Arctic ecosystems are poised to undergo heightened impacts from climate change, with air temperatures rising at twice the global average rate and 40% of existing permafrost predicted to thaw over the next 80 years (Chadburn et al., 2017; Schuur et al., 2015). Permafrost thaw and associated changes to the biogeochemical function of Arctic terrestrial systems are difficult to predict due to the unique soil processes characteristic of cold regions (Biskaborn et al., 2019; Brown & Romanovsky, 2008). Freeze-thaw, a dominant process in permafrost soils, is expected to increase in frequency and penetration depth, reaching previously frozen soil horizons. Our understanding of how the disruptive process of freeze-thaw will transform the Arctic soil environment hinges on investigating the response of thawing permafrost to repeated freeze-thaw at multiple scales.

Freeze-thaw drives soil development processes in permafrost landscapes such as frost heave, cryoturbation, and the expression of surface morphological properties including ice wedge polygons, sorted circles, and hummocks (Mackay, 1980; Ping et al., 2015; Rempel, 2010). Cryoturbation, or the sorting and mixing of different horizons, can dictate carbon distribution and protection by redistributing material from upper horizons to deeper in the profile where cold permafrost temperatures decrease microbial activity and promote organic matter persistence (Ping et al., 2008, 2015). Freeze-thaw events also regulate surface water flow and accumulation by influencing the formation of patterned ground features and associated saturation gradients (Ping et al., 2008). Shifts in microbial community function, abundance, and composition (Blackwell et al., 2010; Soulides & Allison, 1961; Storey & Storey, 2005) as well as nitrogen and phosphorus availability (Freppaz et al., 2019; D. Gao et al., 2018; Song et al., 2017; Ying Zhao et al., 2021) have been observed following single or multiple freeze-thaw events. Freeze-thaw impacts particle reorganization at the microscale which propagates to the macro-scale, emphasizing the importance of microenvironment susceptibility and response to freezing processes. The upscaled effects of pore network evolution resulting from continued freeze-thaw is demonstrated in the structural and spatial differences of pores associated with hummocks versus interhummocks in an alpine meadow study in the Qinghai Lake watershed (Z. Gao et al., 2021). The study reported an association between individual surface features and macropore morphology as well as response to freeze-thaw. The shifting of physical properties following freeze-thaw remains less studied in thawing permafrost soil but may reflect recent findings in non-permafrost soil such as an increase in pore deformation and heightened pore connectivity after multiple freeze-thaw cycles (B. Liu, Ma, et al., 2021; Ma et al., 2021; Yunduo Zhao et al., 2021). Changes to the pore network architecture can have potential ramifications for organic matter decomposition (Waring et al., 2020), oxygen availability, and water flow (Wanzek et al., 2018). Given the impacts of freeze-thaw to the micro-scale biogeochemical properties and function of permafrost, additional pore-scale investigations in permafrost soils are required to better understand the impact of freeze-thaw on soils that have undergone little to no temperature fluctuations above 0˚C in recent years. Defining the response of the soil pore network to freeze-thaw is central to predicting hydrologic and carbon distribution changes within the active layer of permafrost-affected soils as well as upscaling the impacts of these changes to surface morphologic and vegetation shifts following increased warming.

The microscale response and evolution of pore networks within thawing permafrost soils represents an important knowledge gap given our limited ability to predict how pore connectivity and pore throat size distribution will change following freeze-thaw. Applying X-ray imaging (micro-computed tomography; µ-XCT) to the study of freeze-thaw in permafrost soils provides insight into how previously frozen soils may respond at the pore-level to freeze-thaw cycles (B. Liu, Fan, et al., 2021; B. Liu, Ma, et al., 2021; Ma et al., 2021; Yunduo Zhao et al., 2021). The impact of changes in porosity and pore connectivity on water holding capacity were reported in a recent experiment that found increased pore sizes within the 100-500 µm range following treatments of up to twenty freeze-thaw cycles (-10˚C to 6˚C) in a silty loam Mollisol from northeast China using XCT analysis (B. Liu, Fan, et al., 2021). Microscale responses of the pore networks in permafrost to freeze-thaw deformation require additional investigation, especially in the 20-100 µm range where soil water holding capacity and pore connectivity may be impacted. Pore-level responses can change the saturation-pressure relationship (thus altering water retention and drainage) through collapse or expansion of pore throats within critical size ranges for water holding capacity (B. Liu, Fan, et al., 2021). Changes in pore connectivity, pore size, and pore throat size could impact microbial accessibility to nutrients and other compounds exerting influence over decomposition rates and organic matter persistence (Waring et al., 2020). Freeze-thaw has been reported to alter pore throat morphology (B. Liu, Ma, et al., 2021) with an increasing number of freeze-thaw cycles corresponding to changes in the pore throat length, pore throat count, and pore throat surface area. Exposing non-permafrost, silty loam soil cores to seven freeze-thaw cycles (-10˚C to 7˚C) contributed to a loss of resilience in pore response as defined by the inability of the pore network to retain its original structure and connectivity following freeze-thaw, with lower resilience evidenced by pore expansion and increased connectivity of the pore network as measured through XCT (Ma et al., 2021). Conversely, an earlier study using XCT to assess two soil textures (silty clay loam and loamy sand) from an agricultural soil in Norway found that six freeze-thaw cycles (-15˚C to 40˚C) reduced macro-porosity and decreased pore specific surface area of macropores, with greater effects to aggregates with coarser soil textures (Starkloff et al., 2017). A depth-based freeze-thaw study examining the impact of fluctuations between -10˚C and 20˚C in an alpine permafrost meadow soil identified decreases in pore connectivity (XCT) following five freeze-thaw cycles and decreased water infiltration following ten freeze-thaw cycles within the first 7.5 cm of the soil, with a variation of freeze-thaw response of the pore network by soil depth and soil texture (Yunduo Zhao et al., 2021).

The objective of our research was to measure the impact of repeated freeze-thaw cycles on the physical structure of permafrost aggregates using non-destructive, high resolution imaging capabilities (XCT) at resolutions of 20 µm. Specifically, we measured how soil pore networks in macroaggregates (2.5 cm^3) subsampled from permafrost soils (Toolik, AK) responded to five experimental freeze-thaw cycles (-10°C to 20°C) that simulated conditions relevant to Arctic surface environments (National Ecological Observatory Network, 2021d). We investigated pore morphology and deformation due to freeze-thaw by measuring pore connectivity and pore throat diameter distribution before and after freeze-thaw events. We hypothesized that freeze-thaw would increase pore connectivity across all aggregates through the expansion of smaller pore throats (<50 microns), based on findings from prior work (Deprez et al., 2020; B. Liu, Ma, et al., 2021; Ma et al., 2021; Starkloff et al., 2017). We provide a pore-scale perspective on changes to the pore network occurring at this incipient stage of permafrost warming, specifically within the first five freeze-thaw cycles following thaw. Our work contributes to the current understanding of freeze-thaw deformation while providing data needed for future predictions of how climate warming will alter the physical properties of globally important Arctic landscapes.

2. Materials and Methods

2.1. Field setting selection

The National Ecological Observatory Network (NEON) Toolik site is part of the Toolik Field Station, located at 828 meters above sea level within the Arctic foothills of the Brooks Range, with tussock tundra and dwarf shrub comprising the dominant vegetation (National Ecological Observatory Network, 2019). Mean annual precipitation is 316 mm (including an average of 176 mm of precipitation as snow) with a dominant southerly wind direction, a mean annual temperature of 10.1°C, and an average snow depth of 50 cm (DeMarco et al., 2011; National Ecological Observatory Network, 2021a; T. Wang et al., 2012). Toolik, Alaska was an ideal study area due to its shallow active layer, minimal freeze-thaw history, and available soil temperature instrumentation. The site falls within the continuous permafrost zone with soils classified as Gelisols (National Ecological Observatory Network, 2021c; Soil Survey Staff, 1999) derived from Holocene glacial moraines and alluvial deposits (U.S. Geological Survey, 2005). Three soil cores (less than one meter in depth) were collected from the Toolik site on an east-facing slope shoulder toward the base of a plateau in April of 2016 (Fig. 2.1). Cores were extracted using a Gidding’s probe (Giddings Machine Company, Windsor, CO, USA), and shipped frozen to Oregon State University (OSU) and preserved at -40 °C.

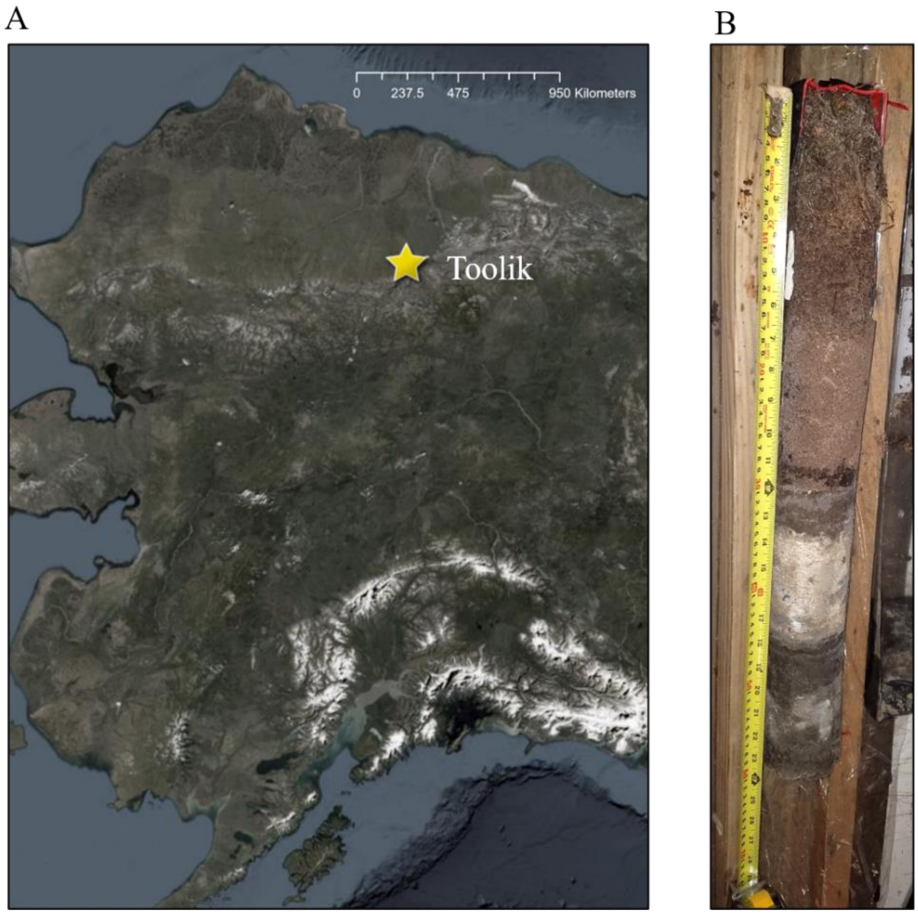

Figure 2.1 (A) Map of Alaska with Toolik Field Station indicated by yellow star. (B) 67 cm soil core collected from the NEON site at Toolik, AK and sampled for XCT analysis.

To confirm that Toolik experiences little to no recent freeze-thaw cycling at the depths sampled (to allow us to target incipient stages of deformation following permafrost thaw), we used temperature data available for the site (National Ecological Observatory Network, 2021d) and calculated the number of freeze-thaw cycles by season between 2018 and 2020 (fall, winter, spring, summer) using the *FTCQuant* R package (Boswell et al., 2020b). For computational functionality, soil temperature data from sensor units were excluded if missing data exceeded 3% of measurement time points within each analysis time frame, resulting in one to five usable time series measurements for each depth by season combination. Freeze-thaw analysis within the *FTCQuant* package uses time series temperature data to estimate the number of times soil temperature was below and above a defined temperature cutoff for more than a defined duration of time. For this analysis, we defined freeze-thaw cycles as soil temperature fluctuations persisting for a minimum of twelve hours < -2°C and a minimum of twelve hours > 2°C. These parameters align with previously published freeze-thaw methods (Boswell et al., 2020; Henry, 2008; Ma et al., 2021). The results from this analysis can be found in Appendix Figure A1.

2.2 Sample preparation

Cores were described morphologically according to pedological characteristics including organic and mineral material (Ping et al., 2015; Soil Survey Staff, 2014). Six aggregates (two per core) were collected from upper mineral permafrost horizons (Fig. 2.2). The aggregates were ~2.5 cm in diameter and were collected from the same morphological horizon within each core. Sampled depths targeted uniform soil texture, classified as silt loam (23.07% sand, 56.8% silt, and 20.13% clay) with ~11% organic carbon content (Nave et al., 2021). Core A aggregates were sampled between 28-38 cm, Core B aggregates sampled between 40-50 cm, and Core C aggregates sampled between 41-50 cm.

Samples were collected from each core using a chisel and mini sledgehammer to create 5-10 cm thick soil disks, allowing natural aggregates to separate as disks broke apart. Aggregates were air-dried at 20°C for 24 hours and then re-wet with deionized water using a sterile dropper to moisture contents of either 12-16% or 28% weight water content. The aggregates were air-dried in order to ensure both consistent moisture content and adequate aggregate strength to avoid sample loss during freeze-thaw treatments and scanning with XCT prior to and following the freeze-thaw treatments. Once rewet to the target moisture, aggregates were fit tightly (aggregates edges were in contact with the tube walls) into 15 mL plastic conical-bottom centrifuge tubes for the remainder of the experiment to hold aggregates in a set position and identical orientation for the before and after freeze-thaw scans. The two moisture contents were selected to represent the potential for seasonal variability in soil wetness, both saturation (28%) and dry conditions (12-16%).

2.3 Freeze-thaw incubation

Each aggregate underwent five freeze thaw cycles of 20°C (thaw) to -10°C (freeze) in a temperature-controlled chamber (Refrigerator/Freezer Isotemp, Fisher Scientific) with each full cycle taking four days (two days for thaw and two days for freeze). The large range in soil temperature and duration was selected to ensure that each freeze-thaw cycle occurred fully and equally throughout the soil. Full freezing/thawing was achieved in less than 24 hours for the amount of soil used (2.5 cm diameter aggregate), however an extra 24 hours was added to ensure completion of the freeze-thaw cycle (Ma et al., 2021). Aggregates were maintained in a closed system (Parafilm and tight-fitting lids over centrifuge tubes) to prevent moisture loss.

2.4 XCT scanning and image segmentation

Soil aggregate samples were imaged before and after the freeze-thaw incubation in plastic conical-bottom centrifuge tubes using XCT on an X-Tek/Metris XTH 320/225 kV scanner (Nikon Metrology, Belmont, CA). Data were collected at 100 kV and 400 μA X-ray power. A 0.5-mm thick Cu filter was used to enhance image contrast by blocking out low-energy X-rays. The samples were rotated continuously during the scans with momentary stops to collect each projection (shuttling mode) while minimizing ring artifacts. A total of 3000 projections were collected over 360˚ rotation recording 4 frames per projection with 708 ms exposure time per frame. Image voxel size was 10.2 microns. The images were reconstructed to obtain 3D datasets using CT Pro 3D (Metris XT 2.2, Nikon Metrology). Representative slice and 3D images were created using VG Studio MAX 2.1 (Volume Graphics GmbH, Heidelberg Germany) and Avizo 2019.2 (Thermo Fisher Scientific, Waltham, MA). Image processing and porosity analysis was carried out using Avizo 2019.2. The reconstructed 3D volume data was filtered using a median filter and cropped to comparable (between aggregates) rectangular prism shaped volumes of an average of 620 x 674 x 792 voxels to exclude surrounding air space while maximizing the analyzed soil volume.

2.5 XCT Data Processing

The XCT data processing method followed a multistep protocol outlined in Appendix Figure A2. Each image was first segmented into air, water, low-density soil, and high-density soil, based on manual thresholding (Appendix Figures A3-A5). Each voxel was assigned a value between 1 and 4 that correlated to its assigned component (i.e., air, water, soil, and high-density soil). Air and water voxels were then selected from the segmented image and an "OR" operation (binary operation to provide all the voxels that are water **or** air) was conducted to create a binary image that combined water and air. We used both the air and water voxels as the pores are connected by waterways, even if individual pores were not connected directly by air space. Following segmentation, we extracted (1) air and water-filled pore volumes from both the connected pore network and unconnected pores, (2) pore coordination numbers (defined below), and (3) pore throat diameters (Fig. 2.2). These data were obtained for soil pores down to a resolution of 20 microns. This minimum resolution was twice the resolution of measured voxels.

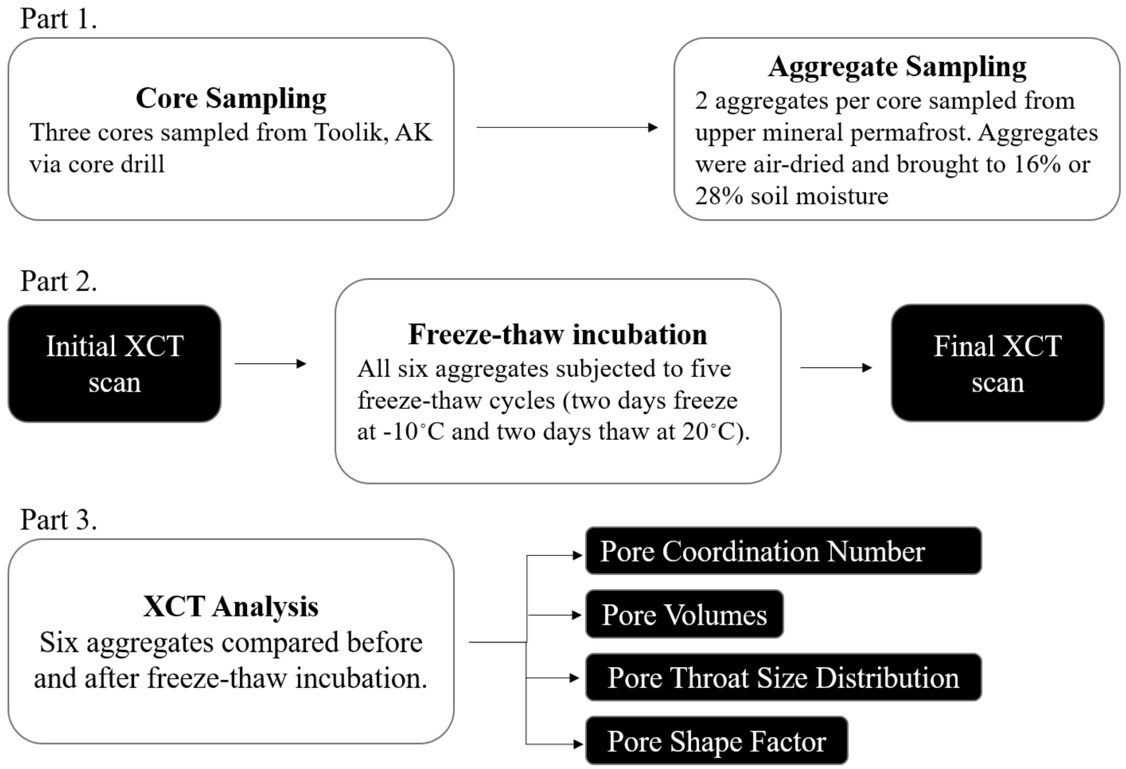

Figure 2.2: Experimental Design. Three cores were sampled from Toolik, AK. Two aggregates per core were sampled from upper mineral permafrost horizons. Aggregates underwent five freeze-thaw cycles with XCT scans performed at the beginning and end of the freeze-thaw incubation.

2.5.1. Pore connectivity

Determining pore connectivity required the selection of parameters that pores must adhere to in order to be considered “connected” and part of the main pore network. Using the Axis Connectivity Module in Avizo, we required pore networks to extend between two opposing faces of the volume’s bounding box. The opposing faces were defined as two planes normal to the either the X, Y, or Z axis depending on which axis was most suitable to the pore network of each individual sample. In cases where no volumes satisfied the axis connectivity requirements, we defined the connected pores as the connected group of water/air with the largest volume using the Filter by Measure module in Avizo.

2.5.2. Pore coordination numbers

Coordination number represents the number of other pores to which a specific pore is connected. Coordination numbers were obtained by converting pore structure into a ball (pore node) and stick (connected paths between pore nodes) model (Li et al., 2019). The number of nodes a given node is directly connected to dictates its coordination number, i.e., a pore node connected to three other pore nodes has a coordination number of “3” (Appendix Figure A6). This metric provides information about the connectivity of the pore network, with before and after freeze-thaw comparisons of the distribution of coordination numbers to illuminate if and how connectivity is changing.

2.5.3. Pore throat diameter distributions

The watershed algorithm was used to separate and define individual pore regions within the pore network as distinct objects (interpretation: 3D; Neighborhood: 26; Marker Extent: 27; Output type: Split; Algorithm Mode: Repeatable) (Ferreira et al., 2018). Following delineation of individual pore regions, connected and unconnected pores and pore throats were identified using the “XOR binary operation” (to quantify the difference between all pore network voxels and distinct pore voxels) (e.g., shown in Figure

2.3). Volume measurements for pore regions were extracted using the AVIZO software for unconnected and connected pore regions delineated by water and air. Pore regions were defined as the pore area that was not included in the pinch point between two pores. Pore throats are conventionally defined as the constrictive region (pinch point) between pores (Nimmo, 2013). Within an XCT context we defined pore throats as connecting regions (voxels of equivalent grey scale intensity to those of pores) between individual pores within the connected pore network. Throats were not part of the distinct individual pores but rather pinch points representing the connecting region between two neighboring pores. Each pore throat was manually given a unique label before the volume, equivalent radius, surface area, feret width, feret length, and feret breadth were calculated and then compared to a manually measured pore throat diameter to determine which metric was most representative. Feret breadth was not significantly different from manually calculated pore throat diameter (LME, F = 3.7265, P = 0.1258) and was highly correlated with the manually calculated diameters ($R^2 = 0.96$, P = 0.01) (Appendix Table A1, Appendix Figure A7). Equivalent radius was less accurate than feret breadth for the pore throat sizes we studied (Appendix Figure A8). Thus, we used breadth as a proxy for pore throat diameter herein.

2.5.4. Pore Shape Factor

Pore shape factor for pore throats was calculated as the ratio between the pore throat's surface area and its spherical equivalent surface area, which is the surface area of a sphere with the same volume as the pore throat. Spherical pore throats contain pore shape factors between 0.75-1.00 versus ratios <0.75 for more irregular or elongated pore throats <0.75. The equation for pore shape factor:

$$SF = \frac{A_o}{A}$$

A_o represents the spherical equivalent surface area while A is the actual surface area (Wadell, 1933). The spherical equivalent surface area formula was:

$$A_o = 4\pi\left(\sqrt[3]{\frac{3}{4\pi}V}\right)^2$$

With V being the volume of the pore throat. This formula used the volume of a sphere solved in terms of the radius, $r = \sqrt[3]{\frac{3}{4\pi}V}$, and the formula for the surface area of the sphere, $A = 4\pi r^2$.

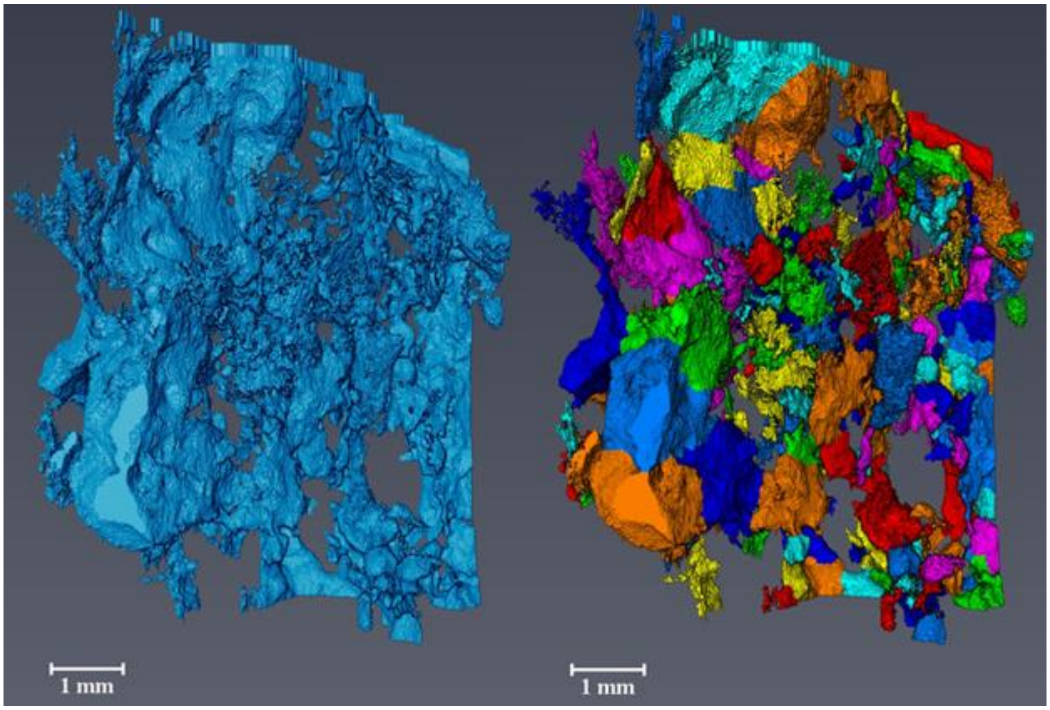

Figure 2.3 Rendering of the connected pore network from Aggregate $C_{28\%}$. Example of (left) the unseparated pore network and (right) separating objects as connected objects, representing individual pores in our analysis.

2.6 Post processing and filtering

Artifacts were identified and removed by filtering the data post-processing. Artifacts included incorrectly identified pore throats (noise) composed of less than five voxels as well as large, distinct regions of the pore network erroneously separated into two separate regions, falsely creating pore throats. Both types of artifacts were identified based on their volumes and were filtered out of the data by removing all pore throats with a volume greater than 0.5 mm^3 or less than five voxels. Occasionally, pore nodes were also filtered out when errors in the pore network model created pore nodes with coordination numbers of zero. All filtering was done within Microsoft Excel prior to data analysis in R/RStudio.

2.7 Data analysis

We used linear mixed-effects models (LME) to test the effect of freeze-thaw cycles on pore volumetric fractions, pore coordination number, and pore throat count. Sample number and/or moisture content was used as a random effect. Statistical significance was determined at $\alpha = 0.05$ given the heterogeneous pore morphology and the limited number of samples available due to the time-intensive nature of the XCT analyses. All data analyses were performed in R version 4.0.1 (2020-06-06) (R Core Team, 2020), using primarily the *dplyr v1.0.1* (Wickham et al., 2020) package for data processing and analysis, and *ggplot2 v3.3.2* (Wickham, 2016) and *PNWColors* (Lawlor, 2020) packages for data visualization. All data and scripts are available at https://github.com/Erin-Rooney/XCT-freeze-thaw and archived and searchable at https://search.emsl.pnnl.gov.

3. Results

3.1. Pore morphology

All six aggregates displayed soil pore networks with distinctive pore morphologies (Fig. 2.4), indicating a variation in physical microenvironments that was also observed in differing median pore throat diameter (LME, F = 15.3894, P = 0.0047) and mean pore throat diameter (LME, F = 9.9005, P = 0.0125) across aggregates (Appendix Table A3). Despite variation in pore morphology across aggregates, we observed structural similarities shared between aggregates of the same core (Fig. 2.4). For example, both aggregates sampled from Core A at a depth of 28-38 cm contained large, irregularly shaped pore structures ranging from 0.75 to 2 mm (Fig. 2.4a-b). The pore morphologies of the two aggregates sampled from Core B were similar to each other while differing visibly from Core A and C aggregates. Both $B_{16\%}$ and $B_{28\%}$ contained large platy pores (reminiscent of ice-lenses) that were intersected perpendicularly by a large tubular feature (Fig. 2.4c-d). The two aggregates from Core C contained several larger pore structures surrounded by many small to medium irregularly shaped pore structures (Fig. 2.4e-f). $C_{16\%}$ contained large tubular structures similar to those in Core B but were not seen in $C_{28\%}$. There were also similar platy pores occurring perpendicular to the tubular channel for $C_{16\%}$, although the pores were less prominent in comparison to the platy pores observed in the aggregates from Core B (Fig. 2.4e). The second aggregate, $C_{28\%}$, had several large, connected, irregularly shaped pore structures and no tubular pores (Fig. 2.4f).

3.2 Pore connectivity and volumetric fractions

Connected water-filled pore volumetric fraction decreased following freeze-thaw (LME, F = 9.19774, P = 0.0142; Fig. 2.4). All aggregates displayed this decrease in the connected water-filled pore volume with the exception of $B_{28\%}$. Despite decreasing volumes of connected pores there was no corresponding increase in any other volumetric fraction (e.g., connected air-filled pores, unconnected air-filled pores, unconnected water-filled pores) in any aggregate.

While we were unable to test for a statistical relationship between pore morphology and connectivity changes following freeze-thaw, there was a variation in the magnitude of changes following freeze-thaw. Subtle changes occurred in aggregates $A_{16\%,}$ $B_{16\%,}$ and $B_{28\%}$ with all pore types (air-filled, water-filled, connected and unconnected) showing low magnitude response to freeze-thaw (Fig. 2.4a, c, d). In contrast, $C_{16\%}$ and $C_{28\%}$ showed some of the largest reductions in the connected water-filled pore volumetric fraction, while $C_{16\%}$ demonstrated the only case of a large tubular pore structure detaching from the connected pore network following freeze-thaw (Fig. 2.4e-f). It is difficult to determine if the changes in pore volumetric fractions observed in $A_{28\%}$ are the result of freeze-thaw or primarily because pre and post freeze-thaw scans were made in two different regions of the same aggregate (Fig. 2.4b).

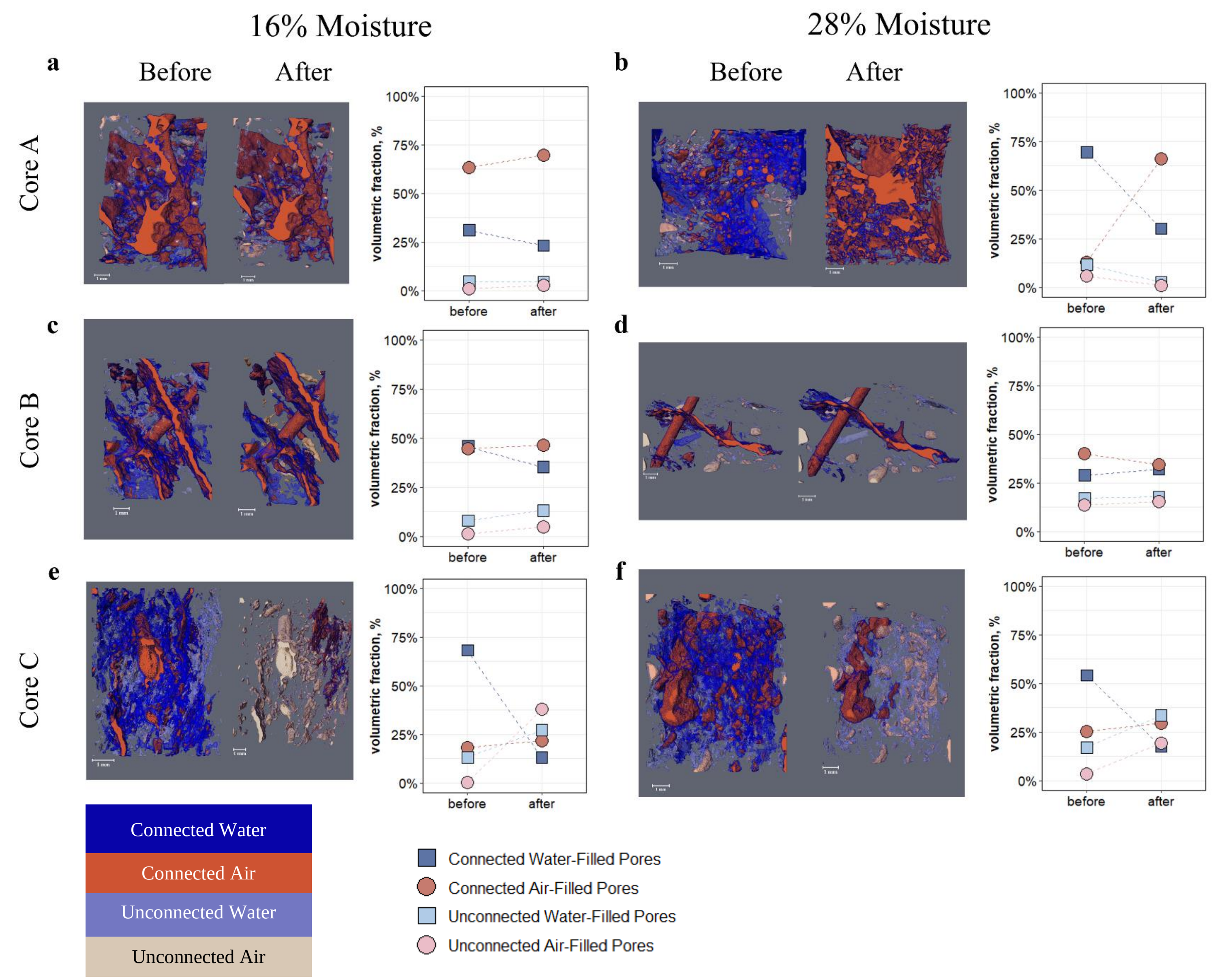
16% Moisture
28% Moisture
a
b
c
d
e
f
Before
After
Before
After
Core A
Core B
Core C
1 mm
volumetric fraction, %
100%
75%
50%
25%
0%
before
after
Connected Water
Connected Air
Unconnected Water
Unconnected Air
Connected Water-Filled Pores
Connected Air-Filled Pores
Unconnected Water-Filled Pores
Unconnected Air-Filled Pores

Figure 2.4 XCT images of aggregates before and after freeze-thaw with connectivity and type indicated by color. Connected water-filled pores are blue, connected air-filled pores are red, unconnected water-filled pores are light blue, and unconnected-air filled pores are tan/pink. The volumetric fractions (in percent) of connected and unconnected air and water-filled pores (measured through XCT) across the six experimental aggregates before and after freeze-thaw. Dashed lines provided for ease of viewing. Change in the connected water volumetric fraction was significant (LME, F = 9.1977, P = 0.0142). No changes in any other volumetric fraction were significant.

The variation in pore structure between the before and after scans of $A_{28\%}$ taken from different regions of the same aggregate indicated the potential for physical heterogeneity both across aggregates and within aggregates at a spatial difference of less than 2.5 cm (Fig. 2.4). Despite morphologic differences between two regions of the same aggregate, there were marked similarities in freeze-thaw response between $A_{28\%}$ and the other aggregate from Core A ($A_{16\%}$) including the pore throat diameter and pore coordination number distributions (Fig. 2.5-2.6, Appendix Table A2). The differing pore morphology within the same aggregate combined with similarities in freeze-thaw response observed in the Core A aggregates is contrasted by the aggregates from Core B. The Core B aggregates, despite similar pore morphologies, displayed differences in the response outcomes of freeze-thaw (Fig 2.4). $B_{16\%}$ responded to freezing and thawing in a similar fashion as the other four aggregates. In contrast, $B_{28\%}$ was the only aggregate to have an increase in the connected water-filled pore volumetric fraction (where all other aggregates showed decreases) and a decrease in the frequency of less connected pores following freeze-thaw. The effect of freeze-thaw on pore connectivity differed by pore coordination number (LME, F = 5.8401, $P < 0.0001$) with the greatest impact on pore coordination number 1 (Fig. 2.5). Before freeze-thaw, approximately 20% of pores had a pore coordination number of 1 whereas this percentage increased to 40-60% for half the aggregates following freeze-thaw (Fig. 2.5, Appendix Table A2). For pore coordination numbers 2-16 we saw variable response and in the highest pore coordination numbers we saw little to no response to freeze-thaw. There was no effect of freeze-thaw on total connected pore volume, defined as the combined connected air and water volumetric fractions.

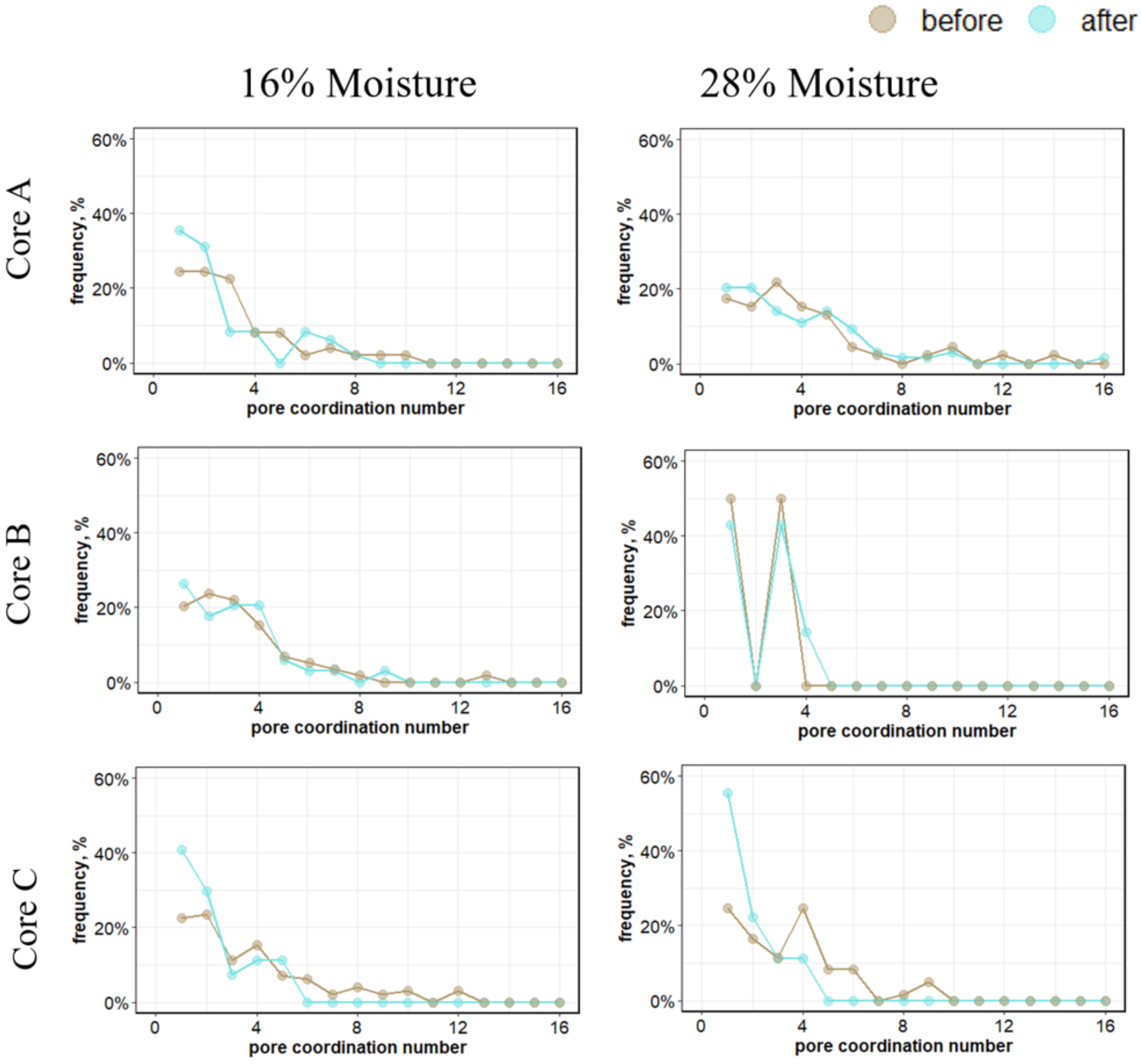

Figure 2.5 Pore coordination number frequency before and after freeze-thaw. Higher frequencies indicate an increase in the occurrence of a pore coordination number. Frequency was calculated as the count/total count. The effect of freeze/thaw differed by pore coordination number (LME, F = 5.84007, P < 0.0001).

3.3 Pore throat diameter

Pore networks showed aggregate-specific responses to freeze-thaw, but with consistent patterns associated with specific pore throat diameter sizes (Fig. 2.6). Across all aggregates, pore throats in the 30 to 50-micron diameter range responded to freeze-thaw with both increasing and decreasing pore throat diameters, resulting in non-uniform changes to the pore throat diameter distributions within that range.

We tested pore shape factor of pore throats to identify the type of deformation (elongation or sphericalness) occurring within changing pore throat sizes. However, pore shape factor did not change significantly following freeze-thaw across any pore throat size ranges (LME, F = 1.1556, P = 0.1295, Appendix Figure A9). Pore throats up to 100 microns in diameter showed a difference in frequency following freeze-thaw, although the direction of change varied across all aggregates and moisture contents. The frequency of pore throats over 50 microns decreased following freeze-thaw primarily in the higher moisture (28% moisture) aggregates (Fig. 2.6).

4. Discussion

4.1. Pore morphology

The complex relationship between initial pore morphology and pore network response to freeze-thaw highlights the potential for heterogeneity of microbial habitats within thawing permafrost soils (Bailey et al., 2013; Wanzek et al., 2018; Waring et al., 2020). Water flow and subsequent nutrient diffusion and redox conditions have been correlated with pore connectivity (Wanzek et al., 2018). Pore size and structure have also been posited to play a role in organic matter persistence or decomposition, with a recent model simulation (PROMISE) suggesting greater potential for microbial-facilitated chemical transformations in the “flow-permitting pore size class” of macropores over 1 μm in size (Waring et al., 2020). The variability in freeze-thaw response of the individual pore architecture of each aggregate and the potential dependence on initial pore morphology indicates a complexity in structural changes of the pore environment under freeze-thaw action, with implications for predictive modeling of water flow, redox chemistry, and organic matter persistence.

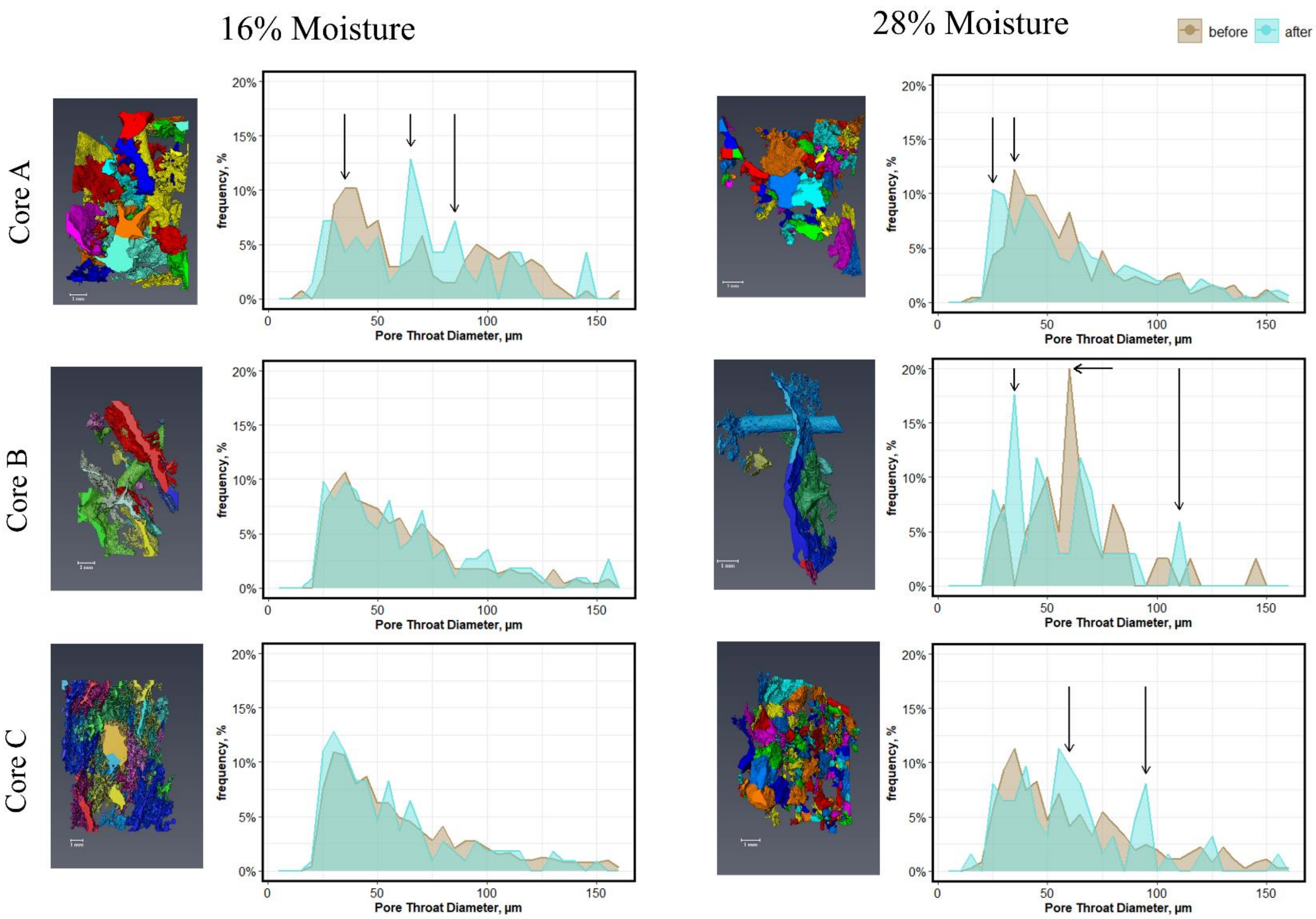

Figure 2.6 Connected pore network with individual pore regions highlighted by color and pore throat diameter distribution frequencies (bin size = 5 microns) before and after freeze-thaw for each aggregate. Frequency was calculated as the count/total count. Arrows represent regions with the largest changes in frequency following freeze-thaw.

As indicated by the pore morphologies represented within our study, we suggest that platy/lenticular pores—such as those associated with ice-lens development, (Darrow & Lieblappen, 2020; Rempel, 2010)—may result in higher variability of structural freeze-thaw-response than other types of pore morphologies observed within aggregates (e.g., large, asymmetrical pores or tubular pores surrounded by small, spherical pores). The two aggregates from Core B with similarly platy pore structures showed heterogeneous responses in shifting pore coordination numbers and connected water-filled pore volumetric fraction changes following freeze-thaw. $B_{28\%}$ displayed decreases in the frequency of less connected pores and increases in the connected water-filled pore volumetric fraction while $B_{16\%}$ aligned more closely with changes in pore connectivity shown by aggregates from Core A and Core C. The potential for specific pore morphologies to respond in characteristic ways to freeze-thaw requires additional investigation, with implications for permafrost soils that show variable responses to freeze-thaw in terms of pore connectivity and pore throat size distribution. This pore architecture-based variability would need to be accounted for in predictions for how water, gas flow, and carbon protection could change following increased freeze-thaw in previous permafrost. For example, the high carbon content associated with deeper soil horizons with cryoturbation history (Jelinski et al., 2019; Ping et al., 2008, 2015) occurs at depths that are likely to undergo additional freeze-thaw action under warming (Wei et al., 2021).

The pore morphologies in both aggregates from Core B are similar to ice-lenses, that form as a result of frost heave and are prominent features within the active layers of documented permafrost soil profiles (Andersland & Ladanyi, 2004; Mackay, 1980; Rempel, 2010). The presence of these pores was unexpected since the aggregates were purposefully selected from the permafrost horizon of the soil profile. Previous research has found that isothermal frost deformation that generates these features could occur at subzero temperatures due to pore-scale heterogeneities causing pressure gradients and thus seepage of water from smaller pores to larger pores (Rempel & van Alst, 2013). It is also notable that the pore morphologies from both aggregates in Core B contain a large tubular channel running perpendicular through the platy pore structures that could be formed by root penetration or frost heave. If root-caused, the tubular channel may have resulted in compressive forces that facilitated development of the ice-lens-like pore structures, offering an alternate explanation for their occurrence. However, our review of the literature shows little research conducted in this area with no identification of platy pores co-occurring with root deformation (Veelen et al., 2020), leaving this possibility in need of further examination. While aggregates from Cores A and C did not display ice-lens-like pore structures, it is possible that frost heave processes following active layer thickening and permafrost thaw could result in a higher occurrence of these pore morphologies in the future following continued freeze-thaw and subsequent frost heave (Ping et al., 2015; Rempel, 2010). A shift from pore networks consisting of high densities of smaller pores toward networks composed of larger, elongated pores following freeze-thaw is supported by recent findings which posited that these channel pores may also be partially caused by breakage along internal structural weaknesses of the aggregates exploited by freeze-thaw (B. Liu, Ma, et al., 2021; Ma et al., 2021).

4.2 Pore connectivity and volumetric fractions

Based on the differences in initial pore network morphology across aggregates from Cores A, B, and C, we expected to see large variability in freeze-thaw response, with the most similar freeze-thaw responses occurring in aggregates that shared similar pore network morphologies and architecture. Instead, we found that five aggregates (all but $B_{28\%}$) shared similar responses to freeze-thaw in pore coordination number frequency and pore throat diameter distribution, whereas $B_{28\%}$ consistently showed a divergent response. The inconsistent response to freeze-thaw by pore networks comprising platy pores intersecting tubular pores necessitates expanded testing to identify if response variability is a widespread trend amongst that particular pore morphology. The common changes we observed across pore networks with contrasting pore morphologies—pore coordination number frequency increasing for less connected pores and pore throat diameter distributions showing increased response to freeze-thaw in the 30–50-micron range—should also be investigated for wider trends in aggregate response to freeze-thaw.

The decreasing volumes observed in connected water-filled pores do not correspond with an increase in any other volumetric fraction (Fig. 2.4), raising questions of what freezing-associated intra-aggregate mechanisms or method artifacts may be causing these decreases. We speculate that the increase in air-filled pores for $A_{28\%}$ is indeed an artifact of different regions sampled for the post-freeze-thaw scan and the pre-freeze-thaw scan (this was the only aggregate in which different regions were scanned). While the volumetric fraction of connected water-filled pores was reduced following freeze-thaw, there was not a significant decrease in total connected pore volume. Rather, there is a shift toward fewer pore connections reflected in the lower pore coordination number following freeze-thaw (Fig. 2.5). The decrease in well-connected pores (directly connected to eight or more other pores) and increase in singly connected pores indicates that while connectivity may not be decreasing within the first five freeze-thaw cycles, the pore network is becoming more vulnerable to future responses of pores and pore throats to deformation that could result in decreased connectivity and isolation of portions of the pore network. Previous findings by Ma et al. (2021) linked freeze-thaw to increased pore connectivity, a significant finding in the context of previous studies that emphasize the importance of network connectivity in oxygen availability, water transport, and nutrient diffusion (Wanzek et al., 2018). However, findings from Ma et al. (2021) specified increasing porosity following seven freeze-thaw cycles (and up to 20 freeze-thaw cycles), with pore connectivity showing unpredictable response up through the first seven freeze-thaw cycles. The inconsistent response of connected pore volumes to freeze-thaw observed in our experiment aligns with these findings and suggests a potential difficulty in predicting pore connectivity and thus redox chemistry and nutrient diffusion in the incipient stages of freeze-thaw following permafrost thaw. Ma et al. (2021) also observed decreases in the total number of pores following multiple freeze-thaw cycles. We found no statistical change in the number of pore throats following freeze-thaw, likely due to the high variability in pore throat counts across the replicates (ranging from 23 to 552). However, five out of six aggregates ($A_{28\%}$ excluded) did show decreased pore throat counts following freeze-thaw (ST3), aligning with Ma et al. (2021).

The decrease in the number of connected pore throats following freeze-thaw contrasts findings from Liu et al. (2021b) where an increase in the number of pores in aggregates occurred following freeze-thaw cycling (resolution > 25 µm). One possible explanation for the differences observed between the two studies may relate to non-complementary experimental designs. Liu et al. (2021b) studied freeze-thaw response in soil columns whereas our work focused on soil aggregates. The impact of freeze-thaw on a soil column is influenced by the constraints of the core jacket and by the uniform dimensions provided by the core. The irregular and less constrained shapes of the aggregates (like those used within our study) may provide uneven stress to the samples during freezing, encouraging expansion toward regions of the aggregate not constrained by the sample holder while a fully contained core will likely undergo evenly distributed stress throughout. These differences in constraint and subsequent impacts to expansion during freezing could affect pore and pore throat deformation, although in reviewing the literature we were unable to find any studies that quantify the impact of structural constraints on expansion in aggregates and cores during freezing.

The increasing frequency of singly connected pores (pore coordination number 1) could be the result of either expansion or contraction resulting from freeze-thaw deformation. Smaller pores and pore throats (less than 20 microns) may be undergoing expansion following freeze-thaw (as reported by Chamberlain et al., 1990), enabling their detection at our 20-micron analysis resolution and thus contributing to the increased frequency in lower pore coordination numbers post-freeze-thaw. However, more well-connected pores could be undergoing throat contraction or collapse, resulting in increased frequencies of smaller pore throats. We also observed decreases in the total number of pore throats in most aggregates following freeze-thaw. A decrease in pore throat counts contradicts the suggestion that there is an influx of smaller pore throats that are expanding into resolution and provides support for contraction causing the increased frequency in smaller pore throat diameters (ST3). The potential for deformation highlights the importance of examining freeze-thaw response of the structure and size of micropores (<25 µm) due to the pivotal role they play in microbial activity and organic matter decomposition (Ruamps et al., 2011; Waring et al., 2020).

4.3 Pore throat diameter

Overall, we did not find evidence of uniform expansion or uniform collapse within certain pore throat diameter ranges. The occurrence of peaks splitting (a pre-freeze-thaw peak splitting into two smaller peaks that are positioned to each side of the original peak) is widespread across the pore throat diameter distributions of all aggregates (Fig. 2.6) indicating that crystallization pressure acting on diameters of 30-40 microns may result in both collapsing and expanding pore throats. This lack of cohesive trend in pore throat size supports previous observations of fluctuating pore size in freeze-thaw incubations with less than seven freeze-thaw cycles (Ma et al., 2021). Combined expansion of some and collapse of other pore throats may be driven by fluid pressure gradients across the soil pore network controlled by both temperature gradients (Rempel, 2010; Wettlaufer et al., 1996; Wilen & Dash, 1995) and by crystallization pressures across different pore sizes, which would result in a variable combination of both expansion and contraction throughout pore throats of different sizes. This network approach complicates current interpretations of freeze-thaw data that suggest deformation type is dependent on pore size (Chamberlain & Gow, 1979; Starkloff et al., 2017). Ma et al. (2021) identified a general shift in pore size dimensions following (but not prior to) seven freeze-thaw cycles, suggesting that deformation resilience (or recovery following crystal deformation) may weaken as soil aggregates undergo more freeze-thaw cycles. Following 20 freeze-thaw cycles, Ma et al. (2021) found an overall increase in pore size and thus air infiltration rates. The potential to increase overall pore connectivity beyond the first stages of freeze-thaw encourages further investigation as increases in pore and pore throat size as well as changing connectivity could impact gas release from thawing permafrost through increased substrate-microbe interactions and availability of previously isolated substrates (Ananyeva et al., 2013; V. L. Bailey et al., 2017; Strong et al., 2004; Wanzek et al., 2018; Waring et al., 2020).

Based on the changes we identified in pore throat size and pore connectivity—which provide evidence that deformation is occurring within pore throats following freeze-thaw—and the findings of Ma et al. (2021) regarding changes to pore shape factor, we anticipated pore throat deformation being visible in either increasing sphericity or elongation of pore throats. We interpret the lack of change in pore shape factor within the most impacted pore throat sizes to indicate that pore network response to freeze-thaw resulting in clear elongation or sphericity of pore throats is not yet evident during incipient stage of deformation. Despite less deformation than may be observed in further freeze-thaw cycles, the incipient stage does show evidence for changing pore network connectivity and pore throat size distribution.

5. Conclusions

Freeze-thaw impacts to the pore network occur within the first five freeze-thaw cycles and may be dependent on initial pore morphology. Changes in connectivity following freeze-thaw were complex, with overall connected pore volume showing no response to freeze-thaw while shifts in individual pore connectedness and pore throat size distribution provided evidence for widespread contraction of pore throats. Our findings indicate that this early deformation could lower the resiliency of the pore network to future freeze-thaw deformation by decreasing pore connections and subsequently increasing vulnerability of the pore network to disconnection. The incipient stage of deformation encompasses the freeze-thaw cycles following initial permafrost thaw, co-occurring with heightened microbial activity and organic matter decomposition due to warming (Cavicchioli et al., 2019; M. Liu et al., 2020). Predicting biogeochemical function and transformation following thaw requires understanding how soil properties, which control those functions, also shift following repeated freeze-thaw.

The role that pore morphology plays in the magnitude and outcome of freeze-thaw response warrants further investigation, as deformation during freeze-thaw may be linked to that initial pore structure. This is especially pertinent in permafrost soils characterized by distinct pore structures associated with cryogenic processes (Ping et al., 2015). We posit that aggregates containing platy-pore structures intersecting channel pores may respond to freeze-thaw with greater variability than aggregates with more homogenous pore morphologies. Future work should also aim to untangle how initial saturation levels and freezing rates may contribute to variability of freeze-thaw response by the soil pore network.

Impacts of freeze-thaw at the micro-scale are responsible for ecologically important soil processes, such as water holding capacity and microbial access to and subsequent decomposition of carbon compounds (Wanzek et al., 2018; Waring et al., 2020). As the Arctic continues to change under warming conditions, our ability to understand the guiding processes of permafrost landscape transition relies upon an enhanced knowledge of how freeze-thaw will affect soil properties at the micro- and macro-scale. Examining the response of soil physical properties to freeze-thaw is vital to predicting the behavior of future permafrost landscapes.

Acknowledgments

This research was supported by the U.S. Department of Energy, Office of Science, Biological and Environmental Research as part of the Environmental System Science Program. The Pacific Northwest National Laboratory is operated for DOE by Battelle Memorial Institute under contract DE-AC05-76RL01830. A portion of this research was performed using EMSL (grid.436923.9), a DOE Office of Science user facility sponsored by the Department of Energy’s Office of Biological and Environmental Research and located at Pacific Northwest National Laboratory. NEON is sponsored by the National Science Foundation (NSF) and operated under cooperative agreement by Battelle. This material is based in part upon work supported by NSF through the NEON program.

Data Availability

All data and scripts are available at https://github.com/Erin-Rooney/XCT-freezethaw and archived and searchable at https://search.emsl.pnnl.gov.

Author Contributions

ECR, RAL, MD, and OQ designed the experiment. ECR, MS, and ACG sampled and/or processed the cores. OQ performed the freeze-thaw incubations. TV, ACB, AKB, and LR performed the XCT analysis. ACB developed the method for XCT pore diameter measurements. ECR, ARP, and KFP performed data analysis. ECR wrote the manuscript with input from all authors.

References Cited

Ananyeva, K., Wang, W., Smucker, A.J.M., Rivers, M.L., Kravchenko, A.N., 2013. Can intra-aggregate pore structures affect the aggregate's effectiveness in protecting carbon? Soil Biology and Biochemistry 57, 868–875. https://doi.org/10.1016/j.soilbio.2012.10.019

Andersland, O.B., Ladanyi, B., 2004. Frozen Ground Engineering, Second Edition. ed. John Wiley & Sons.

Bailey, V.L., Fansler, S.J., Stegen, J.C., McCue, L.A., 2013. Linking microbial community structure to β-glucosidic function in soil aggregates. The ISME Journal 7. https://doi.org/10.1038/ismej.2013.87

Bailey, V.L., Smith, A.P., Tfaily, M., Fansler, S.J., Bond-Lamberty, B., 2017. Differences in soluble organic carbon chemistry in pore waters sampled from different pore size domains. Soil Biology and Biochemistry 107, 133–143. https://doi.org/10.1016/j.soilbio.2016.11.025

Biskaborn, B.K., Smith, S.L., Noetzli, J., Matthes, H., Vieira, G., Streletskiy, D.A., Schoeneich, P., Romanovsky, V.E., Lewkowicz, A.G., Abramov, A., Allard, M., Boike, J., Cable, W.L., Christiansen, H.H., Delaloye, R., Diekmann, B., Drozdov, D., Etzelmüller, B., Grosse, G., Guglielmin, M., Ingeman-Nielsen, T., Isaksen, K., Ishikawa, M., Johansson, M., Johannsson, H., Joo, A., Kaverin, D., Kholodov, A., Konstantinov, P., Kröger, T., Lambiel, C., Lanckman, J.P., Luo, D., Malkova, G., Meiklejohn, I., Moskalenko, N., Oliva, M., Phillips, M., Ramos, M., Sannel, A.B.K., Sergeev, D., Seybold, C., Skryabin, P., Vasiliev, A., Wu, Q., Yoshikawa, K., Zheleznyak, M., Lantuit, H., 2019. Permafrost is warming at a global scale. Nature Communications 10. https://doi.org/10.1038/s41467-018-08240-4

Blackwell, M.S.A., Brookes, P.C., de la Fuente-Martinez, N., Gordon, H., Murray, P.J., Snars, K.E., Williams, J.K., Bol, R., Haygarth, P.M., 2010. Phosphorus Solubilization and Potential Transfer to Surface Waters from the Soil Microbial Biomass Following Drying–Rewetting and Freezing–Thawing, in: Advances in Agronomy. Academic Press Inc., pp. 1–35. https://doi.org/10.1016/S0065-2113(10)06001-3

Boswell, E.P., Balster, N.J., Bajcz, A.W., Thompson, A.M., 2020a. Soil aggregation returns to a set point despite seasonal response to snow manipulation. Geoderma 357. https://doi.org/10.1016/j.geoderma.2019.113954

Boswell, E.P., Thompson, A.M., Balster, N.J., Bajcz, A.W., 2020b. Novel determination of effective freeze–thaw cycles as drivers of ecosystem change. Journal of Environmental Quality 49, 314–323. https://doi.org/10.1002/jeq2.20053

Brown, J., Romanovsky, V.E., 2008. Report from the International Permafrost Association: State of permafrost in the first decade of the 21st century, in: Permafrost and Periglacial Processes. pp. 255–260. https://doi.org/10.1002/ppp.618

Cavicchioli, R., Ripple, W.J., Timmis, K.N., Azam, F., Bakken, L.R., Baylis, M., Behrenfeld, M.J., Boetius, A., Boyd, P.W., Classen, A.T., Crowther, T.W., Danovaro, R., Foreman, C.M., Huisman, J., Hutchins, D.A., Jansson, J.K., Karl, D.M., Koskella, B., Mark Welch, D.B., Martiny, J.B.H., Moran, M.A., Orphan, V.J., Reay, D.S., Remais, J. v., Rich, V.I., Singh, B.K., Stein, L.Y., Stewart, F.J., Sullivan, M.B., van Oppen, M.J.H., Weaver, S.C., Webb, E.A., Webster, N.S., 2019. Scientists' warning to humanity: microorganisms and climate change. Nature Reviews Microbiology 17. https://doi.org/10.1038/s41579-019-0222-5

Chadburn, S.E., Burke, E.J., Cox, P.M., Friedlingstein, P., Hugelius, G., Westermann, S., 2017. An observation-based constraint on permafrost loss as a function of global warming. Nature Climate Change 7, 340–344. https://doi.org/10.1038/nclimate3262

Chamberlain, E.J., Gow, A.J., 1979. Effect of freezing and thawing on the permeability and structure of soils. Engineering Geology 13, 73–92.

Darrow, M.M., Lieblappen, R.M., 2020. Visualizing cation treatment effects on frozen clay soils through μCT scanning. Cold Regions Science and Technology 175. https://doi.org/10.1016/j.coldregions.2020.103085

DeMarco, J., Mack, M.C., Bret-Harte, M.S., 2011. The Effects of Snow, Soil Microenvironment, and Soil Organic Matter Quality on N Availability in Three Alaskan Arctic Plant Communities. Ecosystems 14. https://doi.org/10.1007/s10021-011-9447-5

Deprez, M., de Kock, T., de Schutter, G., Cnudde, V., 2020. The role of ink-bottle pores in freeze-thaw damage of oolithic limestone. Construction and Building Materials 246. https://doi.org/10.1016/j.conbuildmat.2020.118515

Ferreira, T.R., Pires, L.F., Wildenschild, D., Heck, R.J., Antonino, A.C.D., 2018. X-ray microtomography analysis of lime application effects on soil porous system. Geoderma 324, 119–130. https://doi.org/10.1016/j.geoderma.2018.03.015

Freppaz, M., Viglietti, D., Balestrini, R., Lonati, M., Colombo, N., 2019. Climatic and pedoclimatic factors driving C and N dynamics in soil and surface water in the alpine tundra (NW-Italian Alps). Nature Conservation 34. https://doi.org/10.3897/natureconservation.34.30737

Gao, D., Zhang, L., Liu, J., Peng, B., Fan, Z., Dai, W., Jiang, P., Bai, E., 2018. Responses of terrestrial nitrogen pools and dynamics to different patterns of freeze-thaw cycle: A meta-analysis. Global Change Biology 24, 2377–2389. https://doi.org/10.1111/gcb.14010

Gao, Z., Hu, X., Li, X.-Y., Li, Z.-C., 2021. Effects of freeze-thaw cycles on soil macropores and its implications on formation of hummocks in alpine meadows in the Qinghai Lake watershed, northeastern Qinghai-Tibet Plateau. Journal of Soils and Sediments 21. https://doi.org/10.1007/s11368-020-02765-2

Henry, H.A.L., 2008. Climate change and soil freezing dynamics: Historical trends and projected changes. Climatic Change 87, 421–434. https://doi.org/10.1007/s10584-007-9322-8

Jelinski, N.A., Sousa, M.J., Williams, A., GreyBear, E., Finnesand, K., Mulligan, D., Cole, C., Stillinger, M.D., Feinberg, J.M., 2019. Cryoturbation and Carbon Stocks in Gelisols under Late-Successional Black Spruce Forests of the Copper River Basin, Alaska. Soil Science Society of America Journal 83. https://doi.org/10.2136/sssaj2019.07.0212

Lawlor, J., 2020. PNWColors: Color Palettes Inspired by Nature in the US Pacific Northwest. Zenodo.

Li, X., Lu, Yudong, Zhang, X., Fan, W., Lu, Yangchun, Pan, W., 2019. Quantification of macropores of Malan loess and the hydraulic significance on slope stability by X-ray computed tomography. Environmental Earth Sciences 78. https://doi.org/10.1007/s12665-019-8527-2

Liu, B., Fan, H., Han, W., Zhu, L., Zhao, X., Zhang, Y., Ma, R., 2021a. Linking soil water retention capacity to pore structure characteristics based on X-ray computed tomography: Chinese Mollisol under freeze-thaw effect. Geoderma 401. https://doi.org/10.1016/j.geoderma.2021.115170

Liu, B., Ma, R., Fan, H., 2021b. Evaluation of the impact of freeze-thaw cycles on pore structure characteristics of black soil using X-ray computed tomography. Soil and Tillage Research 206. https://doi.org/10.1016/j.still.2020.104810

Liu, M., Feng, F., Cai, T., Tang, S., 2020. Soil Microbial Community Response Differently to the Frequency and Strength of Freeze–Thaw Events in a Larix gmelinii Forest in the Daxing’an Mountains, China. Frontiers in Microbiology 11. https://doi.org/10.3389/fmicb.2020.01164

Ma, R., Jiang, Y., Liu, B., Fan, H., 2021. Effects of pore structure characterized by synchrotron-based micro-computed tomography on aggregate stability of black soil under freeze-thaw cycles. Soil and Tillage Research 207. https://doi.org/10.1016/j.still.2020.104855

Mackay, J.R., 1980. The origin of hummocks, western Arctic coast, Canada, J. Earth Sci.

NEON (National Ecological Observatory Network). RELEASE-2021 (DP1.00041.001). Dataset accessed from https://data.neonscience.org on June 29, 2021.

NEON (National Ecological Observatory Network). Bundled data products - eddy covariance, RELEASE-2021 (DP4.00200.001). Dataset accessed from https://data.neonscience.org on June 29, 2021.

NEON (National Ecological Observatory Network). Soil physical and chemical properties, Megapit, RELEASE-2021 (DP1.00096.001). Dataset accessed from https://data.neonscience.org on June 29, 2021.

NEON (National Ecological Observatory Network). Soil physical and chemical properties, distributed initial characterization, RELEASE-2021 (DP1.10047.001). Dataset accessed from https://data.neonscience.org on June 29, 2021.

NEON (National Ecological Observatory Network), 2019. Terrestrial Observation System (TOS) Site Characterization Report: Domain 18.

Nimmo, J.R., 2013. Porosity and Pore Size Distribution, in: Reference Module in Earth Systems and Environmental Sciences. Elsevier. https://doi.org/10.1016/B978-0-12-409548-9.05265-9

Ping, C.L., Jastrow, J.D., Jorgenson, M.T., Michaelson, G.J., Shur, Y.L., 2015. Permafrost soils and carbon cycling. SOIL 1, 147–171. https://doi.org/10.5194/soil-1-147-2015

Ping, C.L., Michaelson, G.J., Kimble, J.M., Romanovsky, V.E., Shur, Y.L., Swanson, D.K., Walker, D.A., 2008. Cryogenesis and soil formation along a bioclimate gradient in Arctic North America. Journal of Geophysical Research: Biogeosciences 113. https://doi.org/10.1029/2008JG000744

R Core Team, 2020. R: A language and environment for statistical computing.

Rempel, A.W., 2010. Frost heave.

Rempel, A.W., van Alst, L.J., 2013. Potential gradients produced by pore-space heterogeneities: Application to isothermal frost damage and submarine hydrate anomalies.

Ruamps, L.S., Nunan, N., Chenu, C., 2011. Microbial biogeography at the soil pore scale. Soil Biology and Biochemistry 43. https://doi.org/10.1016/j.soilbio.2010.10.010

Schuur, E.A.G., McGuire, A.D., Schädel, C., Grosse, G., Harden, J.W., Hayes, D.J., Hugelius, G., Koven, C.D., Kuhry, P., Lawrence, D.M., Natali, S.M., Olefeldt, D., Romanovsky, V.E., Schaefer, K., Turetsky, M.R., Treat, C.C., Vonk, J.E., 2015. Climate change and the permafrost carbon feedback. Nature. https://doi.org/10.1038/nature14338

Soil Survey Staff, 2014. Keys to Soil Taxonomy, 12th ed. USDA-Natural Resources Conservation Service, Washington, DC.

Soil Survey Staff, 1999. Soil taxonomy: A basic system of soil classification for making and interpreting soil surveys, 2nd edition. ed. Natural Resources Conservation Service, U.S. Department of Agriculture Handbook 436.

Song, Y., Zou, Y., Wang, G., Yu, X., 2017. Altered soil carbon and nitrogen cycles due to the freeze-thaw effect: A meta-analysis. Soil Biology and Biochemistry 109, 35–49. https://doi.org/10.1016/j.soilbio.2017.01.020

Soulides, D.A., Allison, F.E., 1961. Effect of drying and freezing soils on carbon dioxide production, available mineral nutrients, aggregation, and bacterial population. Soil Science 91. https://doi.org/10.1097/00010694-196105000-00001

Starkloff, T., Larsbo, M., Stolte, J., Hessel, R., Ritsema, C., 2017. Quantifying the impact of a succession of freezing-thawing cycles on the pore network of a silty clay loam and a loamy sand topsoil using X-ray tomography. Catena 156, 365–374. https://doi.org/10.1016/j.catena.2017.04.026

Storey, K.B., Storey, J.M., 2005. FREEZE TOLERANCE.

Strong, D.T., de Wever, H., Merckx, R., Recous, S., 2004. Spatial location of carbon decomposition in the soil pore system. European Journal of Soil Science 55, 739–750. https://doi.org/10.1111/j.1365-2389.2004.00639.x

U.S. Geological Survey, 2005. Mineral Resources Data System: U.S. Geological Survey, Reston, Virginia.

Veelen, A., Koebernick, N., Scotson, C.S., McKay-Fletcher, D., Huthwelker, T., Borca, C.N., Mosselmans, J.F.W., Roose, T., 2020. Root-induced soil deformation influences Fe, S and P: rhizosphere chemistry investigated using synchrotron XRF and XANES. New Phytologist 225. https://doi.org/10.1111/nph.16242

Wadell, H., 1933. Sphericity and Roundness of Rock Particles. The Journal of Geology 41.

Wang, T., Hamann, A., Spittlehouse, D.L., Murdock, T.Q., 2012. ClimateWNA—High-Resolution Spatial Climate Data for Western North America. Journal of Applied Meteorology and Climatology 51. https://doi.org/10.1175/JAMC-D-11-043.1

Wanzek, T., Keiluweit, M., Varga, T., Lindsley, A., Nico, P.S., Fendorf, S., Kleber, M., 2018. The Ability of Soil Pore Network Metrics to Predict Redox Dynamics is Scale Dependent. Soil Systems 2. https://doi.org/10.3390/soilsystems2040066

Waring, B.G., Sulman, B.N., Reed, S., Smith, A.P., Averill, C., Creamer, C.A., Cusack, D.F., Hall, S.J., Jastrow, J.D., Jilling, A., Kemner, K.M., Kleber, M., Liu, X.A., Pett-Ridge, J., Schulz, M., 2020. From pools to flow: The PROMISE framework for new insights on soil carbon cycling in a changing world. Global Change Biology 26. https://doi.org/10.1111/gcb.15365

Wei, C., Yu, S., Jichun, W., Yaling, C., Erxing, P., Leonid, G., 2021. Soil hydrological process and migration mode influenced by the freeze-thaw process in the activity layer of permafrost regions in Qinghai-Tibet Plateau. Cold Regions Science and Technology 184. https://doi.org/10.1016/j.coldregions.2021.103236

Wettlaufer, J.S., Worster, M.G., Wilen, L.A., Dash, J.G., 1996. A Theory of Premelting Dynamics for all Power Law Forces.

Wickham, H., 2016. ggplot2: Elegant Graphics for Data Analysis. Springer.

Wickham, H., François, R., Henry, L., 2020. dplyr: A grammar of Data Manipulation.

Wilen, L.A., Dash, J.G., 1995. Frost Heave Dynamics.

Zhao, Yunduo, Hu, X., Li, X., Jiang, L., Gao, Z., 2021. Evaluation of the impact of freeze–thaw cycles on the soil pore structure of alpine meadows using X-ray computed tomography. Soil Science Society of America Journal. https://doi.org/10.1002/saj2.20256

Zhao, Ying, Li, Y., Yang, F., 2021. Critical review on soil phosphorus migration and transformation under freezing-thawing cycles and typical regulatory measurements. Science of The Total Environment 751. https://doi.org/10.1016/j.scitotenv.2020.141614

Chapter 3 The role of canopy in soil function across a Fairbanks hillslope in discontinuous permafrost

Abstract

Topography and canopy cover drive ground temperature in warming permafrost landscapes, yet the small-scale heterogeneities of soil temperatures and freeze-thaw cycle frequency introduced at the meter-scale and subsequent impacts to carbon dynamics are understudied. Buffering of permafrost-affected soils against warming air temperatures in boreal forests depends on canopy cover type, with open cover reported to result in increased ground warming compared with closed cover. We sampled a hillslope catena transect in a discontinuous permafrost zone near Fairbanks, Alaska to test the small-scale (1 to 3 meter) impacts of slope position and cover type. Mineral active layer samples were collected from backslope, low backslope, and footslope positions. We combined mineralogical compositions, soil moisture, total carbon and nitrogen analyses, and organic mat thickness measurements with an assessment of soil organic matter (SOM) composition as examined using Fourier-transform ion Cyclotron Resonance Mass Spectrometry (FT-ICR-MS). Our results demonstrate that the effect of tree canopy cover varied with slope position. Soils on the backslope showed a higher oxidation of FT-ICR-MS resolved peaks under open cover compared with closed cover. In contrast, canopy on the low backslope showed higher oxidation under closed cover whereas little to no effect of canopy was observed for soils in the footslope position. We attributed this, in part, to the strong impact of soil moisture content in soil organic carbon dynamics in the water-gathering footslope position, which contained 11 to 20 % more soil moisture than soils on the low backslope and backslope. We also posit that the thin organic mat under open cover on the backslope position further drove differences in carbon oxidation under open vs closed canopy, with a thinner organic mat failing to buffer underlying soil against warm season air temperatures and thus increasing carbon decomposition. Our findings indicate that the role of canopy in carbon dynamics depends on landscape position and soil properties, resulting in condition-specific heterogeneity of SOM composition under small-scale differences in open and closed cover and highlighting the protective effect of canopy for soils in backslope positions.

1. Introduction

Rapidly warming air temperatures in high latitudes are making permafrost ecosystems unstable, with consequences for atmospheric greenhouse gas concentrations as permafrost thaws (Biskaborn et al., 2019). Vegetation canopy plays a key role in both soil temperature and moisture in boreal forests located within the discontinuous permafrost zone (Chasmer et al., 2011; Chen et al., 2020; Shur & Jorgenson, 2007; Stuenzi et al., 2021; Williams & Quinton, 2013). The effect of tree canopy can decrease at lower slope positions, where cold and wet conditions favor smaller trees with less ability to decrease snow thickness on closed canopy soils compared with larger trees and drier upslope positions (J. R. Brooks et al., 1998). Hillslope processes also create conditions for contrasting distribution of soil organic matter (SOM) and soil properties (i.e., particle size class, mineralogy, and soil moisture), with greater preservation and accumulation of carbon reported at lower slope positions (compared with upslope positions) (Berhe et al., 2012; Ping et al., 2005; Shelef et al., 2017). Variation in particle size distribution and mineralogy across slope positions may be exacerbated by the mass wasting and soil churning that result from cryogenic processes in permafrost environments (i.e., solifluction, cryoturbation) (Ping et al., 2005), with potential impacts to SOM storage and transformation. Predicting carbon mineralization and release in a warming Arctic requires improving our understanding of the fine-scale heterogeneity of temperature-driven surface processes in forested landscapes destabilized by permafrost thaw.

Beyond regulating soil moisture and temperature, the relationship between permafrost thaw and canopy cover is complex and interconnected, with some studies reporting a positive feedback cycle in which canopy loss triggers thaw, with additional vegetation death occurring as a result of that thaw (Chasmer et al., 2011; Quinton et al., 2009). Other studies have demonstrated the importance of Black spruce canopy in permafrost protection (Shur & Jorgenson, 2007). One mechanism proposed is that spruce tree canopies may stabilize permafrost by collecting snow and reducing insulation to underlying soil during cold months. More information is needed to determine the impact of spruce canopy cover on permafrost hillslopes where localized differences in ground temperature at the meter-level may result in variation of thaw depth and increased winter freeze-thaw cycles, with both contributing subsequent impacts to carbon chemistry (P. D. Brooks et al., 2011; Chasmer et al., 2011; Chen et al., 2020; Schmidt & Lipson, 2004). The canopy-dependent protection against snowpack insulation and warming is lost when trees die or fail to thrive; depending on the timing and amount of snow precipitation, tree loss can increase the susceptibility of soils to increased freeze-thaw cycle frequency (Chen et al., 2020). Freeze-thaw acts as a mechanism in soil biogeochemical transformation, altering mineral-organic matter interactions and affecting microbial cell death and subsequent activity (Bailey et al., 2019; Edwards, 2013; Makusa et al., 2014; Yu et al., 2010). The impact of freeze-thaw and a rise in ground temperatures under insulating snow cover in open canopy can alter carbon chemistry, with decomposition and emissions pathways determined by moisture conditions and nutrient profiles (P. D. Brooks et al., 2011; Schmidt & Lipson, 2004).

Hillslope dynamics also influence SOM composition in Arctic landscapes through a combination of erosion deposition and cryogenic processes/features such as solifluction, cryoturbation, and permafrost protection of carbon (Ping et al., 2015; Shelef et al., 2017). An Arctic tundra hillslope experiment investigating high resolution dissolved organic matter composition in organic and mineral soils across two landscape positions (hillslope and riparian) found a greater range in the chemical composition of SOM molecules within the riparian soils compared with upper hillslope soils (Lynch et al., 2019). Another study targeting the effect of hillslope dynamics on carbon and nitrogen distribution in on Hershel Island (Yukon Territory, Canada) found the largest SOM stocks at the toeslope position (Ramage et al., 2019). The authors attributed the high SOM content of lower slope positions to accumulation of organic materials in a location with high biomass production while backslope positions had lower SOM content. Despite the known accumulation processes that occur at toeslopes, permafrost landscapes represent large uncertainty in terms of the size of toeslope carbon stocks across the Arctic, with that uncertainty attributed to insufficient field data (Shelef et al., 2017). While this uncertainty is more focused on deep permafrost (> 3 meters), understanding the role of canopy-driven temperature variation in SOM composition at these pivotal lower slope positions can assist in predicting what mechanisms will drive mineralization and decomposition as permafrost continues to thaw. Consequently, the potential for varying SOM content, composition, and moisture conditions across a hillslope highlight the importance of understanding how variable canopy-driven temperature dynamics at each position impact the decomposability and chemical structure of organic carbon. Using a forested hillslope, we investigated whether differences in SOM composition between open and closed cover could be identified at the meter-scale in a permafrost landscape, with the goal of contributing to the quantification of canopy-driven soil heterogeneity in discontinuous permafrost regions.

Our study aims to investigate how and at what resolution SOM content and composition vary across a forested hillslope as a result of contrasting temperature, moisture, slope, and soil properties. We examined the interactions between canopy and hillslope processes in a discontinuous permafrost landscape near Fairbanks, AK that has been prone to rapid thaw. We tested the effect of tree canopy consisting of Black spruce and White spruce (*Picea glauca*) on carbon chemistry in active layer soils across three hillslope positions (backslope, low backslope, and footslope) under open and closed canopy cover. Carbon chemistry was investigated via Fourier-transform ion cyclotron resonance mass spectrometry (FT-ICR-MS) and combined with soil mineralogy and total carbon and nitrogen elemental data. We hypothesized that there would be a greater oxidation of carbon molecules and a lower relative abundance of simple carbon compounds, such as aliphatics, under open cover as a result of warmer subsoil temperatures and increased freeze-thaw cycle frequency compared with soils under closed cover. Similarly, we expected that subsoils under closed cover would reflect the effects of thinner winter snowpack (colder ground temperatures and less frequent freeze-thaw), with less oxidized carbon compounds and a more abundant aliphatic pool. The effect of canopy should be weakest for soils in the footslope position where snow accumulation would be thicker under closed cover due to smaller black spruce trees compared with larger white spruce trees on the upslope positions. Our findings will improve the understanding of the fine-scale heterogeneity of temperature-driven surface processes in forested landscapes containing discontinuous permafrost.

2. Materials and Methods

2.1 Site description

The Y1 transect in Fairbanks, Alaska (lat: 64.864103° | long: -147.843800°) is located in the northern part of the Yukon-Tanana terrane. The slope ranges from 54° to 60° with an aspect of approximately 330° (Northwest facing) (USGS et al., 2018). The site has a mean annual temperature of -3˚C and mean annual precipitation of ~ 500 mm (B. Wang et al., 2019). The lithology is composed of gneiss (Augen most common), schist, amphibolite, and quartzite with some ultramafic rocks in isolated outcrops (Foster et al., 1994).

2.2 Sampling

Three slope positions (footslope, low backslope, and backslope) along the Y1 near Fairbanks, Alaska were selected for study (Fig. 3.1C). We sampled a total of eighteen soil pits, including six soil pits per slope position: three under canopy (closed) and three under no canopy (open) (Fig. 3.1A-B). Only active layer mineral soil horizons were sampled address our experimental focus on temperature and freeze-thaw cycles, with sampling occurring via soil knife or hand drill depending on frozen conditions. One to three active layer mineral soil horizons were sampled at each plot and pooled by plot for statistical analyses (for a total of three replicates per each slope position and cover type combination). All SOM data is shown across individual horizons in the appendices (Table B2-B4, B7-B9). Samples were kept frozen (< 0 ˚C) and transported to Oregon State University for analysis and storage. Samples were kept at -20˚C in a laboratory freezer.

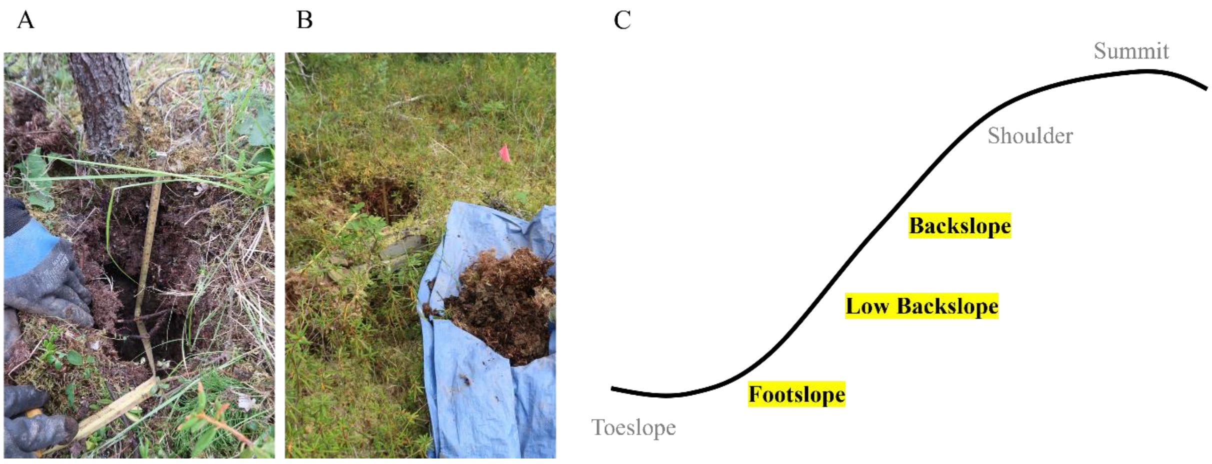

Figure 3.1 A) Photograph, sampling plot under closed cover (low backslope); B) Sampling plot under open cover (footslope); C) Diagram, hillslope positions (footslope, low backslope, and backslope). Mineral soil horizons from open (n = 3) and closed cover (n = 3) plots were sampled at each hillslope position.

2.3 Temperature dynamics

Soil temperatures at the surface (5 cm) and subsurface (75 cm) were recorded at the backslope position via borehole for years 2017 through 2021. Surface and subsurface soils under open cover were warmer compared with closed cover. Warmer temperatures under open cover did not result in increased freeze-thaw cycle frequency in surface soils. Instead, the surface soils under closed cover had greater freeze-thaw both in spring and fall (Fig. 3.2). In contrast, warmer temperatures under open cover did result in slightly higher freeze-thaw cycle frequency (1 to 2 more freeze-thaw cycles) in subsurface soils compared with closed cover.

Temperature differences between open and closed cover were not measured at the lower hillslope positions. However, tree canopy characteristics varied with slope position, with the footslope dominated by black spruce trees while both backslope and low backslope positions were dominated by white spruce trees. Tree trunk diameters were largest at the low backslope position, second largest at the backslope position, and smallest on the footslope (Figure B1; ANOVA and Tukey HSD, $P < 0.05$). Differences in tree diameter and overall size of canopy may have resulted in variation in snow cover across slope positions under closed cover.

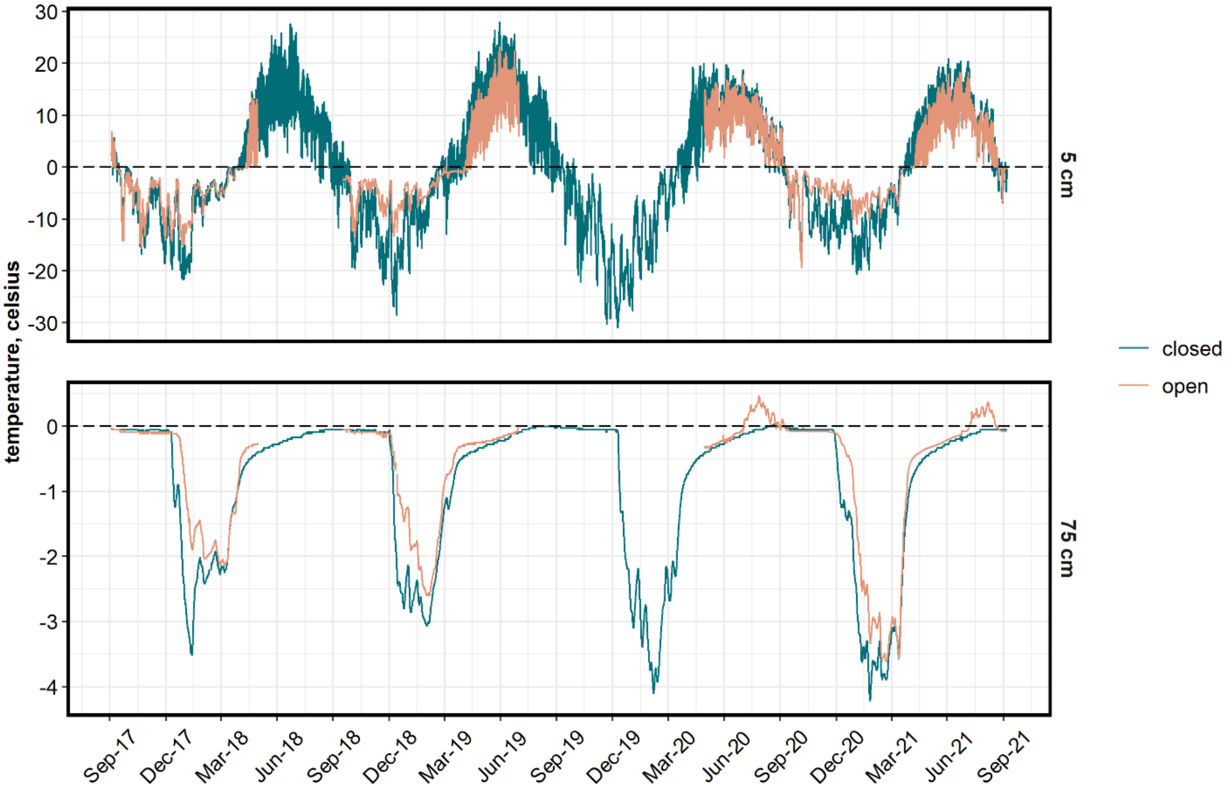

Figure 3.2 Temperature fluctuations at 5 cm (upper panel) and 75 cm (lower panel). Temperature measured from open cover (tan) and closed cover (green) at the research area from 2017 to 2021. Temperature data missing for open cover during summer 2018 and 2019.

2.4 Soil morphology, texture, SOM, and pH

Master horizons and subordinate distinctions were described and documented during sampling according to Soil Survey Staff (2014). Munsell color was recorded in the laboratory under indirect sunlight. Soil particle size distribution was analyzed by the Soil Health Lab (Oregon State University) using the hydrometer method (Gee & Bauder, 1986). Soil organic matter (SOM) percentage was measured via loss on ignition (16 hours at 385 °C on a Thermolyne F-A1730 oven). Soil pH was measured at a 1:2 soil to water ratio on air-dried, sieved, and ground soils using a Hanna HI5522 benchtop meter.

2.5 Fourier transform ion cyclotron resonance mass spectrometry

Soils were subsampled by horizon and analyzed for high resolution carbon characteristics using water extractions at the Environmental Molecular Sciences Laboratory (Richland, WA). FT-ICR-MS analysis was performed on fresh, field moist soil samples. Samples were prepared as water-extractable organic carbon (WEOC) and analyzed via automated direct infusion on a 21 T FT-ICR mass spectrometer. Soil (300 mg) was weighed into 2 mL microsolv vials with 1 mL of MilliQ added. Vials were shaken on a thermo mixer for 2 hours at 2000 RPM at room temperature and then filtered through 0.45 µm Hydrophilic PTFE filters for WEOC extracts.

Samples were randomized for analysis following ionization through dilution with methanol (MeOH) at a ratio of 1:2 (Sample:MeOH). One hundred and forty-four individual scans were averaged for each sample to improve the overall abundance of ions detected. Bruker Data Analysis (signal to noise ratio of 7) was used for peak selection and calibration. Formulae were assigned using the in-house *Formularity* software, with further data processing performed with the *fticrrr* R package (K. F. Patel, 2020). All peaks were analyzed on a presence/absence basis with only peaks occurring in ⅔ of replicates considered to be present. Only carbon-containing formulas between 200 and 900 m/zmass were included. Compound classification was conducted via modified Aromaticity Index (AImod) (Eq 1), hydrogen to carbon (H/C), and oxygen to carbon (O/C) ratio, and the nominal oxidation state of carbon (NOSC) (Eq. 2) (LaRowe & van Cappellen, 2011).

(1): Aromaticity Index (AImod)

$$AImod = \frac{1 + C - (0.5 \times O) - S - (0.5 \times (N + P + H)))}{(C - (0.5 \times O) - S - N - P}$$

(2): Nominal Oxidation State of Carbon (NOSC)

$$NOSC = \frac{4 - (((4 \times C) + H - (3 \times N) - (2 \times O) - (2 \times S))}{C}$$

In which C = carbon, H = hydrogen, O = oxygen, S = sulfur, N = nitrogen, P = phosphorus.

Identified molecules were separated into four compound classes using the AImod and H/C and O/C ratios. Following Seidel et al. (2014) we used formulas, rather than molecular structure, to delineate by biomolecular groupings. The Seidel classification system (organized by molecular O/C and H/C ratios) defines compound classes as (1) condensed aromatics (AImod > 0.66); (2) aromatic compounds (0.66 > AImod > 0.50); (3) highly unsaturated and lignin-like compounds (AImod < 0.50 and H/C < 1.5); and (4) aliphatic compounds (> H/C ≥ 1.5) (Seidel et al., 2014). Relative abundances were calculated as the number of unique peaks (formulas) within a specific compound class compared with the total number of unique peaks across all compound classes.

We compared <u>total peaks</u> across canopy cover type and hillslope positions as well as peaks <u>unique</u> to open cover and peaks <u>unique</u> to closed cover to identify chemical differences. Ratios of H/C and O/C are depicted on van Krevelen plots, with different regions associated with specific compound classes (Fig. 3.3). We used NOSC to analyze thermodynamic favorability of compounds and potential microbial oxidation. The association between NOSC and thermodynamics assumes oxic conditions and use of oxygen as the dominant terminal electron acceptor, reflected in the established relationship between Gibbs Free Energy and NOSC (Graham et al., 2017; LaRowe & van Cappellen, 2011).

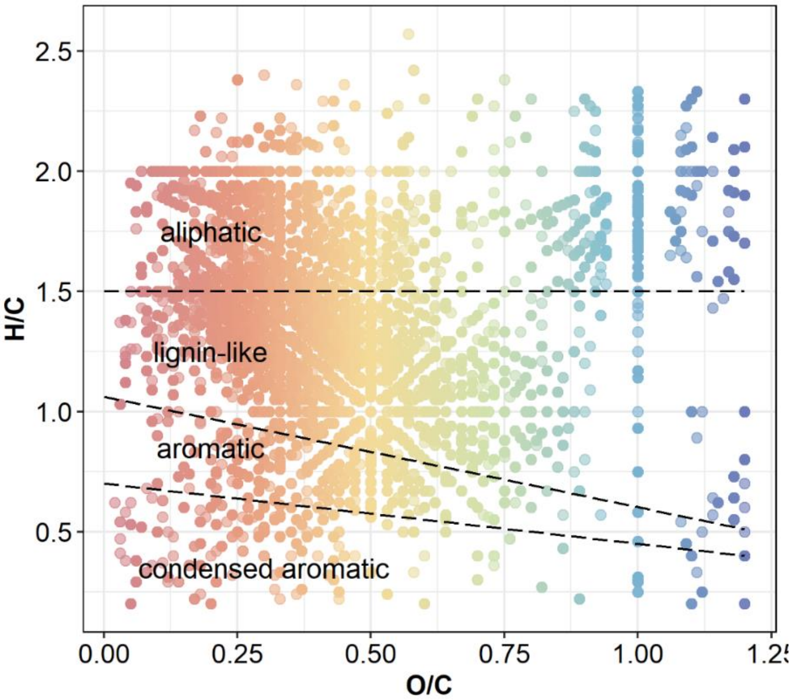

Figure 3.3 van Krevelen regions of carbon compound classes based on H/C to O/C ratios. Points show the distribution of all assigned peaks for the full data set.

2.6 X-ray diffraction, total carbon, and total nitrogen

Soils were air-dried, sieved to < 2 mm and ground to < 50 µm. Subsamples were analyzed at Environmental Molecular Sciences Laboratory (Pacific Northwest National Laboratory). Powder x-ray diffraction (XRD) patterns were collected using a Rigaku SmartLab SE diffractometer on powders packed into zero-background well holders. The diffractometer used Bragg-Brentano geometry with a Cu X-ray source (λ = 1.5418 Å), a variable divergence slit, and a high-speed D/teX Ultra 250 1D detector. Patterns were collected between 2 and 100 °2θ at intervals of 0.01 °2θ, scanning at 2°2θ/min. Quantitation of minerals was performed by the Rietveld method using TOPAS (v6, Bruker AXS). The Rietveld method combines calculated XRD patterns from the substituent minerals to provide the best fit with the observed pattern. For each mineral, the scale factor, cell parameters (constrained within ca. 0.5 % of the expected values), and crystallite size (constrained between 50 and 500 nm) were refined. A preferred orientation correction was refined for minerals consisting of platy morphologies. The scale factors from the Rietveld refinement were used to determine the relative quantities of the minerals, which are presented scaled to a total of 100%. Allowing for minimization of structural factors including lattice parameters, intensity, coherent scattering domain size, and preferred orientation bias, final model results were achieved with typical weighted profile residual (Rwp) ranging from 5.43 to 12 %.

2.7 Total C and N

Samples were air-dried, sieved, and ground prior to analysis for nitrogen and carbon on a Vario EL Cube Elemental Analyzer (Elementar Analysensysteme GmbH, Langenselbold, Germany). Homogenized samples were weighed and sealed into tin boats (Elemental Microanalysis Ltd, Devon, United Kingdom). Samples were combusted at 1150˚C in the presence of Oxygen. The signals for nitrogen and carbon were measured using a Thermal Conductivity Detector (TCD). The detector response was calibrated using Aspartic Acid and checked using a Soil Reference Material.

2.8 Statistics

FT-ICR-MS data were analyzed using univariate linear mixed-effects models (LME) and principal components analysis (PCA) to test the effect of slope position (backslope, low backslope, and footslope) and cover type (closed and open) and their interactions on the relative abundance of compound classes and the nominal oxidation state of carbon. X-ray diffraction mineral abundances were tested using ANOVAs, with HSD tests used to determine statistical differences across the three hillslope positions. Tree diameter (DBH) was tested with ANOVA and Tukey HSD. The effect of cover type and hillslope position on soil pH was tested via LME (horizonation as a random effect) and supplemented with ANOVA and a Tukey HSD test. Statistical significance for LME, ANOVA, and Tukey HSD was determined at $\alpha = 0.05$. Data analysis and visualization were performed using R version 4.0.1 (2020-06-06) with RStudio version 1.4.1106 (Core R Team, 2019). Data processing and analysis was conducted using *dplyr v1.0.1* (Wickham et al., 2020) and *vegan v2.5-6* (Oksanen et al., 2019) packages. Data visualization was conducted using *ggplot2 v3.3.2* (Wickham, 2016). The Algorithms for Quantitative Pedology (AQP) suite of R packages (*aqp*, *soilDB*, *sharpshootR*) were used to compile and visualize morphologic and soil color data. All data and scripts are available at https://github.com/Erin-Rooney/Y1_fairbanks and archived and searchable at https://search.emsl.pnnl.gov.

3. Results

3.1 Soil properties

All slope positions and cover types showed common soil morphologic characteristics, with peat and mucky peat O horizons overlying A or Bw horizons (Figure B2). Organic mat thickness varied across slope positions, with soils in the footslope position displaying thicker organic mat depths compared with upslope positions (ANOVA, F = 14.458, P = 0.0006). There was an interaction of slope position with cover type (ANOVA, F = 7.498, P = 0.008) despite cover type alone showing no effect on organic mat thickness (P = 0.5) (Table 2). Soils under open cover presented greater organic mat thicknesses than under closed on the low backslope and footslope. Soil under open cover had OM thicknesses of 24.3 ± 2.4 cm on the low backslope and 36 ± 3 cm on the footslope, yet organic mats were thinner in soils under open cover at the backslope position (18 ± 1 cm) compared with soils under closed cover on the backslope (25.3 ± 1.8 cm). The soil texture for all soils was silt loam with the exception of loam soils under closed cover at the backslope position (Table 3.1).

Table 3.1 Particle size class as determined by hydrometer method. All values reported in percentages with standard error.

		closed (%)	open (%)
backslope	clay	16.67 ± 1.67	17 ± 1.22
	silt	45 ± 2.89	56 ± 5.79
	sand	38.33 ± 3.33	27 ± 6.63
	textural class	loam	silt loam
low backslope	clay	20.71 ± 1.7	19.25 ± 1
	silt	51.43 ± 3.73	59.62 ± 2.98
	sand	27.86 ± 4.61	21.12 ± 2.68
	textural class	silt loam	silt loam
footslope	clay	20.11 ± 1.18	17.5 ± 1.12
	silt	72 ± 1.86	71.67 ± 3.8
	sand	7.89 ± 1.67	10.83 ± 3.96
	textural class	silt loam	silt loam

Footnote: Sand defined as 50 microns to 2 mm, silt defined as 2 to 50 microns, clay defined as <2 microns.

Total carbon and nitrogen showed a greater distribution in soils on the footslope position compared to the backslope position (ANOVA, $P < 0.05$; Table 3.2, Table B2-B4). Soils on the backslope and low backslope had the lowest SOM content under open cover with respective values of 1.5 ± 0.2 % and 2.8 ± 0.6 % versus 10.9 ± 5.4 % in the footslope. Carbon to nitrogen ratio varied across slope positions (ANOVA, $F = 7.875$, $P = 0.0006$), with the highest C:N ratio of 21:1 occurring at the footslope position according to a Tukey HSD test compared to 19:1 in both low backslope and backslope positions. There was an interaction of slope and cover type (ANOVA, $F = 6.609$, $P = 0.002$), although cover type on its own showed no effect. Gravimetric water also varied across slope positions (ANOVA, $F = 9.841$, $P = 0.0004$). Footslope had the highest moisture content (37.5 to 42.4 %) while backslope and low backslope soils had mean moisture contents of 20.8 to 26.5 %. Soil water did not differ with cover type. Our analyses indicated that pH differed by hillslope position (LME, $F = 56.55$, $P < 0.001$) with soils under open cover having soil pH values of 7.66 ± 0.06 in the backslope position, 6.98 ± 0.11 in low backslope position, and 6.04 ± 0.17 in the footslope position (Table 3.2). Soil pH did not vary significantly by cover type. A Tukey HSD test showed that pH was highest on the backslope, second highest on the low backslope, and lowest on the footslope.

The analyses of soil mineralogical abundance and composition indicated that the mineral composition of the soils was consistent across cover type and slope positions with some small differences in abundance (Fig. 3.4; Table B1; Figures B3-B5). Overall, the mineralogical assemblage for the soils in the field area were predominately composed of quartz, anorthite, albite, and mica with more minor amounts of chlorite, microcline, hornblende, ankerite. The footslope position had higher muscovite mica (13 to 14 %) and chlorite (6 to 8 %) compared to respective values of 9 to 10 % (mica) and 5 to 6 % (chlorite) in both the low backslope position and backslope positions (ANOVA, $P < 0.05$; Table B1). Quartz and ankerite values were also lowest for soils in the footslope position with respective percentages of 40 to 41 % and 0.29 to 0.34 %. Low backslope soils had 42 to 44 % quartz and 0.55 to 0.8 % ankerite while backslope soils had 43 to 46 % quartz and 0.58 to 0.84 % ankerite (ANOVA, $P < 0.05$).

Table 3.2 Soil properties including soil moisture, total carbon and nitrogen, carbon to nitrogen ratio, SOM % as determined by loss on ignition, organic mat (OM) thickness, and pH. Data was pooled across all depths within each replicate and then averaged across each cover type and slope position combination. Standard error is reported.

	Gravimetric water %	**Total C %**	**Total N %**	**C:N ratio**	**SOM %**	**OM (cm)**	**pH**
Backslope							
Closed	22.7 ± 1.8	1.008 ± 0.14	0.054 ± 0.01	19:1	3.5 ± 0.8	25.3 ± 1.8	7.35 ± 0.23
Open	20.8 ± 1.2	0.439 ± 0.05	0.028 ± 0.00	16:1	1.5 ± 0.2	18 ± 1	7.66 ± 0.06
Low Backslope							
Closed	26.5 ± 3.9	1.433 ± 0.29	0.084 ± 0.02	17:1	4.9 ± 2.8	22 ± 2.1	6.86 ± 0.1
Open	23.4 ± 1.1	1.818 ± 0.32	0.097 ± 0.02	19:1	2.8 ± 0.6	24.3 ± 2.4	6.98 ± 0.11
Footslope							
Closed	37.5 ± 3.7	2.538 ± 0.35	0.133 ± 0.02	19:1	5.1 ± 1	27.7 ± 1.3	6.27 ± 0.07
Open	42.4 ± 7.9	4.428 ± 0.97	0.212 ± 0.04	21:1	10.9 ± 5.4	36 ± 3	6.04 ± 0.17

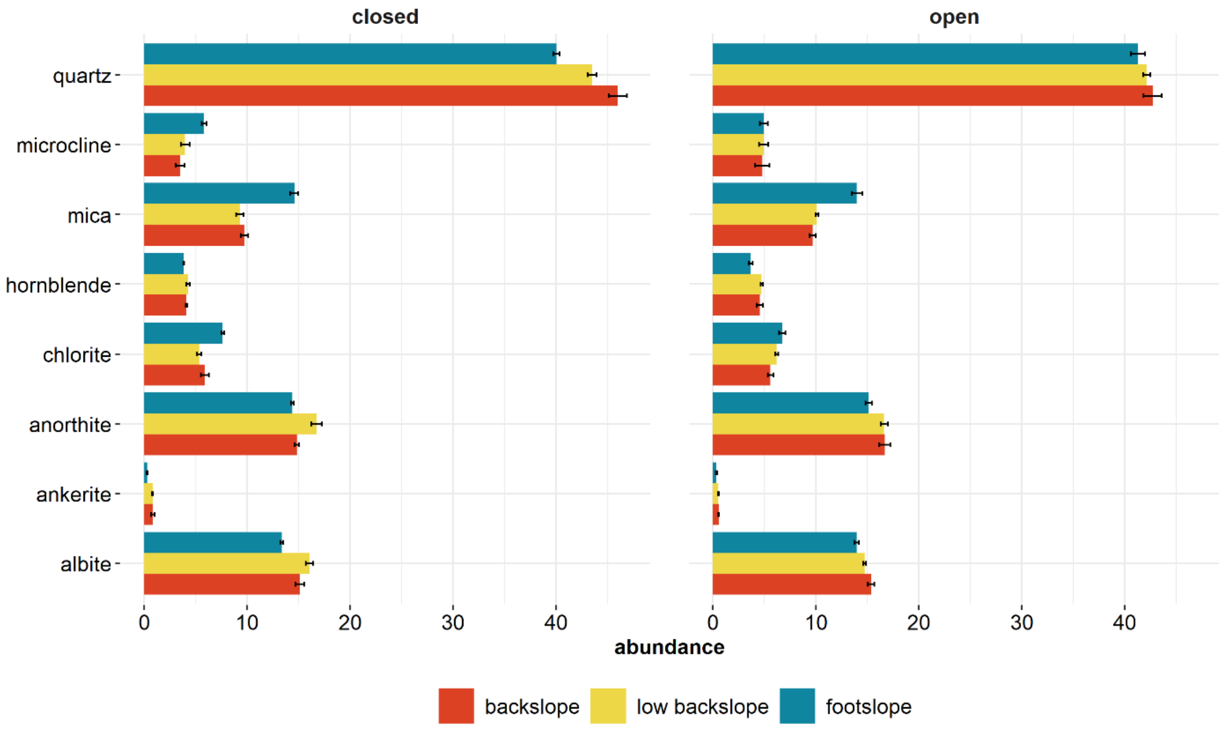

Figure 3.4 X-ray diffraction, mineral abundances with comparisons between hillslope positions within cover types. Statistical comparisons are within cover types between slope positions (backslope, low backslope, and footslope). All values are percentages (%).

3.2 Carbon Chemistry

FT-ICR-resolved carbon composition varied by hillslope position and cover type (Fig. 3.5-3.6). A Principal Components Analysis (PCA) showed an effect of slope position with the largest separation occurring between footslope and backslope positions. SOM composition at the footslope position was strongly influenced by lignin-like compounds while backslope soils had more aliphatic and condensed aromatic compounds (Fig. 3.5). The total number of FT-ICR-MS resolved peaks varied with slope position and cover type (Table 3.3; Fig. 3.6). Peak richness differed by slope position. The backslope position had < 3000 peaks under both open and closed cover while the low backslope and footslope positions had > 6000 peaks (and up to 10,000 peaks under closed cover on the footslope) (Table 3.3; Fig. 3.6). Despite differences in peak count, the overall O:C and H:C ratios were comparable across all slope positions and cover types.

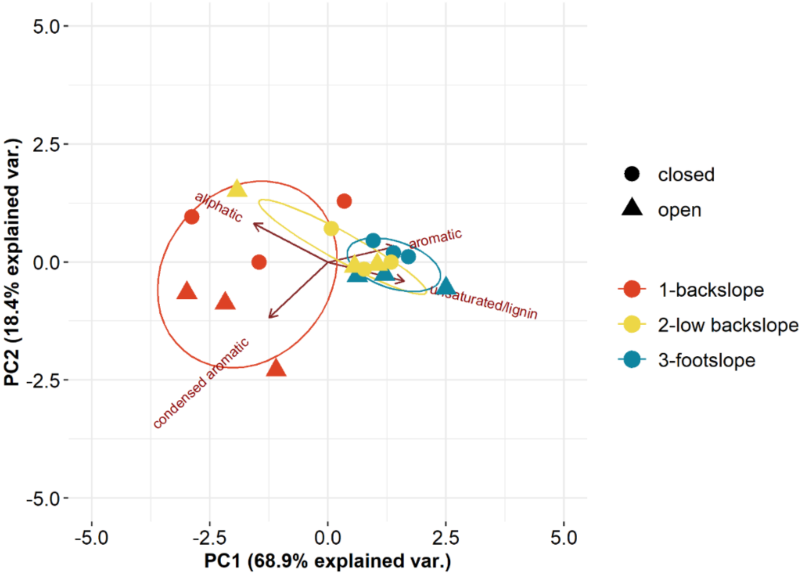

Figure 3.5 Principal Components Analysis biplot of FT-ICR-MS data showing separation by hillslope position for both closed (circles) and open (triangle). Ellipses represent 95% confidence intervals.

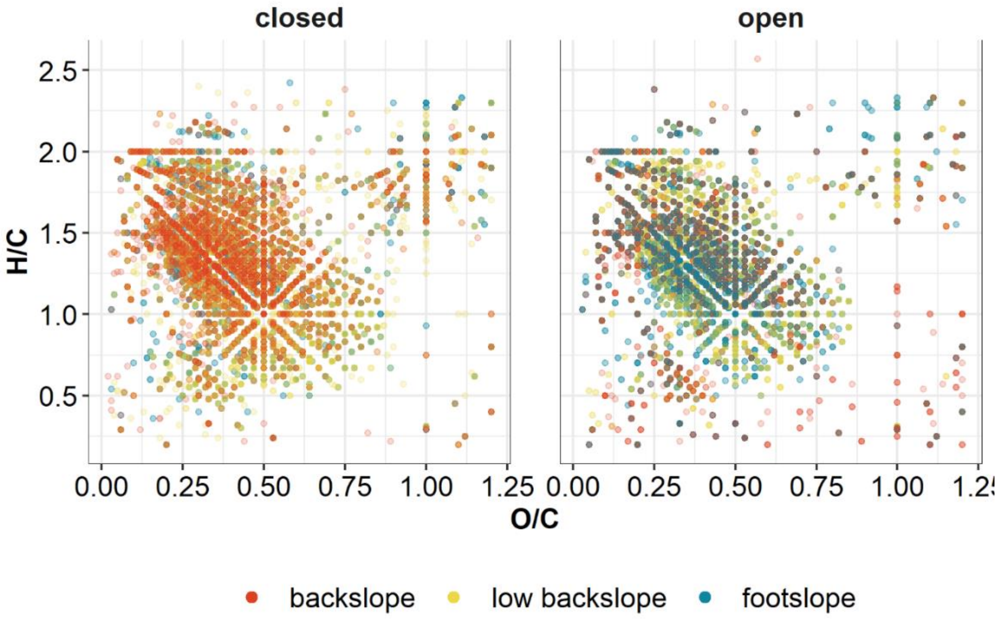

Figure 3.6 Van Krevelen plots showing organic compounds by slope position and cover type. Molecules are plotted as functions of their H-to-C and O-to-C ratios.

Table 3.3 Total FT-ICR-MS resolved peaks by treatment. Peaks calculated across all replicates.

	open	closed
backslope	2768	2296
low backslope	6238	7365
footslope	6965	10041

In addition to the total identified FT-ICR-MS resolved peaks within all treatments, we also investigated differences in peaks unique to cover type and slope position. We found that slope position and cover type affected the NOSC of unique peaks both separately and in combination (ANOVA, $P < 0.005$). A Tukey HSD test showed that NOSC was lower in FT-ICR-MS resolved peaks unique to soils from the footslope position compared with peaks unique to the backslope and low backslope.

ANOVA and HSD tests of total peaks reported a higher relative abundance of lignin-like compounds at the footslope compared with the backslope position (~ 8 % higher under closed and 12 % higher under open; P < 0.05). The relative abundance of aliphatics followed a similar trend, decreasing by ~ 9 % from the backslope to the footslope (Fig 3.7; Table B5; P < 0.05).

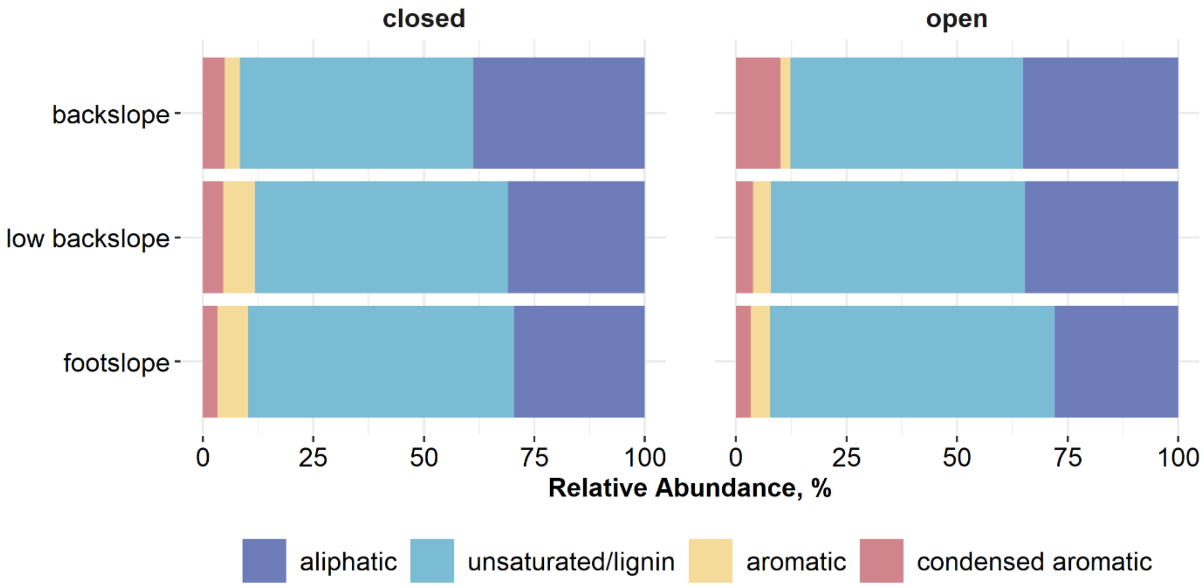

Figure 3.7 Relative abundances of carbon compound classes with comparisons between slope positions. Differences were determined at significance 0.05. Statistical comparisons are between slope positions within cover types. All values are percentages (%).

Our analysis of unique peaks revealed NOSC was higher under open cover than under closed cover on the backslope, but the opposite was true in low backslope soils (NOSC was higher under closed cover than open cover) (ANOVA, HSD test, P < 0.05; Fig. 3.8A). There was no difference in NOSC under open or closed cover in soils from the footslope position. In the associated van Krevelen diagram, there is a notable separation between cover type for high O/C ratio (> 0.75 O/C) compounds at the backslope position. The separation in high O/C molecules by cover type occurs at 1.5 H/C (the delineation between aliphatic and lignin-like compounds) (Fig. 3.8B). Specifically, the van Krevelen showed lignin-like, aromatic, and condensed aromatic molecules with high O/C (> 0.75 O/C) ratios under open cover but not closed cover on the backslope. This delineation by cover type is not observed in high O/C molecules in low backslope and footslope soils. High O/C ratio aliphatics are shown under closed cover at all hillslope positions.

A NOSC breakdown by class explores this finding further, showing diverging oxidation states across compound classes in unique peaks associate with open and closed cover types at all slope positions (Fig. B6). As indicated by the van Krevelen (Fig. 3.7) and further supported by the NOSC breakdown by carbon class (Fig. B6), aromatics and lignin-like compounds were more oxidized under open canopy compared with closed in backslope soils. Notably, we made a contrasting observation on the low backslope where both aliphatic and lignin-like compounds were less oxidized under open cover compared with closed cover. At the footslope position, aromatics were more oxidized under open cover while aliphatics were less oxidized (Fig. B6). In addition to our unique peak analyses, we also found differences in the relative abundance of carbon classes across total FT-ICR-MS detected peaks between open and closed cover at each slope position (Table B6). On the backslope position, the relative abundance of condensed aromatics was twice as high under open cover (~ 10 %) compared with closed cover (~ 5 %). On the low backslope position, the relative abundance of aromatics was lower under open cover (~ 4 %) compared with closed cover (~ 7.2 %). On the footslope position, the relative abundance of lignin-like compounds was higher under open cover (~ 64.3 %) compared with closed cover (~ 60.2 %).

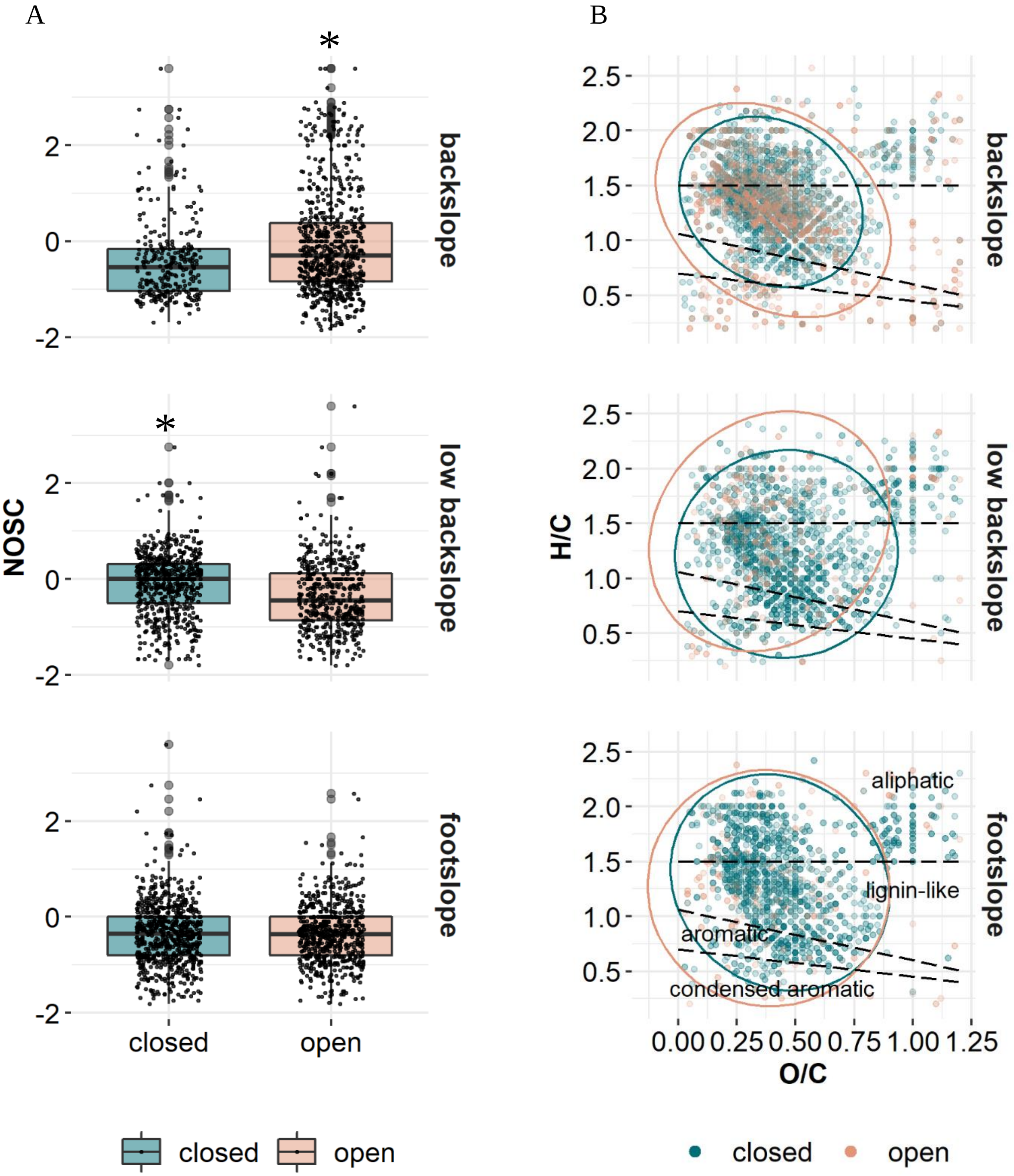

Figure 3.8 Backslope soils under open cover had higher NOSC, with lignin-like, condensed aromatic, and aromatic molecules showing greater oxidation. Low backslope soils under open had lower NOSC under open. (A) NOSC of compounds unique to each cover type by slope position. (B) Van Krevelen plot showing organic compounds unique to each cover type by slope position. Molecules are plotted as functions of their H-to-C and O-to-C ratios. Ellipses represent 95% confidence intervals.

4. Discussion

4.1 Organic mat thickness and soil temperature

The effects of open versus closed cover on carbon chemistry were most prevalent for soils in the backslope and low backslope positions. Our findings showed evidence for meter-scale differences (1 to 3 meters) in FT-ICR-MS resolved carbon chemistry. Backslope soils were more oxidized under open cover, with aromatics and lignin-like compounds showing increased oxidization and a higher relative abundance of condensed aromatics compared with closed cover. At the low backslope position, soils were less oxidized under open cover, with both aliphatic and lignin-like compounds showing decreased oxidization and lower relative abundance of aromatics compared with closed cover. The diverging observations for the carbon dynamics are notable given that the data coincide with DBH results that found statistically larger tree trunk diameters at the low backslope position compared to the backslope position (Fig. B1). We expected that the larger tree canopy would have resulted in greater differences in ground temperature at the low backslope as snow cover would be more effectively held in the canopy. However, contrasting organic mat thicknesses of 18 ± 1 cm in soils under open cover on the backslope and 24.3 ± 2.4 cm in soils under open cover on the low backslope position may be playing an enhanced role in ground temperature dynamics across cover type at both slope positions.

Canopy cover is known to regulate organic matter mat thickness in forest systems underlain with permafrost (Loranty et al., 2018). The backslope position was the only slope position to have lower OM thickness under open cover compared with closed, with the opposite (greater OM thickness under open cover) occurring at both the low backslope and footslope positions. Previous work has identified a buffering effect of the organic mat on soil temperature in permafrost environments, with a higher probability of permafrost in soils underlying thicker organic mats (Johnson et al., 2013; Shur & Jorgenson, 2007). A larch canopy study in northeastern Siberia reported thinner organic layers of 6.0 cm and higher August ground temperatures (4.1 to 4.4 ˚C) under open canopy cover compared to 12.3 cm and

2.1 to 2.9 ˚C under closed cover (Loranty et al., 2018). Notably, while the role of organic mat thickness in mediating soil temperature is well documented, the effect can depend on additional factors. A Northwest Territories boreal forest study examining the impact of canopy and other factors on active layer thickness reported a modified effect of organic layer thickness on thaw depth depending on the degree of slope, with more shallow slopes (6.99 ˚ and 3.45 ˚) showing a stronger relationship between the two than steeper slopes (10.5 ˚) (Fisher et al., 2016). Interestingly, this contrasts with our findings at the backslope position, where slopes exceeded 50 degrees. Our SOM composition results (Fig. 3.8) as well as the temperature data (Fig. 3.2) indicate that thinner organic mats may have made soils under the open cover on the backslope more vulnerable to air temperature penetration during warmer months while snow cover insulated against cooler temperatures during winter.

4.2 Vegetation and soil moisture

The variable role of canopy on SOM composition indicates that the impact of small-scale differences in cover type in thawing permafrost systems depend on multiple site factors. For example, there may be circumstances that increase the vulnerability of soil to temperature-driven disturbance under open and closed cover, such as we observed in the higher NOSC and lower SOM content in soils under open cover (compared to closed cover) at the backslope position. The backslope-specific interaction of organic mat thickness and canopy cover is likely driving ground temperature differences and subsequent impacts to carbon compound oxidation and relative abundances of lignin-like and aliphatic compounds. However, there were canopy-driven differences in NOSC at the lower slope positions as shown by the compound class breakdown.

The lower NOSC of aliphatic and lignin-like compounds under open cover on the low backslope (compared with closed) and the higher NOSC in aliphatics and aromatics under open on the footslope position are not easily explained by differences in temperature alone. Other factors, such as differences in vegetation type could play a similar role in our study as in the Siberian canopy study (Loranty et al., 2018). Notably, the Siberian larch canopy study found no canopy-driven differences in heterotrophic respiration, a finding that was attributed to the mediative effect of contrasting productivity in open (lichen) and closed (shrubs and mosses) vegetation species (Loranty et al., 2018). In our experiment, small-scale differences in vegetation biomass and productivity could explain the noted variation in NOSC under open and closed cover at the low backslope and backslope positions. Additionally, even if ground temperatures are not directly responsible for differences in SOM composition, contrasting soil temperatures can promote differences in biomass production, as observed in a snow manipulation study in Arctic tundra experiment (Natali et al., 2012). Subsurface soil moisture can inform canopy-driven impacts to ground temperature. Decreased active layer thicknesses under canopy were dependent on soil moisture content in the Northwest Territories boreal forest study noted above, with greater moisture content corresponding to less permafrost thaw (Fisher et al., 2016).

4.3 Hillslope processes

Soil properties and SOM composition differed across slope positions (regardless of cover type), with the footslope having higher total carbon and nitrogen content as well as a higher relative abundance of lignin-like compounds and lower abundance of aliphatics in comparison to soils at the backslope position. Erosion deposition is likely driving the higher SOM content at the lower slope positions. The process of increased preservation of SOM materials in deposition landform positions compared with erosion positions is well known, with a non-permafrost study finding less transformed SOM at depositional positions (Berhe et al., 2012). The process is especially pertinent in permafrost environments where solifluction, organic matter accumulation, and cold temperatures provide ideal conditions for downslope movement and preservation of SOM (Shelef et al., 2017). The accumulation of SOM content that we found in soils at the footslope position aligns well with the peak richness we observed in those same footslope soils compared with the backslope. The OM molecular richness (as referred to as peak richness), which demonstrates a wider variety of m/z peaks detected by FT-ICR-MS (Smith et al., 2017), is supported by findings from the Arctic tundra hillslope experiment (mentioned above in Chapter 3;

section 1. Introduction) which reported a larger array of SOM molecules in down-slope riparian soils compared with up-slope soils (Lynch et al., 2019).

In combination with the low NOSC values and high moisture content, the higher abundance of lignin-like compounds at the footslope position also aligns well with previous literature that identified accumulations of lignin in anaerobic soils due to the O_2 requirement of initial enzymes needed for depolymerization of lignin molecules (Freeman et al., 2001; Huang et al., 2020). Other studies have confirmed the lack of O_2 requirements for decomposition of simple carbon compounds such as aliphatics (Kirk & Farrell, 1987). The higher oxidation of lignin-like compounds under open cover unique to the backslope position aligns well with our understanding of lignin degradation. Mineralogy may also be responsible for variations in SOM composition across hillslope positions. The higher mica concentrations at the footslope position may have offered more sorption sites to SOM molecules, allowing for mineral protection from decomposition and oxidation and mitigating the impact of temperature in open vs closed cover. In our study, the backslope position had a higher quartz concentration, indicating mineralogy with less reactive sites for SOM protection and potentially allowing for soil temperature to play a larger role in SOM composition under open and closed cover.

5. Conclusion

Our findings indicate that differences in carbon chemistry under open and closed cover are negligible under certain topographic conditions (i.e., footslope soils). However, differences in organic mat thickness, lower availability of mineral protection, and shifts in vegetation are likely to introduce the type of fine-scale heterogeneity we observed at the backslope position. Notably, the higher moisture content and anaerobic conditions at the footslope position may have decreased heterogeneity between open and closed cover positions if anaerobic processes and metabolic pathways overshadowed the effect of cover type. While moisture would explain the lack of differences between open and closed cover at the footslope position, it does not explain the SOM differences under open and closed cover at the low backslope position where moisture contents were comparable to backslope soils. The increased SOM oxidation under open cover at the backslope position (but not other positions) leads us to infer that the role of canopy and temperature at the Fairbanks hillslope was driven by both moisture conditions and organic mat thickness.

Predictions of carbon decomposition and greenhouse gas emissions in boreal forests underlain by permafrost may require an understanding of how small-scale differences in canopy, organic mat thickness, mineralogy, and soil moisture may drive heterogeneity in soil temperature and carbon response at the meter-scale. As local climate conditions undergo change, the upscaled impacts of fine-scale ground temperature heterogeneity require additional investigation to determine the extent to which this heterogeneity may impact accuracy in predictions for permafrost thaw and warming in high latitude regions.

Acknowledgments

We would like to thank Mark Bowden, Tom Wietsma, Rosalie K. Chu, and Jason Toyoda their expertise and assistance with this experiment. We would like to thank Adam Fund, Kristin McAdow, Gloria Ambrowiak, and the Soil Health Laboratory at Oregon State University for their help with soil characterization analyses.

Data availability statement

All data and scripts are available at https://github.com/Erin-Rooney/Y1_fairbanks and archived and searchable at https://search.emsl.pnnl.gov.

References Cited

Bailey, V. L., Pries, C. H., & Lajtha, K. (2019). What do we know about soil carbon destabilization? *Environmental Research Letters*, *14*(8), 083004. https://doi.org/10.1088/1748-9326/ab2c11

Berhe, A. A., Harden, J. W., Torn, M. S., Kleber, M., Burton, S. D., & Harte, J. (2012). Persistence of soil organic matter in eroding versus depositional landform positions. *Journal of Geophysical Research: Biogeosciences*, *117*(G2), n/a-n/a. https://doi.org/10.1029/2011JG001790

Biskaborn, B. K., Smith, S. L., Noetzli, J., Matthes, H., Vieira, G., Streletskiy, D. A., et al. (2019). Permafrost is warming at a global scale. *Nature Communications*, *10*(1). https://doi.org/10.1038/s41467-018-08240-4

Brooks, J. R., Flanagan, L. B., & Ehleringer, J. R. (1998). Responses of boreal conifers to climate fluctuations: indications from tree-ring widths and carbon isotope analyses. *Canadian Journal of Forest Research*, *28*(4), 524–533. https://doi.org/10.1139/cjfr-28-4-524

Brooks, P. D., Grogan, P., Templer, P. H., Groffman, P., Öquist, M. G., & Schimel, J. (2011). Carbon and Nitrogen Cycling in Snow-Covered Environments. *Geography Compass*, *5*(9), 682–699. https://doi.org/10.1111/j.1749-8198.2011.00420.x

Chasmer, L., Quinton, W., Hopkinson, C., Petrone, R., & Whittington, P. (2011). Vegetation Canopy and Radiation Controls on Permafrost Plateau Evolution within the Discontinuous Permafrost Zone, Northwest Territories, Canada. *Permafrost and Periglacial Processes*, n/a-n/a. https://doi.org/10.1002/ppp.724

Chen, L., Chen, Z., Jia, G., Zhou, J., Zhao, J., & Zhang, Z. (2020). Influences of forest cover on soil freeze-thaw dynamics and greenhouse gas emissions through the regulation of snow regimes: A comparison study of the farmland and forest plantation. *Science of The Total Environment*, *726*, 138403. https://doi.org/10.1016/j.scitotenv.2020.138403

Edwards, L. M. (2013). The effects of soil freeze–thaw on soil aggregate breakdown and concomitant sediment flow in Prince Edward Island: A review. *Canadian Journal of Soil Science*, *93*(4), 459–472. https://doi.org/10.4141/cjss2012-059

Fisher, J. P., Estop-Aragonés, C., Thierry, A., Charman, D. J., Wolfe, S. A., Hartley, I. P., et al. (2016). The influence of vegetation and soil characteristics on active-layer thickness of permafrost soils in boreal forest. *Global Change Biology*, *22*(9), 3127–3140. https://doi.org/10.1111/gcb.13248

Foster, H. L., Keith, T. E. C., & Menzie, W. D. (1994). *Geology of the Yukon-Tanana area of east-central Alaska*.

Freeman, C., Ostle, N., & Kang, H. (2001). An enzymic "latch" on a global carbon store. *Nature*, *409*(6817), 149–149. https://doi.org/10.1038/35051650

Gee, G. W., & Bauder, J. W. (1986). Particle-size analysis. In A. Klute (Ed.), *Methods of soil analysis. Part 1.* (2nd ed., pp. 383–411). Madison, WI.: Agron. Monogr. 9. ASA and SSSA.

Graham, E. B., Tfaily, M. M., Crump, A. R., Goldman, A. E., Bramer, L. M., Arntzen, E., et al. (2017). Carbon Inputs From Riparian Vegetation Limit Oxidation of Physically Bound Organic Carbon Via Biochemical and Thermodynamic Processes. *Journal of Geophysical Research: Biogeosciences*, *122*(12), 3188–3205. https://doi.org/10.1002/2017JG003967

Huang, W., Ye, C., Hockaday, W. C., & Hall, S. J. (2020). Trade-offs in soil carbon protection mechanisms under aerobic and anaerobic conditions. *Global Change Biology*, *26*(6), 3726–3737. https://doi.org/10.1111/gcb.15100

Johnson, K. D., Harden, J. W., David McGuire, A., Clark, M., Yuan, F., & Finley, A. O. (2013). Permafrost and organic layer interactions over a climate gradient in a discontinuous permafrost zone. *Environmental Research Letters*, *8*(3), 035028. https://doi.org/10.1088/1748-9326/8/3/035028

Kirk, T. K., & Farrell, R. L. (1987). Enzymatic "Combustion": The Microbial Degradation of Lignin. *Annual Review of Microbiology*, *41*(1), 465–501. https://doi.org/10.1146/annurev.mi.41.100187.002341

LaRowe, D. E., & van Cappellen, P. (2011). Degradation of natural organic matter: A thermodynamic analysis. *Geochimica et Cosmochimica Acta*, *75*(8), 2030–2042. https://doi.org/10.1016/j.gca.2011.01.020

Loranty, M. M., Berner, L. T., Taber, E. D., Kropp, H., Natali, S. M., Alexander, H. D., et al. (2018). Understory vegetation mediates permafrost active layer dynamics and carbon dioxide fluxes in open-canopy larch forests of northeastern Siberia. *PLOS ONE*, *13*(3), e0194014. https://doi.org/10.1371/journal.pone.0194014

Lynch, L. M., Machmuller, M. B., Boot, C. M., Covino, T. P., Rithner, C. D., Cotrufo, M. F., et al. (2019). Dissolved Organic Matter Chemistry and Transport Along an Arctic Tundra Hillslope. *Global Biogeochemical Cycles*, *33*(1), 47–62. https://doi.org/10.1029/2018GB006030

Makusa, G. P., Bradshaw, S. L., Berns, E., Benson, C. H., & Knutsson, S. (2014). Freeze–thaw cycling concurrent with cation exchange and the hydraulic conductivity of geosynthetic clay liners. *Canadian Geotechnical Journal*, *51*(6), 591–598. https://doi.org/10.1139/cgj-2013-0127

Natali, S. M., Schuur, E. A. G., & Rubin, R. L. (2012). Increased plant productivity in Alaskan tundra as a result of experimental warming of soil and permafrost. *Journal of Ecology*, *100*(2), 488–498. https://doi.org/10.1111/j.1365-2745.2011.01925.x

Oksanen, J., Blanchet, F. G., Friendly, M., Kindt, R., Legendre, P., McGlinn, D., et al. (2019). Vegan: Community Ecology Package. R Package.

Patel, K. F. (2020). fticrrr. *R Package*. Zenodo, DOI:10.5281/zenodo.3893246.

Ping, C. L., Michaelson, G. J., Packee, E. C., Stiles, C. A., Swanson, D. K., & Yoshikawa, K. (2005). Soil Catena Sequences and Fire Ecology in the Boreal Forest of Alaska. *Soil Science Society of America Journal*, *69*(6), 1761–1772. https://doi.org/10.2136/sssaj2004.0139

Ping, C. L., Jastrow, J. D., Jorgenson, M. T., Michaelson, G. J., & Shur, Y. L. (2015). Permafrost soils and carbon cycling. *SOIL*, *1*(1), 147–171. https://doi.org/10.5194/soil-1-147-2015

Quinton, W. L., Hayashi, M., & Chasmer, L. E. (2009). Peatland Hydrology of Discontinuous Permafrost in the Northwest Territories: Overview and Synthesis. *Canadian Water Resources Journal*, *34*(4), 311–328. https://doi.org/10.4296/cwrj3404311

Ramage, J. L., Fortier, D., Hugelius, G., Lantuit, H., & Morgenstern, A. (2019). Distribution of carbon and nitrogen along hillslopes in three valleys on Herschel Island, Yukon Territory, Canada. *CATENA*, *178*, 132–140. https://doi.org/10.1016/j.catena.2019.02.029

Schmidt, S. K., & Lipson, D. A. (2004). Microbial growth under the snow: Implications for nutrient and allelochemical availability in temperate soils. *Plant and Soil*, *259*(1/2), 1–7. https://doi.org/10.1023/B:PLSO.0000020933.32473.7e

Seidel, M., Beck, M., Riedel, T., Waska, H., Suryaputra, I. G. N. A., Schnetger, B., et al. (2014). Biogeochemistry of dissolved organic matter in an anoxic intertidal creek bank. *Geochimica et Cosmochimica Acta*, *140*, 418–434. https://doi.org/10.1016/j.gca.2014.05.038

Shelef, E., Rowland, J. C., Wilson, C. J., Hilley, G. E., Mishra, U., Altmann, G. L., & Ping, C. (2017). Large uncertainty in permafrost carbon stocks due to hillslope soil deposits. *Geophysical Research Letters*, *44*(12), 6134–6144. https://doi.org/10.1002/2017GL073823

Shur, Y. L., & Jorgenson, M. T. (2007). Patterns of permafrost formation and degradation in relation to climate and ecosystems. *Permafrost and Periglacial Processes*, *18*(1), 7–19. https://doi.org/10.1002/ppp.582

Smith, A. P., Bond-Lamberty, B., Benscoter, B. W., Tfaily, M. M., Hinkle, C. R., Liu, C., & Bailey, V. L. (2017). Shifts in pore connectivity from precipitation versus groundwater rewetting increases soil carbon loss after drought. *Nature Communications*, *8*(1), 1335. https://doi.org/10.1038/s41467-017-01320-x

Soil Survey Staff. (2014). Keys to Soil Taxonomy, 12th ed. *USDA-Natural Resources Conservation Service, Washington, DC.*

Stuenzi, S. M., Boike, J., Cable, W., Herzschuh, U., Kruse, S., Pestryakova, L. A., et al. (2021). Variability of the surface energy balance in permafrost-underlain boreal forest. *Biogeosciences*, *18*(2), 343–365. https://doi.org/10.5194/bg-18-343-2021

USGS, S. of A., Polar Geospatial Center, U. of M., National Science Foundation, National Geospatial-Intelligence Agency, & DigitalGlobe. (2018). Arctic DEM. Esri, ArcGIS.

Wang, B., Hults, C. P., Eberl, D. D., Woodruff, L. G., Cannon, W. F., & Gough, L. P. (2019). *Studies by the U.S. Geological Survey in Alaska, Volume 15: Soil Mineralogy and Geochemistry Along a North-South Transect in Alaska and the Relation to Source-Rock Terrane*. Reston, Virginia.

Wickham, H. (2016). ggplot2: Elegant Graphics for Data Analysis. *Springer*.

Wickham, H., François, R., & Henry, L. (2020). dplyr: A grammar of Data Manipulation.

Williams, T. J., & Quinton, W. L. (2013). Modelling incoming radiation on a linear disturbance and its impact on the ground thermal regime in discontinuous permafrost. *Hydrological Processes*, *27*(13), 1854–1865. https://doi.org/10.1002/hyp.9792

Yu, X., Zhang, Y., Zhao, H., Lu, X., & Wang, G. (2010). Freeze-thaw effects on sorption/desorption of dissolved organic carbon in wetland soils. *Chinese Geographical Science*, *20*(3), 209–217. https://doi.org/10.1007/s11769-010-0209-7

THE IMPACT OF FREEZE-THAW HISTORY ON SOIL CARBON RESPONSE TO EXPERIMENTAL FREEZE-THAW CYCLES

Erin C. Rooney, Vanessa L. Bailey, Kaizad F. Patel, Angela R. Possinger, Adrian C. Gallo, Maya Bergmann, Michael SanClements, Rebecca A. Lybrand

Journal of Geophysical Research: Biogeosciences
United States

Chapter 4 The impact of freeze-thaw history on soil carbon response to experimental freeze-thaw cycles

Abstract

Freeze-thaw is a disturbance process in cold regions where permafrost soils are becoming vulnerable to temperature fluctuations above 0˚C. Freeze-thaw alters soil physical and biogeochemical properties with implications for carbon persistence and emissions in Arctic landscapes. We examined whether different freeze-thaw histories in two soil systems led to contrasting biogeochemical responses under a laboratory-controlled freeze-thaw incubation. We investigated controls on carbon composition through Fourier-transform ion cyclotron resonance mass spectroscopy (FT-ICR-MS) to identify nominal carbon oxidation states and relative abundances of carbon compound classes in both surface and subsurface soils. Soil cores (~ 60 cm-depth) were sampled from two sites in Alaskan permafrost landscapes with different *in situ* freeze-thaw characteristics: Healy (>40 freeze-thaw cycles annually) and Toolik (<15 freeze-thaw cycles annually). FT-ICR-MS was coupled with *in situ* temperature data and soil properties (i.e., soil texture, mineralogy) to assess (1) differences in SOM composition associated with previous freeze-thaw history and (2) sensitivity to experimental freeze-thaw in the extracted cores. Control (freeze-only) samples showed greater carbon oxidation in Healy soils compared with Toolik, even in lower mineral horizons where freeze-thaw history was comparable across both sites. Healy showed the most loss of carbon compounds following experimental freeze-thaw in the lower mineral depths, including a decrease in aliphatics. Toolik soils responded more slowly to freeze-thaw as shown by intermediary carbon oxidation distributed across multiple carbon compound classes. Variations in the response of permafrost carbon chemistry to freeze-thaw is an important factor for predicting changes in soil function as permafrost thaws in high northern latitudes.

Plain Language Summary

As global warming progresses, permafrost (soils frozen for two or more consecutive years) is undergoing thaw. However, the process of permafrost thaw is more than a simple transition from frozen to thawed.

Instead, thawing permafrost undergoes repeated freeze-thaw cycles on an annual, seasonal, and daily basis. Freeze-thaw cycles impact soils by changing soil nutrient availability and biological activity with implications for carbon decomposition. We investigated two types of freeze-thaw response: (1) how previous freeze-thaw history influenced current soil function and (2) how soils responded to experimental freeze-thaw. We tested both types of soil response to freeze-thaw cycles by evaluating the chemical composition of soil carbon. We found that soil response to freeze-thaw differed by site, even in the lower soil depths with little exposure to prior freeze-thaw. Our findings indicate that as permafrost thaws and begins to undergo freeze-thaw cycles, the response to those freeze-thaw cycles may differ by site. Variation in soil response could play a crucial role in predicting greenhouse gas emissions and rates of emission from thawing Arctic landscapes.

Key words: Freeze-thaw, permafrost, organic carbon, Arctic, soil

1. Introduction

Freeze-thaw cycles are a deformation process that shape soil function in warming permafrost landscapes and represent an intrinsic component of thaw (Henry, 2008; Ping et al., 2015; Yi et al., 2015). Freeze-thaw occurs in the surface or subsurface of the active layer during any season depending on air temperature, snowpack, and organic mat thickness (Boswell, Thompson, et al., 2020; Ping et al., 2015; Sharratt et al., 1992). Disturbance from freeze-thaw alters the soil environment through the reorganization of the physical soil structure (Konrad & McCammon, 1990; Ma et al., 2021; Rooney et al., 2022), increases in extractable carbon and nitrogen as well as higher solute concentrations (Bing et al., 2015; Kaizad F. Patel et al., 2021), and microbial death and stimulated activity following cell lysis (Blackwell et al., 2010; Schimel & Clein, 1996), with potential implications for permafrost soil carbon loss. As the Arctic continues to warm, projected increases in freeze-thaw cycle frequency and permafrost thaw make soil response a critical component for predicting soil carbon-climate feedbacks. While the effect of experimental freeze-thaw has been studied in the active layer (Z. Gao et al., 2021; Larsen et al., 2002; Schimel & Mikan, 2005) and permafrost (Rooney et al., 2022) separately, we still need to identify how freeze-thaw dynamics manifest collectively as a function of freeze-thaw history, soil type, and depth. Prior work demonstrated the importance of site and soil properties for predicting how permafrost soils will adapt to a warming climate (Chou & Wang, 2021; Guo & Wang, 2013; Park et al., 2015; Jingyuan Wang et al., 2019). The interaction of freeze-thaw history with soil properties requires further examination to expand our understanding of how the permafrost carbon cycle, including carbon chemistry, will respond to the occurrence of more freeze-thaw cycles predicted with climate change (Henry, 2008; Yi et al., 2015).

Freeze-thaw disturbance presents important implications for mineral-organic matter associations in both non-permafrost and permafrost soils (Bailey et al., 2019; G.-P. Wang et al., 2007; Yu et al., 2010). An experiment using wetland soils in the Sanjiang Plain of Northeast China (mean annual temperature of 3°C) found that freeze-thaw cycles increased sorption of dissolved organic carbon and suggested that changes to the physical structure of soil components (such as hydrous mica) increased the mineral surface area and sorption positions available to carbon (Yu et al., 2010). The study also found evidence that cumulative freeze-thaw effects on mineralogy could include greater concentrations of amorphous iron oxides, with additional contributions to the increased sorption capacity of soils. Freeze-thaw also influenced carbon response through changes to soil aggregates, including the deformation and physical structure of aggregates through aggregate breakage and decreased water stability (Vanessa L Bailey et al., 2019). A study in Prince Edward Island found that the vulnerability of soils to aggregate breakage under freeze-thaw was lower in soils containing higher clay and oxide contents relative to coarse soil textures (Edwards, 2013). The changes to aggregate structure result in more stable aggregates remaining intact following freeze-thaw disturbance (Vanessa L Bailey et al., 2019). Furthermore, changes to aggregate stability and organo-mineral associations may affect carbon chemistry due to changes in the protection of organic matter through physical occlusion in aggregates or sorption of compounds (von Lützow et al., 2007). The influence of freeze-thaw on soil has been demonstrated previously in controlled laboratory experiments (i.e., Henry, 2007; Liu et al., 2021; Ma et al., 2021; Rooney et al., 2022; Jiaoyue Wang et al., 2014) and field experiments (Arndt et al., 2020; Boswell, Balster, et al., 2020; Kaizad F. Patel et al., 2018). Yet, identifying how previous freeze-thaw history influences carbon chemistry across thawing permafrost landscapes remains understudied.

Recent advances in analytical techniques and capabilities have provided molecular-scale insight into the soil chemical composition of permafrost landscapes with important advancements that support the study of freeze-thaw dynamics (Antony et al., 2017; Leewis et al., 2020; MacDonald et al., 2021; Textor et al., 2019). Fourier transform ion cyclotron resonance mass spectrometry (FT-ICR-MS) has been employed to: investigate and compare organic matter composition across a range of permafrost landscapes in the western Canadian Arctic (MacDonald et al., 2021), identify drivers of biodegradability in the soil organic matter of thawing Arctic permafrost (Textor et al., 2019), and detect dissolved organic matter transformations by microbial communities in Antarctic snowpack (Antony et al., 2017). The capabilities of FT-ICR-MS are centered around identifying the presence of unique molecular formulae within soil extracts (Kujawinski et al., 2002). Previous work coupled molecular formulae with calculations of the nominal oxidation state of carbon (NOSC), aromatic indices (AI_{mod}), as well as hydrogen to carbon (H:C) and oxygen to carbon (O:C) ratios to characterize the thermodynamic favorability and relative contribution of carbon compound classes across water-extractable organic carbon (LaRowe & van Cappellen, 2011; Seidel et al., 2014). Carbon compound classes and NOSC were used to compare the carbon chemistry and metabolism of permafrost ranging from 19,000 to 33,000 years in age (Leewis et al., 2020). The authors found that both permafrost age and paleoclimate influenced the molecular composition of carbon with NOSC decreasing as permafrost age increased. Thaw in older permafrost soils may trigger a faster microbial response than in younger permafrost soils due to differences in the composition and bioavailability of the carbon pool with age (Leewis et al., 2020). Comparisons of permafrost carbon chemistry in the western Canadian Arctic also revealed compositional differences associated with parent material and past soil modification processes including thaw, peat formation, and permafrost aggradation (MacDonald et al., 2021). The effect of freeze-thaw disturbance on the molecular characteristics of organic carbon remains unexamined in the Arctic, which is needed to assess soil response to increased freeze-thaw in permafrost environments under warming climate conditions.

The objective of this research was to determine how freeze-thaw history influenced the response of soil organic matter to experimental freeze-thaw disturbance as examined through a laboratory incubation experiment. We used upland permafrost soils from Alaska with contrasting freeze-thaw histories to test two hypotheses (Figure 4.1) (National Ecological Observatory Network, 2021d). H1: Soil depths at Healy and Toolik with the highest previous freeze-thaw frequency (Healy mineral depths and Toolik organic depth) will be composed of more lignin-like and aromatic compounds due to preferential turnover of simple aliphatic compounds during prior freeze-thaw or extended periods of thaw. H2: Following experimental freeze-thaw, soil with little freeze-thaw history (all mineral depths at Toolik and the lower mineral depth at Healy) will show a decrease in the aliphatic pool compared with the lignin-like and aromatic carbon pools, as microbial death and lysis would provide substrates that stimulate activity of the remaining microbes. We also expected that freeze-thaw would result in an overall increase in the oxidation of molecules, likely as a result of carbon desorption associated with ionic fluctuations. We used FT-ICR-MS to characterize the soil carbon composition (i.e., aliphatic and lignin-like compounds) and combined this information with soil physical and mineralogical properties (i.e., texture, mineralogical abundance, and iron/aluminum crystallinity) to test the effects of freeze-thaw history, soil type, depth and experimental freeze-thaw on carbon chemistry in permafrost-affected soils. Here, we specifically define permafrost carbon chemistry as the identified molecules in water-extractable soil organic carbon resolved by FT-ICR-MS. Our findings contribute to an improved understanding of how thawing permafrost soils will respond to the increase in freeze-thaw cycles expected during warming as well as how that response may vary based on the history of a site including previous exposure to freeze-thaw.

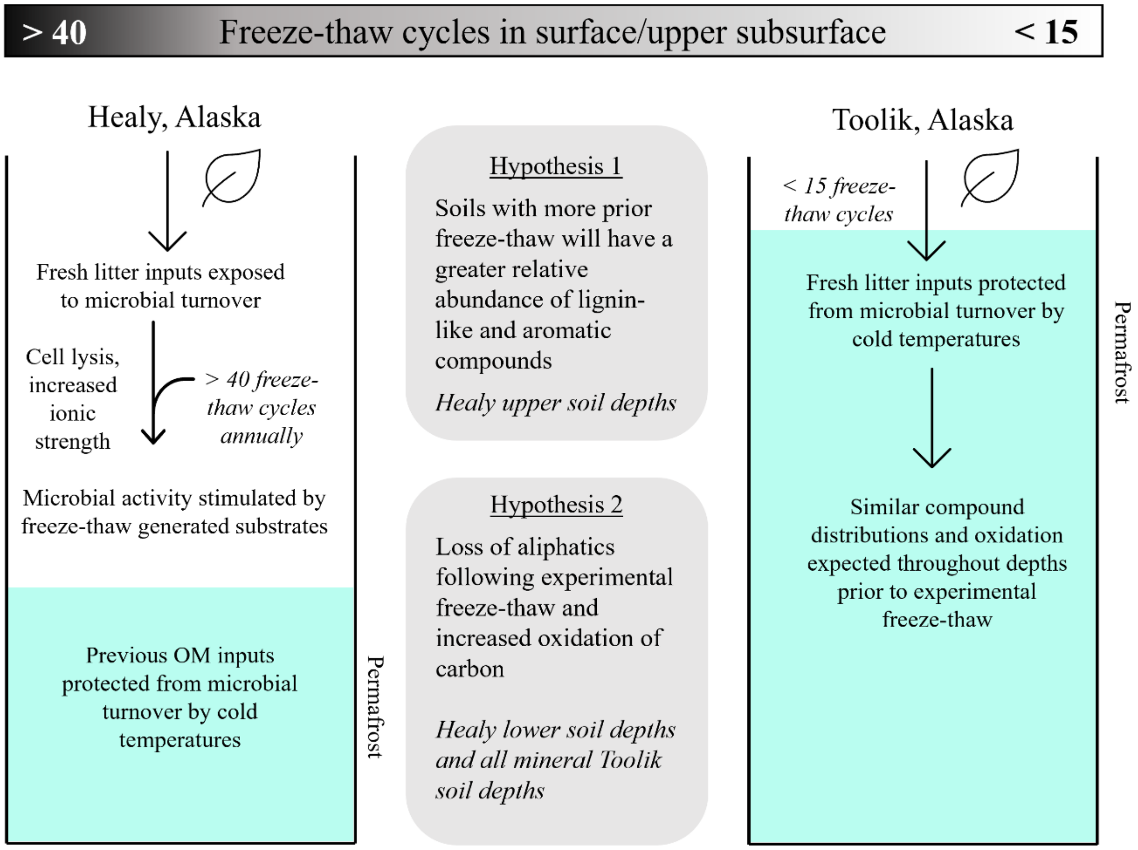

Figure 4.1 Visual hypothesis: Left soil profile is a high freeze-thaw frequency site (Healy), and the right profile is a low freeze-thaw frequency site (Toolik). Freeze-thaw cycles across both sites were measured via the *FTCQuant* package in R (Boswell, Thompson, et al., 2020) using temperature data from the National Ecological Observatory Network (National Ecological Observatory Network, 2021d).

2. Materials and Methods

2.1 Site description and soil sampling

We selected two sites along a latitudinal temperature gradient in Alaska: Toolik and Healy, both of which are part of the National Ecological Observatory Network (NEON) and have permafrost within two meters of the surface. Both sites are in tussock tundra with slopes of < 3 %. The sites exhibit differences in mean annual temperature (MAT) with slight variations in mean annual precipitation (MAP) (Appendix Figure C1; Appendix Table C1). Toolik has a MAT of -9°C and a MAP of 31.6 cm compared to Healy with mean values of -1.3°C and a MAP of 38.5 cm, respectively.

The Toolik core collection site (lat 68.66045, lon -149.37013) is located in tussock tundra in the Arctic foothills of the Brooks Range. Toolik falls within the Philip Smith Mts. quadrangle (Quaternary) composed of unconsolidated surficial alluvial and glacial deposits (Brosgé et al., 2001; Wilson et al., 2015). Vegetation includes dwarf shrubs, sedge, and herbaceous plants. Species include *Eriophorum vaginatum* (tussock cottongrass), *Carex* sp. (true sedges), and *Vaccinium vitis-idaea* (lingonberry) (National Ecological Observatory Network, 2019). The soils at the sampling location were mapped as Typic Histoturbels, which are soils with thick organic horizons that present evidence for cryoturbation and permafrost in the subsurface (National Ecological Observatory Network, 2019).

The Healy core collection area (lat 63.87980, lon -149.21539) occurs in a tussock tundra in central Alaska that is dominated by dwarf shrubs and sedge meadows (National Ecological Observatory Network, 2019). Species include *Betula glandulosa* (American dwarf birch), *Picea glauc*a (white spruce), and *Ledum palustre* (marsh Labrador tea) (National Ecological Observatory Network, 2019). The site falls within the Healy quadrangle and has been characterized as Nenana Gravel (Tertiary, Pliocene, and upper Miocene) with a composition of poorly to moderately consolidated conglomerate and coarse-grained sandstone with interbedded mudflow deposits and thin claystone layers, and local thin lignite beds (Csejtey et al., 1992;

Wilson et al., 2015). Similar to Toolik, the soils at the sampling location were also classified as Typic Histoturbels (National Ecological Observatory Network, 2019).

Three permafrost cores (one meter depth) were sampled from each field site (Toolik and Healy) for a total of six cores. The cores were collected within the footprint of the NEON flux towers in April of 2016. Cores were extracted using a Gidding’s probe (Giddings Machine Company, Windsor, CO, USA). At Toolik, cores were extracted from tundra on the shoulder near the base of a plateau on an east facing slope. At Healy, cores were extracted from a flat tundra with sparse small spruce. Cores were shipped frozen to Oregon State University (OSU) and preserved at -40 °C.

2.1.1 Calculating *in situ* freeze-thaw cycles

The freeze-thaw cycle calculation method was adapted and modified from Rooney et al. (2022) using the FTCQuant R package (Boswell, Thompson, et al., 2020). The number of freeze-thaw cycles was calculated by season (fall, Sept-Nov; winter, Dec-Feb; spring, Mar-May; summer, June-Aug) from three years of collected data (temperature data available from NEON 2018, 2019, and 2020). The *FTCQuant* package requires the selection of freeze-thaw cycle magnitude and duration to define a freeze-thaw cycle. We defined freeze-thaw cycles as soil temperature fluctuations persisting for a minimum of four hours < -1.5°C and a minimum of four hours > 0°C (Elliott & Henry, 2009; Henry, 2007; Rooney et al., 2022). We used soil temperature data for each site (National Ecological Observatory Network, 2021d) to calculate *in situ* freeze-thaw cycle counts. Sensors (Thermometrics - Climate RTD 100-ohm Probes) were placed at 5-cm increments in the top 10 cm, and then at 10-cm increments in the 10 to 80 cm depths. Data were collected by NEON in 30-minute increments for each depth from continuous temperature measurements averaged and recorded every 30 minutes. Individual sensor data were excluded if 3% or more of measurement time points were missing within each analysis time frame. The method ensured that there would be a minimum of one to five usable time series measurements for each depth by season combination. Freeze-thaw counts from 2018 to 2020 were used to infer general characterizations of different freeze-thaw histories across sites and depths.

2.2 Freeze-thaw incubation

We conducted laboratory incubations that exposed a subset of soils from Toolik and Healy to six experimental freeze-thaw cycles, followed by soil chemical analyses. Parent cores (N = 3 for each site) were separated by morphologic horizon designation into incubation units (Table 4.1). All subsequent incubation experiments and soil analyses were performed on incubation units, which represented a distinct combination of depth increment and genetic horizon type (Table 4.1). For data interpretation and statistical analyses, incubation units were classified as follows for comparisons: All major O horizons (or combination horizons dominated by O material) were classified as “organic.” All A/Bw horizons underlying the organic deposits were classified as “upper mineral” material. All Bw/C/Bf horizons beneath the upper mineral depths were classified as “lower mineral” depths.

Incubation units were incubated in 480 mL glass jars for two months. The freeze-thaw incubation parameters included a total of six freeze-thaw cycles consisting of five days for thaw (+2˚C) followed by five days for freeze (-5˚C), for a total of ten days per freeze-thaw cycle. Control soils were kept at -5˚C for a freeze-only treatment throughout the incubation. Parent core subsampling for incubation units and soil morphologic descriptions were conducted in a cold room (-10˚C). Major horizons and sub horizon designations, cryostructures, and coarse fragment estimates were recorded according to Soil Survey Staff (2015), Soil Science Division Staff (2017), and Ping et al. (2015). The incubations were performed in a temperature controlled environmental chamber (Hoffman Manufacturing Inc., SG2-22 Dual Environment Controlled Chamber). Soils were preserved to the greatest degree possible during subsampling (parent core into incubation unit) to retain original soil structure (Appendix Figure C2). Samples were incubated at *in situ* (field moist) moisture to simulate field conditions. Due to the ample headspace of the jars, limited thaw time, and low thaw temperature (+2˚C), the jars were able to remain sealed for the duration of the incubation to reduce the chance for unintentional moisture loss via evaporation and to limit exposure to temperatures over 2˚C. Following the incubation, soils were destructively sampled, and subsamples of each incubation unit were allocated directly to water extraction for FT-ICR-MS, or air-dried and sieved for subsequent analyses (i.e., XRD, texture, and pH/EC).

Table 4.1 Healy and Toolik soil morphology with depth (cm), horizon designation, and material type (organic, upper mineral, and lower mineral).

depth (cm)	horizon designation	material	depth (cm)	horizon designation	material
	Toolik Core 1			**Healy Core 1**	
0-10	Oa/Oi	Organic	0-12	Oe	Organic
10-30	Oe/Oa	Organic	12-24	Oa/Oejj	Organic
30-40	Oea/Bw	Organic	24-33	B/Oajj	Upper Mineral
40-60	Bw	Upper Mineral	33-50	B/Oajj	Upper Mineral
60-67	C	Lower Mineral	50-60	B/Oafjj	Lower Mineral
	Toolik Core 2			**Healy Core 2**	
0-16	Oa/Oe/Oi	Organic	0-12	Oi/Oe	Organic
10-28	Oa	Organic	12-20	Oae	Organic
28-38	Bw	Upper Mineral	20-28	Oe/Bjj	Organic
38-44	Bjj	Upper Mineral	28-34	B/Oajj	Upper Mineral
44-58	BC/Oajj	Lower Mineral	34-47	B/Oafjj	Upper Mineral
			47-68	Bf	Lower Mineral
	Toolik Core 3			**Healy Core 3**	
0-14	Oi	Organic	0-9	Oi	Organic
14-35	Oea	Organic	9-16	Oe	Organic
35-41	BC/Oajj	Upper Mineral	16-30	Oa/Afjj	Organic
41-50	Bw	Upper Mineral	30-38	Af	Upper Mineral
50-58	BC/Oajj	Lower Mineral	40-54	BCg	Lower Mineral

2.3 Fourier transform ion cyclotron resonance mass spectrometry

Following the incubation experiment, incubation units were subsampled for water extraction directly from the incubation. FT-ICR-MS analysis was performed on water-extractable organic carbon (WEOC) via automated direct infusion at the Environmental Molecular Sciences Laboratory (EMSL) in Richland, WA on a 21 T FT-ICR mass spectrometer using negative mode electrospray ionization. Soil (300 mg wet weight) was subsampled from each incubation unit and weighed into 2 mL glass vials (MicroSolv) with 1 mL of MilliQ water added. Vials were shaken on a thermo mixer (Eppendorf ThermoMixer C) for 2 hours at 448 Relative Centrifugal Force (RCF) at room temperature and then filtered through 0.45 µm Hydrophilic PTFE filters (Thermo Scientific) for WEOC extracts. The filtered extracts were prepared for FT-ICR-MS analysis using Bond Elut PPL solid phase extraction cartridges (Agilent, USA) following Dittmar et al., (2008).

WEOC extracts were diluted 1:2 (sample: methanol by volume) to aid ionization and then randomized for analysis. One hundred and forty-four individual scans were averaged for each sample to improve the overall abundance of ions detected. Peak selection and calibration filtered data to a signal-to-noise ratio of 7. Datasets were aligned and formulae were assigned using the in-house *Formularity* software (Kujawinski & Behn, 2006; Tolić et al., 2017). Further data processing was performed using the *fticrrr* R package (Patel, 2020). All peaks were analyzed on a presence/absence basis with only peaks occurring in ⅔ of replicates considered to be present (Kujawinski et al., 2002). Only carbon-containing formulas between 200 and 900 m/z were included. The modified aromaticity Index (AI_{mod}) (Eq 1) was calculated for each formula to help with compound classification (Koch & Dittmar, 2006).

Eq. 1: Aromaticity Index (AI_{mod})

$$AImod = \frac{1 + C - (0.5 \times O) - S - (0.5 \times (N + P + H)))}{(C - (0.5 \times O) - S - N - P)}$$

Eq. 2: Nominal Oxidation State of Carbon (NOSC)

$$NOSC = \frac{4 - (((4 \times C) + H - (3 \times N) - (2 \times O) - (2 \times S))}{C}$$

In which C = carbon, H = hydrogen, O = oxygen, S = sulfur, N = nitrogen, P = phosphorus.

The identified molecules were separated into four compound classes using the AI_{mod} and H/C and O/C ratios, following Seidel et al. (2014): (1) condensed aromatics ($AI_{mod} > 0.66$); (2) aromatic compounds ($0.66 > AI_{mod} > 0.50$); (3) highly unsaturated and lignin-like compounds ($AI_{mod} < 0.50$ and $H/C < 1.5$);

and (4) aliphatic compounds (> $H/C \geq 1.5$) (Appendix Figure C3). Relative abundances were calculated as the number of unique peaks (formulas) within a specific compound class compared with the total number of unique peaks across all compound classes. We used the nominal oxidation state of carbon (NOSC, equation 2) to analyze thermodynamic favorability of compounds to determine which compound classes and depths were most susceptible to microbial oxidation at each site. The association between NOSC and thermodynamics is based on the assumption of oxic conditions and use of oxygen as the dominant terminal electron acceptor, allowing for a relationship between Gibbs Free Energy and NOSC established in previous literature (Graham et al., 2017; LaRowe & van Cappellen, 2011).

2.4 Soil properties and characterization

Following the incubation, freeze-only (control) samples were subsampled for soil physical-chemical properties and analyzed for soil particle size, pH, electrical conductivity, and gravimetric moisture by the Oregon State University Soil Health Laboratory. Soil pH and electrical conductivity (EC) were measured on sieved (<2mm), air-dried soils. Deionized water was added to the soil (1:1 w/w) to form a soil slurry and then analyzed via pH/EC meter (Hanna H15522) (Miller et al., 2013; Thomas, 2018) (Table 4.2). Gravimetric moisture was determined on 1-1.5 g field moist samples by oven drying for 24 hours at 105°C. Gravimetric moisture, pH, and EC were analyzed on the control samples of all depths and then pooled within each material class for statistical analysis (i.e., organic, upper mineral, lower mineral) (Table 4.2).

Table 4.2 Soil characterization properties for Healy and Toolik soil depths, reported as mean +/- standard error. Moisture is reported as gravimetric moisture content. Particle size classes were determined only for upper and lower mineral soil depths, via the sieve and pipette method.

						Particle size analysis			
	pH	EC (dS/cm)	Soil Moisture (%)	Total C (%)	Total N (%)	Sand (%)	Silt (%)	Clay (%)	Texture Class
Healy									
Organic	4.55 ± 0.08	0.06 ± 0.01	439.19 ± 141.6	38.54 ± 1.4	1.27 ± 0.06	*NA*	*NA*	*NA*	*NA*
Upper Mineral	5 ± 0.15	0.03 ± 0	203.47 ± 9.91	20.27 ± 1.79	0.85 ± 0.09	24 ± 3	45 ± 4	31 ± 3	Clay Loam
Lower Mineral	5.36 ± 0.13	0.02 ± 0	122.8 ± 33.04	10.96 ± 0.41	0.42 ± 0.01	36 ± 5	40 ± 4	23 ± 2	Loam
Toolik									
Organic	5.07 ± 0.18	0.03 ± 0	420.73 ± 55.62	41.04 ± 0.89	1.96 ± 0.14	*NA*	*NA*	*NA*	*NA*
Upper Mineral	5.31 ± 0.09	0.02 ± 0	35.73 ± 6.91	11.34 ± 0.6	0.42 ± 0.02	47 ± 6	29 ± 1	25 ± 3	Loam
Lower Mineral	5.29 ± 0.11	0.03 ± 0	30.85 ± 4.58	11.75 ± 0.97	0.44 ± 0.05	48 ± 7	27 ± 0	25 ± 1	Sandy Clay Loam

Footnote: Sand defined as 50 microns to 2 mm, silt defined as 2 to 50 microns, clay defined as <2 microns.

Particle size distribution was determined on mineral horizon samples via the sieve and pipette method (Gee & Bauder, 1986; Köhn, 1928; Sheldrick & Wang, 1993). Control samples from every mineral depth were air dried and sieved to < 2 mm, with two depths excluded due to too little sample mass. Both upper mineral and lower mineral depth classes had an N = 3 at each site, with the exception of Toolik lower mineral which had an N = 2 (particle size analysis only) due to a limited sample. Preceding analysis, organic matter and other cementing agents were removed from soil. Sodium hexametaphosphate was added to the soil suspension and shaken overnight. Sand size fractions were separated by wet sieving through 2000 µm, oven dried, and then sieved through a series of sieves (50 to 100 µm, 100 to 250 µm, 250 to 500 µm, 500 to 1000 µm, and 1000 to 2000 µm). The remaining silt and clay suspension was brought to a volume of 1 liter and specific aliquots of fluid were removed by pipette at time and depth points to capture silt and clay particles in accordance with Stokes' Law (Table 4.2). Following data collection, particle size fractions were averaged within each depth class (i.e., upper mineral, lower mineral) (Table 4.1).

Following incubation, control samples only were air-dried, sieved, and ground prior to analysis for nitrogen and carbon on a Vario EL Cube Elemental Analyzer (Elementar Analysensysteme GmbH, Langenselbold, Germany). Homogenized samples were weighed and sealed into tin boats, and then combusted at 1150˚C in the presence of oxygen. The signals for nitrogen and carbon were measured using a Thermal Conductivity Detector (TCD). The detector response was calibrated using aspartic acid and validated using a soil reference material.

2.5 X-ray diffraction

Powder x-ray diffraction (XRD) patterns were collected from powders packed into zero-background well holders using a SmartLab SE diffractometer (Rigaku, Japan). The instrument employed Bragg-Brentano geometry with a Cu X-ray source ($\lambda = 1.5418$ Å), a variable divergence slit, and a high-speed D/teX Ultra 250 1D detector. Patterns were collected between 2 and 100 °2θ at intervals of 0.01 °2θ, scanning at 2°2θ/min. Quantitation of minerals was performed by the Rietveld method using TOPAS (v6, Bruker AXS). This method combines calculated XRD patterns from the substituent minerals to provide the best fit with the observed pattern. For each mineral, the scale factor, cell parameters (constrained within ca. 0.5 % of the expected values), and crystallite size (constrained between 50 and 500 nm) were refined. For minerals with a platy morphology, a preferred orientation correction was also refined. The scale factors from the Rietveld refinement were used to determine the relative quantities of the minerals, which are presented scaled to a total of 100%.

2.6 NEON geochemical data for soil characterization

We accessed NEON geochemical data for both sites from NEON distributed plot initial characterization, which provides site-level differences for soil properties at Healy and Toolik (National Ecological Observatory Network, 2021b) Dithionite citrate-extractable (DC) (captures total non-silicate crystalline iron oxides, substituted aluminum in iron oxides, and both organically-complexed and poorly crystalline iron and aluminum) as well as ammonium oxalate-extractable (AO) (captures organically-complexed and poorly crystalline iron and aluminum) values were used to determine crystalline Fe + Al (Eq. 3) (Figure 3; Shang & Zelazny, 2015).

Eq. 3: Crystalline iron (Fe) and aluminum (Al)

$$Crystalline\ Fe + \ Al = (DC\ Fe - \ AO\ Fe) + (DC\ Al - AO\ Al)$$

2.7 Supplemental respiration experiment

After the freeze-thaw incubation, soils were subsampled for respiration measurements which were used determine the relationship between the FT-ICR-MS profile and response of aerobic respiration to freeze-thaw cycles. Aerobic incubations were conducted using 20 to 30 g of soil subsampled from select incubation units following the freeze-thaw incubation. The samples were stored in 50-mL specimen cups placed inside air-tight quart-size Mason jars that had an internal volume of 946 mL, with 2 mL of water added to the bottom of the jar to reduce evaporation. The Mason jar lids were fitted with rubber septa to collect headspace samples. The aerobic incubation was conducted over two weeks in a dark cabinet at 20˚C. Gas samples were taken from the mason jars at 1, 4, 7, and 14 days and immediately analyzed on a Picarro [A0311] gas analyzer for CO_2 concentration. After each measurement, jar lids were opened, and the airspace of each jar was cleared using a laboratory vacuum at a low suction for one minute each and then left open for 10 minutes to allow for air circulation. Soils were maintained at their time-zero moisture content. Results from this experiment are included in Appendix Text C2 and Appendix Figure C8.

2.8 Statistics

FT-ICR-MS data were analyzed using univariate linear mixed-effects models (LME), permutational multivariate analysis of variance (PERMANOVA), and principal components analysis (PCA) to test the effect of site (Healy and Toolik), depth (organic, upper mineral, and lower mineral), treatment (freeze-thaw vs. control), and their interactions on the relative abundance of compound classes and the nominal oxidation state of carbon. When testing the effect of site and treatment on the NOSC of compound classes, depth was used as a random effect. For the FT-ICR-MS data, we tested the effects of site, depth, and treatment on all soil depths as well as on mineral only soil depths due to the unique behavior of organic soil horizons (with mineral-only data noted in the text). We tested the effects of site and material as well as their interaction on X-ray diffraction mineral abundances and the ratio of crystalline to poorly crystalline Fe + Al forms using analysis of variance (ANOVA). Statistical significance was determined at $\alpha = 0.05$. Data analysis and visualization were performed using R version 4.0.1 (2020-06-06) with RStudio version 1.4.1106 (R Core Team, 2020; RStudio Team, 2019). Diffractogram patterns were visualized using the *powdR* package version 1.3.0 (Butler et al., 2021). Data processing and analysis was conducted using *dplyr v1.0.1* (Wickham et al., 2020) and *vegan v2.5-6* (Oksanen et al., 2019) packages. Data visualization was conducted using *ggplot2 v3.3.2* (Wickham, 2016) and *PNWColors* (Lawlor, 2020). All data and scripts are available at https://github.com/Erin-Rooney/FTC-FTICR and archived and searchable at https://search.emsl.pnnl.gov.

3. Results

3.1 Characterization of control soils

We observed evidence for contrasting freeze-thaw histories between the two study sites and as a function of depth using temperature data collected by NEON from 2018 to 2020 (Fig. 4.2) (National Ecological Observatory Network, 2021d). Healy soils experienced the greatest freeze-thaw cycle frequency, with the majority (61 to 65 %) of freeze-thaw cycles occurring in organic soil depths during spring (March to May). During spring, organic soils experienced > 35 cycles while upper mineral soils underwent 13 cycles in both fall and spring, with the majority (8 freeze-thaw cycles) occurring in fall (Fig. 4.2). In contrast, Toolik experienced fewer freeze-thaw cycles, with the majority of the cycles (88 to 93 %) occurring in the fall (< 15 freeze-thaw cycles in the surface soils). The lower mineral soils experienced very few freeze-thaw cycles at both sites, approximately 1-2 per year.

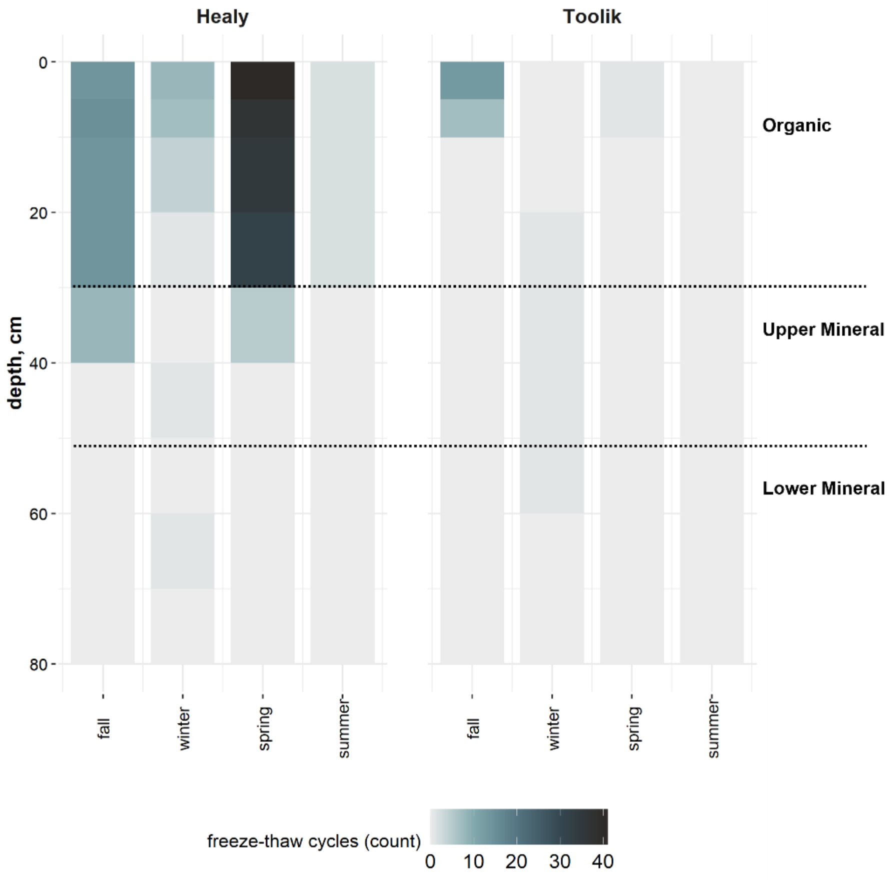

Figure 4.2 Short duration freeze-thaw cycles (four hours < -1.5°C and a minimum of four hours > 0°C) measured by site and depth using NEON temperature data from 2018-2020 and calculated using the *FTCQuant* Package (Boswell, Thompson, et al., 2020; National Ecological Observatory Network, 2021d).

Soil morphological observations, horizon designations, pH, EC, and texture classes were similar across sites (Tables 4.1-4.2). We observed thicker ice layers in mineral horizons at Healy (1 to 3 cm) compared to Toolik (< 1 mm), which aligned with the large variations in gravimetric moisture percentages identified in the samples between sites (Appendix Table C1; Table 4.2). Healy and Toolik showed some contrast in soil particle size distribution across mineral soil depths, with Healy composed of clay loam and loam soils versus the loam and sandy clay loam soils identified at Toolik (Table 4.2). Clay percent varied from 31% to 23% in the upper and lower mineral soils at Healy, respectively, whereas clay percentages for the Toolik mineral soils remained constant at ~25% throughout.

Mineralogical composition for mineral soils at both Healy and Toolik was relatively similar with quartz and feldspar minerals comprising the most abundant mineral phases, although we did observe notable differences in mineral abundance (Appendix Figure C4). Toolik mineral soils were dominated by quartz (~ 80 %), with minor amounts of mica (~ 6.6 %), albite (~ 4.4 %), and chlorite (~ 4.7 %). Conversely, Healy soils contained less quartz (~ 46 %), greater proportions of mica (~ 21 %), and albite (~ 16 %). When comparing mineralogical abundance between sites, Healy consistently contained more phyllosilicate (e.g., mica, kaolinite) and inosilicate minerals (e.g., hornblende) compared to Toolik (ANOVA, $P < 0.05$). Healy also contained more potassium-rich feldspar (microcline), plagioclase feldspar (albite), and chlorite compared to Toolik soils (ANOVA, $P < 0.05$) (Appendix Figure C4). Depth did not have a significant effect on mineral composition, nor did we find an interaction of site and depth (Appendix Figure C4-C5). We also integrated geochemical data generated by NEON into our analysis to compare differences in the ratio of crystalline to poorly crystalline Fe + Al forms. We found that Toolik exhibited a higher proportion of crystalline Fe + Al compounds compared with Healy, which had a higher proportion of poorly crystalline Fe + Al (ANOVA, $F = 12.726$, $P < 0.001$) (National Ecological Observatory Network, 2021b) (Figure 4.3).

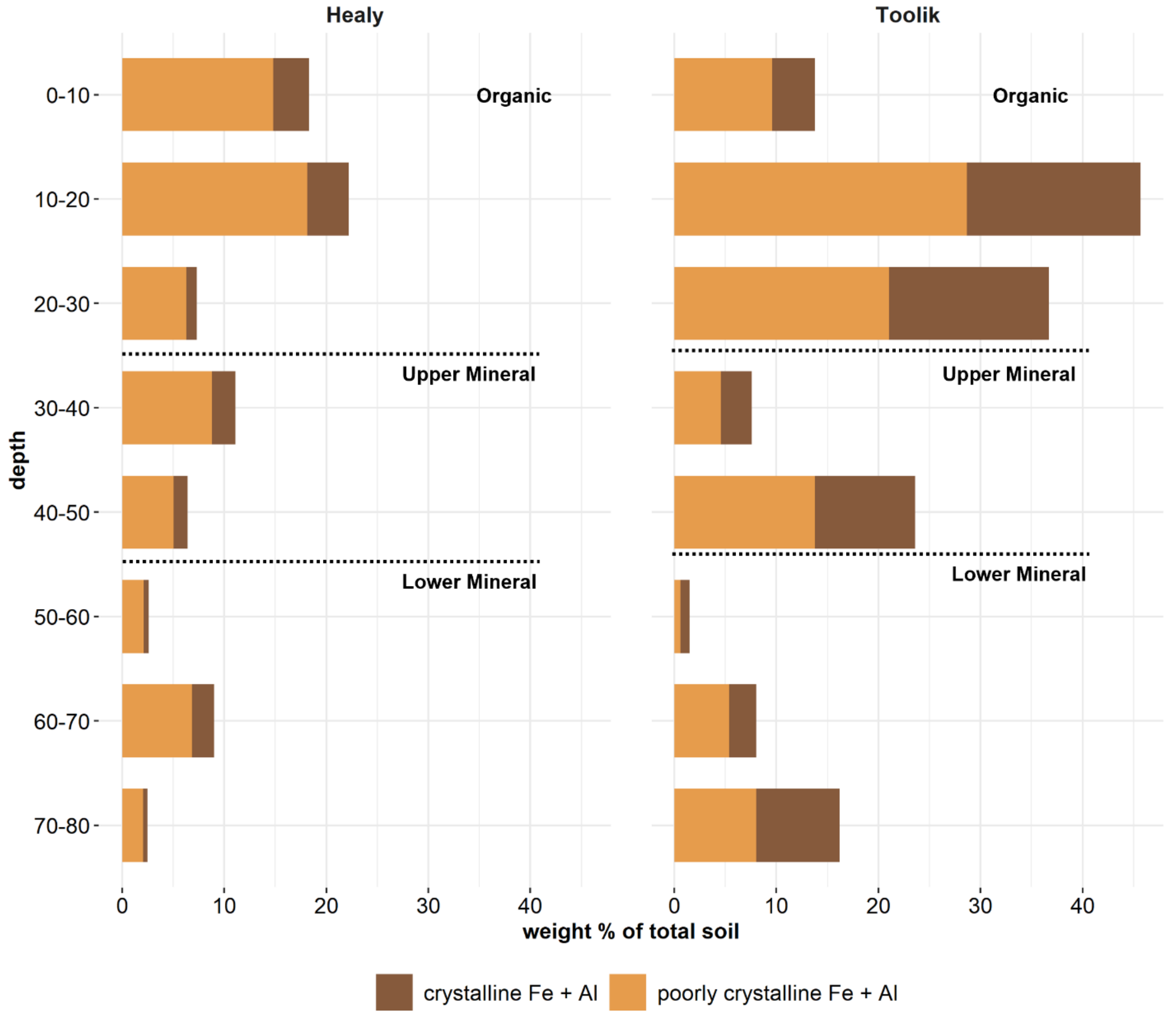

Figure 4.3 Crystalline and poorly crystalline iron and aluminum, reported as percent weight of soil. Toolik had a higher proportion of crystalline iron and aluminum compared with Healy, which was dominated by poorly crystalline compounds (ANOVA, $P < 0.001$). Data from NEON distributed plot soil chemistry data, 2021 release (National Ecological Observatory Network, 2021b).

3.2 SOM composition of control soils

SOM composition of the control soils (incubated as freeze-only) varied with depth (PERMANOVA, $P = 0.001$; Fig. 4.4) but did not differ by site (PERMANOVA, $P = 0.815$). The surface organic soils showed similar chemical compositions across both sites, with lignin-like molecules comprising ~ 50 % and aliphatic molecules comprising ~ 35 % of the total identified peaks (Figure 4.5; Fig. 4.4A). We identified a stronger separation between sites for the lower mineral soil depth versus the organic or upper mineral soils after accounting for intra-depth variability using between-site Euclidean distances (Fig. 4.4B). The Healy lower mineral soils were strongly influenced by aromatic and lignin-like molecules compared to Toolik lower mineral soils, which were more influenced by condensed aromatic molecules (Fig. 4.4A).

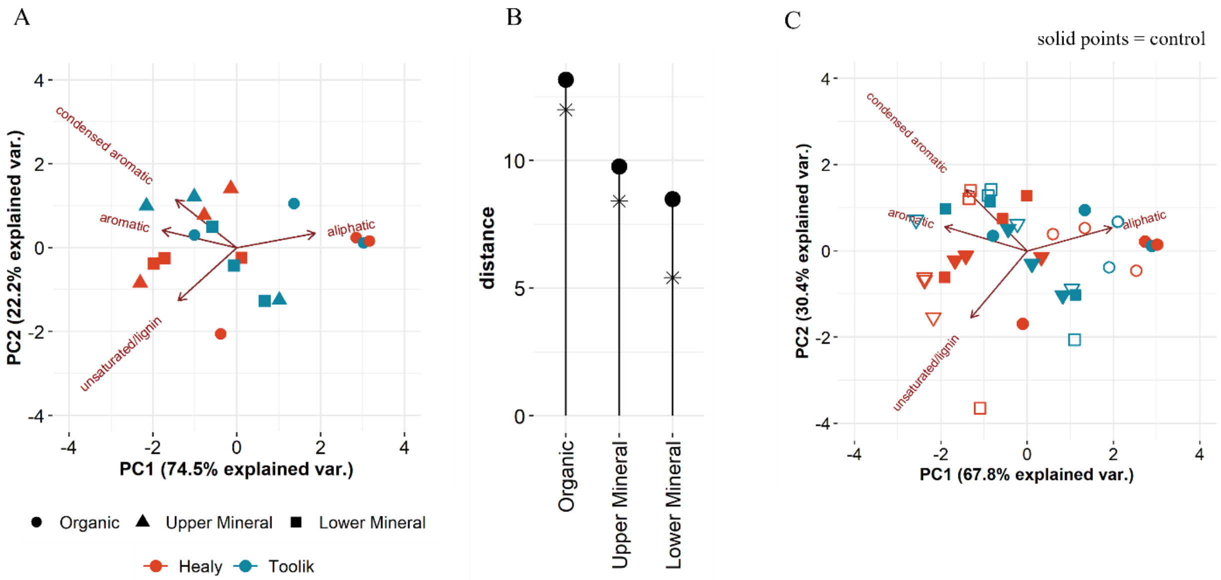

Figure 4.4 (A) Principal Components Analysis biplot of FT-ICR-MS data showing separation by site for control samples. (B) Euclidean distances between sites for each soil depth (controls only). Black stars indicate intra-depth variability at each site whereas the black circles represent the Euclidean distance between sites at each depth. (C) Principal Components Analysis biplot of FT-ICR-MS data showing separation by site for all samples. Solid points = control (freeze-only) samples, open points = FTC treated samples.

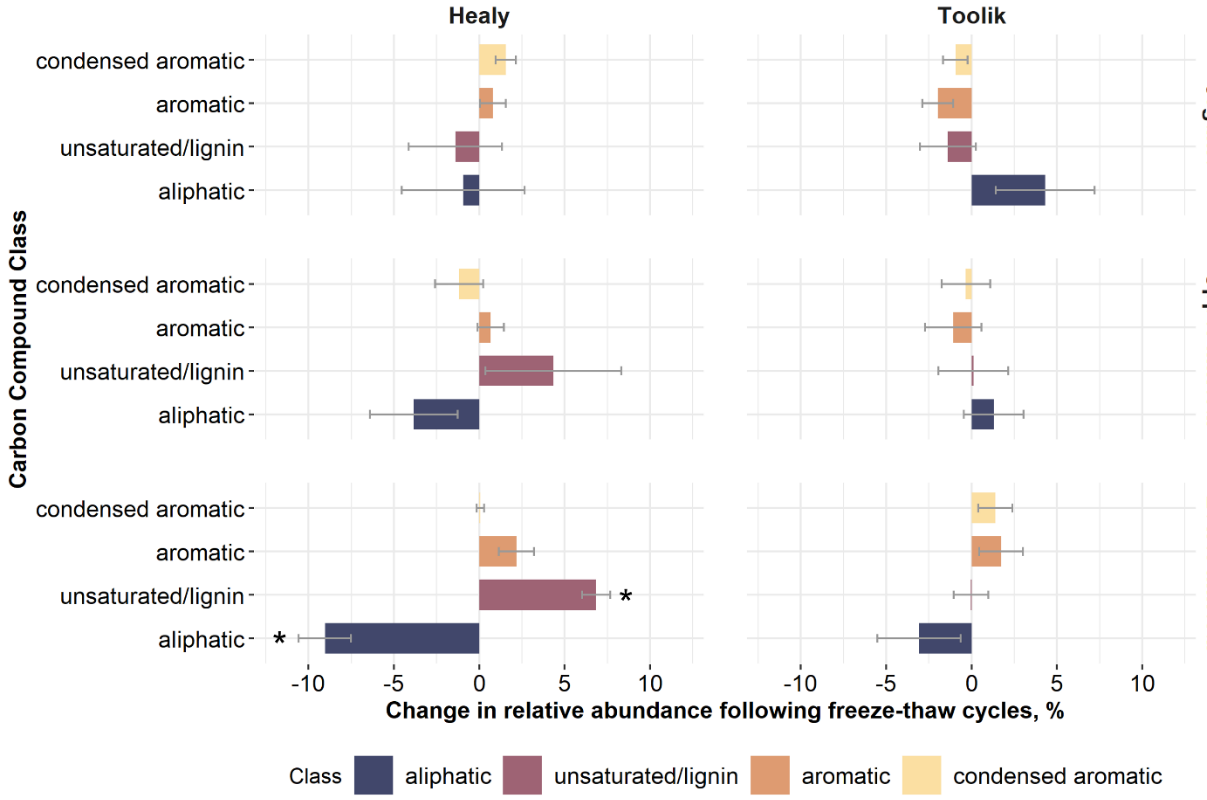

Figure 4.5 The change in relative abundances (percentage) of carbon compound classes following freeze-thaw cycles within each material grouping from Healy and Toolik. Asterisks denote significant differences between control and freeze-thaw, at α = 0.05. Error bars represent standard error calculated by propagation of error.

3.3 SOM composition following experimental freeze-thaw

The freeze-thaw laboratory incubations caused shifts in the FT-ICR-MS-resolved SOM composition in the lower mineral horizons at Healy (Fig. 4.4C & 4.5). Following the freeze-thaw incubations, the organic horizon soils at both sites remained strongly influenced by aliphatic molecules following freeze-thaw at both sites (~35 to 38 % across both Toolik and Healy), with as much intra-site variability as inter-site variability in organic depths (Fig 4.4C, Appendix Figure C6). There was a stronger separation by site in the lower mineral depths (Fig 4.4C). For example, Healy soils exhibited an increase of ~7% in the relative abundance of lignin-like molecules and a decrease of ~9% in aliphatics whereas Toolik soils experienced only minor, non-significant changes in the relative abundances of the compound classes (Fig 4.4C; Fig

4.5). The supplemental respiration experiment showed carbon losses as CO_2 from both Healy and Toolik, with the largest CO_2 production occurring during days 1 and 4 in control samples from Toolik's lower mineral depths. In contrast, Healy showed the largest concentration of CO_2 during day 1 in the lower mineral freeze-thaw samples (Appendix Figure S8).

We found that sample depth had a larger effect on FT-ICR-MS resolved SOM composition compared to site or freeze-thaw treatment when including organic as well as mineral horizons in the PERMANOVA analysis. Sample depth accounted for 12 % of total variation in compound classes across <u>all samples</u> (PERMANOVA, $P = 0.01$) and site accounted for 5 % of variation ($P = 0.07$) whereas freeze-thaw did not have a significant effect on SOM composition ($P = 0.545$). When we analyzed <u>only the mineral soil depths</u>, site accounted for 17 % of total variation ($P = 0.031$), whereas freeze-thaw still did not have a significant effect (PERMANOVA, $P = 0.231$). Notably, the PCA showed a greater separation of control vs. freeze-thaw soils in the lower mineral depth of Healy relative to intra-treatment variability. All other depths within both sites had as much intra-treatment variability as distance between freeze-thaw and control, with no significant effect of the interaction between freeze-thaw treatment and site ($P= 0.3$; Fig. 4.4C, Appendix Figure C6).

The Healy organic and mineral soils showed strong shifts in SOM composition following freeze-thaw incubation (Figs. 4.6, 4.7). Following experimental freeze-thaw, Healy upper mineral soils experienced a net increase in the unique peaks identified, as peaks were lost from the aliphatic and lignin-like regions, and new peaks were identified in the same regions. In contrast, the Healy lower mineral soils experienced a net loss in peaks identified, as peaks were mostly lost from all regions. Additionally, the loss and gain of unique compounds across Healy's organic, upper mineral, and lower mineral depths follow a sequential shift. The gained peaks in the organic and upper mineral depths overlap with the lost peaks in the upper mineral and lower mineral depths, respectively (Fig. 4.6). It is important to note that organic carbon was not standardized during FT-ICR-MS analysis. It is likely that some peak count differences may be attributed to variability in SOM content across samples, although the low variability within depth classes and across the organic and lower mineral depths of both sites (Table 4.2) reduces this concern. In addition to changes in peak count following freeze-thaw, there were shifts in the NOSC values of the identified peaks. Prior to freeze-thaw, Healy had higher NOSC values at all three depths compared with Toolik (LME, $P < 0.005$) (Appendix Figure C7). Following freeze-thaw, Healy upper mineral soils experienced a net gain of identified molecules (477 peaks), whereas the lower mineral soils experienced a net loss (646 peaks) (Fig. 4.6), with site, treatment, and depth having variable effects on NOSC values of gained and lost compounds. In Toolik, increased NOSC occurred in aliphatic compounds gained following freeze-thaw. Conversely, increases in NOSC for the Healy samples only occurred in the aromatic and lignin-like compounds gained following freeze-thaw (Fig. 4.8).

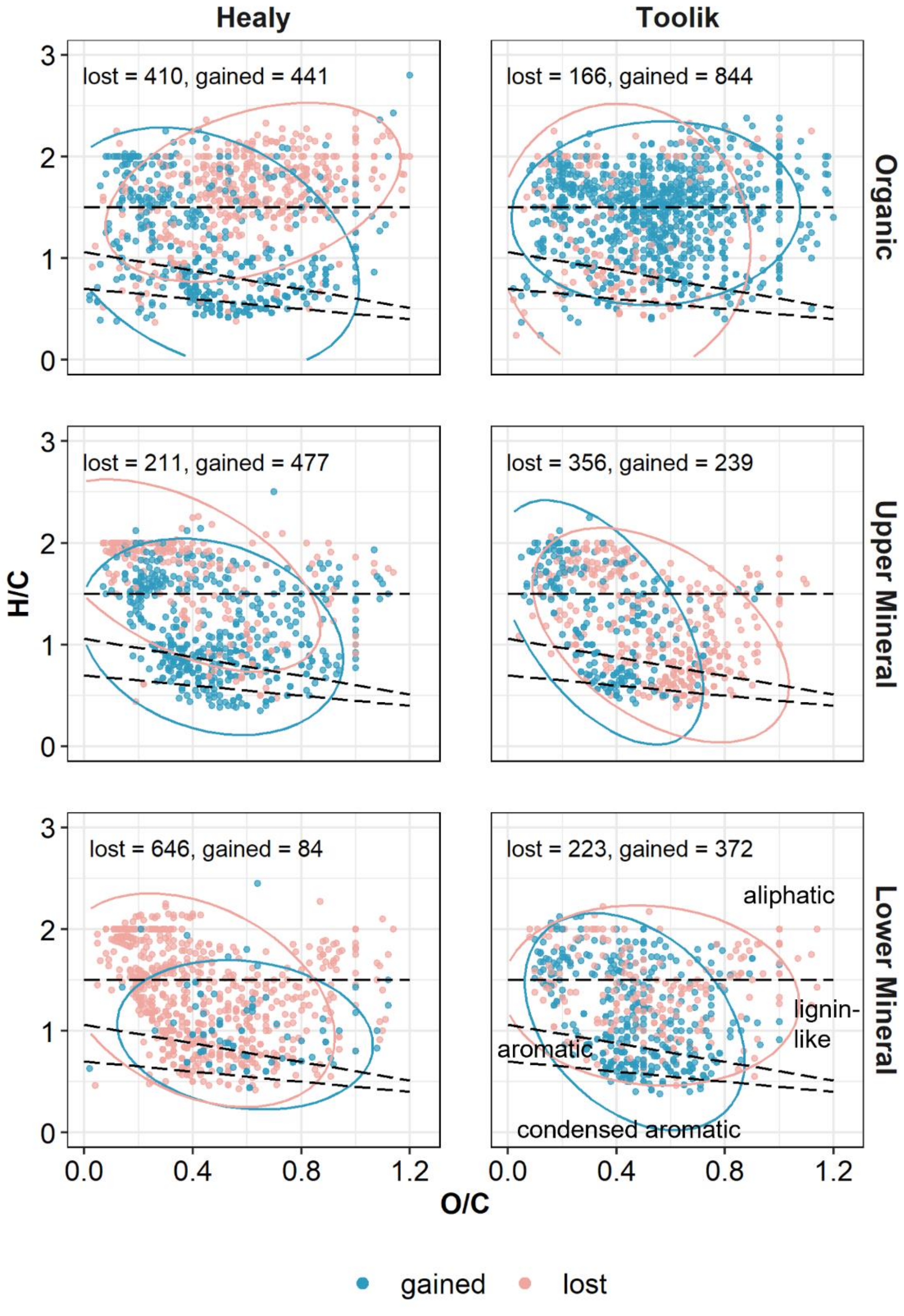

Figure 4.6 Van Krevelen plots showing organic compounds gained (newly identified) and lost following freeze-thaw, by site and depth. Molecules are plotted as functions of their H-to-C and O-to-C ratios. Ellipses represent 95% confidence intervals. See Appendix Figure C3 for illustration of van Krevelen diagram interpretation.

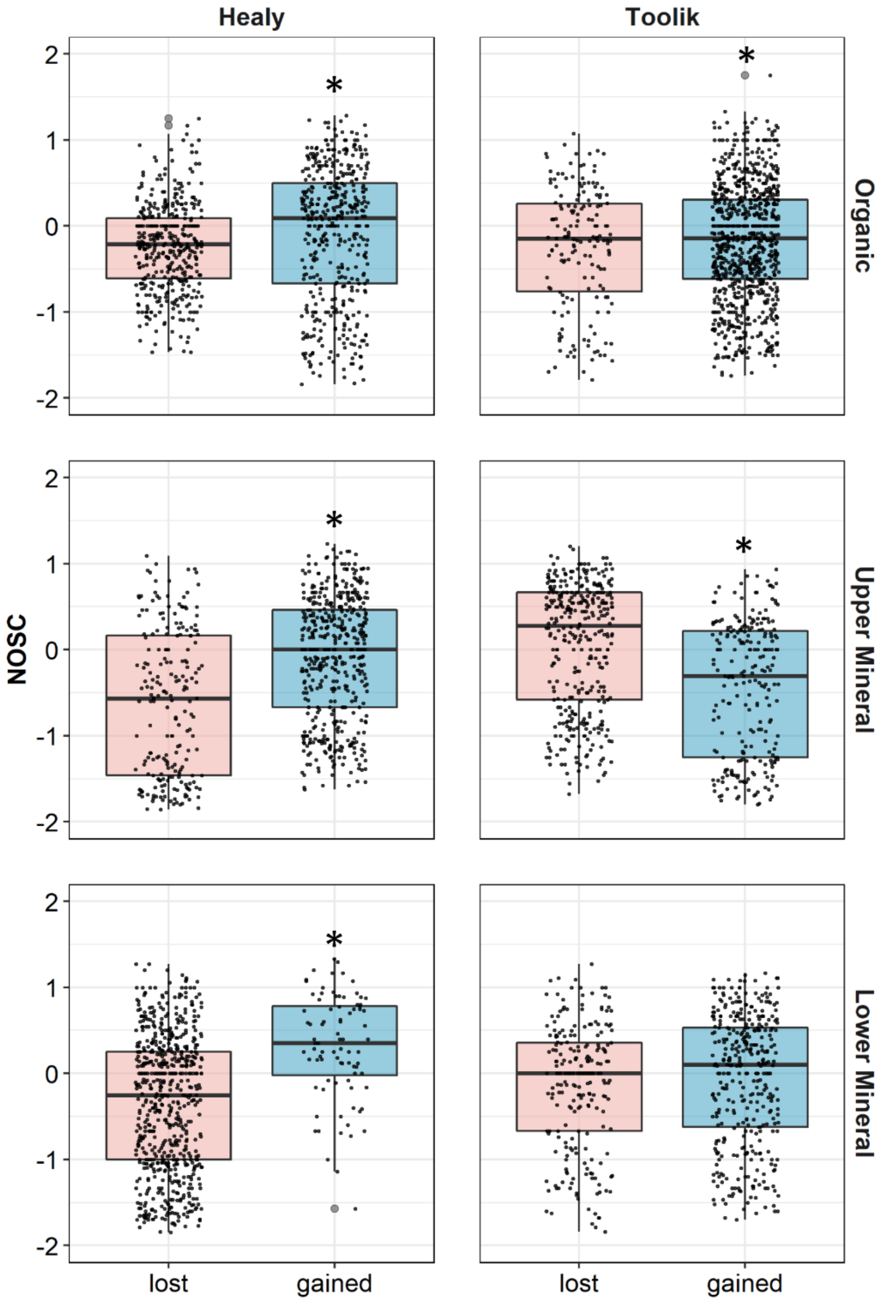

Figure 4.7 Nominal oxidation state of carbon (NOSC) for molecules lost or gained (newly identified) following freeze-thaw, by site and depth. Asterisks denote statistically significant differences between treatments at α = 0.05. For Healy soils, NOSC of newly identified compounds was greater than NOSC of compounds lost, for all depths. For Toolik organic soils, NOSC of gained > lost, whereas for Toolik upper mineral soils, NOSC of lost > gained following freeze-thaw.

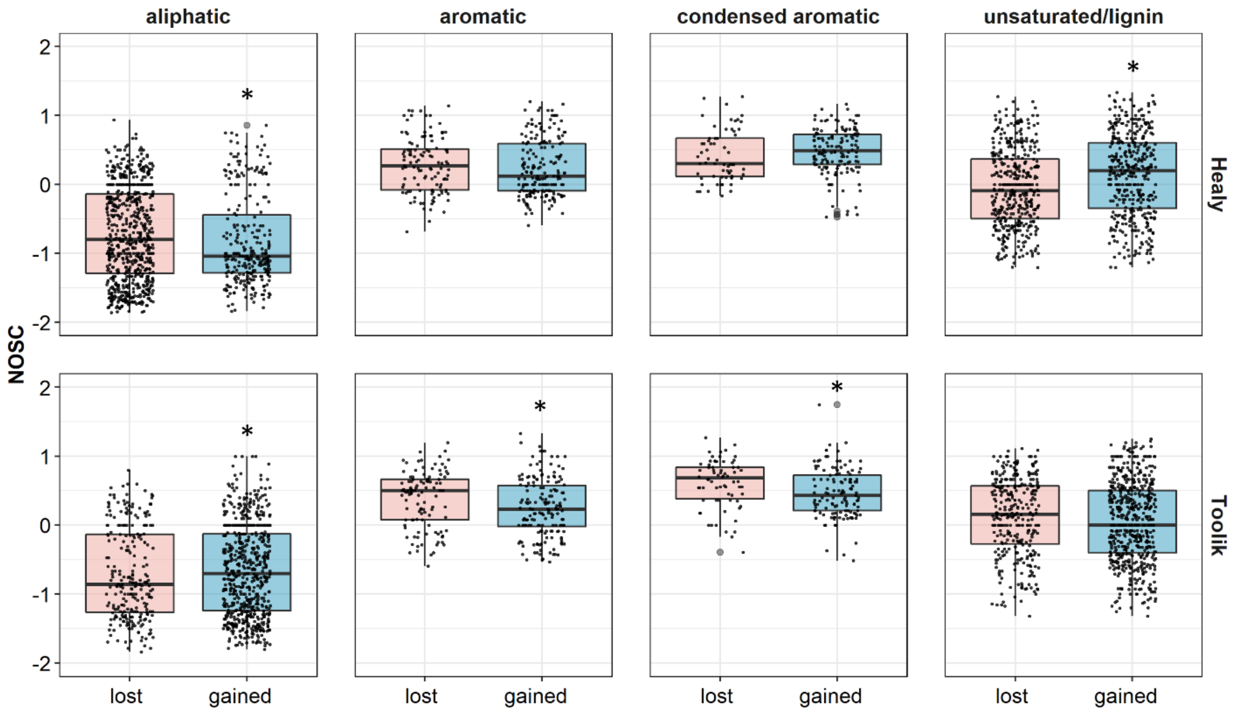

Figure 4.8 Nominal oxidation state of carbon (NOSC) for compounds lost or gained (newly identified) following freeze-thaw, by site and compound class (all depths). Statistical significance was determined at α = 0.05. There were significant increases in the NOSC of gained compounds (compared to lost compounds) in lignin-like compounds in Healy soils and aliphatic compounds in Toolik. There were significant decreases in the NOSC of gained compounds (compared to lost compounds) in Healy aliphatics as well as Toolik aromatics and condensed aromatics.

4. Discussion

4.1 Freeze-thaw history and SOM composition

The recent freeze-thaw history captured by available NEON soil temperature data (2018-2020) and our *FTCQuant* analysis (Boswell, Thompson, et al., 2020) indicated the largest difference in prior freeze-thaw occurred between organic horizons at Healy and Toolik. We detected evidence for ~40 annual freeze-thaw cycles in organic soils from Healy versus ~15 annual freeze-thaw cycles in those from Toolik. However, the organic soils from both sites were compositionally similar, with comparable relative abundances of lignin-like compounds and aliphatics. We made similar observations for the upper mineral soils, which again differed by site in terms of prior freeze-thaw but were compositionally alike.

Hypothesis 1 predicted that soil depths at Healy and Toolik with the highest previous freeze-thaw frequency (Healy mineral depths and Toolik organic depth) would be composed of more lignin-like and aromatic compounds due to preferential turnover of simple aliphatic compounds during prior freeze-thaw or extended periods of thaw. We infer from the SOM compositions of the organic horizons at the landscape surface that carbon composition and carbon oxidation states may not vary considerably between sites even in cases where annual freeze-thaw differs by 25 freeze-thaw cycles, contradicting Hypothesis 1. Our findings further question the effect of cumulative freeze-thaw cycles on SOM composition, aligning with prior literature that reported negligible differences between concentrations of ammonium (Kaizad F. Patel et al., 2021) and microbial biomass carbon (Song et al., 2017) following the first freeze-thaw cycle and subsequent freeze-thaw cycles following a prolonged state of thaw or freezing. The disruption to microbes associated with initial freeze-thaw was well illustrated by the decreasing microbial N and increasing available N reported in high alpine soils in the Lys Vallée of Northwest Italy (Freppaz et al., 2007). These findings have led to the conclusion that most lysis and impact to microbial biomass occurs during the first freeze-thaw cycle, although some potential for additional disturbance and impacts to SOM content and nutrient cycling were reported in the same studies (Freppaz et al., 2007;

Song et al., 2017). Our findings contribute a longer timeframe than typically studied. We found that contrasting freeze-thaw cycle frequencies did not result in differences in carbon compound class and oxidation states within FT-ICR-MS resolved SOM compositions. In contrast to surface soils with large differences in freeze-thaw history, we detected differences in the FT-ICR-MS profile of deeper mineral subsoils with similar freeze-thaw history. This suggests that other factors, such as particle size distribution, may exert stronger control on SOM composition in soils with smaller amounts of prior freeze-thaw. Differences in particle size class can result in contrasting oxygen limitations that may be responsible for differing mineralization rates and selectivity in carbon compound protection (Keiluweit et al., 2017). Specifically, the presence of anaerobic microsites attributed to finer textured soils has been associated with decreased mineralization. However, the higher NOSC of the finer-textured Healy control soils contradicts the selective protection and decreased mineralization described by Keiluweit et al. (2017) in finer particle sizes (25 to 45 µm) compared with coarser particle sizes (150 to 250 µm). The response of Healy lower mineral soils to freeze-thaw also showed increased mineralization compared with Toolik soils. Healy's lower mineral soils had a larger loss of unique peaks across all compound classes (and complementary increase in respiration shown in Appendix Figure C8) and increase in oxidation in the finer textured soils (Healy samples). Consequently, the differences in SOM composition between Healy and Toolik soils are likely the result of a combination of biogeochemical factors which may have played a role in driving differences in SOM response to experimental freeze-thaw.

4.2 SOM response to experimental freeze-thaw

One of the largest differences in freeze-thaw response occurred between Healy and Toolik samples in the soil depths with the most similar prior freeze-thaw history: lower mineral soil depths (Fig. 4.2; Figs 4.5-4.8). The upper and lower mineral soils at Toolik were the only samples to not undergo an overall increase in NOSC following experimental freeze-thaw, although there was an increase in the NOSC of aliphatic molecules in the lower mineral soils (Fig. 4.7, Fig 4.8). The lower mineral soils from

Healy were the only samples to undergo changes in relative abundance of carbon classes (with lignin-like compounds increasing and aliphatics decreasing) as well as the only samples to lose more carbon compounds than were gained. Total carbon content was similar across lower mineral samples from both sites, which reduces concerns that the FT-ICR-MS analysis protocol did not control the amount of organic matter in each sample injected for analysis. However, we do acknowledge that this protocol does limit the interpretation of changes in peak count.

Hypothesis 2 predicted a loss of aliphatics in soils with little prior freeze-thaw as temperature-driven protection from turnover was lost during experimental freeze-thaw. While we did not observe the expected loss in simple aliphatic molecules, the increase in the NOSC (the oxidation of carbon molecules) of aliphatics in Toolik samples following freeze-thaw, accompanied by a decrease in NOSC in aromatics and condensed aromatics, could indicate that the carbon metabolism in the Toolik lower mineral depth was slower than in Healy soils and distributed across multiple carbon classes rather than targeted at aliphatics. The aliphatic components from Toolik samples showing increased NOSC traits may be intermediate metabolites, not completely oxidized to CO_2. The divergent responses to freeze-thaw by aliphatic and aromatic/condensed aromatic molecules in the Toolik soils could indicate targeted oxidation of both compound groups (compared to selective decomposition of aliphatics only). We posit that, in both sites, microbes consuming the most oxidized aromatic and condensed aromatic molecules may leave behind the less thermodynamically favorable molecules, thus lowering the overall NOSC of aromatic and condensed aromatic pools but still indicating mineralization processes. Meanwhile, microbial oxidation of the aliphatic pool would increase its thermodynamic favorability for future microbial use as we observed in Toolik soils.

The changes in NOSC at both sites following experimental freeze-thaw indicate that the potential for carbon decomposition in mineral depths increased following repeated freeze-thaw. The results of the supplementary respiration experiment included in our study align with the expected increase in carbon decomposition following freeze-thaw in Healy's lower mineral soils, with freeze-thaw samples from that depth showing the highest production of CO_2 compared with Healy's upper mineral and organic depths. Interestingly, the largest losses of carbon as CO_2 from Toolik soils occurred in the control samples from the lower mineral depths (Figure S8), with comparable but smaller CO_2 concentrations in the freeze-thaw samples from Toolik. The greater response by Toolik in the supplemental respiration experiment coincides with the slower response of aliphatics to experimental freeze-thaw in Toolik's lower mineral samples (increased NOSC but no difference in relative abundance). Notably, Healy aliphatics decreased in NOSC following experimental freeze-thaw. Similar to aromatic and condensed aromatic molecules from the Toolik soil samples, the decrease in NOSC at Healy may be due to the overall loss of higher NOSC aliphatics following microbial use and respiration at Healy. The loss of aliphatics from Healy serves as a potential explanation for the lesser CO_2 production from Healy's lower mineral samples (compared with Toolik samples) during the supplemental respiration experiment (Figure S8).

The variable responses of aliphatic compounds in the lower mineral horizons from Healy and Toolik following freeze-thaw illuminate differences in soil response to experimental freeze-thaw cycles. Variation in the short-term response of SOM could be introduced by freeze-thaw processes that promote microbial lysis and substrate input as well as disruption to soil aggregation (Freppaz et al., 2007; Oztas & Fayetorbay, 2003). Differences may also be attributed to contrasting site latitudes. Selective utilization of aliphatic compounds (56 % loss of aliphatic molecules) for dissolved organic carbon in the active layer from Alaskan soils in discontinuous permafrost was observed during a 28-day bioincubation at 20˚C by Textor et al. (2019). The selective utilization of aliphatic compounds observed in a discontinuous permafrost soil may not be occurring in permafrost soil which has undergone little prior freeze-thaw and is located in higher latitudes with continuous permafrost, such as Toolik. A Siberian permafrost study presenting detailed molecular composition of SOM identified increased bioavailability following thaw of *both* complex and simple carbon compounds in permafrost soils from continuous permafrost zones (Dao et al., 2022). Diverging soil responses under warming compared with freeze-thaw conditions requires further investigation.

4.3 The role of mineralogy and moisture conditions in freeze-thaw response of SOM in lower mineral soils

Additional factors could be responsible for contrasts in microbial oxidation of carbon and the relative abundance of lignin-like compounds including the higher water content present in the Healy samples as well as differences in iron crystallinity between both sites. In the relatively high-moisture lower mineral soils from Healy, O_2 availability may have been limiting for lignin depolymerization, aligning well with the increased relative abundance of lignin under experimental freeze-thaw. Anaerobic decomposition pathways are often guided by the availability of reactive iron species, allowing for microbial oxidation of carbon in saturated conditions and potentially leading to the diverging FT-ICR-MS profiles in subsoils from both sites with similar freeze-thaw histories but differences in moisture, iron reactivity, and mineralogical composition (Lentini et al., 2012).

The differences in clay content and mineralogy—specifically crystalline vs poorly crystalline iron and aluminum—between sites may have influenced the biogeochemical response to freeze-thaw through contrasting mineral-organic matter interactions. A study by Gentsch et al. (2015) reported slow microbial transformation of organic molecules in permafrost on the scale of millennia. The study attributed the accumulation of SOM in permafrost soils to a combination of microbial transformation and mineral-associations, with reactive iron and aluminum as well as clay minerals adsorbing organic molecules and decreasing availability even under warming conditions (Gentsch et al., 2015). We infer a higher sorption potential in Healy soils based on higher clay content, larger concentrations of poorly crystalline iron and aluminum, and greater concentrations of feldspars such as microcline and albite, as well as mica. Interestingly, the greater loss of aliphatics and overall loss of peaks from lower mineral depths at Healy suggest that some (but not all, i.e., Healy upper mineral and organic) soils containing minerals with more sorption potential showed greater loss of FT-ICR-MS resolved peaks during the experimental freeze-thaw incubation compared to soils containing silicate minerals with lower charge density (quartz) and lower clay contents. These results contrast previous literature which found greater SOM protection through organo-mineral interactions in soils with similar mineralogy and texture as in the Healy soils (Baldock & Skjemstad, 2000; Kögel-Knabner et al., 2008; Sollins et al., 1996), allowing for the possibility that freeze-thaw may be responsible for changing carbon dynamics in newly thawed permafrost with less prior freeze-thaw history. Notably, the Healy soil's upper mineral and organic horizons, which had more prior freeze-thaw than in the lower mineral horizon, did not undergo the same loss of peaks and decrease in aliphatics observed in Healy's lower mineral horizon. The only horizon from the Healy soils to display carbon loss, oxidation, and a decrease in aliphatics following freeze-thaw was the lower mineral horizon which had the least prior freeze-thaw.

The interaction of organic carbon and reactive iron is especially relevant in current permafrost research, with a recent study finding that iron-associated organic carbon was ~ 7 % higher in cryoturbated soils compared with non-cryoturbated organic and mineral soils (Joss et al., 2022). While both Healy and Toolik presented evidence for cryoturbation (i.e., Table 4.1), Healy soils—with a higher proportion of poorly crystalline iron and aluminum—underwent greater loss of FT-ICR-MS resolved carbon peaks compared with Toolik soils. The loss of peaks observed in Healy soils contrasts the expected stabilization of carbon in soils containing both cryoturbation and oxidized poorly crystalline iron species, suggesting that iron-mediated anaerobic decomposition pathways may be a more important control on organic matter stabilization in this system.

However, the direct role of mineral-associated SOM transformation in mediating loss of carbon and decrease in aliphatics from Healy may not be captured by the FT-ICR-MS approach. With 10 % SOC in Healy soils, we do not expect the full SOM pool to be extracted and identifiable via FT-ICR-MS (Kim et al., 2022). Our analyses using water-extractable organic matter are likely targeting readily available SOM, which is more vulnerable to microbial action and not as protected by mineral stabilization (Gentsch et al., 2015). While FT-ICR-MS is a powerful technique that offers a glimpse into SOM composition, additional techniques (i.e., density separations, radiocarbon dating) are needed to provide further insight into the role and mechanisms of mineral-associated SOM in freeze-thaw response.

There is potential for impacts to sorption capacity in soil following freeze-thaw. A previous study using geosynthetic clay liners identified mineral dissolution during freeze-thaw as a driver of displacement on cation exchange sites, although these impacts were only seen after 15 to 20 freeze-thaw cycles (Makusa et al., 2014). The study investigated freeze-thaw as a wetting-drying process with the ability to drive changes in hydraulic conductivity and dissolution. Dissolution and ion displacement triggered by freeze-thaw may have altered mineral-organic matter interactions in Healy soils by increasing competition for sorption sites on clay minerals and poorly crystalline iron oxides. Increased dissolution following freeze-thaw and subsequent competition for mineral sorption could partially explain the increasing the vulnerability of carbon compounds in Healy samples to microbial mineralization despite previous studies that have found an increase in carbon sorption on clay and mica minerals following freeze-thaw (G.-P. Wang et al., 2007; Yu et al., 2010).

The greater loss of carbon compounds from Healy also aligns with findings from a recent experiment investigating iron mineral and organic carbon interactions during permafrost thaw in Sweden (Patzner et al., 2020). Saturated conditions during permafrost thaw resulted in mobilization of iron and carbon as a result of iron reduction during anaerobic metabolism. In our experiment, the higher ice content (higher water content during the thaw; Table 4.2) at Healy may have driven waterlogging and anaerobic conditions during experimental freeze-thaw or during prior *in situ* freeze-thaw resulting in reactive iron mineral dissolution and subsequent carbon release, consistent with Patzner et al. (2020). It is also possible that the higher proportion of poorly crystalline iron in Healy soils was more readily reduced in saturated conditions compared with the higher proportion of crystalline iron at Toolik, resulting in microbial oxidation of carbon compounds using poorly crystalline iron as a terminal electron acceptor (Lentini et al., 2012; Lovley & Phillips, 1988). Previous studies using laboratory incubations of non-permafrost soil from the Northeastern United States (Lovley & Phillips, 1988) have identified the association of poorly crystalline iron (ferrihydrite) with increased rates of Fe (III) reduction compared with highly crystalline iron (goethite). These potential explanations for the rapid loss of the aliphatic pool following experimental freeze-thaw highlight the importance of reactive iron oxide minerals in carbon destabilization following permafrost thaw.

Permafrost formation mechanisms also likely contributed to the higher thermodynamic favorability of the lower mineral horizons at Healy in addition to the influence of differences in mineralogical abundance between sites. Older permafrost is reported to be more decomposable than younger permafrost on the basis of ammonium concentration, microbial scavenging, as well as fermentation genes and bioproducts increasing with permafrost age (Leewis et al., 2020). However, we posit that permafrost with freeze-thaw history in the form of quasi-syngenetic permafrost; i.e., the upward growth of permafrost into already accumulated peats and sediment (Kanevskiy, 2003; Manies et al., 2021), may result in highly oxygenated carbon compounds primed for rapid decomposition and loss once thaw occurs as seen in the lower mineral depths from Healy. Our interpretation corresponds to prior work conducted in the discontinuous permafrost zone in Fairbanks, Alaska that compared carbon losses from two sites with contrasting permafrost formation (syngenetic vs. quasi-syngenetic) (Manies et al., 2021). The degree of peat decomposition prior to permafrost formation heavily influenced the biolability of organic compounds following permafrost thaw (Manies et al., 2021). Specifically, the manner of permafrost formation (if permafrost formed with or following peat deposition), influenced C:N ratio, with soils that underwent peat formation and microbial decomposition prior to permafrost formation (epigenetic and quasi-syngenetic permafrost) having lower C:N ratios compared with soil that underwent peat and permafrost formation simultaneously (syngenetic permafrost) (Manies et al., 2021). Since the soil morphology at both Toolik and Healy indicates cryoturbation in the lower mineral permafrost horizons, it is possible that both sites underwent either quasi-syngenetic or epigenetic permafrost formation. However, the SOC composition of the control soils indicates higher thermodynamic favorability in Healy, suggesting that processes preceding permafrost formation at the Healy site resulted in higher NOSC values and more vulnerable aliphatics compared to Toolik. These processes could reflect timing (how long peat decomposed prior to permafrost aggradation) or the contrasting soil characteristics including mineralogy and iron and aluminum crystallinity.

5. Conclusions

Our findings indicate that a combination of freeze-thaw history and soil properties may dictate soil response to future freeze-thaw cycles. Lower mineral soils from Healy and Toolik with the least prior freeze-thaw history had diverging FT-ICR-MS resolved soil chemistry responses to future freeze-thaw cycles, likely as a function of differences in soil moisture and mineralogy. Specifically, lower mineral soils from Healy (a lower latitude permafrost soil with higher freeze-thaw cycle frequency at upper depths) appeared to have more short-term carbon metabolism within the aliphatic pool compared to soils from Toolik (a higher latitude permafrost soil with lower freeze-thaw cycle frequency at upper depths) following experimental freeze-thaw, resulting in a net loss of carbon compounds in Healy soils. Based on these findings, we posit that future increases in freeze-thaw in both the active layer and thawing permafrost may result in contrasting carbon response depending on site-specific characteristics, such as oxygen-availability following thaw, concentrations of reactive iron and aluminum, and prior permafrost formation processes. Interactions among texture, mineralogy, saturation, Fe and Al reactivity, and nutrient regimes likely vary based on freeze-thaw history as demonstrated by the contrasting SOM response between the upper and lower mineral horizons of Healy soils. Understanding freeze-thaw in warming Arctic landscapes is central to predicting how thawing permafrost will behave in the coming decades, with implications for carbon respiration and greenhouse gas release. The variation in freeze-thaw response across the Arctic has the potential to further complicate our predictive abilities, necessitating further study of how previous site-specific freeze-thaw may alter biogeochemical processes during thaw.

Acknowledgments

We would like to thank David Myrold, Jeff Hatten, Jennifer Fedenko, Ruben Aleman, Holly Golightly, Mark Bowden, Tom Wietsma, Rosalie K. Chu, Jason Toyoda, and Ashley Waggoner for their expertise and assistance with this experiment. We would like to thank Adam Fund, Kristin McAdow, and the Soil Health Laboratory at Oregon State University for their help with soil characterization analyses. This research was supported by the U.S. Department of Energy, Office of Science, Biological and Environmental Research as part of the Environmental System Science Program. The Pacific Northwest National Laboratory is operated for DOE by Battelle Memorial Institute under contract DE-AC05-76RL01830. A portion of this research was performed using EMSL (grid.436923.9), a DOE Office of Science user facility sponsored by the Department of Energy's Office of Biological and Environmental Research and located at Pacific Northwest National Laboratory. This material is based in part upon work supported by NSF through the NEON program. NEON is sponsored by the National Science Foundation (NSF) and operated under cooperative agreement by Battelle.

Data Availability

All data and scripts are available at https://github.com/Erin-Rooney/FTC-FTICR and are archived and searchable at https://search.emsl.pnnl.gov.

References Cited

Antony, R., Willoughby, A. S., Grannas, A. M., Catanzano, V., Sleighter, R. L., Thamban, M., et al. (2017). Molecular Insights on Dissolved Organic Matter Transformation by Supraglacial Microbial Communities. *Environmental Science & Technology*, *51*(8), 4328–4337. https://doi.org/10.1021/acs.est.6b05780

Arndt, K. A., Lipson, D. A., Hashemi, J., Oechel, W. C., & Zona, D. (2020). Snow melt stimulates ecosystem respiration in Arctic ecosystems. *Global Change Biology*, *26*(9). https://doi.org/10.1111/gcb.15193

Bailey, V. L., Pries, C. H., & Lajtha, K. (2019). What do we know about soil carbon destabilization? *Environmental Research Letters*, *14*(8), 083004. https://doi.org/10.1088/1748-9326/ab2c11

Baldock, J. A., & Skjemstad, J. O. (2000). Role of the soil matrix and minerals in protecting natural organic materials against biological attack. *Organic Geochemistry*, 697–710.

Bing, H., He, P., & Zhang, Y. (2015). Cyclic freeze–thaw as a mechanism for water and salt migration in soil. *Environmental Earth Sciences*, *74*(1), 675–681. https://doi.org/10.1007/s12665-015-4072-9

Blackwell, M. S. A., Brookes, P. C., de la Fuente-Martinez, N., Gordon, H., Murray, P. J., Snars, K. E., et al. (2010). Phosphorus Solubilization and Potential Transfer to Surface Waters from the Soil Microbial Biomass Following Drying–Rewetting and Freezing–Thawing. In *Advances in Agronomy* (Vol. 106, pp. 1–35). Academic Press Inc. https://doi.org/10.1016/S0065-2113(10)06001-3

Boswell, E. P., Thompson, A. M., Balster, N. J., & Bajcz, A. W. (2020). Novel determination of effective freeze–thaw cycles as drivers of ecosystem change. *Journal of Environmental Quality*, *49*(2), 314–323. https://doi.org/10.1002/jeq2.20053

Boswell, E. P., Balster, N. J., Bajcz, A. W., & Thompson, A. M. (2020). Soil aggregation returns to a set point despite seasonal response to snow manipulation. *Geoderma*, *357*. https://doi.org/10.1016/j.geoderma.2019.113954

Brosgé, W. P., Reiser, H. N., Dutro, J. T. , Jr., Detterman, R. L., & Tailleur, I. L. (2001). *Geologic map of the Arctic Quadrangle, Alaska: U.S. Geological Survey Geologic Investigations Series Map 2673, 38 p., 1 sheet. U.S. Geological Survey* .

Butler, B., Hillier, S., Beaudette, D., & Eberl, D. (2021). Full Pattern Summation of X-Ray Powder Diffraction Data. *PowdR*. CRAN Repository.

Chou, Y., & Wang, L. (2021). Seasonal freezing-thawing process and hydrothermal characteristics of soil on the Loess Plateau, China. *Journal of Mountain Science*, *18*(11), 3082–3098. https://doi.org/10.1007/s11629-020-6599-9

Csejtey, B. Jr., Mullen, M. W., Cox, D. P., & Stricker, G. D. (1992). *Geology and geochronology of the Healy Quadrangle, south-central Alaska*. https://doi.org/10.3133/i1961

Dao, T. T., Mikutta, R., Sauheitl, L., Gentsch, N., Shibistova, O., Wild, B., et al. (2022). Lignin Preservation and Microbial Carbohydrate Metabolism in Permafrost Soils. *Journal of Geophysical Research: Biogeosciences*, *127*(1). https://doi.org/10.1029/2020JG006181

Dittmar, T., Koch, B., Hertkorn, N., & Kattner, G. (2008). A simple and efficient method for the solid-phase extraction of dissolved organic matter (SPE-DOM) from seawater. *Limnology and Oceanography: Methods*, *6*(6), 230–235. https://doi.org/10.4319/lom.2008.6.230

Edwards, L. M. (2013). The effects of soil freeze–thaw on soil aggregate breakdown and concomitant sediment flow in Prince Edward Island: A review. *Canadian Journal of Soil Science*, *93*(4), 459–472. https://doi.org/10.4141/cjss2012-059

Elliott, A. C., & Henry, H. A. L. (2009). Freeze-thaw cycle amplitude and freezing rate effects on extractable nitrogen in a temperate old field soil. *Biology and Fertility of Soils*, *45*(5), 469–476. https://doi.org/10.1007/s00374-009-0356-0

Freppaz, M., Williams, B. L., Edwards, A. C., Scalenghe, R., & Zanini, E. (2007). Simulating soil freeze/thaw cycles typical of winter alpine conditions: Implications for N and P availability. *Applied Soil Ecology*, *35*(1), 247–255. https://doi.org/10.1016/j.apsoil.2006.03.012

Gao, Z., Hu, X., Li, X.-Y., & Li, Z.-C. (2021). Effects of freeze-thaw cycles on soil macropores and its implications on formation of hummocks in alpine meadows in the Qinghai Lake watershed, northeastern Qinghai-Tibet Plateau. *Journal of Soils and Sediments*, *21*(1). https://doi.org/10.1007/s11368-020-02765-2

Gee, G. W., & Bauder, J. W. (1986). Particle-size analysis. In A. Klute (Ed.), *Methods of soil analysis. Part 1.* (2nd ed., pp. 383–411). Madison, WI.: Agron. Monogr. 9. ASA and SSSA.

Gentsch, N., Mikutta, R., Shibistova, O., Wild, B., Schnecker, J., Richter, A., et al. (2015). Properties and bioavailability of particulate and mineral-associated organic matter in Arctic permafrost soils, Lower Kolyma Region, Russia. *European Journal of Soil Science*, *66*(4), 722–734. https://doi.org/10.1111/ejss.12269

Graham, E. B., Tfaily, M. M., Crump, A. R., Goldman, A. E., Bramer, L. M., Arntzen, E., et al. (2017). Carbon Inputs From Riparian Vegetation Limit Oxidation of Physically Bound Organic Carbon Via Biochemical and Thermodynamic Processes. *Journal of Geophysical Research: Biogeosciences*, *122*(12), 3188–3205. https://doi.org/10.1002/2017JG003967

Guo, D., & Wang, H. (2013). Simulation of permafrost and seasonally frozen ground conditions on the Tibetan Plateau, 1981-2010. *Journal of Geophysical Research: Atmospheres*, *118*(11), 5216–5230. https://doi.org/10.1002/jgrd.50457

Henry, H. A. L. (2007, May). Soil freeze-thaw cycle experiments: Trends, methodological weaknesses and suggested improvements. *Soil Biology and Biochemistry*. https://doi.org/10.1016/j.soilbio.2006.11.017

Henry, H. A. L. (2008). Climate change and soil freezing dynamics: Historical trends and projected changes. *Climatic Change*, *87*(3–4), 421–434. https://doi.org/10.1007/s10584-007-9322-8

Joss, H., Patzner, M. S., Maisch, M., Mueller, C. W., Kappler, A., & Bryce, C. (2022). Cryoturbation impacts iron-organic carbon associations along a permafrost soil chronosequence in northern Alaska. *Geoderma*, *413*, 115738. https://doi.org/10.1016/j.geoderma.2022.115738

Kanevskiy, M. (2003). Cryogenic structure of mountain slope deposits, northeast Russia. *Paper Presented at the 8th International Conference on Permafrost.*

Keiluweit, M., Wanzek, T., Kleber, M., Nico, P., & Fendorf, S. (2017). Anaerobic microsites have an unaccounted role in soil carbon stabilization. *Nature Communications*, *8*(1), 1771. https://doi.org/10.1038/s41467-017-01406-6

Kim, S., Kim, D., Jung, M., & Kim, S. (2022). Analysis of environmental organic matters by Ultrahigh-Resolution mass spectrometry—A review on the development of analytical methods. *Mass Spectrometry Reviews*, *41*(2), 352–369. https://doi.org/10.1002/mas.21684

Koch, B. P., & Dittmar, T. (2006). From mass to structure: an aromaticity index for high-resolution mass data of natural organic matter. *Rapid Communications in Mass Spectrometry*, *20*(5), 926–932. https://doi.org/10.1002/rcm.2386

Kögel-Knabner, I., Guggenberger, G., Kleber, M., Kandeler, E., Kalbitz, K., Scheu, S., et al. (2008). Organo-mineral associations in temperate soils: Integrating biology, mineralogy, and organic matter chemistry. *Journal of Plant Nutrition and Soil Science*, *171*(1), 61–82. https://doi.org/10.1002/jpln.200700048

Köhn, M. (1928). Bemerkungen zur mechanischen Bodenanalyse. III. Ein neuer Pipettapparat. *Zeitschrift Für Pflanzenernährung, Düngung, Bodenkunde, A, Wissenschaftlicher Teil*, *11*(1), 50–54. https://doi.org/10.1002/jpln.19280110104

Konrad, J.-M., & McCammon, A. W. (1990). Solute partitioning in freezing soils. *Canadian Geotechnical Journal*, *27*(6), 726–736. https://doi.org/10.1139/t90-086

Kujawinski, E. B., & Behn, M. D. (2006). Automated Analysis of Electrospray Ionization Fourier Transform Ion Cyclotron Resonance Mass Spectra of Natural Organic Matter. *Analytical Chemistry*, *78*(13), 4363–4373. https://doi.org/10.1021/ac0600306

Kujawinski, E. B., Hatcher, P. G., & Freitas, M. A. (2002). High-Resolution Fourier Transform Ion Cyclotron Resonance Mass Spectrometry of Humic and Fulvic Acids: Improvements and Comparisons. *Analytical Chemistry*, *74*(2), 413–419. https://doi.org/10.1021/ac0108313

LaRowe, D. E., & van Cappellen, P. (2011). Degradation of natural organic matter: A thermodynamic analysis. *Geochimica et Cosmochimica Acta*, *75*(8), 2030–2042. https://doi.org/10.1016/j.gca.2011.01.020

Larsen, K. S., Jonasson, S., & Michelsen, A. (2002). *Repeated freeze-thaw cycles and their effects on biological processes in two arctic ecosystem types*. *Applied Soil Ecology* (Vol. 21).

Lawlor, J. (2020). PNWColors: Color Palettes Inspired by Nature in the US Pacific Northwest. *Zenodo.*

Leewis, M.-C., Berlemont, R., Podgorski, D. C., Srinivas, A., Zito, P., Spencer, R. G. M., et al. (2020). Life at the Frozen Limit: Microbial Carbon Metabolism Across a Late Pleistocene Permafrost Chronosequence. *Frontiers in Microbiology*, *11*. https://doi.org/10.3389/fmicb.2020.01753

Lentini, C. J., Wankel, S. D., & Hansel, C. M. (2012). Enriched Iron(III)-Reducing Bacterial Communities are Shaped by Carbon Substrate and Iron Oxide Mineralogy. *Frontiers in Microbiology*, *3*. https://doi.org/10.3389/fmicb.2012.00404

Liu, B., Ma, R., & Fan, H. (2021). Evaluation of the impact of freeze-thaw cycles on pore structure characteristics of black soil using X-ray computed tomography. *Soil and Tillage Research*, *206*. https://doi.org/10.1016/j.still.2020.104810

Lovley, D. R., & Phillips, E. J. P. (1988). Novel Mode of Microbial Energy Metabolism: Organic Carbon Oxidation Coupled to Dissimilatory Reduction of Iron or Manganese. *Applied and Environmental Microbiology*, *54*(6), 1472–1480. https://doi.org/10.1128/aem.54.6.1472-1480.1988

von Lützow, M., Kögel-Knabner, I., Ekschmitt, K., Flessa, H., Guggenberger, G., Matzner, E., & Marschner, B. (2007). SOM fractionation methods: Relevance to functional pools and to stabilization mechanisms. *Soil Biology and Biochemistry*, *39*(9), 2183–2207. https://doi.org/10.1016/j.soilbio.2007.03.007

Ma, R., Jiang, Y., Liu, B., & Fan, H. (2021). Effects of pore structure characterized by synchrotron-based micro-computed tomography on aggregate stability of black soil under freeze-thaw cycles. *Soil and Tillage Research*, *207*. https://doi.org/10.1016/j.still.2020.104855

MacDonald, E. N., Tank, S. E., Kokelj, S. v., Froese, D. G., & Hutchins, R. H. S. (2021). Permafrost-derived dissolved organic matter composition varies across permafrost end-members in the western Canadian Arctic. *Environmental Research Letters*, *16*(2). https://doi.org/10.1088/1748-9326/abd971

Makusa, G. P., Bradshaw, S. L., Berns, E., Benson, C. H., & Knutsson, S. (2014). Freeze–thaw cycling concurrent with cation exchange and the hydraulic conductivity of geosynthetic clay liners. *Canadian Geotechnical Journal*, *51*(6), 591–598. https://doi.org/10.1139/cgj-2013-0127

Manies, K. L., Jones, M. C., Waldrop, M. P., Leewis, M., Fuller, C., Cornman, R. S., & Hoefke, K. (2021). Influence of Permafrost Type and Site History on Losses of Permafrost Carbon After Thaw. *Journal of Geophysical Research: Biogeosciences*, *126*(11). https://doi.org/10.1029/2021JG006396

Miller, R. O., Gavlak, R., & Horneck, D. (2013). *Soil, Plant, and Water Reference Methods for the Western Region*. (4th ed.).

National Ecological Observatory Network. (2019). Terrestrial Observation System (TOS) Site Characterization Report: Domain 18. Retrieved from 13/07/2021https://data.neonscience.org/documents/10179/2263491/NEON.DOC.003901vB/f03fb22d-2fcd-10f7-b562-b80bfeca07da

National Ecological Observatory Network. (2021a). Soil physical and chemical properties, distributed initial characterization, RELEASE-2021 (DP1.10047.001). *Https://Doi.Org/10.48443/Tjgd-6m89. Dataset Accessed from Https://Data.Neonscience.Org on June 29, 2021*.

National Ecological Observatory Network. (2021b). Soil temperature, RELEASE-2021 (DP1.00041.001). *Https://Doi.Org/10.48443/9e56-Pj39. Dataset Accessed from Https://Data.Neonscience.Org*.

Oksanen, J., Blanchet, F. G., Friendly, M., Kindt, R., Legendre, P., McGlinn, D., et al. (2019). Vegan: Community Ecology Package. R Package.

Oztas, T., & Fayetorbay, F. (2003). Effect of freezing and thawing processes on soil aggregate stability. *CATENA*, *52*(1), 1–8. https://doi.org/10.1016/S0341-8162(02)00177-7

Park, H., Fedorov, A. N., Zheleznyak, M. N., Konstantinov, P. Y., & Walsh, J. E. (2015). Effect of snow cover on pan-Arctic permafrost thermal regimes. *Climate Dynamics*, *44*(9–10), 2873–2895. https://doi.org/10.1007/s00382-014-2356-5

Patel, K. F., Tatariw, C., MacRae, J. D., Ohno, T., Nelson, S. J., & Fernandez, I. J. (2018). Soil carbon and nitrogen responses to snow removal and concrete frost in a northern coniferous forest. *Canadian Journal of Soil Science*, *98*(3), 436–447. https://doi.org/10.1139/cjss-2017-0132

Patel, K. F., Tatariw, C., MacRae, J. D., Ohno, T., Nelson, S. J., & Fernandez, I. J. (2021). Repeated freeze–thaw cycles increase extractable, but not total, carbon and nitrogen in a Maine coniferous soil. *Geoderma*, *402*. https://doi.org/10.1016/j.geoderma.2021.115353

Patzner, M. S., Mueller, C. W., Malusova, M., Baur, M., Nikeleit, V., Scholten, T., et al. (2020). Iron mineral dissolution releases iron and associated organic carbon during permafrost thaw. *Nature Communications*, *11*(1), 6329. https://doi.org/10.1038/s41467-020-20102-6

Ping, C. L., Jastrow, J. D., Jorgenson, M. T., Michaelson, G. J., & Shur, Y. L. (2015). Permafrost soils and carbon cycling. *SOIL*, *1*(1), 147–171. https://doi.org/10.5194/soil-1-147-2015

R Core Team. (2020). R: A language and environment for statistical computing.

Rooney, E. C., Bailey, V. L., Patel, K. F., Dragila, M., Battu, A. K., Buchko, A. C., et al. (2022). Soil pore network response to freeze-thaw cycles in permafrost aggregates. *Geoderma*, *411*, 115674. https://doi.org/10.1016/j.geoderma.2021.115674

RStudio Team. (2019). RStudio: Integrated Development for R. RStudio, Inc. *Boston, MA, Http://Www.Rstudio.Com/*.

Schimel, J. P., & Clein, J. S. (1996). *MICROBIAL RESPONSE TO FREEZE-THAW CYCLES IN TUNDRA AND TAIGA SOILS*. *Soil Eiot. Biorhem* (Vol. 28).

Schimel, J. P., & Mikan, C. (2005). Changing microbial substrate use in Arctic tundra soils through a freeze-thaw cycle. *Soil Biology and Biochemistry*, *37*(8), 1411–1418. https://doi.org/10.1016/j.soilbio.2004.12.011

Seidel, M., Beck, M., Riedel, T., Waska, H., Suryaputra, I. G. N. A., Schnetger, B., et al. (2014). Biogeochemistry of dissolved organic matter in an anoxic intertidal creek bank. *Geochimica et Cosmochimica Acta*, *140*, 418–434. https://doi.org/10.1016/j.gca.2014.05.038

Shang, C., & Zelazny, L. W. (2015). Selective Dissolution Techniques for Mineral Analysis of Soils and Sediments (pp. 33–80). https://doi.org/10.2136/sssabookser5.5.c3

Sharratt, B. S., Baker, D. G., Wall, D. B., Skaggs, R. H., & Ruschy, D. L. (1992). Snow depth required for near steady-state soil temperatures. *Agricultural and Forest Meteorology*, *57*(4), 243–251. https://doi.org/10.1016/0168-1923(92)90121-J

Sheldrick, B. H., & Wang, C. (1993). Particle Size Analysis. In M. R. Carter (Ed.), *Soil Sampling and Methods of Analysis* (pp. 499–517). Boca Raton: Lewis Publishers.

Sollins, P., Homann, P., & Caldwell, B. A. (1996). Stabilization and destabilization of soil organic matter: mechanisms and controls. *Geoderma*, (74), 65–105.

Song, Y., Zou, Y., Wang, G., & Yu, X. (2017). Altered soil carbon and nitrogen cycles due to the freeze-thaw effect: A meta-analysis. *Soil Biology and Biochemistry*, *109*, 35–49. https://doi.org/10.1016/j.soilbio.2017.01.020

Textor, S. R., Wickland, K. P., Podgorski, D. C., Johnston, S. E., & Spencer, R. G. M. (2019). Dissolved Organic Carbon Turnover in Permafrost-Influenced Watersheds of Interior Alaska: Molecular Insights and the Priming Effect. *Frontiers in Earth Science*, *7*. https://doi.org/10.3389/feart.2019.00275

Thomas, G. W. (2018). Soil pH and Soil Acidity (pp. 475–490). https://doi.org/10.2136/sssabookser5.3.c16

Tolić, N., Liu, Y., Liyu, A., Shen, Y., Tfaily, M. M., Kujawinski, E. B., et al. (2017). Formularity: Software for Automated Formula Assignment of Natural and Other Organic Matter from Ultrahigh-Resolution Mass Spectra. *Analytical Chemistry*, *89*(23), 12659–12665. https://doi.org/10.1021/acs.analchem.7b03318

Wang, G.-P., Liu, J.-S., Zhao, H.-Y., Wang, J.-D., & Yu, J.-B. (2007). Phosphorus sorption by freeze–thaw treated wetland soils derived from a winter-cold zone (Sanjiang Plain, Northeast China). *Geoderma*, *138*(1–2), 153–161. https://doi.org/10.1016/j.geoderma.2006.11.006

Wang, Jiaoyue, Song, C., Hou, A., & Wang, L. (2014). CO2 emissions from soils of different depths of a permafrost peatland, Northeast China: response to simulated freezing–thawing cycles. *Journal of Plant Nutrition and Soil Science*, *177*(4), 524–531. https://doi.org/10.1002/jpln.201300309

Wang, Jingyuan, Luo, S., Li, Z., Wang, S., & Li, Z. (2019). The freeze/thaw process and the surface energy budget of the seasonally frozen ground in the source region of the Yellow River. *Theoretical and Applied Climatology*, *138*(3–4), 1631–1646. https://doi.org/10.1007/s00704-019-02917-6

Wickham, H. (2016). ggplot2: Elegant Graphics for Data Analysis. *Springer*.

Wickham, H., François, R., & Henry, L. (2020). dplyr: A grammar of Data Manipulation.

Wilson, F. H., Hults, C. P., Mull, C. G., & Karl, S. M. (2015). *Geologic map of Alaska: U.S. Geological Survey Scientific Investigations Map 3340, pamphlet 196 p., 2 sheets, scale 1:1,584,000*. *USGS*.

Yi, Y., Kimball, J. S., Rawlins, M. A., Moghaddam, M., & Euskirchen, E. S. (2015). The role of snow cover affecting boreal-arctic soil freeze-thaw and carbon dynamics. *Biogeosciences*, *12*(19), 5811–5829. https://doi.org/10.5194/bg-12-5811-2015

Yu, X., Zhang, Y., Zhao, H., Lu, X., & Wang, G. (2010). Freeze-thaw effects on sorption/desorption of dissolved organic carbon in wetland soils. *Chinese Geographical Science*, *20*(3), 209–217. https://doi.org/10.1007/s11769-010-0209-7

Chapter 5 Conclusion

Soil transformation during permafrost thaw is facilitated by cross-scale physical and biogeochemical responses to freeze-thaw cycles and warming. The experiments in this dissertation target micron to site-level scales at which freeze-thaw dynamics govern soil carbon chemistry and soil structure by examining deformation of the soil pore network at the aggregate scale and SOM composition and oxidation at the canopy, hillslope, and site level. The findings reported herein indicate that the role of freeze-thaw may vary in importance depending on site, plot, and aggregate characteristics. The role of soil and site properties in driving variability of response to freeze-thaw outlines an important challenge in predicting carbon emissions and permafrost thaw in warming Arctic landscapes.

Permafrost thaw is inherently complex, with types of thaw (such as gradual or rapid) reportedly leading to differences in SOM response and carbon release (Turetsky et al., 2020). Similarly, drying or flooding during thaw can increase heterogeneity of thawing permafrost soils by driving microbial metabolism and redox pathways (Johnson et al., 2013). As shown in Chapter 3, temperature differences (both warming and freeze-thaw) on a dry backslope soil may play a larger role in carbon chemistry than in a saturated footslope soil, introducing temperature-driven complexity depending on the interaction of hillslope position and cover type. Similarly, freeze-thaw may accelerate carbon loss from some soils but not others depending on soil characteristics and site properties, as shown in Chapter 4. Chapter 2 demonstrated that initial pore structure and morphology may influence responses to freeze-thaw at the microscale. This dissertation provides data that will assist in determining at what resolution predictions can be formed across sites, slope positions, and aggregates by demonstrating the variability in thawing permafrost response to freeze-thaw and warming at each of those scales.

At the pore scale, the changeability of microbial habitat architecture within just five freeze-thaw cycles demonstrates the potential for transformations of the microenvironment during permafrost thaw. Changes in the microenvironment have cross-scale impacts, with water holding capacity, carbon storage, and gas flow altered by pore connectivity and pore throat diameter distribution. Pore network response requires further investigation to predict aggregate behavior in multiple permafrost soils. Particle size class, lithology and mineralogy, organic matter content, and saturation level could all introduce additional variation in pore deformation during freeze-thaw. The impact of cumulative deformation as freeze-thaw cycles repeat also introduces the potential for more variation in pore response (Liu, Fan, et al., 2021; Liu, Ma, et al., 2021; Ma et al., 2021; Rooney et al., 2021; Starkloff et al., 2017).

At the hillslope scale, SOM composition varied with slope rather than canopy, with moisture conditions playing a larger role in FT-ICR-MS resolved carbon chemistry than cover-driven variations in *in situ* temperature and freeze-thaw. However, the backslope position showed greater carbon oxidation under open cover compared with closed cover, indicating that in soils with lower moisture content the effects of canopy and temperature can be seen across distances of 1 to 3 meters. The importance of canopy-driven differences in soil temperature and freeze-thaw versus the importance of moisture as a driver of SOM composition and decomposability requires further investigation. Soils with biotite mica and higher iron oxide content show changes sorption potential if freeze-thaw increases sorption sites on minerals (Yu et al., 2010), increasing the importance of soil temperature and providing redox pathways for carbon oxidation in saturated soils (Lentini et al., 2012). Similarly, dry conditions may increase the importance of canopy at the plot-scale in permafrost-affected soils.

At the site-scale, a combination of recent freeze-thaw history and soil properties dictated soil response to experimental freeze-thaw cycles. The two soils with the least prior freeze-thaw showed diverging responses to freeze-thaw, likely due to soil moisture and mineralogy. The soil with less historic exposure to freeze-thaw and greatest percentages of mica and feldspars, and higher clay content was more sensitive to carbon loss and presented greater losses of simple carbon molecules (i.e., aliphatic groups) following experimental freeze-thaw. The findings from Chapter 4 indicate that future increases in freeze-thaw in both the active layer and thawing permafrost may result in contrasting carbon responses across sites. The findings also demonstrate the need to understand how permafrost history, from formation (Manies et al., 2021) to recent freeze-thaw, determines carbon loss and decomposition following thaw and during initial freeze-thaw.

While the experiments included in this dissertation assess the aggregate, slope, and site scale in isolation, the responses to freeze-thaw and the processes driving them occur across multiple scales. We cannot understand the impacts of freeze-thaw at the hillslope or site level without acknowledging the variability in soil structure response at the pore scale. Nor can we fully understand how responses differ across sites without also acknowledging the variation that can occur at the hillslope and canopy scale. Two soils from contrasting sites may vary in freeze-thaw response as a result of differences in site-level characteristics (parent material, mineralogy, soil texture), but some of that variation in response may originate from deformation at the pore scale. A cross-scale approach to freeze-thaw in thawing permafrost also provides a more robust understanding of broader impacts. Chapter 4 demonstrates the potential for larger impacts in response variability to freeze-thaw as carbon compounds were preferentially lost from the Healy soil (lower latitude) compared with the Toolik soil (higher latitude) despite similarities in recent freeze-thaw history. The loss of carbon compounds, which were interpreted to be the result of microbial oxidation and respiration, indicate the potential for contrasting carbon emissions depending on freeze-thaw response at the site level. The pore-scale helps us understand the processes occurring at larger scales. But to contextualize impact, future investigations of the freeze-thaw response at the pore scale should also include larger scale impacts from freeze-thaw.

Arctic permafrost is in transition. Formed by cryogenic processes and able to preserve materials from past millennia, these inherently complex landscapes are morphologically and biogeochemically dissimilar to any others across the globe. Our findings indicate that soil transformation during permafrost thaw introduces cross-scale variability as a result of physical and biogeochemical responses to freeze-thaw and warming, which can vary by site, depth, and aggregate. The fate of organic carbon in thawing permafrost soils will impact the global climate, and may be determined in part by the importance of and response to freeze-thaw within a given permafrost soil. Predicting the impacts of permafrost thaw to the global atmosphere is vital to our ability to prepare for the future of global warming. The findings of this dissertation indicate that the accuracy of those predictions depend upon first understanding how previously frozen soils are transformed by exposure to freeze-thaw while accounting for the variability of response inherent in these dynamic and heterogenous permafrost soils currently undergoing thaw.

References

Ananyeva, K., Wang, W., Smucker, A. J. M., Rivers, M. L., & Kravchenko, A. N. (2013). Can intra-aggregate pore structures affect the aggregate's effectiveness in protecting carbon? *Soil Biology and Biochemistry*, *57*, 868–875. https://doi.org/10.1016/j.soilbio.2012.10.019

Andersland, O. B., & Ladanyi, B. (2004). *Frozen Ground Engineering*. (P. J. Williams, Ed.) (Second Edition). John Wiley & Sons.

Anthony, K. M. W., Zimov, S. A., Grosse, G., Jones, M. C., Anthony, P. M., III, F. S. C., et al. (2014). A shift of thermokarst lakes from carbon sources to sinks during the Holocene epoch. *Nature*, *511*(7510), 452–456. https://doi.org/10.1038/nature13560

Antony, R., Willoughby, A. S., Grannas, A. M., Catanzano, V., Sleighter, R. L., Thamban, M., et al. (2017). Molecular Insights on Dissolved Organic Matter Transformation by Supraglacial Microbial Communities. *Environmental Science & Technology*, *51*(8), 4328–4337. https://doi.org/10.1021/acs.est.6b05780

Arndt, K. A., Lipson, D. A., Hashemi, J., Oechel, W. C., & Zona, D. (2020). Snow melt stimulates ecosystem respiration in Arctic ecosystems. *Global Change Biology*, *26*(9). https://doi.org/10.1111/gcb.15193

Bailey, V. L., Smith, A. P., Tfaily, M., Fansler, S. J., & Bond-Lamberty, B. (2017). Differences in soluble organic carbon chemistry in pore waters sampled from different pore size domains. *Soil Biology and Biochemistry*, *107*, 133–143. https://doi.org/10.1016/j.soilbio.2016.11.025

Bailey, Vanessa L, Fansler, S. J., Stegen, J. C., & McCue, L. A. (2013). Linking microbial community structure to β-glucosidic function in soil aggregates. *The ISME Journal*, *7*(10). https://doi.org/10.1038/ismej.2013.87

Bailey, Vanessa L, Pries, C. H., & Lajtha, K. (2019). What do we know about soil carbon destabilization? *Environmental Research Letters*, *14*(8), 083004. https://doi.org/10.1088/1748-9326/ab2c11

Baldock, J. A., & Skjemstad, J. O. (2000). Role of the soil matrix and minerals in protecting natural organic materials against biological attack. *Organic Geochemistry*, 697–710.

Berhe, A. A., Harden, J. W., Torn, M. S., Kleber, M., Burton, S. D., & Harte, J. (2012). Persistence of soil organic matter in eroding versus depositional landform positions. *Journal of Geophysical Research: Biogeosciences*, *117*(G2), n/a-n/a. https://doi.org/10.1029/2011JG001790

Bing, H., He, P., & Zhang, Y. (2015). Cyclic freeze–thaw as a mechanism for water and salt migration in soil. *Environmental Earth Sciences*, *74*(1), 675–681. https://doi.org/10.1007/s12665-015-4072-9

Biskaborn, B. K., Smith, S. L., Noetzli, J., Matthes, H., Vieira, G., Streletskiy, D. A., et al. (2019). Permafrost is warming at a global scale. *Nature Communications*, *10*(1). https://doi.org/10.1038/s41467-018-08240-4

Blackwell, M. S. A., Brookes, P. C., de la Fuente-Martinez, N., Gordon, H., Murray, P. J., Snars, K. E., et al. (2010). Phosphorus Solubilization and Potential Transfer to Surface Waters from the Soil Microbial Biomass Following Drying–Rewetting and Freezing–Thawing. In *Advances in Agronomy* (Vol. 106, pp. 1–35). Academic Press Inc. https://doi.org/10.1016/S0065-2113(10)06001-3

Boswell, E. P., Thompson, A. M., Balster, N. J., & Bajcz, A. W. (2020). Novel determination of effective freeze–thaw cycles as drivers of ecosystem change. *Journal of Environmental Quality*, *49*(2), 314–323. https://doi.org/10.1002/jeq2.20053

Boswell, E. P., Balster, N. J., Bajcz, A. W., & Thompson, A. M. (2020). Soil aggregation returns to a set point despite seasonal response to snow manipulation. *Geoderma*, *357*. https://doi.org/10.1016/j.geoderma.2019.113954

Brooks, J. R., Flanagan, L. B., & Ehleringer, J. R. (1998). Responses of boreal conifers to climate fluctuations: indications from tree-ring widths and carbon isotope analyses. *Canadian Journal of Forest Research*, *28*(4), 524–533. https://doi.org/10.1139/cjfr-28-4-524

Brooks, P. D., Grogan, P., Templer, P. H., Groffman, P., Öquist, M. G., & Schimel, J. (2011). Carbon and Nitrogen Cycling in Snow-Covered Environments. *Geography Compass*, *5*(9), 682–699. https://doi.org/10.1111/j.1749-8198.2011.00420.x

Brosgé, W. P., Reiser, H. N., Dutro, J. T. , Jr., Detterman, R. L., & Tailleur, I. L. (2001). *Geologic map of the Arctic Quadrangle, Alaska: U.S. Geological Survey Geologic Investigations Series Map 2673, 38 p., 1 sheet. U.S. Geological Survey* .

Brown, J., & Romanovsky, V. E. (2008). Report from the International Permafrost Association: State of permafrost in the first decade of the 21st century. In *Permafrost and Periglacial Processes* (Vol. 19, pp. 255–260). https://doi.org/10.1002/ppp.618

Butler, B., Hillier, S., Beaudette, D., & Eberl, D. (2021). Full Pattern Summation of X-Ray Powder Diffraction Data. *PowdR*. CRAN Repository.

Cavicchioli, R., Ripple, W. J., Timmis, K. N., Azam, F., Bakken, L. R., Baylis, M., et al. (2019). Scientists' warning to humanity: microorganisms and climate change. *Nature Reviews Microbiology*, *17*(9). https://doi.org/10.1038/s41579-019-0222-5

Chadburn, S. E., Burke, E. J., Cox, P. M., Friedlingstein, P., Hugelius, G., & Westermann, S. (2017). An observation-based constraint on permafrost loss as a function of global warming. *Nature Climate Change*, *7*(5), 340–344. https://doi.org/10.1038/nclimate3262

Chamberlain, E. J., & Gow, A. J. (1979). Effect of freezing and thawing on the permeability and structure of soils. *Engineering Geology*, *13*, 73–92.

Chasmer, L., Quinton, W., Hopkinson, C., Petrone, R., & Whittington, P. (2011). Vegetation Canopy and Radiation Controls on Permafrost Plateau Evolution within the Discontinuous Permafrost Zone, Northwest Territories, Canada. *Permafrost and Periglacial Processes*, n/a-n/a. https://doi.org/10.1002/ppp.724

Chen, L., Chen, Z., Jia, G., Zhou, J., Zhao, J., & Zhang, Z. (2020). Influences of forest cover on soil freeze-thaw dynamics and greenhouse gas emissions through the regulation of snow regimes: A comparison study of the farmland and forest plantation. *Science of The Total Environment*, *726*, 138403. https://doi.org/10.1016/j.scitotenv.2020.138403

Chou, Y., & Wang, L. (2021). Seasonal freezing-thawing process and hydrothermal characteristics of soil on the Loess Plateau, China. *Journal of Mountain Science*, *18*(11), 3082–3098. https://doi.org/10.1007/s11629-020-6599-9

Csejtey, B. Jr., Mullen, M. W., Cox, D. P., & Stricker, G. D. (1992). *Geology and geochronology of the Healy Quadrangle, south-central Alaska*. https://doi.org/10.3133/i1961

Dao, T. T., Mikutta, R., Sauheitl, L., Gentsch, N., Shibistova, O., Wild, B., et al. (2022). Lignin Preservation and Microbial Carbohydrate Metabolism in Permafrost Soils. *Journal of Geophysical Research: Biogeosciences*, *127*(1). https://doi.org/10.1029/2020JG006181

Darrow, M. M., & Lieblappen, R. M. (2020). Visualizing cation treatment effects on frozen clay soils through µCT scanning. *Cold Regions Science and Technology*, *175*. https://doi.org/10.1016/j.coldregions.2020.103085

DeMarco, J., Mack, M. C., & Bret-Harte, M. S. (2011). The Effects of Snow, Soil Microenvironment, and Soil Organic Matter Quality on N Availability in Three Alaskan Arctic Plant Communities. *Ecosystems*, *14*(5). https://doi.org/10.1007/s10021-011-9447-5

Deprez, M., de Kock, T., de Schutter, G., & Cnudde, V. (2020). The role of ink-bottle pores in freeze-thaw damage of oolithic limestone. *Construction and Building Materials*, *246*. https://doi.org/10.1016/j.conbuildmat.2020.118515

Dittmar, T., Koch, B., Hertkorn, N., & Kattner, G. (2008). A simple and efficient method for the solid-phase extraction of dissolved organic matter (SPE-DOM) from seawater. *Limnology and Oceanography: Methods*, *6*(6), 230–235. https://doi.org/10.4319/lom.2008.6.230

Edwards, L. M. (2013). The effects of soil freeze–thaw on soil aggregate breakdown and concomitant sediment flow in Prince Edward Island: A review. *Canadian Journal of Soil Science*, *93*(4), 459–472. https://doi.org/10.4141/cjss2012-059

Elliott, A. C., & Henry, H. A. L. (2009). Freeze-thaw cycle amplitude and freezing rate effects on extractable nitrogen in a temperate old field soil. *Biology and Fertility of Soils*, *45*(5), 469–476. https://doi.org/10.1007/s00374-009-0356-0

Ferreira, T. R., Pires, L. F., Wildenschild, D., Heck, R. J., & Antonino, A. C. D. (2018). X-ray microtomography analysis of lime application effects on soil porous system. *Geoderma*, *324*, 119–130. https://doi.org/10.1016/j.geoderma.2018.03.015

Fisher, J. P., Estop-Aragonés, C., Thierry, A., Charman, D. J., Wolfe, S. A., Hartley, I. P., et al. (2016). The influence of vegetation and soil characteristics on active-layer thickness of permafrost soils in boreal forest. *Global Change Biology*, *22*(9), 3127–3140. https://doi.org/10.1111/gcb.13248

Foster, H. L., Keith, T. E. C., & Menzie, W. D. (1994). *Geology of the Yukon-Tanana area of east-central Alaska*.

Freeman, C., Ostle, N., & Kang, H. (2001). An enzymic "latch" on a global carbon store. *Nature*, *409*(6817), 149–149. https://doi.org/10.1038/35051650

Freppaz, M., Williams, B. L., Edwards, A. C., Scalenghe, R., & Zanini, E. (2007). Simulating soil freeze/thaw cycles typical of winter alpine conditions: Implications for N and P availability. *Applied Soil Ecology*, *35*(1), 247–255. https://doi.org/10.1016/j.apsoil.2006.03.012

Freppaz, M., Viglietti, D., Balestrini, R., Lonati, M., & Colombo, N. (2019). Climatic and pedoclimatic factors driving C and N dynamics in soil and surface water in the alpine tundra (NW-Italian Alps). *Nature Conservation*, *34*. https://doi.org/10.3897/natureconservation.34.30737

Fu, Q., Hou, R., Li, T., Yan, P., & Ma, Z. (2017). The critical depth of freeze-thaw soil under different types of snow cover. *Water (Switzerland)*, *9*(6). https://doi.org/10.3390/w9060370

Gao, D., Zhang, L., Liu, J., Peng, B., Fan, Z., Dai, W., et al. (2018). Responses of terrestrial nitrogen pools and dynamics to different patterns of freeze-thaw cycle: A meta-analysis. *Global Change Biology*, *24*(6), 2377–2389. https://doi.org/10.1111/gcb.14010

Gao, Z., Hu, X., Li, X.-Y., & Li, Z.-C. (2021). Effects of freeze-thaw cycles on soil macropores and its implications on formation of hummocks in alpine meadows in the Qinghai Lake watershed, northeastern Qinghai-Tibet Plateau. *Journal of Soils and Sediments*, *21*(1). https://doi.org/10.1007/s11368-020-02765-2

Gee, G. W., & Bauder, J. W. (1986). Particle-size analysis. In A. Klute (Ed.), *Methods of soil analysis. Part 1.* (2nd ed., pp. 383–411). Madison, WI.: Agron. Monogr. 9. ASA and SSSA.

Gentsch, N., Mikutta, R., Shibistova, O., Wild, B., Schnecker, J., Richter, A., et al. (2015). Properties and bioavailability of particulate and mineral-associated organic matter in Arctic permafrost soils, Lower Kolyma Region, Russia. *European Journal of Soil Science*, *66*(4), 722–734. https://doi.org/10.1111/ejss.12269

Graham, E. B., Tfaily, M. M., Crump, A. R., Goldman, A. E., Bramer, L. M., Arntzen, E., et al. (2017). Carbon Inputs From Riparian Vegetation Limit Oxidation of Physically Bound Organic Carbon Via Biochemical and Thermodynamic Processes. *Journal of Geophysical Research: Biogeosciences*, *122*(12), 3188–3205. https://doi.org/10.1002/2017JG003967

Guo, D., & Wang, H. (2013). Simulation of permafrost and seasonally frozen ground conditions on the Tibetan Plateau, 1981-2010. *Journal of Geophysical Research: Atmospheres*, *118*(11), 5216–5230. https://doi.org/10.1002/jgrd.50457

Henry, H. A. L. (2007, May). Soil freeze-thaw cycle experiments: Trends, methodological weaknesses and suggested improvements. *Soil Biology and Biochemistry*. https://doi.org/10.1016/j.soilbio.2006.11.017

Henry, H. A. L. (2008). Climate change and soil freezing dynamics: Historical trends and projected changes. *Climatic Change*, *87*(3–4), 421–434. https://doi.org/10.1007/s10584-007-9322-8

Huang, W., Ye, C., Hockaday, W. C., & Hall, S. J. (2020). Trade-offs in soil carbon protection mechanisms under aerobic and anaerobic conditions. *Global Change Biology*, *26*(6), 3726–3737. https://doi.org/10.1111/gcb.15100

Jelinski, N. A., Sousa, M. J., Williams, A., GreyBear, E., Finnesand, K., Mulligan, D., et al. (2019). Cryoturbation and Carbon Stocks in Gelisols under Late-Successional Black Spruce Forests of the Copper River Basin, Alaska. *Soil Science Society of America Journal*, *83*(6). https://doi.org/10.2136/sssaj2019.07.0212

Johnson, K. D., Harden, J. W., David McGuire, A., Clark, M., Yuan, F., & Finley, A. O. (2013). Permafrost and organic layer interactions over a climate gradient in a discontinuous permafrost zone. *Environmental Research Letters*, *8*(3), 035028. https://doi.org/10.1088/1748-9326/8/3/035028

Joss, H., Patzner, M. S., Maisch, M., Mueller, C. W., Kappler, A., & Bryce, C. (2022). Cryoturbation impacts iron-organic carbon associations along a permafrost soil chronosequence in northern Alaska. *Geoderma*, *413*, 115738. https://doi.org/10.1016/j.geoderma.2022.115738

Kanevskiy, M. (2003). Cryogenic structure of mountain slope deposits, northeast Russia. *Paper Presented at the 8th International Conference on Permafrost.*

Keiluweit, M., Wanzek, T., Kleber, M., Nico, P., & Fendorf, S. (2017). Anaerobic microsites have an unaccounted role in soil carbon stabilization. *Nature Communications*, *8*(1), 1771. https://doi.org/10.1038/s41467-017-01406-6

Kim, S., Kim, D., Jung, M., & Kim, S. (2022). Analysis of environmental organic matters by Ultrahigh-Resolution mass spectrometry—A review on the development of analytical methods. *Mass Spectrometry Reviews*, *41*(2), 352–369. https://doi.org/10.1002/mas.21684

Kirk, T. K., & Farrell, R. L. (1987). Enzymatic "Combustion": The Microbial Degradation of Lignin. *Annual Review of Microbiology*, *41*(1), 465–501. https://doi.org/10.1146/annurev.mi.41.100187.002341

Kobayashi, H., Suzuki, R., Nagai, S., Nakai, T., & Kim, Y. (2014). Spatial Scale and Landscape Heterogeneity Effects on FAPAR in an Open-Canopy Black Spruce Forest in Interior Alaska. *IEEE Geoscience and Remote Sensing Letters*, *11*(2), 564–568. https://doi.org/10.1109/LGRS.2013.2278426

Koch, B. P., & Dittmar, T. (2006). From mass to structure: an aromaticity index for high-resolution mass data of natural organic matter. *Rapid Communications in Mass Spectrometry*, *20*(5), 926–932. https://doi.org/10.1002/rcm.2386

Kögel-Knabner, I., Guggenberger, G., Kleber, M., Kandeler, E., Kalbitz, K., Scheu, S., et al. (2008). Organo-mineral associations in temperate soils: Integrating biology, mineralogy, and organic matter chemistry. *Journal of Plant Nutrition and Soil Science*, *171*(1), 61–82. https://doi.org/10.1002/jpln.200700048

Köhn, M. (1928). Bemerkungen zur mechanischen Bodenanalyse. III. Ein neuer Pipettapparat. *Zeitschrift Für Pflanzenernährung, Düngung, Bodenkunde, A, Wissenschaftlicher Teil*, *11*(1), 50–54. https://doi.org/10.1002/jpln.19280110104

Konrad, J.-M., & McCammon, A. W. (1990). Solute partitioning in freezing soils. *Canadian Geotechnical Journal*, *27*(6), 726–736. https://doi.org/10.1139/t90-086

Koponen, H. T., Jaakkola, T., Keinänen-Toivola, M. M., Kaipainen, S., Tuomainen, J., Servomaa, K., & Martikainen, P. J. (2006). Microbial communities, biomass, and activities in soils as affected by freeze thaw cycles. *Soil Biology and Biochemistry*, *38*(7), 1861–1871. https://doi.org/10.1016/j.soilbio.2005.12.010

Kujawinski, E. B., & Behn, M. D. (2006). Automated Analysis of Electrospray Ionization Fourier Transform Ion Cyclotron Resonance Mass Spectra of Natural Organic Matter. *Analytical Chemistry*, *78*(13), 4363–4373. https://doi.org/10.1021/ac0600306

Kujawinski, E. B., Hatcher, P. G., & Freitas, M. A. (2002). High-Resolution Fourier Transform Ion Cyclotron Resonance Mass Spectrometry of Humic and Fulvic Acids: Improvements and Comparisons. *Analytical Chemistry*, *74*(2), 413–419. https://doi.org/10.1021/ac0108313

LaRowe, D. E., & van Cappellen, P. (2011). Degradation of natural organic matter: A thermodynamic analysis. *Geochimica et Cosmochimica Acta*, *75*(8), 2030–2042. https://doi.org/10.1016/j.gca.2011.01.020

Larsen, K. S., Jonasson, S., & Michelsen, A. (2002). *Repeated freeze-thaw cycles and their effects on biological processes in two arctic ecosystem types*. *Applied Soil Ecology* (Vol. 21).

Lawlor, J. (2020). PNWColors: Color Palettes Inspired by Nature in the US Pacific Northwest. *Zenodo.*

Leewis, M.-C., Berlemont, R., Podgorski, D. C., Srinivas, A., Zito, P., Spencer, R. G. M., et al. (2020). Life at the Frozen Limit: Microbial Carbon Metabolism Across a Late Pleistocene Permafrost Chronosequence. *Frontiers in Microbiology*, *11*. https://doi.org/10.3389/fmicb.2020.01753

Lentini, C. J., Wankel, S. D., & Hansel, C. M. (2012). Enriched Iron(III)-Reducing Bacterial Communities are Shaped by Carbon Substrate and Iron Oxide Mineralogy. *Frontiers in Microbiology*, *3*. https://doi.org/10.3389/fmicb.2012.00404

Li, X., Jin, R., Pan, X., Zhang, T., & Guo, J. (2012). Changes in the near-surface soil freeze–thaw cycle on the Qinghai-Tibetan Plateau. *International Journal of Applied Earth Observation and Geoinformation*, *17*, 33–42. https://doi.org/10.1016/j.jag.2011.12.002

Li, X., Lu, Y., Zhang, X., Fan, W., Lu, Y., & Pan, W. (2019). Quantification of macropores of Malan loess and the hydraulic significance on slope stability by X-ray computed tomography. *Environmental Earth Sciences*, *78*(16). https://doi.org/10.1007/s12665-019-8527-2

Liu, B., Ma, R., & Fan, H. (2021). Evaluation of the impact of freeze-thaw cycles on pore structure characteristics of black soil using X-ray computed tomography. *Soil and Tillage Research*, *206*. https://doi.org/10.1016/j.still.2020.104810

Liu, B., Fan, H., Han, W., Zhu, L., Zhao, X., Zhang, Y., & Ma, R. (2021). Linking soil water retention capacity to pore structure characteristics based on X-ray computed tomography: Chinese Mollisol under freeze-thaw effect. *Geoderma*, *401*. https://doi.org/10.1016/j.geoderma.2021.115170

Liu, M., Feng, F., Cai, T., & Tang, S. (2020). Soil Microbial Community Response Differently to the Frequency and Strength of Freeze–Thaw Events in a Larix gmelinii Forest in the Daxing'an Mountains, China. *Frontiers in Microbiology*, *11*. https://doi.org/10.3389/fmicb.2020.01164

Loranty, M. M., Berner, L. T., Taber, E. D., Kropp, H., Natali, S. M., Alexander, H. D., et al. (2018). Understory vegetation mediates permafrost active layer dynamics and carbon dioxide fluxes in open-canopy larch forests of northeastern Siberia. *PLOS ONE*, *13*(3), e0194014. https://doi.org/10.1371/journal.pone.0194014

Lovley, D. R., & Phillips, E. J. P. (1988). Novel Mode of Microbial Energy Metabolism: Organic Carbon Oxidation Coupled to Dissimilatory Reduction of Iron or Manganese. *Applied and Environmental Microbiology*, *54*(6), 1472–1480. https://doi.org/10.1128/aem.54.6.1472-1480.1988

von Lützow, M., Kögel-Knabner, I., Ekschmitt, K., Flessa, H., Guggenberger, G., Matzner, E., & Marschner, B. (2007). SOM fractionation methods: Relevance to functional pools and to stabilization mechanisms. *Soil Biology and Biochemistry*, *39*(9), 2183–2207. https://doi.org/10.1016/j.soilbio.2007.03.007

Lynch, L. M., Machmuller, M. B., Boot, C. M., Covino, T. P., Rithner, C. D., Cotrufo, M. F., et al. (2019). Dissolved Organic Matter Chemistry and Transport Along an Arctic Tundra Hillslope. *Global Biogeochemical Cycles*, *33*(1), 47–62. https://doi.org/10.1029/2018GB006030

Ma, R., Jiang, Y., Liu, B., & Fan, H. (2021). Effects of pore structure characterized by synchrotron-based micro-computed tomography on aggregate stability of black soil under freeze-thaw cycles. *Soil and Tillage Research*, *207*. https://doi.org/10.1016/j.still.2020.104855

MacDonald, E. N., Tank, S. E., Kokelj, S. v., Froese, D. G., & Hutchins, R. H. S. (2021). Permafrost-derived dissolved organic matter composition varies across permafrost end-members in the western Canadian Arctic. *Environmental Research Letters*, *16*(2). https://doi.org/10.1088/1748-9326/abd971

Mackay, J. R. (1980). *The origin of hummocks, western Arctic coast, Canada*. *J. Earth Sci* (Vol. 17).

Makusa, G. P., Bradshaw, S. L., Berns, E., Benson, C. H., & Knutsson, S. (2014). Freeze–thaw cycling concurrent with cation exchange and the hydraulic conductivity of geosynthetic clay liners. *Canadian Geotechnical Journal*, *51*(6), 591–598. https://doi.org/10.1139/cgj-2013-0127

Manies, K. L., Jones, M. C., Waldrop, M. P., Leewis, M., Fuller, C., Cornman, R. S., & Hoefke, K. (2021). Influence of Permafrost Type and Site History on Losses of Permafrost Carbon After Thaw. *Journal of Geophysical Research: Biogeosciences*, *126*(11). https://doi.org/10.1029/2021JG006396

McGuire, A. D., Lawrence, D. M., Koven, C., Clein, J. S., Burke, E., Chen, G., et al. (2018). Dependence of the evolution of carbon dynamics in the northern permafrost region on the trajectory of climate change. *Proceedings of the National Academy of Sciences*, *115*(15), 3882–3887. https://doi.org/10.1073/pnas.1719903115

Miller, R. O., Gavlak, R., & Horneck, D. (2013). *Soil, Plant, and Water Reference Methods for the Western Region.* (4th ed.).

Natali, S. M., Schuur, E. A. G., & Rubin, R. L. (2012). Increased plant productivity in Alaskan tundra as a result of experimental warming of soil and permafrost. *Journal of Ecology*, *100*(2), 488–498. https://doi.org/10.1111/j.1365-2745.2011.01925.x

National Ecological Observatory Network. (2019). Terrestrial Observation System (TOS) Site Characterization Report: Domain 18. Retrieved from 13/07/2021https://data.neonscience.org/documents/10179/2263491/NEON.DOC.003901vB/f03fb22d-2fcd-10f7-b562-b80bfeca07da

National Ecological Observatory Network. (2021a). Bundled data products - eddy covariance, RELEASE-2021 (DP4.00200.001). *Dataset Accessed from Https://Data.Neonscience.Org on June 29, 2021*.

National Ecological Observatory Network. (2021b). Soil physical and chemical properties, distributed initial characterization, RELEASE-2021 (DP1.10047.001). *Https://Doi.Org/10.48443/Tjgd-6m89. Dataset Accessed from Https://Data.Neonscience.Org on June 29, 2021*.

National Ecological Observatory Network. (2021c). Soil physical and chemical properties, Megapit, RELEASE-2021 (DP1.00096.001). *Dataset Accessed from Https://Data.Neonscience.Org on June 29, 2021*.

National Ecological Observatory Network. (2021d). Soil temperature, RELEASE-2021 (DP1.00041.001). *Https://Doi.Org/10.48443/9e56-Pj39. Dataset Accessed from Https://Data.Neonscience.Org*.

Nimmo, J. R. (2013). Porosity and Pore Size Distribution. In *Reference Module in Earth Systems and Environmental Sciences*. Elsevier. https://doi.org/10.1016/B978-0-12-409548-9.05265-9

Oksanen, J., Blanchet, F. G., Friendly, M., Kindt, R., Legendre, P., McGlinn, D., et al. (2019). Vegan: Community Ecology Package. R Package.

Oztas, T., & Fayetorbay, F. (2003). Effect of freezing and thawing processes on soil aggregate stability. *CATENA*, *52*(1), 1–8. https://doi.org/10.1016/S0341-8162(02)00177-7

Park, H., Fedorov, A. N., Zheleznyak, M. N., Konstantinov, P. Y., & Walsh, J. E. (2015). Effect of snow cover on pan-Arctic permafrost thermal regimes. *Climate Dynamics*, *44*(9–10), 2873–2895. https://doi.org/10.1007/s00382-014-2356-5

Patel, K. F. (2020). fticrrr. *R Package*. Zenodo, DOI:10.5281/zenodo.3893246.

Patel, Kaizad F., Tatariw, C., MacRae, J. D., Ohno, T., Nelson, S. J., & Fernandez, I. J. (2018). Soil carbon and nitrogen responses to snow removal and concrete frost in a northern coniferous forest. *Canadian Journal of Soil Science*, *98*(3), 436–447. https://doi.org/10.1139/cjss-2017-0132

Patel, Kaizad F., Tatariw, C., MacRae, J. D., Ohno, T., Nelson, S. J., & Fernandez, I. J. (2021). Repeated freeze–thaw cycles increase extractable, but not total, carbon and nitrogen in a Maine coniferous soil. *Geoderma*, *402*. https://doi.org/10.1016/j.geoderma.2021.115353

Patzner, M. S., Mueller, C. W., Malusova, M., Baur, M., Nikeleit, V., Scholten, T., et al. (2020). Iron mineral dissolution releases iron and associated organic carbon during permafrost thaw. *Nature Communications*, *11*(1), 6329. https://doi.org/10.1038/s41467-020-20102-6

Ping, C. L., Michaelson, G. J., Packee, E. C., Stiles, C. A., Swanson, D. K., & Yoshikawa, K. (2005). Soil Catena Sequences and Fire Ecology in the Boreal Forest of Alaska. *Soil Science Society of America Journal*, *69*(6), 1761–1772. https://doi.org/10.2136/sssaj2004.0139

Ping, C. L., Michaelson, G. J., Kimble, J. M., Romanovsky, V. E., Shur, Y. L., Swanson, D. K., & Walker, D. A. (2008). Cryogenesis and soil formation along a bioclimate gradient in Arctic North America. *Journal of Geophysical Research: Biogeosciences*, *113*(3). https://doi.org/10.1029/2008JG000744

Ping, C. L., Jastrow, J. D., Jorgenson, M. T., Michaelson, G. J., & Shur, Y. L. (2015). Permafrost soils and carbon cycling. *SOIL*, *1*(1), 147–171. https://doi.org/10.5194/soil-1-147-2015

Quinton, W. L., Hayashi, M., & Chasmer, L. E. (2009). Peatland Hydrology of Discontinuous Permafrost in the Northwest Territories: Overview and Synthesis. *Canadian Water Resources Journal*, *34*(4), 311–328. https://doi.org/10.4296/cwrj3404311

R Core Team. (2020). R: A language and environment for statistical computing.

Ramage, J. L., Fortier, D., Hugelius, G., Lantuit, H., & Morgenstern, A. (2019). Distribution of carbon and nitrogen along hillslopes in three valleys on Herschel Island, Yukon Territory, Canada. *CATENA*, *178*, 132–140. https://doi.org/10.1016/j.catena.2019.02.029

Rempel, A. W. (2010). *Frost heave*.

Rempel, A. W., & van Alst, L. J. (2013). *Potential gradients produced by pore-space heterogeneities: Application to isothermal frost damage and submarine hydrate anomalies*.

Rooney, E. C., Bailey, V. L., Patel, K. F., Dragila, M., Battu, A. K., Buchko, A. C., et al. (2022). Soil pore network response to freeze-thaw cycles in permafrost aggregates. *Geoderma*, *411*, 115674. https://doi.org/10.1016/j.geoderma.2021.115674

RStudio Team. (2019). RStudio: Integrated Development for R. RStudio, Inc. *Boston, MA, Http://Www.Rstudio.Com/*.

Ruamps, L. S., Nunan, N., & Chenu, C. (2011). Microbial biogeography at the soil pore scale. *Soil Biology and Biochemistry*, *43*(2). https://doi.org/10.1016/j.soilbio.2010.10.010

Sawicka, J. E., Robador, A., Hubert, C., Jørgensen, B. B., & Brüchert, V. (2010). Effects of freeze–thaw cycles on anaerobic microbial processes in an Arctic intertidal mud flat. *The ISME Journal*, *4*(4), 585–594. https://doi.org/10.1038/ismej.2009.140

Schimel, J. P., & Clein, J. S. (1996). *MICROBIAL RESPONSE TO FREEZE-THAW CYCLES IN TUNDRA AND TAIGA SOILS*. *Soil Eiot. Biorhem* (Vol. 28).

Schimel, J. P., & Mikan, C. (2005). Changing microbial substrate use in Arctic tundra soils through a freeze-thaw cycle. *Soil Biology and Biochemistry*, *37*(8), 1411–1418. https://doi.org/10.1016/j.soilbio.2004.12.011

Schmidt, S. K., & Lipson, D. A. (2004). Microbial growth under the snow: Implications for nutrient and allelochemical availability in temperate soils. *Plant and Soil*, *259*(1/2), 1–7. https://doi.org/10.1023/B:PLSO.0000020933.32473.7e

Schuur, E. A. G., McGuire, A. D., Schädel, C., Grosse, G., Harden, J. W., Hayes, D. J., et al. (2015, April 9). Climate change and the permafrost carbon feedback. *Nature*. Nature Publishing Group. https://doi.org/10.1038/nature14338

Seidel, M., Beck, M., Riedel, T., Waska, H., Suryaputra, I. G. N. A., Schnetger, B., et al. (2014). Biogeochemistry of dissolved organic matter in an anoxic intertidal creek bank. *Geochimica et Cosmochimica Acta*, *140*, 418–434. https://doi.org/10.1016/j.gca.2014.05.038

Shang, C., & Zelazny, L. W. (2015). Selective Dissolution Techniques for Mineral Analysis of Soils and Sediments (pp. 33–80). https://doi.org/10.2136/sssabookser5.5.c3

Sharratt, B. S., Baker, D. G., Wall, D. B., Skaggs, R. H., & Ruschy, D. L. (1992). Snow depth required for near steady-state soil temperatures. *Agricultural and Forest Meteorology*, *57*(4), 243–251. https://doi.org/10.1016/0168-1923(92)90121-J

Sheldrick, B. H., & Wang, C. (1993). Particle Size Analysis. In M. R. Carter (Ed.), *Soil Sampling and Methods of Analysis* (pp. 499–517). Boca Raton: Lewis Publishers.

Shelef, E., Rowland, J. C., Wilson, C. J., Hilley, G. E., Mishra, U., Altmann, G. L., & Ping, C. (2017). Large uncertainty in permafrost carbon stocks due to hillslope soil deposits. *Geophysical Research Letters*, *44*(12), 6134–6144. https://doi.org/10.1002/2017GL073823

Shur, Y. L., & Jorgenson, M. T. (2007). Patterns of permafrost formation and degradation in relation to climate and ecosystems. *Permafrost and Periglacial Processes*, *18*(1), 7–19. https://doi.org/10.1002/ppp.582

Skogland, T., Lomeland, S., & Goksøyr, J. (1988). Respiratory burst after freezing and thawing of soil: Experiments with soil bacteria. *Soil Biology and Biochemistry*, *20*(6), 851–856. https://doi.org/10.1016/0038-0717(88)90092-2

Smith, A. P., Bond-Lamberty, B., Benscoter, B. W., Tfaily, M. M., Hinkle, C. R., Liu, C., & Bailey, V. L. (2017). Shifts in pore connectivity from precipitation versus groundwater rewetting increases soil carbon loss after drought. *Nature Communications*, *8*(1), 1335. https://doi.org/10.1038/s41467-017-01320-x

Soil Survey Staff. (1999). *Soil taxonomy: A basic system of soil classification for making and interpreting soil surveys* (2nd edition). Natural Resources Conservation Service, U.S. Department of Agriculture Handbook 436.

Soil Survey Staff. (2014). Keys to Soil Taxonomy, 12th ed. *USDA-Natural Resources Conservation Service, Washington, DC.*

Sollins, P., Homann, P., & Caldwell, B. A. (1996). Stabilization and destabilization of soil organic matter: mechanisms and controls. *Geoderma*, (74), 65–105.

Song, Y., Zou, Y., Wang, G., & Yu, X. (2017). Altered soil carbon and nitrogen cycles due to the freeze-thaw effect: A meta-analysis. *Soil Biology and Biochemistry*, *109*, 35–49. https://doi.org/10.1016/j.soilbio.2017.01.020

Soulides, D. A., & Allison, F. E. (1961). Effect of drying and freezing soils on carbon dioxide production, available mineral nutrients, aggregation, and bacterial population. *Soil Science*, *91*(5). https://doi.org/10.1097/00010694-196105000-00001

Starkloff, T., Larsbo, M., Stolte, J., Hessel, R., & Ritsema, C. (2017). Quantifying the impact of a succession of freezing-thawing cycles on the pore network of a silty clay loam and a loamy sand topsoil using X-ray tomography. *Catena*, *156*, 365–374. https://doi.org/10.1016/j.catena.2017.04.026

Storey, K. B., & Storey, J. M. (2005). *FREEZE TOLERANCE*. Retrieved from http://www.eolss.net

Strong, D. T., de Wever, H., Merckx, R., & Recous, S. (2004). Spatial location of carbon decomposition in the soil pore system. *European Journal of Soil Science*, *55*(4), 739–750. https://doi.org/10.1111/j.1365-2389.2004.00639.x

Stuenzi, S. M., Boike, J., Cable, W., Herzschuh, U., Kruse, S., Pestryakova, L. A., et al. (2021). Variability of the surface energy balance in permafrost-underlain boreal forest. *Biogeosciences*, *18*(2), 343–365. https://doi.org/10.5194/bg-18-343-2021

Textor, S. R., Wickland, K. P., Podgorski, D. C., Johnston, S. E., & Spencer, R. G. M. (2019). Dissolved Organic Carbon Turnover in Permafrost-Influenced Watersheds of Interior Alaska: Molecular Insights and the Priming Effect. *Frontiers in Earth Science*, *7*. https://doi.org/10.3389/feart.2019.00275

Thomas, G. W. (2018). Soil pH and Soil Acidity (pp. 475–490). https://doi.org/10.2136/sssabookser5.3.c16

Tolić, N., Liu, Y., Liyu, A., Shen, Y., Tfaily, M. M., Kujawinski, E. B., et al. (2017). Formularity: Software for Automated Formula Assignment of Natural and Other Organic Matter from Ultrahigh-Resolution Mass Spectra. *Analytical Chemistry*, *89*(23), 12659–12665. https://doi.org/10.1021/acs.analchem.7b03318

Treat, C. C., Jones, M. C., Camill, P., Gallego-Sala, A., Garneau, M., Harden, J. W., et al. (2016). Effects of permafrost aggradation on peat properties as determined from a pan-Arctic synthesis of plant macrofossils. *Journal of Geophysical Research: Biogeosciences*, *121*(1), 78–94. https://doi.org/10.1002/2015JG003061

Turetsky, M. R., Abbott, B. W., Jones, M. C., Anthony, K. W., Olefeldt, D., Schuur, E. A. G., et al. (2020). Carbon release through abrupt permafrost thaw. *Nature Geoscience*, *13*(2), 138–143. https://doi.org/10.1038/s41561-019-0526-0

U.S. Geological Survey. (2005). Mineral Resources Data System: U.S. Geological Survey, Reston, Virginia. Retrieved from https://mrdata.usgs.gov/mrds/

USGS, S. of A., Polar Geospatial Center, U. of M., National Science Foundation, National Geospatial-Intelligence Agency, & DigitalGlobe. (2018). Arctic DEM. Esri, ArcGIS.

Veelen, A., Koebernick, N., Scotson, C. S., McKay-Fletcher, D., Huthwelker, T., Borca, C. N., et al. (2020). Root-induced soil deformation influences Fe, S and P: rhizosphere chemistry investigated using synchrotron XRF and XANES. *New Phytologist*, *225*(4). https://doi.org/10.1111/nph.16242

Wadell, H. (1933). Sphericity and Roundness of Rock Particles. *The Journal of Geology*, *41*(3).

Wang, B., Hults, C. P., Eberl, D. D., Woodruff, L. G., Cannon, W. F., & Gough, L. P. (2019). *Studies by the U.S. Geological Survey in Alaska, Volume 15: Soil Mineralogy and Geochemistry Along a North-South Transect in Alaska and the Relation to Source-Rock Terrane*. Reston, Virginia.

Wang, G.-P., Liu, J.-S., Zhao, H.-Y., Wang, J.-D., & Yu, J.-B. (2007). Phosphorus sorption by freeze–thaw treated wetland soils derived from a winter-cold zone (Sanjiang Plain, Northeast China). *Geoderma*, *138*(1–2), 153–161. https://doi.org/10.1016/j.geoderma.2006.11.006

Wang, J. Q., Zhao, J. F., Yang, M. J., Li, Y. H., Liu, W. G., & Song, Y. C. (2015). Permeability of laboratory-formed porous media containing methane hydrate: Observations using X-ray computed tomography and simulations with pore network models. *Fuel*, *145*, 170–179. https://doi.org/10.1016/j.fuel.2014.12.079

Wang, Jiaoyue, Song, C., Hou, A., & Wang, L. (2014). CO2 emissions from soils of different depths of a permafrost peatland, Northeast China: response to simulated freezing–thawing cycles. *Journal of Plant Nutrition and Soil Science*, *177*(4), 524–531. https://doi.org/10.1002/jpln.201300309

Wang, Jingyuan, Luo, S., Li, Z., Wang, S., & Li, Z. (2019). The freeze/thaw process and the surface energy budget of the seasonally frozen ground in the source region of the Yellow River. *Theoretical and Applied Climatology*, *138*(3–4), 1631–1646. https://doi.org/10.1007/s00704-019-02917-6

Wang, T., Hamann, A., Spittlehouse, D. L., & Murdock, T. Q. (2012). ClimateWNA—High-Resolution Spatial Climate Data for Western North America. *Journal of Applied Meteorology and Climatology*, *51*(1). https://doi.org/10.1175/JAMC-D-11-043.1

Wanzek, T., Keiluweit, M., Varga, T., Lindsley, A., Nico, P. S., Fendorf, S., & Kleber, M. (2018). The Ability of Soil Pore Network Metrics to Predict Redox Dynamics is Scale Dependent. *Soil Systems*, *2*(4). https://doi.org/10.3390/soilsystems2040066

Waring, B. G., Sulman, B. N., Reed, S., Smith, A. P., Averill, C., Creamer, C. A., et al. (2020). From pools to flow: The PROMISE framework for new insights on soil carbon cycling in a changing world. *Global Change Biology*, *26*(12). https://doi.org/10.1111/gcb.15365

Wei, C., Yu, S., Jichun, W., Yaling, C., Erxing, P., & Leonid, G. (2021). Soil hydrological process and migration mode influenced by the freeze-thaw process in the activity layer of permafrost regions in Qinghai-Tibet Plateau. *Cold Regions Science and Technology*, *184*. https://doi.org/10.1016/j.coldregions.2021.103236

Wettlaufer, J. S., Worster, M. G., Wilen, L. A., & Dash, J. G. (1996). *A Theory of Premelting Dynamics for all Power Law Forces*.

Wickham, H. (2016). ggplot2: Elegant Graphics for Data Analysis. *Springer*.

Wickham, H., François, R., & Henry, L. (2020). dplyr: A grammar of Data Manipulation.

Wilen, L. A., & Dash, J. G. (1995). *Frost Heave Dynamics* (Vol. 74).

Williams, T. J., & Quinton, W. L. (2013). Modelling incoming radiation on a linear disturbance and its impact on the ground thermal regime in discontinuous permafrost. *Hydrological Processes*, *27*(13), 1854–1865. https://doi.org/10.1002/hyp.9792

Wilson, F. H., Hults, C. P., Mull, C. G., & Karl, S. M. (2015). *Geologic map of Alaska: U.S. Geological Survey Scientific Investigations Map 3340, pamphlet 196 p., 2 sheets, scale 1:1,584,000*. *USGS*.

Yi, Y., Kimball, J. S., Rawlins, M. A., Moghaddam, M., & Euskirchen, E. S. (2015). The role of snow cover affecting boreal-arctic soil freeze-thaw and carbon dynamics. *Biogeosciences*, *12*(19), 5811–5829. https://doi.org/10.5194/bg-12-5811-2015

Yu, X., Zhang, Y., Zhao, H., Lu, X., & Wang, G. (2010). Freeze-thaw effects on sorption/desorption of dissolved organic carbon in wetland soils. *Chinese Geographical Science*, *20*(3), 209–217. https://doi.org/10.1007/s11769-010-0209-7

Yuan, F., Liu, J., Zuo, Y., Guo, Z., Wang, N., Song, C., et al. (2020). Rising vegetation activity dominates growing water use efficiency in the Asian permafrost region from 1900 to 2100. *Science of The Total Environment*, *736*. https://doi.org/10.1016/j.scitotenv.2020.139587

Zhao, Ying, Li, Y., & Yang, F. (2021). Critical review on soil phosphorus migration and transformation under freezing-thawing cycles and typical regulatory measurements. *Science of The Total Environment*, *751*. https://doi.org/10.1016/j.scitotenv.2020.141614

Zhao, Yunduo, Hu, X., Li, X., Jiang, L., & Gao, Z. (2021). Evaluation of the impact of freeze–thaw cycles on the soil pore structure of alpine meadows using X-ray computed tomography. *Soil Science Society of America Journal*. https://doi.org/10.1002/saj2.20256

APPENDICES

Appendix A. Soil Pore Network Response to Freeze-thaw Cycles in Permafrost Aggregates

Appendix Information 1: Selection of experimental parameters

Moisture Content selection

Moisture contents were selected to represent the potential seasonal variability in soil wetness. Fluctuation between moisture contents of 16% and 28% may be seen within permafrost-affected soils depending on season, landscape position, and active layer thickness (Yuan et al., 2020). In soil where permafrost thaw has favored drainage, unsaturated soils at close to or under field capacity (12-16%) are also documented throughout the soil profile. These drier conditions can be the result of drainage, evaporation, or a desiccated active layer where water has been pulled bidirectionally along freezing fronts toward the soil surface and underlying permafrost (Mackay, 1980; Rempel, 2010; Yuan et al., 2020).

Temperature Fluctuation selection

Methodological parameters that have been employed in published freeze-thaw incubation experiments are extremely variable in chosen temperature fluctuation, experiment length, and rate of freeze-thaw (Henry, 2007; Ma et al., 2021; Starkloff et al., 2017). The lack of a standard in freeze-thaw methodology is likely due to the need for specific methodologies depending on the targeted analyses and overarching questions. Within this experiment, temperatures were chosen to guarantee full freezing and thawing of the aggregate to ensure comparability across all replicates and freeze-thaw cycles. The more extreme temperature fluctuations within surface and subsurface horizons of permafrost-affected soils were chosen for the aforementioned reason and align with temperature ranges selected by similar porosity focused freeze-thaw experiments (Starkloff et al., 2017; Yunduo Zhao et al., 2021), rather than more subtle temperature changes that would be ideal for a microbially-focused freeze-thaw experiment.

The large range in soil temperature and duration was selected to ensure that each freeze-thaw cycle occurred fully and equally throughout the soil, allowing for comparability of impacts across cycles. Additionally, the focus on physical changes to the soil pore structure further emphasized the importance that the full aggregate undergoes freezing and thawing with no potential for partial freeze or partial thaw during any of the cycles. Full freezing and thawing of 2.5 cm aggregates can occur in 24 hours (Ma et al., 2021). We added an extra 24 hours was added to ensure completion of the freeze-thaw cycle.

Figure A1. Freeze-thaw count across Toolik cores based on NEON instrumentation data and analyzed using the FTCQuant Package (Boswell, 2020). The active layer is indicated by a horizontal black dashed line at 10 cm. Core A aggregates sampled between 28-38 cm, Core B aggregates sampled between 40-50 cm, and Core C aggregates sampled between 41-50 cm. The figure represents three years (2018-2020) of data collection at six distinct 60-cm temperature profiles by NEON at the Toolik Field Station. Temperature data was collected at six depths (every ~10 cm) except for the first two horizons which were collected at 2 cm and 6 cm.

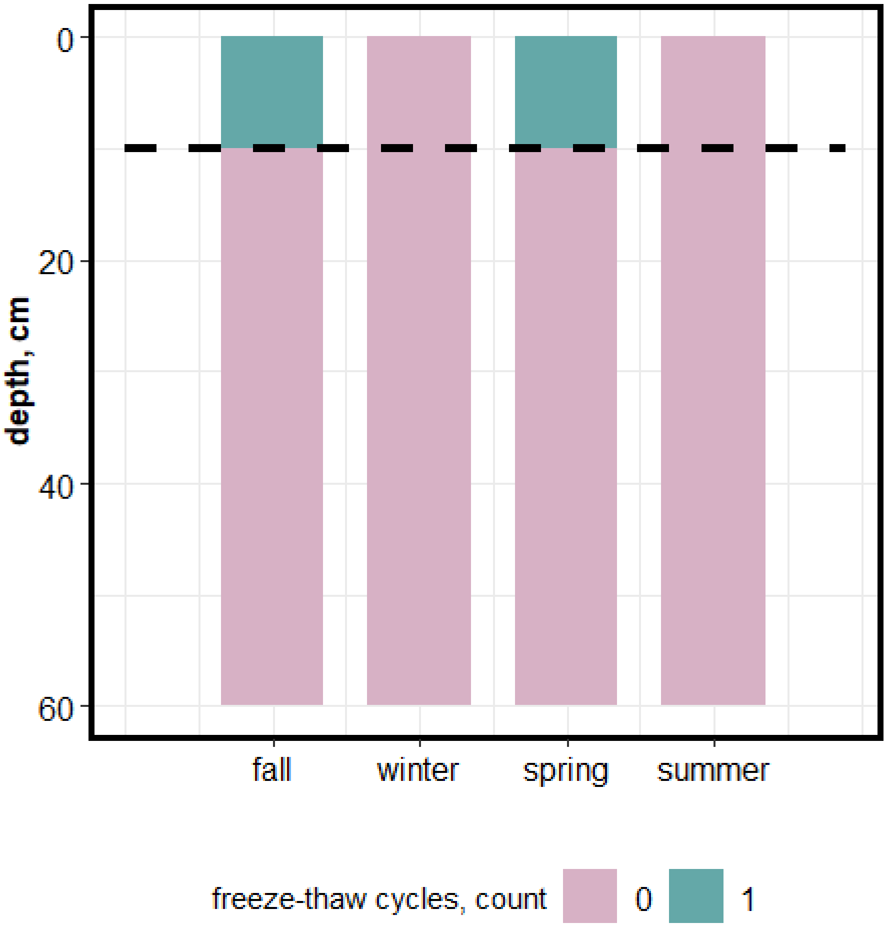

Figure A2. Flowchart demonstrating the XCT data processing method, from image acquisition to the three main result outputs (pore throat diameters, pore coordination numbers, and pore volumes).

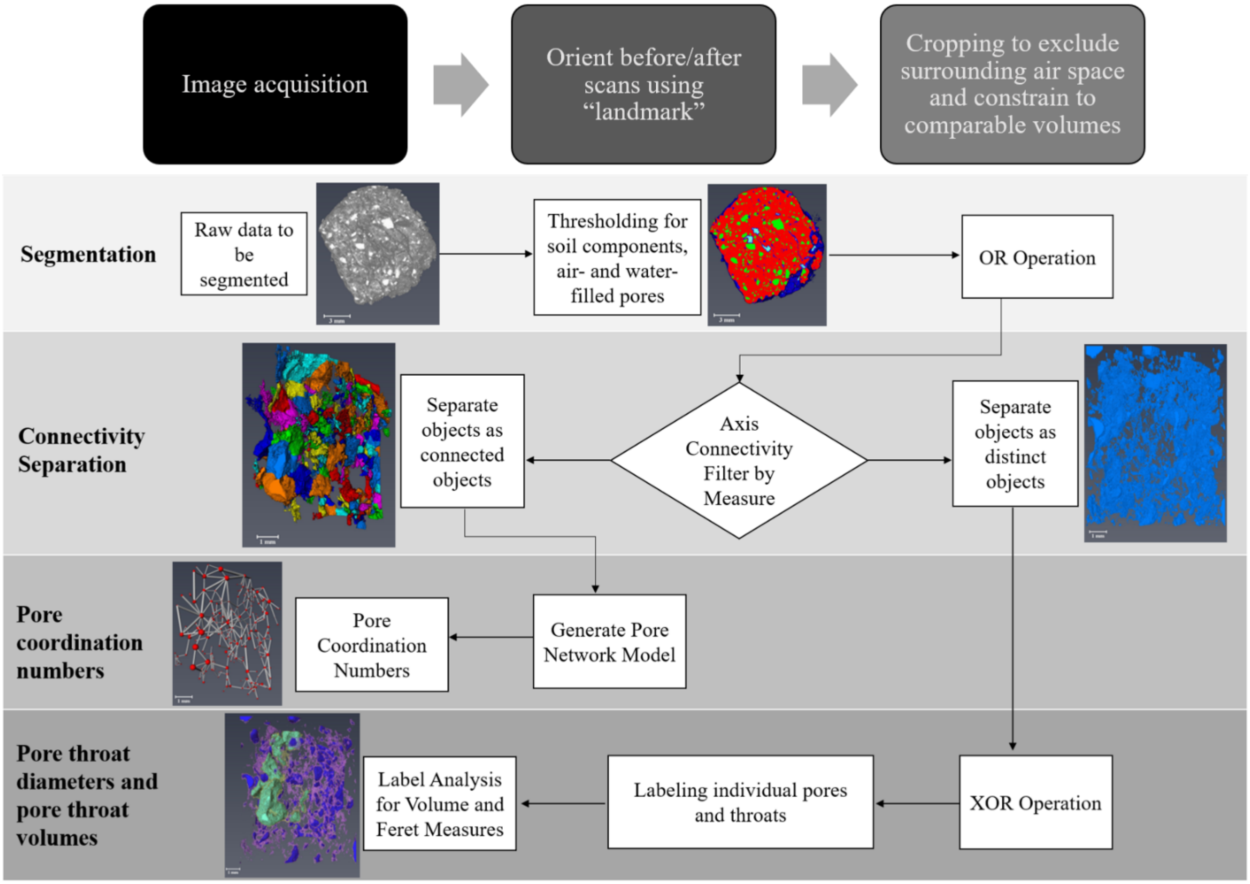

Figure A3. Grayscale scans of the outer aggregate for all six samples prior to freeze-thaw.

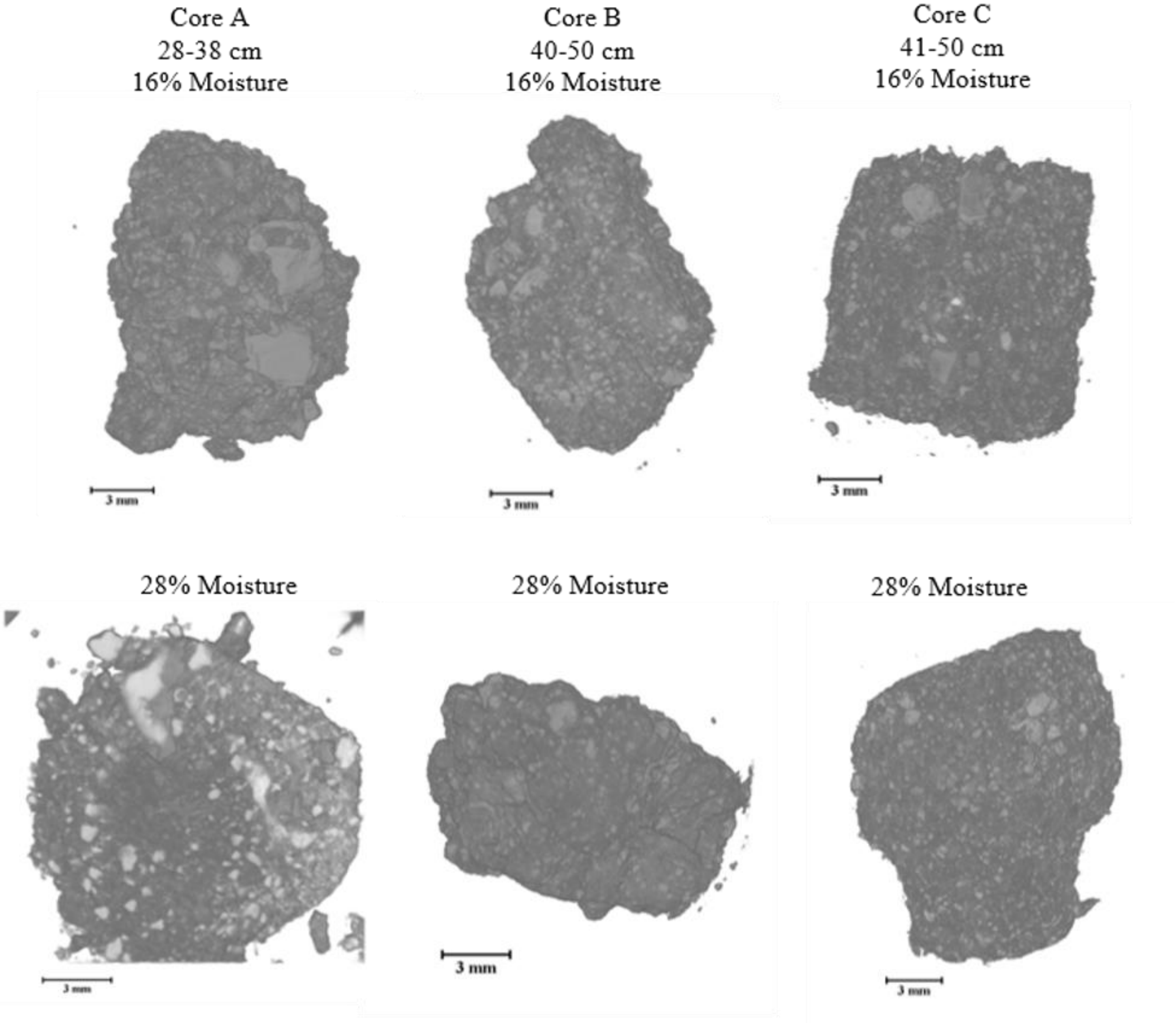

Figure A4. Aggregate scans for each of the six samples with before and after scans segmented into high density soil (green), low density soil (red), water (dark blue), and air (light blue). All aggregates have before/after scans from the same region of the aggregate except for Core A, 28% which has scans from two different regions of the core.

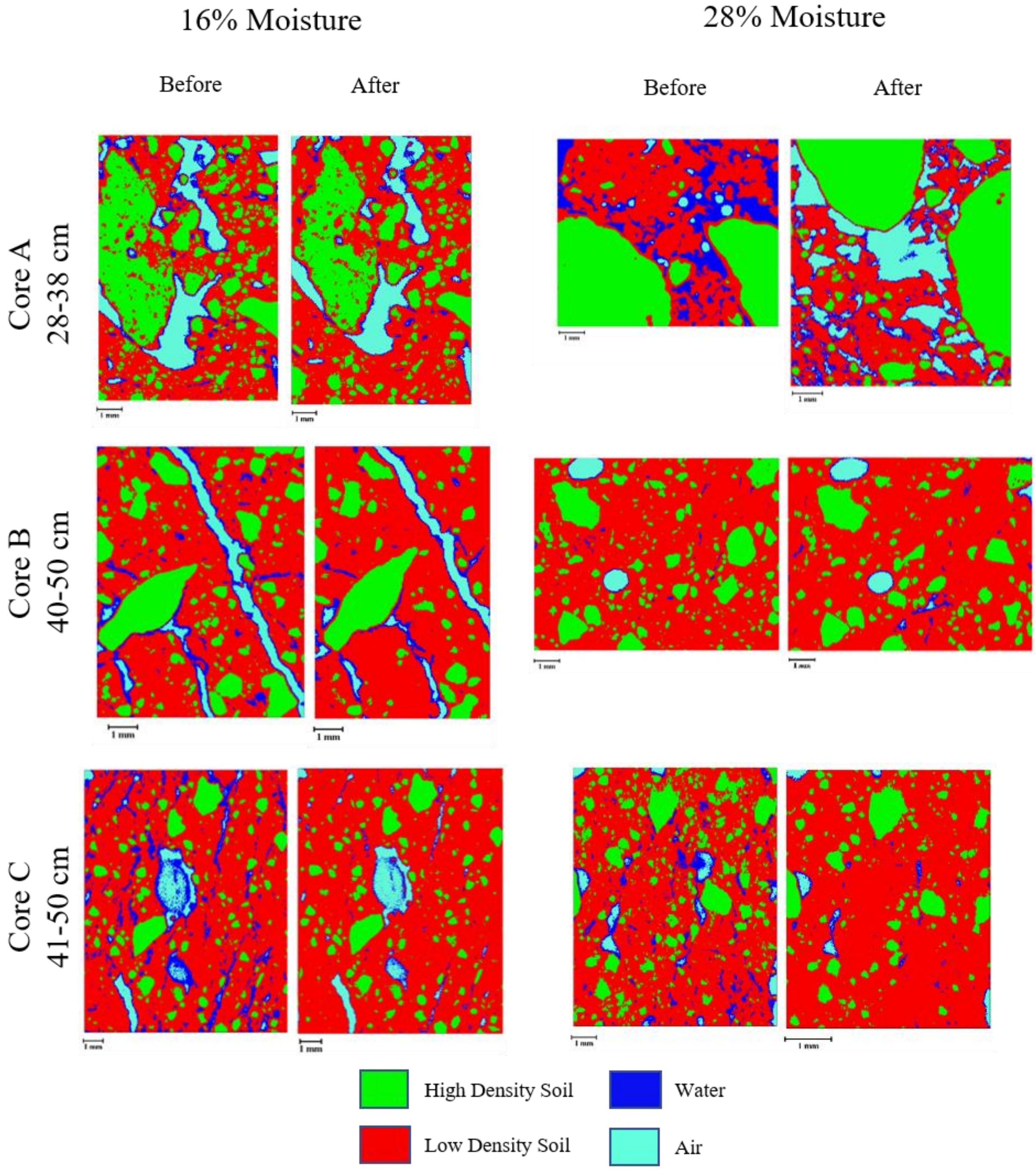

Figure A5. Examples of grayscale and segmented scans (Core A, 28-38 cm (before freeze-thaw). The grayscale scan was segmented into four components: high density soil (73.6 to 344.5 grayscale range), low density soil (25.6 to 73.6 grayscale range), water (13.1 to 25.6 grayscale range) and air (-5.9 to 13.1 grayscale range).

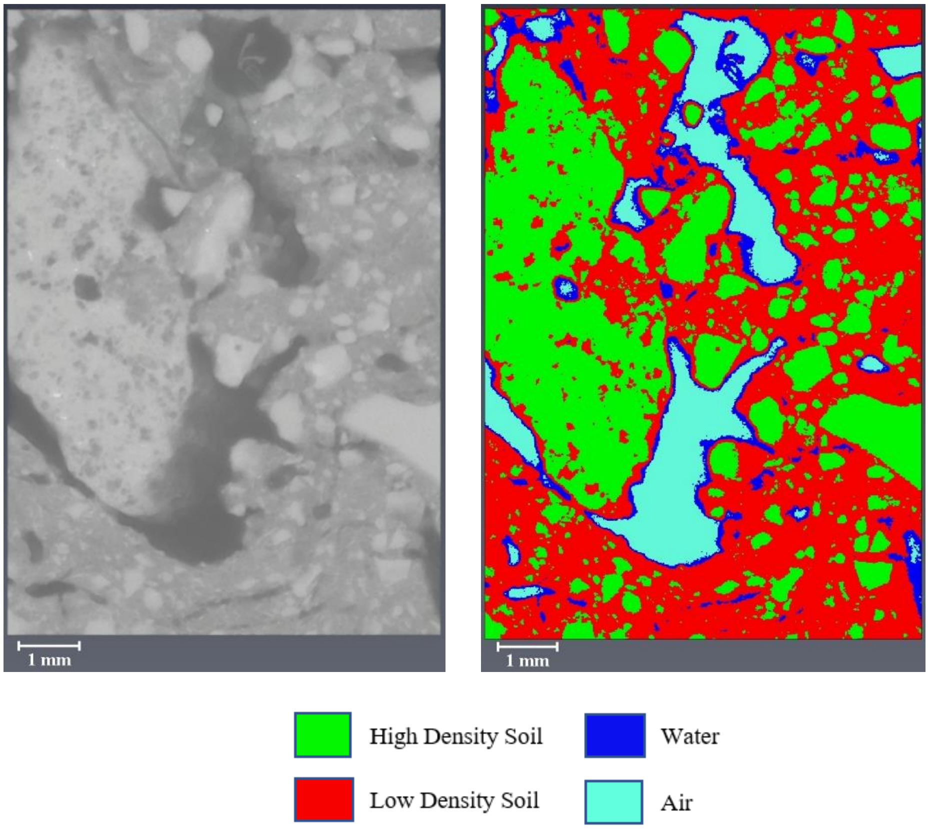

Figure A6. Pore coordination number examples indicated within a ball and stick pore network structure. The model was not used to indicate pore or pore throat geometry and is only provided for connectivity analysis.

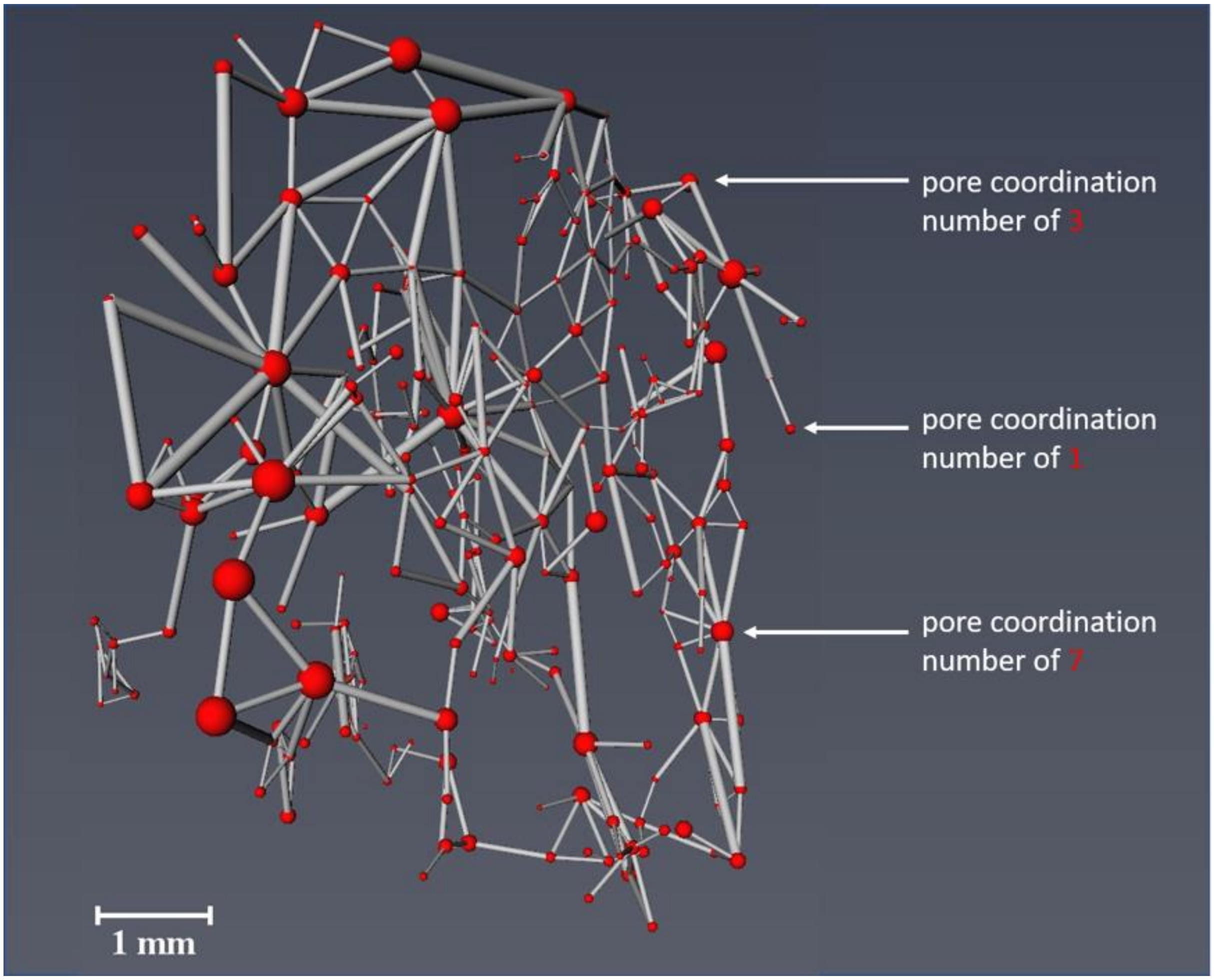

Figure A7. Comparing line of best fit equations and R-squared values for breadth (A) and width (B), we determined that breadth was highly correlated with manually calculated pore throat diameter. Breadth was used as the proxy for pore throat diameter throughout the experiment.

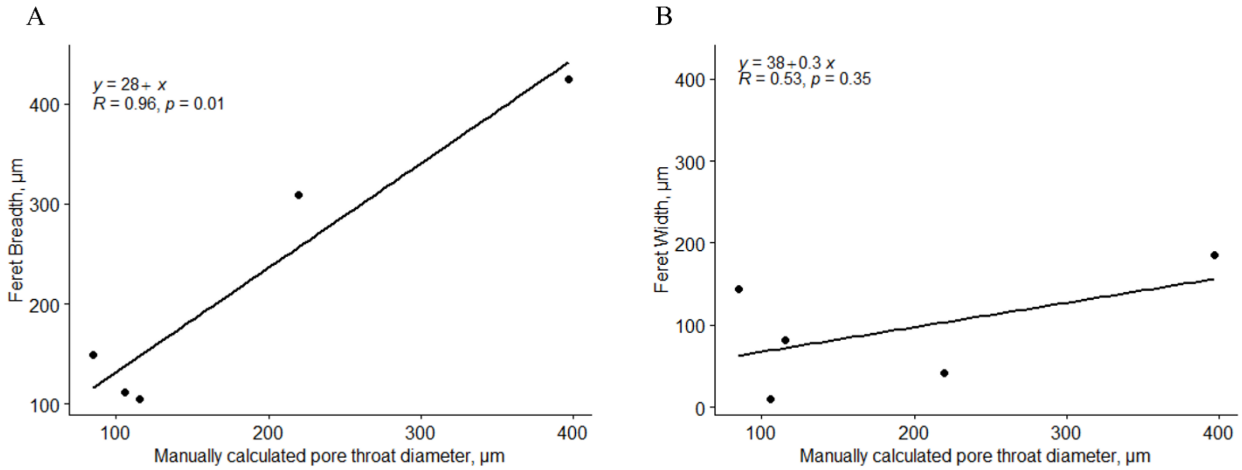

Figure A8. (A) Pore throat diameter distribution using breadth as a proxy for diameter, (B) pore throat diameter distribution using eq radius as a proxy for diameter.

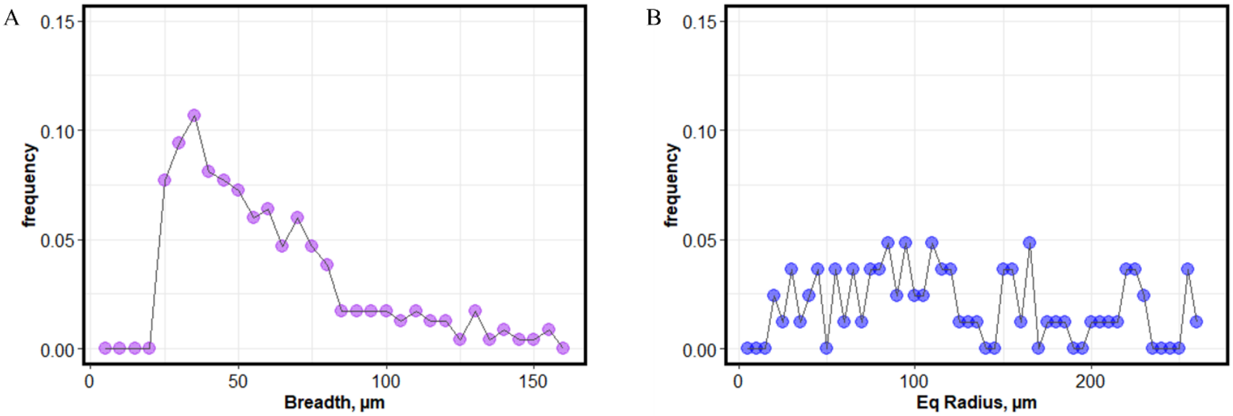

Figure A9. Pore shape factor vs. pore throat diameter, before and after freeze-thaw compared within each aggregate.

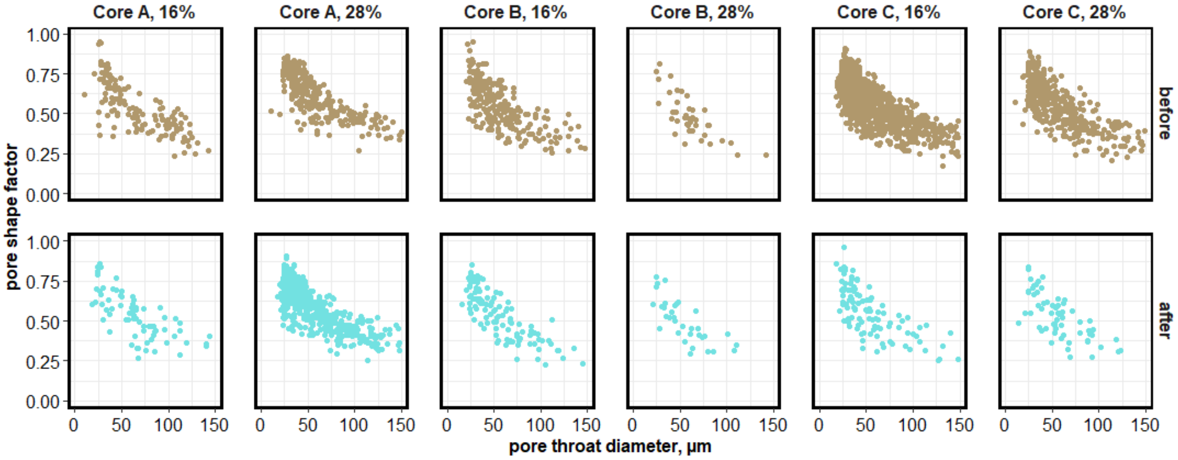

Table A1: Manual test for determining which parameter best serves as a proxy for pore throat diameters and the impact to capillarity (all measurements are in µm). Based on this data we determined width and breadth to be the only measurements not statistically different from the manually calculated pore throat diameters.

Pore throat	**Manually Calculated** (µm)	**Thickness** (µm)	**Width** (µm)	**Breadth** (µm)	**Length** (µm)
pt129	219.39	32.2692	41.084	309.092	404.833
pt165	396.95	83.6418	185.888	424.61	569.505
pt179	84.41	111.319	144.463	148.636	676.301
pt214	105.91	10.5726	10.319	111.914	138.541
pt287	115.49	29.4865	81.1788	105.455	358.464
	F-value	5.309302	3.50844	3.726514	6.895744
	P-value	0.0826	0.1344	0.1258	0.0584

Table A2: Pore coordination number tables with difference in frequency (%) calculated as after frequency – before frequency. Negative values indicate decreases in frequency following freeze-thaw.

	Pore Coordination Number															
Aggregate	1	2	3	4	5	6	7	8	9	10	11	12	13	14	15	16
Core A, 16%	10.927	6.760	-14.116	0.170	-8.163	6.293	2.168	0.043	-2.041	-2.041	0.000	0.000	0.000	0.000	0.000	0.000
Core A, 28%	2.921	5.095	-7.677	-4.280	1.019	5.027	0.951	1.563	-0.611	-1.223	0.000	-2.174	0.000	-2.174	0.000	1.563
Core B, 16%	6.132	-6.082	-1.446	5.334	-0.897	-2.144	-0.449	-1.695	2.941	0.000	0.000	0.000	-1.695	0.000	0.000	0.000
Core B, 28%	-7.143	0.000	-7.143	14.286	0.000	0.000	0.000	0.000	0.000	0.000	0.000	0.000	0.000	0.000	0.000	0.000
Core C, 16%	18.292	6.160	-3.817	-4.195	3.968	-6.122	-2.041	-4.082	-2.041	-3.061	0.000	-3.061	0.000	0.000	0.000	0.000
Core C, 28%	30.965	5.829	-0.364	-13.479	-8.197	-8.197	0.000	-1.639	-4.918	0.000	0.000	0.000	0.000	0.000	0.000	0.000

Table A3: Means (μm), medians (μm), and counts for pore throats in all aggregates before and after freeze-thaw.

Aggregate	Freeze-thaw	Mean, μm	Median, μm	Count
Core A, 16%	before	175.7215	105.5285	104
Core A, 16%	after	196.4028	109.408	76
Core A, 28%	before	137.5552	84.7328	153
Core A, 28%	after	131.2994	88.9013	277
Core B, 16%	before	139.2414	81.9806	149
Core B, 16%	after	161.5435	92.7151	77
Core B, 28%	before	104.7041	66.3251	29
Core B, 28%	after	131.5605	80.0958	23
Core C, 16%	before	114.5306	85.54615	552
Core C, 16%	after	106.0223	84.4904	57
Core C, 28%	before	112.1353	82.3408	225
Core C, 28%	after	143.9181	83.28115	48

Appendix B. The role of canopy in soil function across a Fairbanks hillslope in discontinuous permafrost

Table B1: Mineralogy abundances as determined by x-ray diffraction. All values are in percent (%), standard error.

	mineral	Backslope (%)	Low Backslope (%)	Footslope (%)
closed	albite	15.133 ± 0.809	16.05 ± 0.727	13.367 ± 0.255
	ankerite	0.84 ± 0.349	0.802 ± 0.091	0.29 ± 0.079
	anorthite	14.833 ± 0.41	16.733 ± 1.046	14.4 ± 0.266
	chlorite	5.873 ± 0.772	5.348 ± 0.399	7.628 ± 0.29
	hornblende	4.093 ± 0.136	4.268 ± 0.374	3.85 ± 0.08
	mica	9.727 ± 0.728	9.283 ± 0.742	14.578 ± 0.767
	microcline	3.483 ± 0.86	3.972 ± 0.827	5.803 ± 0.438
	quartz	46 ± 1.762	43.5 ± 0.879	40.022 ± 0.636
open	albite	15.34 ± 0.642	14.738 ± 0.275	13.963 ± 0.452
	ankerite	0.581 ± 0.078	0.545 ± 0.085	0.342 ± 0.111
	anorthite	16.7 ± 1.07	16.625 ± 0.677	15.113 ± 0.606
	chlorite	5.596 ± 0.524	6.202 ± 0.267	6.731 ± 0.622
	hornblende	4.564 ± 0.593	4.735 ± 0.207	3.668 ± 0.359
	mica	9.68 ± 0.592	10.104 ± 0.294	13.975 ± 1.011
	microcline	4.812 ± 1.369	4.915 ± 0.905	4.939 ± 0.757
	quartz	42.72 ± 1.752	42.125 ± 0.672	41.288 ± 1.372

Table B2. Total carbon and nitrogen by horizon for the backslope position. Standard error for instrument/analytical replicates. No statistical differences between open and closed cover. All values in %.

Backslope	replicate	horizon	depth, cm	TC %	TN %
closed	C-A	Bg1	26 - 49	0.494 ± 0.023	0.031 ± 0.001
	C-B	Bg1	28 - 50	1.427 ± 0.009	0.077 ± 0
	C-C	Bg1	22 - 44	1.104 ± 0.008	0.054 ± 0
			grand mean	1.008 ± 0.14	0.054 ± 0.01
open	O-A	Bg1	19 - 46	0.78 ± 0.004	0.048 ± 0.001
	O-B	Bg2	36 - 48	0.278 ± 0.001	0.018 ± 0
	O-B	Bg3	48 – 53	0.414 ± 0.003	0.025 ± 0
	O-B	Bg4	53 – 57	0.484 ± 0.003	0.034 ± 0
	O-C	Bg2	19 - 42	0.238 ± 0.011	0.014 ± 0
			grand mean	0.439 ± 0.05	0.028 ± 0.00

Table B3. Total carbon and nitrogen by horizon for the low backslope position. No statistical differences between open and closed cover. All values in %.

Low Backslope	replicate	horizon	depth, cm	TC %	TN %
closed	C-A	A	26 - 35	3.957 ± 0.009	0.251 ± 0.001
	C-A	Bg1	35 - 40	0.569 ± 0.004	0.033 ± 0
	C-A	Bg2	40 - 45	0.406 ± 0.001	0.026 ± 0
	C-B	Bg	19 - 44	1.168 ± 0.007	0.061 ± 0
	C-C	Bg2	38 - 41	1.248 ± 0.008	0.068 ± 0.002
			grand mean	1.433 ± 0.29	0.084 ± 0.02
open	O-A	Bg1	23 - 35	1.311 ± 0	0.086 ± 0.001
	O-A	Bg2	35 - 39	0.571 ± 0.004	0.035 ± 0.001
	O-A	Bg3	39 - 42	0.464 ± 0.002	0.027 ± 0
	O-B	Bg1	29 - 40	5.628 ± 0.003	0.281 ± 0
	O-B	Bg2	40 - 44	1.479 ± 0.004	0.085 ± 0.001
	O-B	Bg3	44 - 48	1.306 ± 0.004	0.075 ± 0
	O-C	Bg1	30 - 43	2.265 ± 0.006	0.116 ± 0
	O-C	Bg2	43 - 48	1.519 ± 0.004	0.071 ± 0
			grand mean	1.818 ± 0.32	0.097 ± 0.02

Table B4. Total carbon and nitrogen by horizon for the footslope position. No statistical differences between open and closed cover. All values in %.

Footslope	replicate	horizon	depth, cm	TC %	TN %
closed	C-A	Bg2	38 - 43	1.284 ± 0.082	0.076 ± 0.004
	C-A	Bg3	43 - 48	1.752 ± 0.004	0.107 ± 0
	C-B	Bg1	25 - 39	1.555 ± 0.003	0.089 ± 0
	C-B	Bg2	39 - 43	1.318 ± 0.003	0.081 ± 0.001
	C-B	Bg3	43 - 48	1.425 ± 0.002	0.084 ± 0
	C-C	Bg1	29 - 35	4.048 ± 0.013	0.206 ± 0.001
	C-C	Bg2	35 - 40	6.692 ± 0.006	0.315 ± 0.001
	C-C	Bg3	40 - 45	3.485 ± 0.002	0.163 ± 0.001
			grand mean	2.538 ± 0.35	0.133 ± 0.02
open	O-A	Bg1	42 - 48	1.61 ± 0.006	0.091 ± 0.001
	O-A	Bg2	49 - 54	1.49 ± 0.002	0.089 ± 0
	O-B	Bg1	33 - 35	6.247 ± 0.008	0.283 ± 0.005
	O-B	Bg2	35 - 39	5.408 ± 0.006	0.303 ± 0
	O-B	Oe	39 - 44	15.696 ± 0.016	0.682 ± 0.001
	O-C	Bg1	33 - 45	1.191 ± 0.006	0.074 ± 0
	O-C	Bg2	45 - 50	2.275 ± 0.005	0.099 ± 0
	O-C	Bg3	50 - 54	1.503 ± 0.01	0.077 ± 0.001
			grand mean	4.428 ± 0.97	0.212 ± 0.04

Table B5. Relative abundances of carbon compound classes with comparisons between slope positions. Differences were determined at significance 0.05 via ANOVA and HSD tests. Statistical comparisons are between slope positions within cover types. All values are percentages (%).

	class	backslope	low backslope	footslope
closed	aliphatic	38.79 ± 2.56 a	31.07 ± 1.64 ab	29.64 ± 0.95 b
	unsaturated/lignin	52.85 ± 2.32 a	57.17 ± 2.05 a	60.15 ± 0.64 a
	aromatic	3.44 ± 1.48 a	7.17 ± 0.45 a	6.92 ± 0.58 a
	condensed aromatic	4.92 ± 1.28 a	4.6 ± 0.25 a	3.29 ± 0.24 a
open	aliphatic	35.08 ± 3.05 a	34.58 ± 4.1 a	27.95 ± 1.95 a
	unsaturated/lignin	52.62 ± 1.69 b	57.56 ± 3.44 ab	64.31 ± 0.78 a
	aromatic	2.2 ± 0.83 a	4.03 ± 0.69 a	4.41 ± 1.38 a
	condensed aromatic	10.1 ± 0.75 a	3.84 ± 0.14 b	3.33 ± 0.24 b

Table B6. Relative abundances of carbon compound classes with comparisons between cover type at each slope position. Differences were determined at significance 0.05 via ANOVA tests. Statistical comparisons are between slope positions. All values are percentages (%).

	backslope		low backslope		footslope	
Class	closed	open	closed	open	closed	open
aliphatic	38.79 ± 2.56	35.08 ± 3.05	31.07 ± 1.64	34.58 ± 4.1	29.64 ± 0.95	27.95 ± 1.95
lignin-like	52.85 ± 2.32	52.62 ± 1.69	57.17 ± 2.05	57.56 ± 3.44	60.15 ± 0.64	64.31 ± 0.78 *
aromatic	3.44 ± 1.48	2.2 ± 0.83	7.17 ± 0.45	4.03 ± 0.69 *	6.92 ± 0.58	4.41 ± 1.38
cond. aromatic	4.92 ± 1.28	10.1 ± 0.75 *	4.6 ± 0.25	3.84 ± 0.14	3.29 ± 0.24	3.33 ± 0.24

Table B7. Relative abundances of carbon compound classes by horizon for all plots at the backslope position. Statistical comparison between grand means of open vs closed. All values are percentages (%).

Backslope	replicate	horizon	depth, cm	aliphatic	unsaturated/ lignin	aromatic	condensed aromatic
closed	C-A	Bg1	26 - 49	43.81	48.27	1.73	6.19
	C-B	Bg1	28 - 50	35.44	55.83	6.38	2.36
	C-C	Bg1	22 - 44	37.11	54.44	2.22	6.22
			grand mean	38.79 ± 2.56	52.85 ± 2.32	3.44 ± 1.48	4.92 ± 1.28
open	O-A	Bg1	19 - 46	29.2	55.41	3.85	11.54
	O-B	Bg2	36 - 48	42.76	49.82	1.06	6.36
	O-B	Bg3	48 – 53	33.73	53.37	1.79	11.11
	O-B	Bg4	53 – 57	35.98	54.18	1.46	8.37
	O-C	Oi	0 - 8	37.89	50	1.55	10.57
			grand mean	35.08 ± 3.05	52.62 ± 1.69	2.2 ± 0.83	10.1 ± 0.75

Table B8. Relative abundances of carbon compound classes by horizon for all plots at the low backslope position. All values are percentages (%).

Low Backslope	replicate	horizon	depth, cm	aliphatic	unsaturated/ lignin	aromatic	condensed aromatic
closed	C-A	A	26 - 35	24.87	60.51	9.32	5.3
	C-A	Bg1	35 - 40	34.36	56.78	3.76	5.1
	C-A	Bg2	40 - 45	34.27	57.76	4.06	3.92
	C-B	Bg	19 - 44	34.27	53.1	7.82	4.82
	C-C	Bg1	21 - 38	32.84	56.63	7.65	2.88
	C-C	Bg2	38 - 41	26.48	61.01	7.66	4.85
	C-C	Bg3	41 - 45	26.07	62.36	6.63	4.94
			grand mean	31.07 ± 1.64	57.17 ± 2.05	7.17 ± 0.45	4.6 ± 0.25
open	O-A	Bg1	23 - 35	42.31	52.94	2.09	2.66
	O-A	Bg2	35 - 39	41.67	51.11	3.47	3.75
	O-A	Bg3	39 - 42	44.55	48	2.36	5.09
	O-B	Bg1	29 - 40	30.12	60.34	6.09	3.46
	O-B	Bg2	40 - 44	28.81	63.69	4.08	3.42
	O-B	Bg3	44 - 48	30.58	60.5	5.01	3.92
	O-C	Bg1	30 - 43	32.77	59.11	3.93	4.19
	O-C	Bg2	43 - 48	29.78	61.67	4.56	4
			grand mean	34.58 ± 4.1	57.56 ± 3.44	4.03 ± 0.69	3.84 ± 0.14

Table B9. Relative abundances of carbon compound classes by horizon for all plots at the footslope position. All values are percentages (%).

Footslope	replicate	horizon	depth, cm	aliphatic	unsaturated/ lignin	aromatic	condensed aromatic
closed	C-A	Bg1	29 - 38	33.87	56.96	6.88	2.29
	C-A	Bg2	38 - 43	29.61	62.11	5.14	3.14
	C-A	Bg3	43 - 48	30.09	61.27	5.06	3.57
	C-B	Bg1	25 - 39	25.9	64.13	6.89	3.08
	C-B	Bg2	39 - 43	31.59	56.16	8.14	4.11
	C-B	Bg3	43 - 48	29.51	58.51	8.04	3.93
	C-C	Bg1	29 - 35	30.46	59.91	7.07	2.56
	C-C	Bg2	35 - 40	27.54	62.55	6.78	3.13
	C-C	Bg3	40 - 45	26.58	61.87	7.75	3.8
			grand mean	29.64 ± 0.95	60.15 ± 0.64	6.92 ± 0.58	3.29 ± 0.24
open	O-A	Bg1	42 - 48	29.07	64.84	3.25	2.85
	O-A	Bg2	49 - 54	31.85	61.17	2.54	4.44
	O-B	Oe/Bg	33 - 35	24.44	64.89	7.17	3.5
	O-B	Bg1	35 - 39	23.47	66.64	6.92	2.97
	O-B	Bg2	39 - 44	24.55	64.55	7.39	3.51
	O-C	Bg1	33 - 45	26.14	65.91	4.26	3.69
	O-C	Bg2	45 - 50	31.51	64.11	2.3	2.08
	O-C	Bg3	50 - 54	28.9	64.57	3.38	3.15
			grand mean	27.95 ± 1.95	64.31 ± 0.78	4.41 ± 1.38	3.33 ± 0.24

Figure B1. Tree trunk diameters (diameter at breast height). Statistical comparisons are between slope positions (backslope, low backslope, and footslope), P < 0.05. All values are in centimeters.

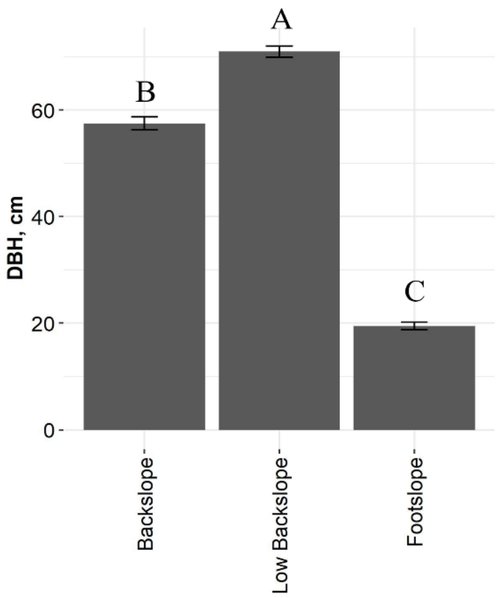

Figure B2. Soil morphological descriptions across hillslope positions and within closed vs. open, including horizon designation, munsell color, and depth.

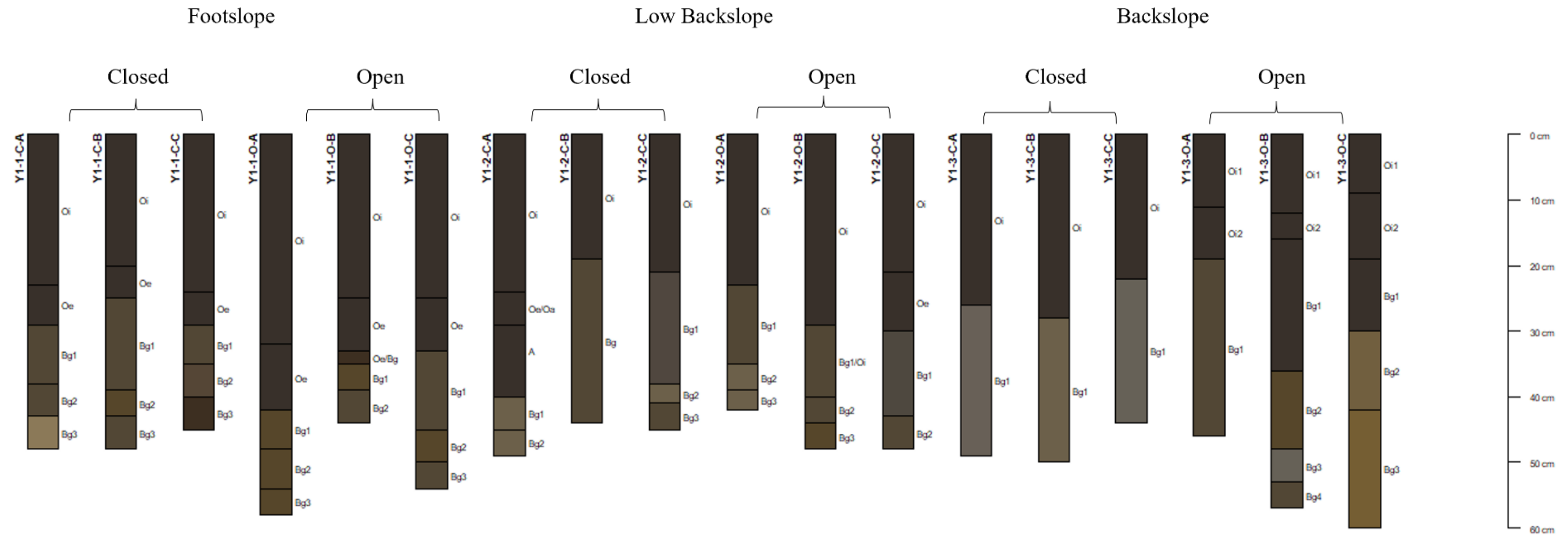

Figure B3. Diffractogram patterns from the x-ray diffraction analysis of the mineral soils at the backslope position under (A) closed and (B) open cover.

(A)

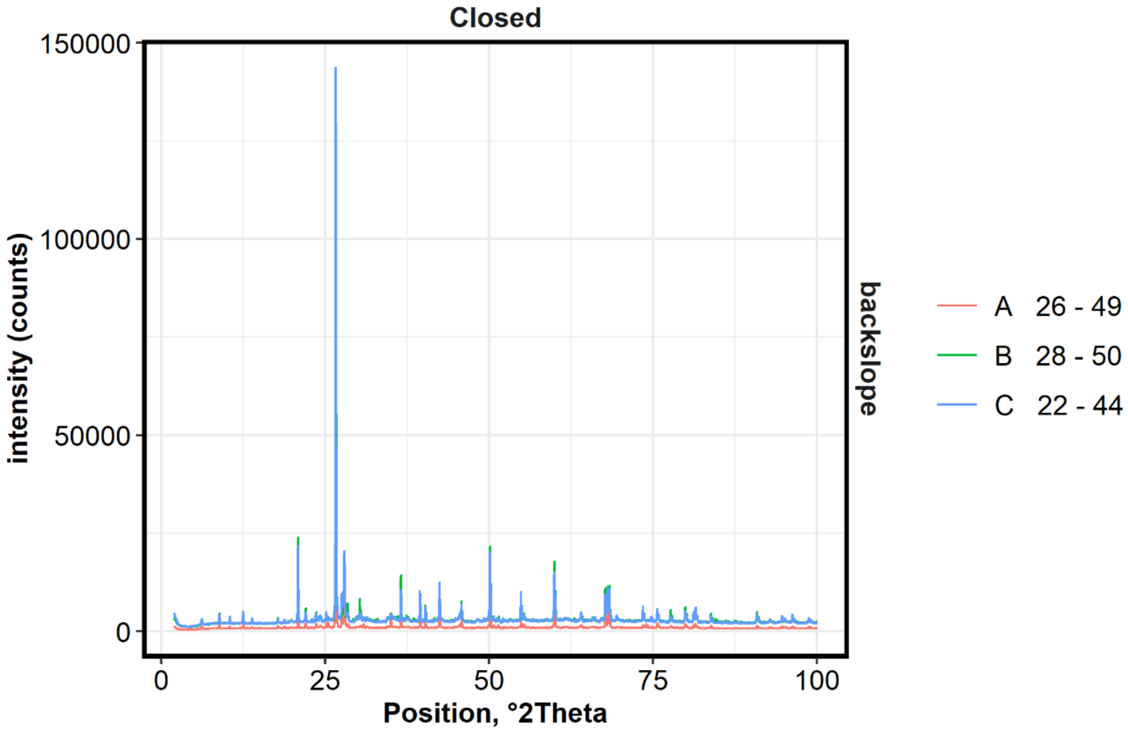

(B)

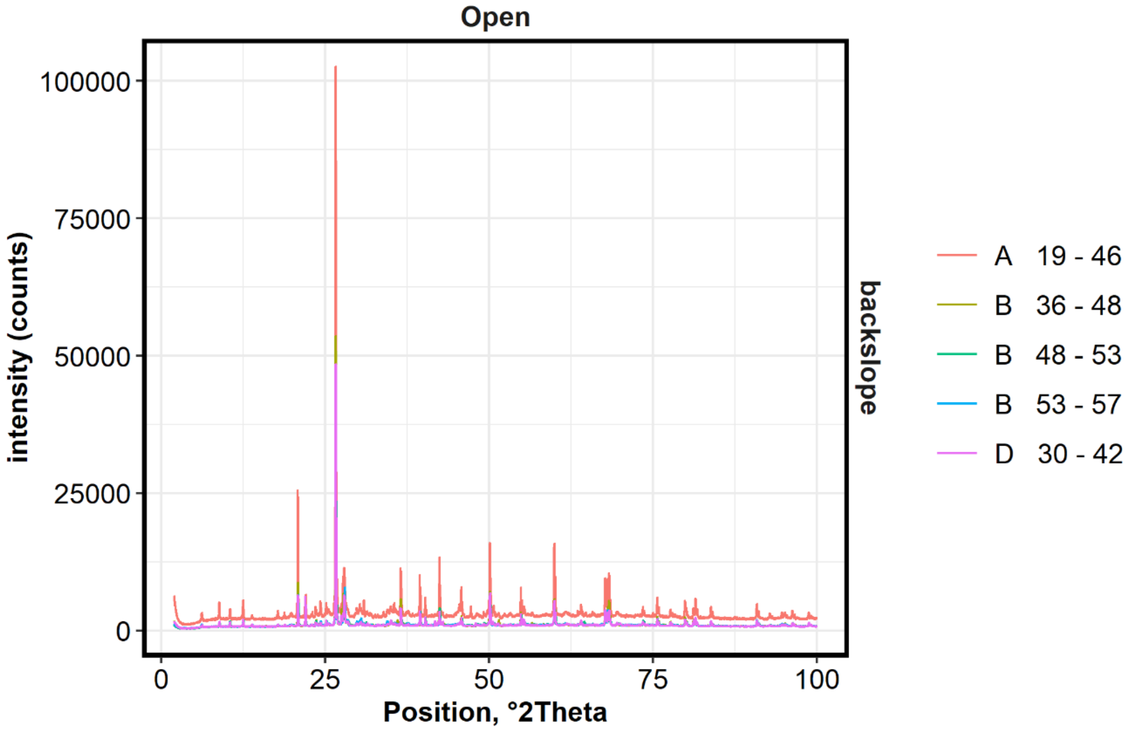

Figure B4. Diffractogram patterns from the x-ray diffraction analysis of the mineral soils at the low backslope position under (A) closed and (B) open cover.

(A)

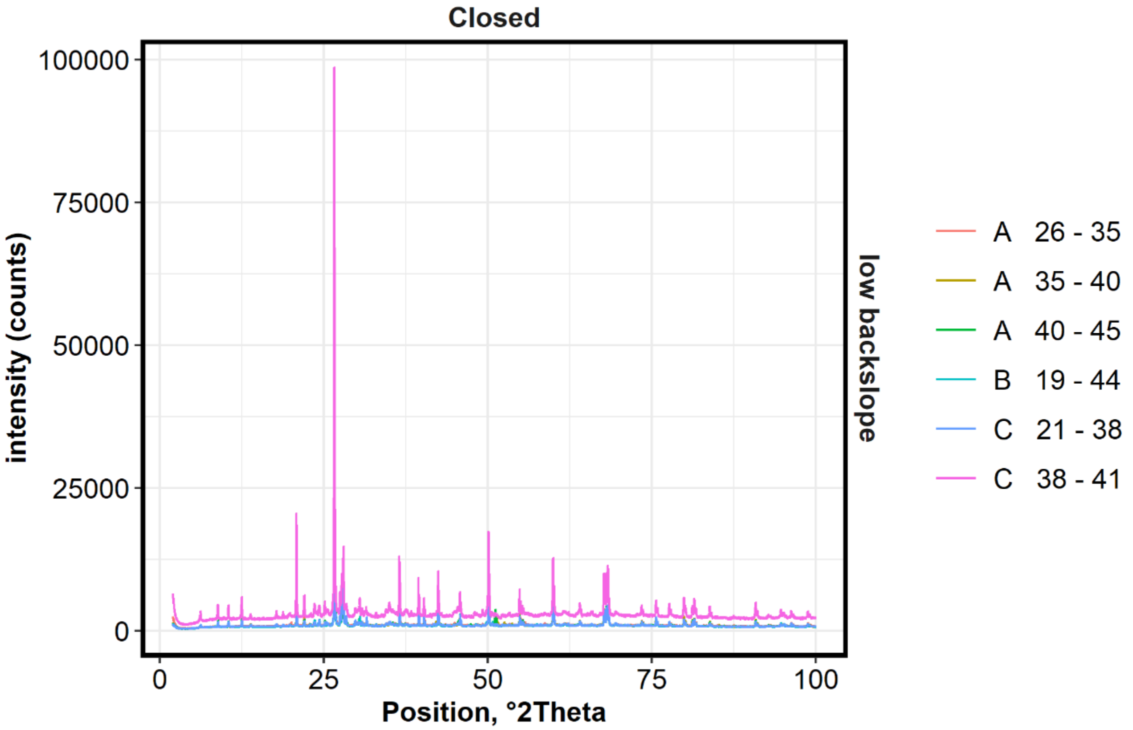

(B)

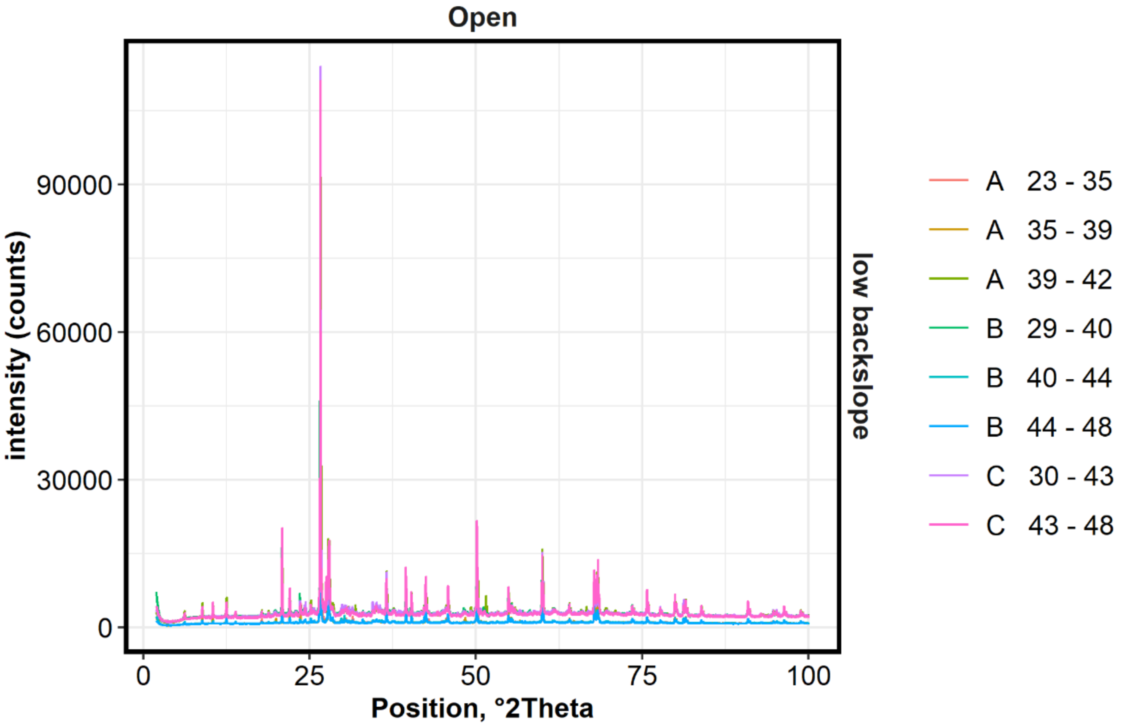

Figure B5. Diffractogram patterns from the x-ray diffraction analysis of the mineral soils at the footslope position under (A) closed and (B) open cover.

(A)

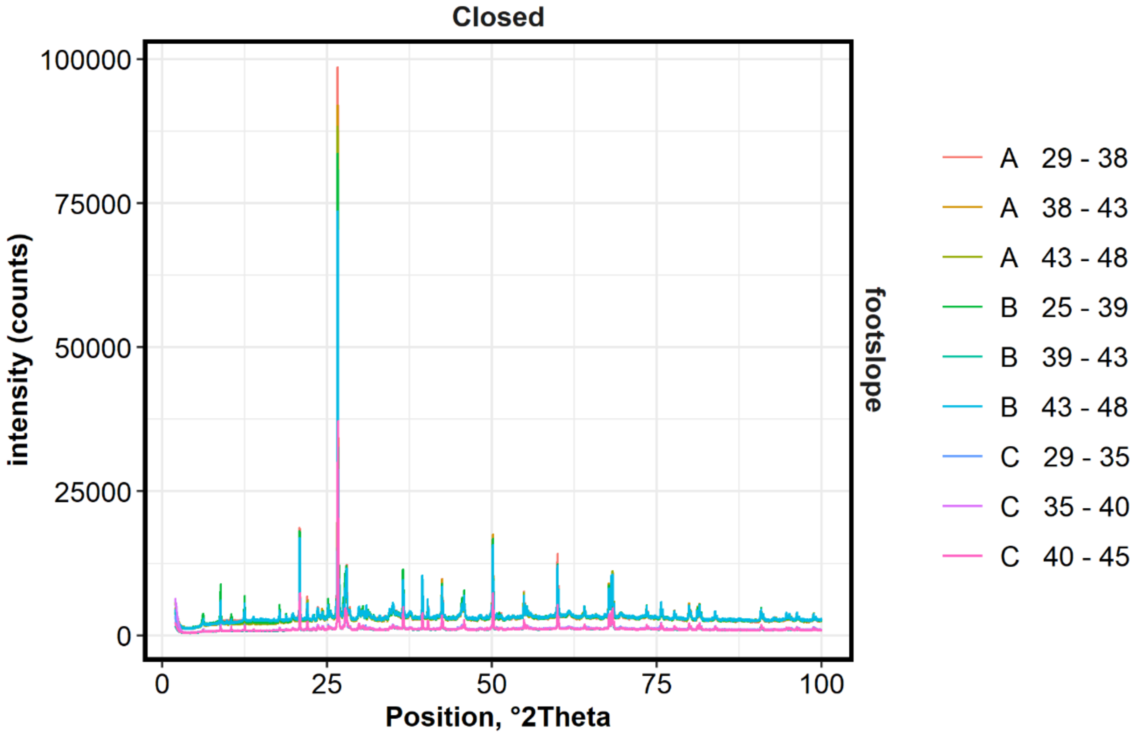

(B)

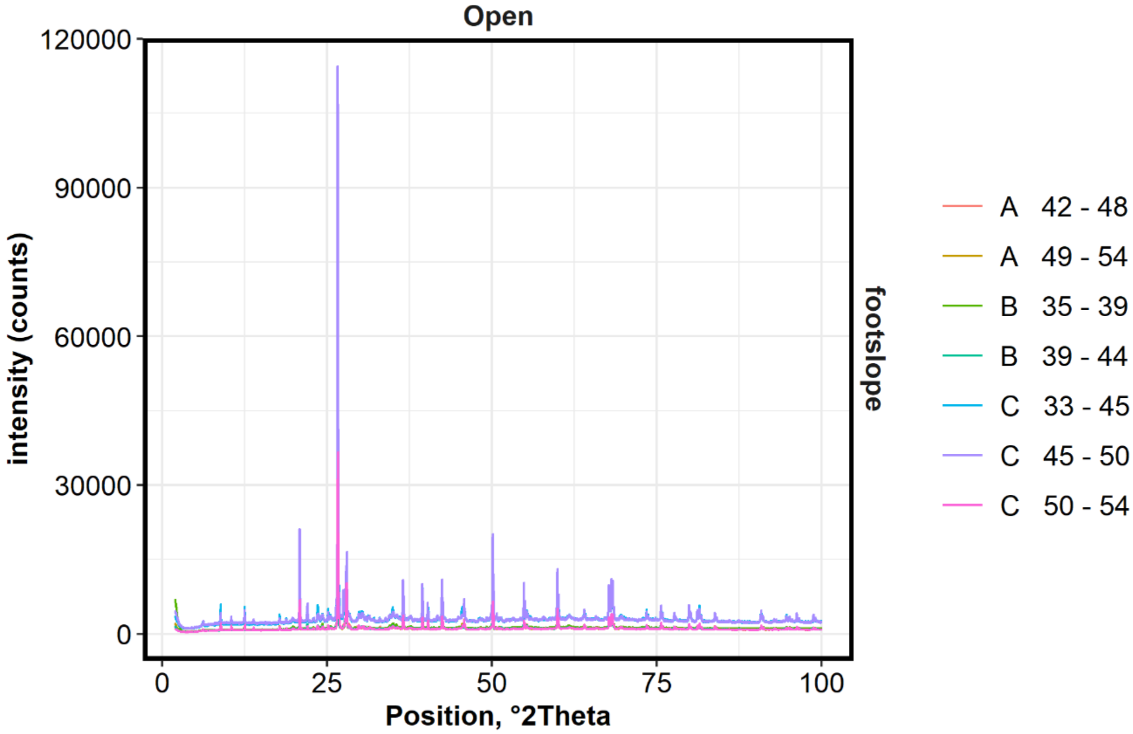

Figure B6. Nominal oxidation state of unique compounds (NOSC) under open and closed cover by slope position and compound class. Statistical significance was determined at α = 0.05. NOSC was higher in aromatic and lignin-like compounds under open cover on the backslope (compared with closed). NOSC was lower in aliphatic and lignin-like compounds under open on the low backslope (compared with closed). NOSC was lower in aliphatics and higher in aromatics under open on the footslope position.

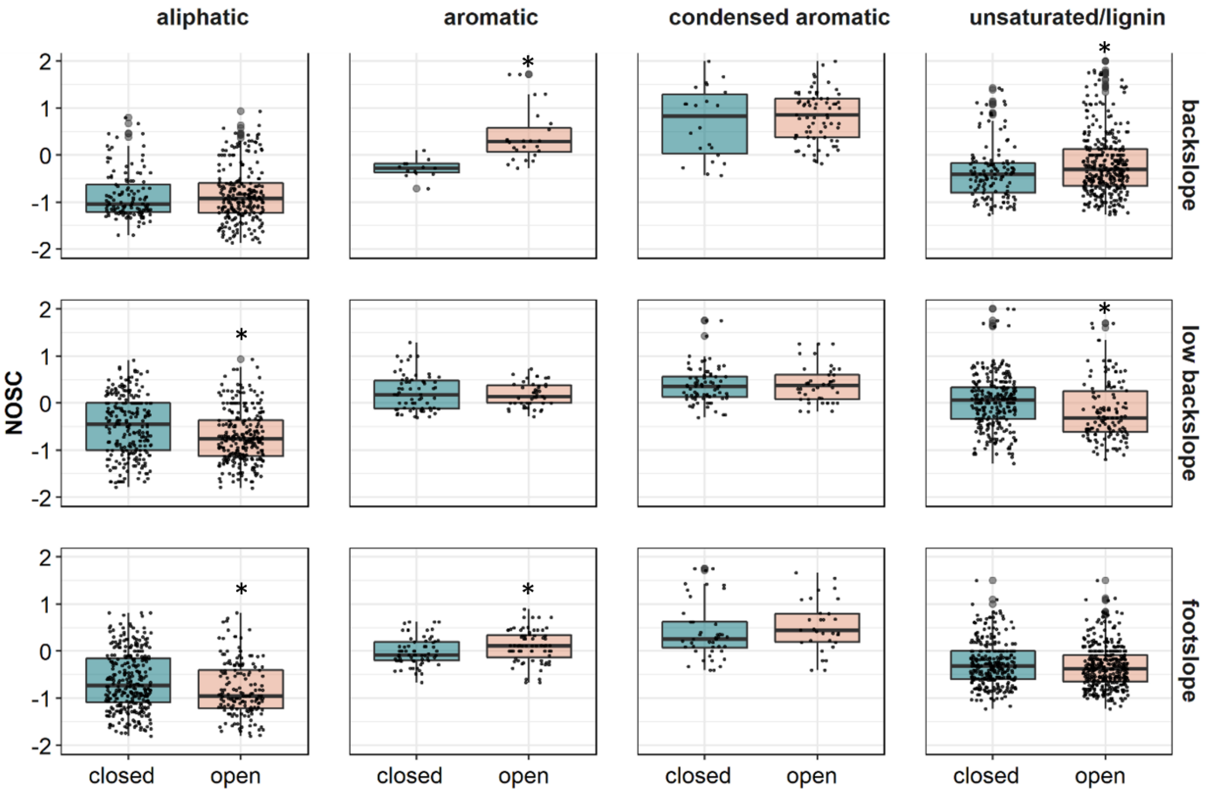

Appendix C. The impact of freeze-thaw history on soil carbon response to experimental freeze-thaw cycles

Appendix Text C1. Soil Morphology

Three cores from Healy and three from Toolik were described morphologically (USDA NRCS Key to Soil Taxonomy). Core lengths ranged between 54 cm and 68 cm. Cores were collected in Spring 2016.

Healy, AK

Organic mat thicknesses fluctuated between cores (core 1: 24 cm, core 2: 20 cm, core 3: 16 cm). Peat, muck, and mucky peat were all represented in Healy organic horizons with two distinct organic materials (Oa/Oejj) cryoturbated together in the upper subsurface (12-24 cm) of Healy of core 1. Peat layers included mosses, sphagnum, and leaf fragments and were often mixed with snow. Frozen water layers were prominent in Healy cores between 28 cm to 60 cm, with multiple horizons designated as Bf and/or Af. All water layers were parallel to the soil surface and contained thickness of ~1 cm to 3 cm.

Small pieces of charcoal (<1 cm^3) were also found in Healy cores at depths of 28-38 cm. One cross section taken from Healy core 3 at depths 34 cm to 38 cm contained an estimated 15% charcoal. Healy core 3 also contained the only A horizon (occurring at 16-30cm and again at 30-38cm) described across all six cores of both sites. Roots (very fine and fine) were documented down to depths of 40 cm in Healy cores.

Cryoturbation occurred in every Healy core, with mixing of mineral and organic material identified as deep as 50-60 cm in core 1, 34-47 cm in core 2, and 16-30 cm in core 3. Core 3 was the only core to contain gleying and redox features (50-54 cm).

Coarse fragment content increases at depths of 38 cm at Healy. Coarse fragments ranged in size, mineralogy, and shape. We identified rounded pebbles, a piece of decomposing granite (2 cm by 1 cm by 1 cm, containing biotite mica, plagioclase, oxidized iron), and several large rocks (~5 cm^3).

Toolik, AK

Organic mat thicknesses were generally around ten centimeters thicker at Toolik compared with Healy, although thicknesses still fluctuated across cores (core 1: 30 cm, core 2: 28 cm, core 3: 35 cm). Similarly to Healy, peat, mucky peat, and muck were all represented in Toolik organic horizons. Unlike Healy, while all three degrees of decomposition were represented in multiple horizons they were not mixed via cryoturbation. Rather, Oi/Oa/Oe in the surface of cores 1 and 2 were distinctly layered as expected with deposition and decomposition. Similar to Healy, mucky peat horizons were occasionally overlaid by muck horizons, indicating inconsistent decomposition with depth. Toolik soils contained fine and very fine roots down to 36 cm.

Frozen water layers in Toolik were much more fine (~1 mm) and resembled ice lenses. Frozen water layers were parallel to the soil surface and occurred repetitively across mineral soil horizons (40-50 cm) with some frozen water layers in the 16-28 cm muck horizon in Toolik core 2. Other cryo-features included visible pores in a cross section of Toolik core 2 between 28-38 cm.

Cryoturbation was identified in Toolik core 2 (28-58 cm) and core 3 (35-41 cm and 50-58 cm) but not in core 1. Unlike Healy, unconsolidated parent materials (C horizons) were identified at the bottom depths of every core. Similarly to Healy, lower depth in Toolik cores contained cryoturbated mineral and organic material (muck), with the exception of core 1. Toolik cores did not contain any gleying or redox features.

Coarse fragment content increased at ~40 cm in Toolik cores. Coarse fragments ranged in size and shape (4 x 1/2 cm between 50-60 cm, small pebbles both rounded and not rounded between 60-70 cm). We observed an increase in coarse fragments across lower depths of all Toolik cores and similarly sized coarse fragments of contrasting mineralogy. Many rocks were vertically oriented, occurring in zones of cryoturbation.

Appendix Text C2. Respiration

In this complementary incubation experiment, lower mineral Healy soils (> 30 cm) had higher respiration rates following freeze-thaw compared with control soils (with a difference of >250 micrograms CO_2 per gram of soil organic carbon) (Appendix Figure C8). In contrast, Toolik soils did not show differences in respiration following freeze-thaw (Appendix Figure C8). These findings are consistent with the increased oxidation state observed in the FTICR-MS analyses (Fig. 4.7) as well as the loss of carbon compounds in the lower mineral depths of Healy (Fig. 4.6).

Figure C1. Site map for location of extracted soil cores (red points) at NEON study sites in Healy and Toolik, Alaska. Map displays topography at ~ 1 km resolution as well as contrasting latitude along a longitudinal transect across Alaska at ~ 100 km resolution. (*Source: State of Alaska, Esri, HERE, Garmin, SafeGraph, METI/NASA, USGS, EPA, NPS, USDA, FAO, NOAA, and the GIS User Community*).

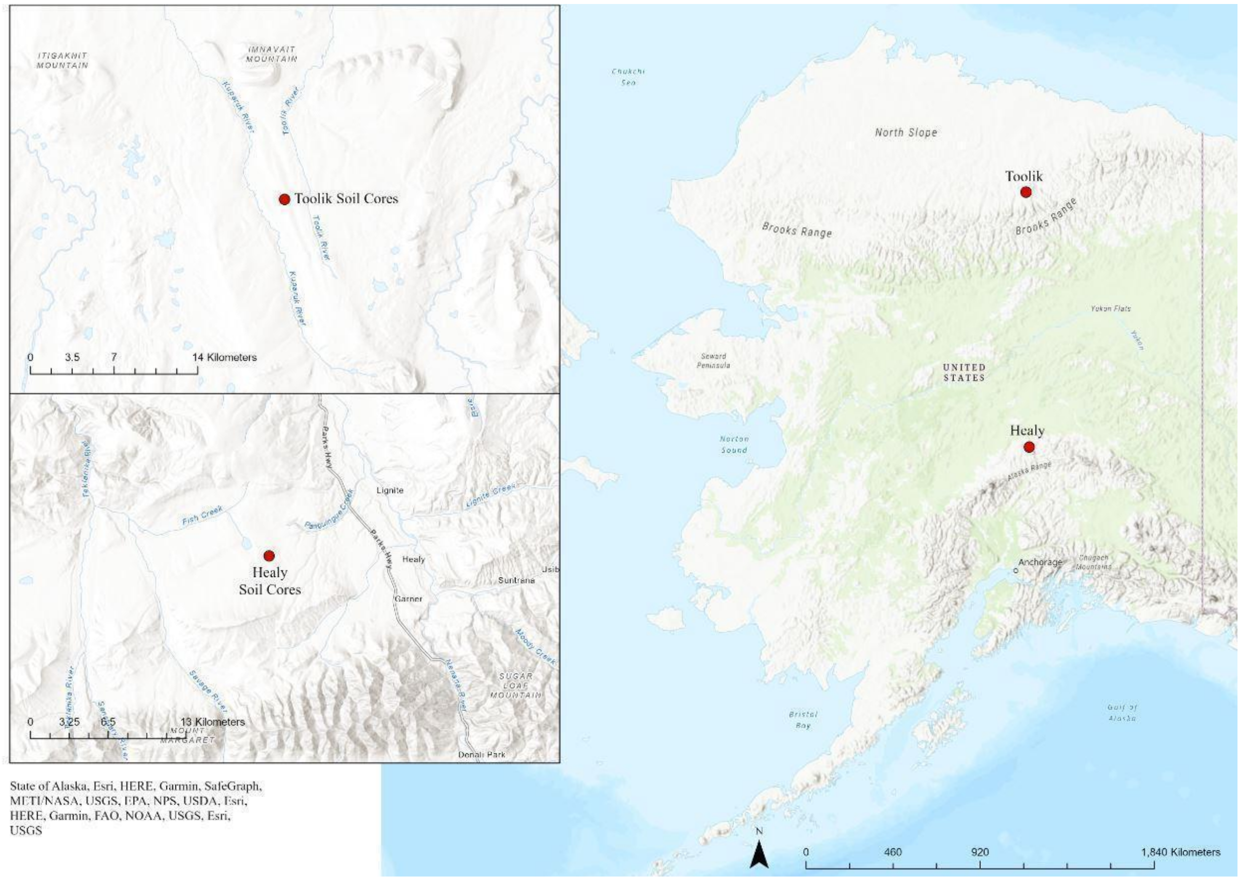

State of Alaska, Esri, HERE, Garmin, SafeGraph, METI/NASA, USGS, EPA, NPS, USDA, Esri, HERE, Garmin, FAO, NOAA, USGS, Esri, USGS

Figure C2. Experimental Design.

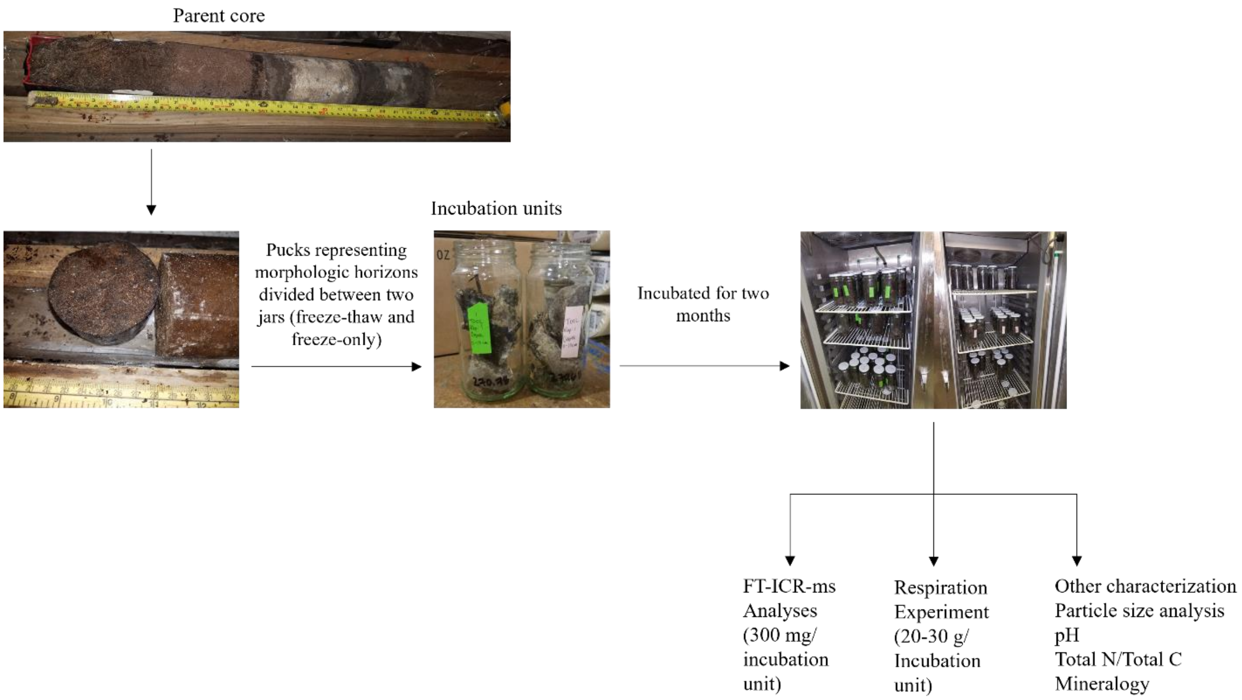

Figure C3. van Krevelen regions of carbon compound classes based on H/C to O/C ratios.

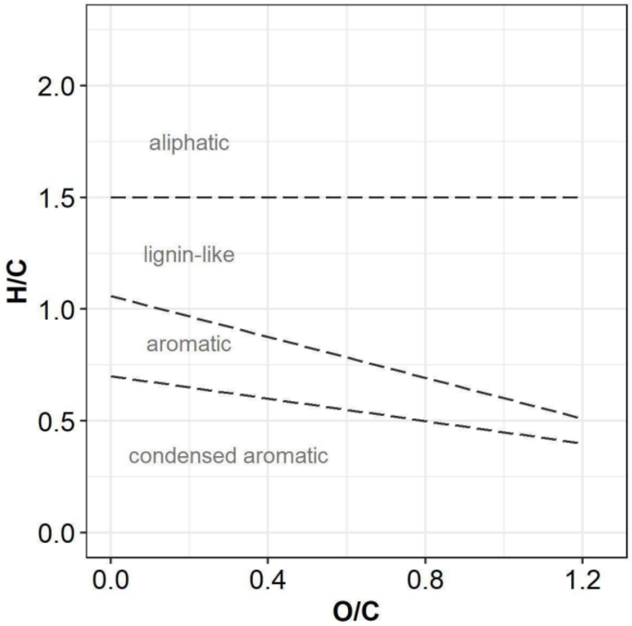

Figure C4. Mineralogical composition of mineral soils at Toolik and Healy (N = 3). Abundance is in percentage (%). Site had a significant effect on every mineral (ANOVA, P < 0.05).

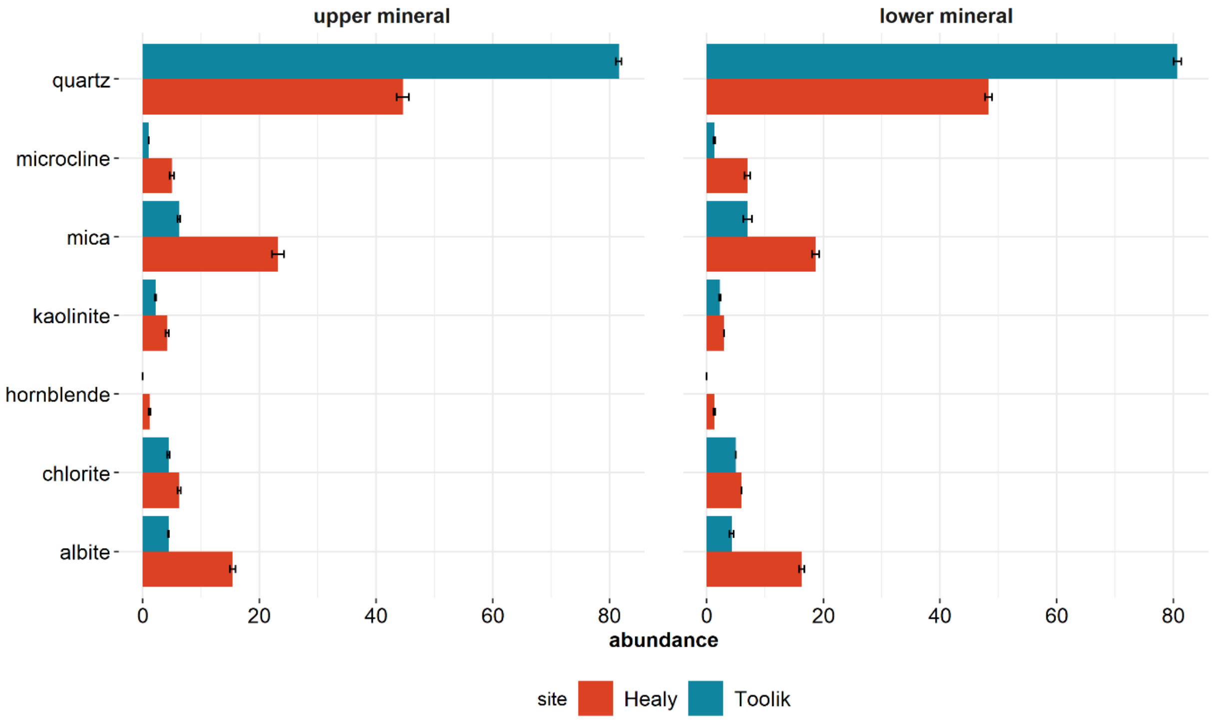

Figure C5. Diffractogram patterns from the x-ray diffraction analysis of mineral soils at (A) Healy and (B) Toolik. Analysis and plotting done using the *powdR* package.

(A)

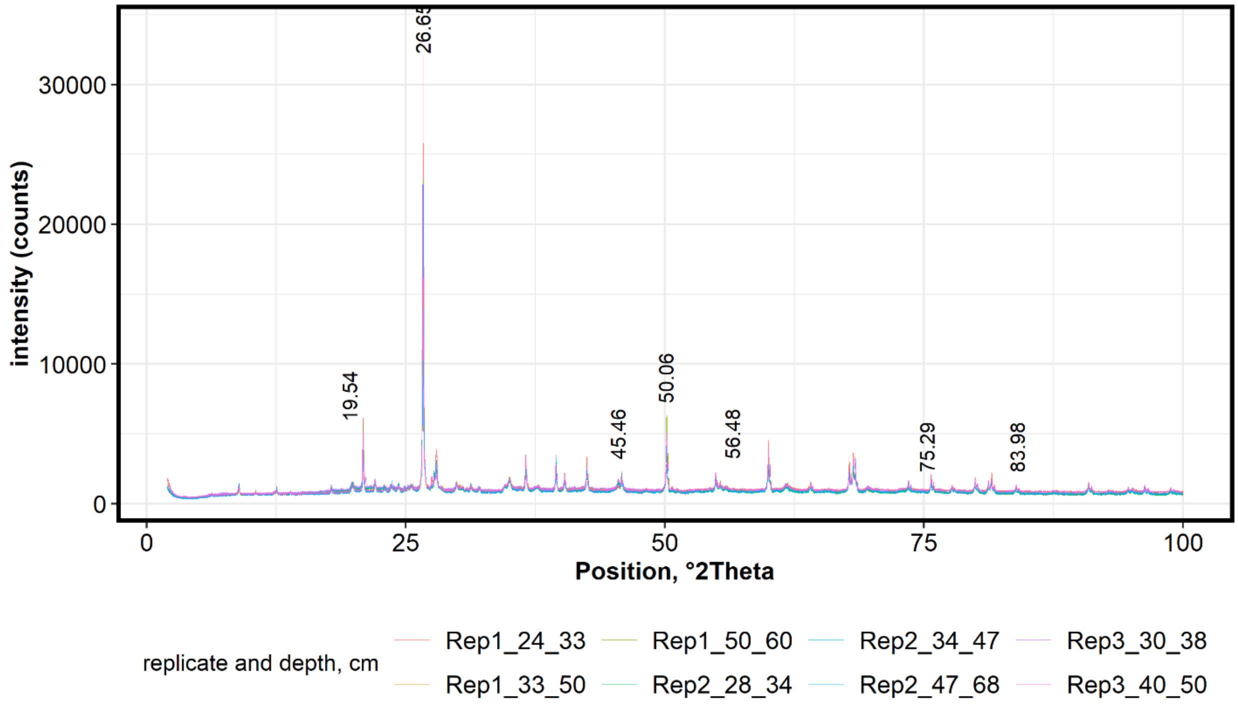

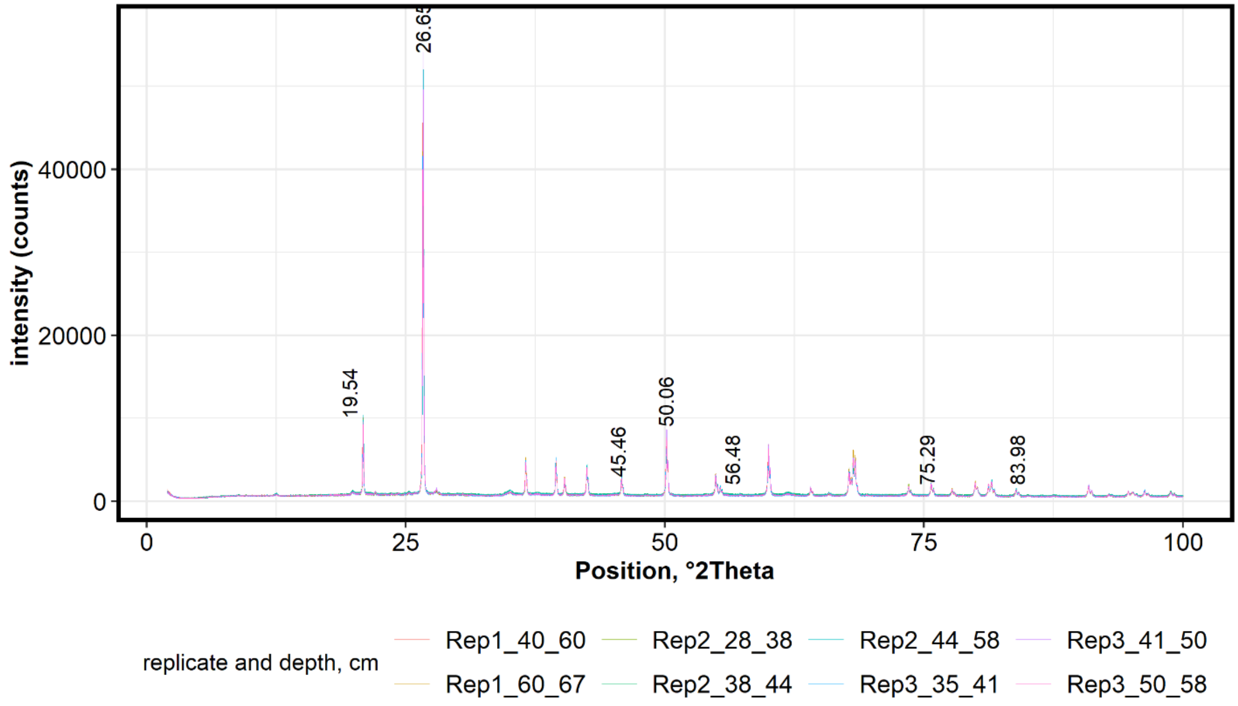

(B)

Figure C6. Euclidean distances between treatments for each soil depth within each site. Black squares indicate intra-depth variability in control samples, yellow squares indicate intra-depth variability in freeze-thaw samples, and the black circles represent the Euclidean distance between treatments at each depth.

solids squares = control

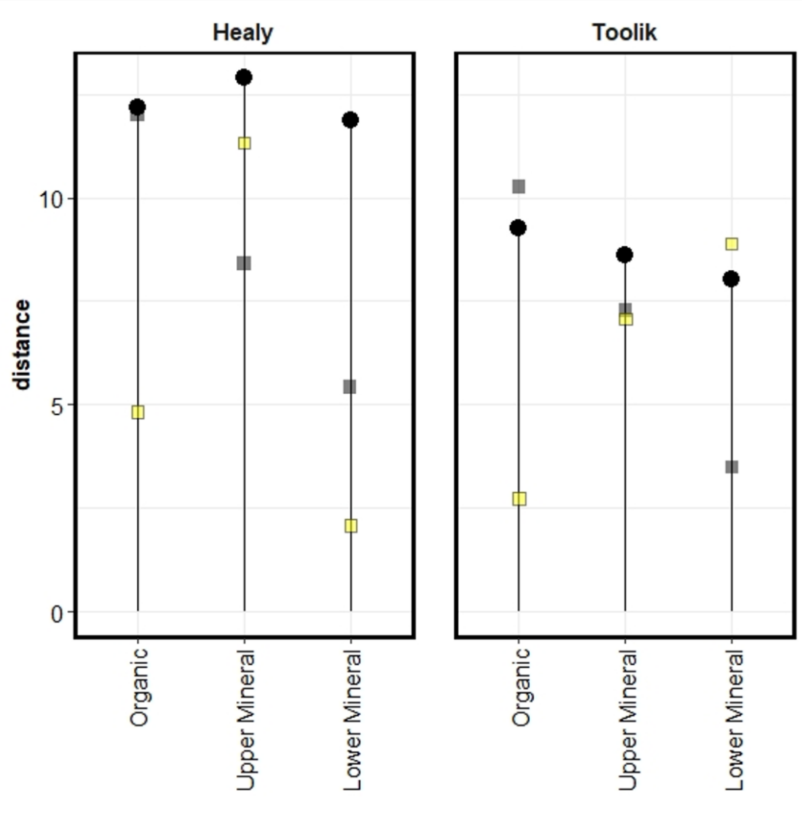

Figure C7. Nominal oxidation state of compounds (NOSC) in control soils by site and depth. Asterisks denote statistically significant differences among treatments at α = 0.05. NOSC was higher in all depths of Healy compared with Toolik.

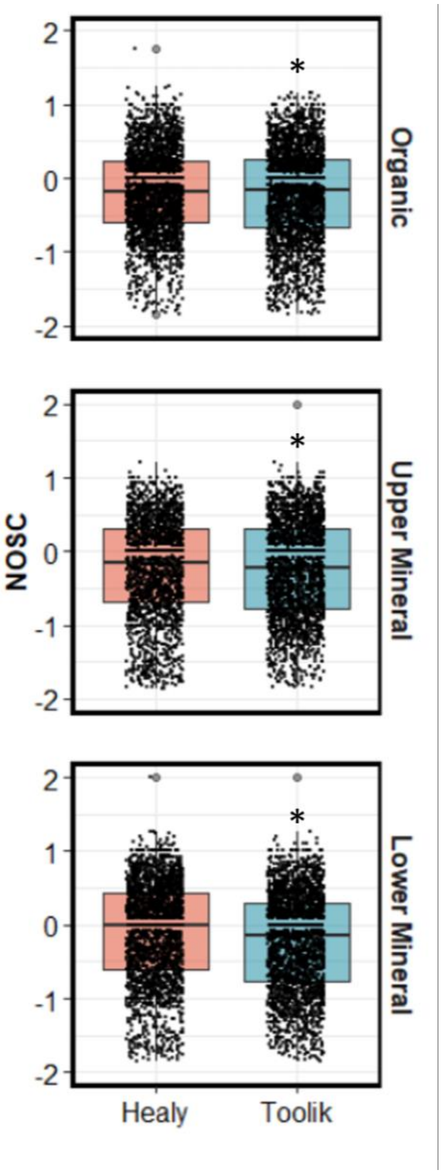

Figure C8. CO_2-C measured by the Picarro at day 1, 4, 7, and 14 of a two-week room temperature (20˚C) incubation on the mineral depths of both control and freeze-thaw soils. One sample per point (no replication). Gain in micrograms of CO_2 per gram of total carbon measures the change in respiration at each sampling time.

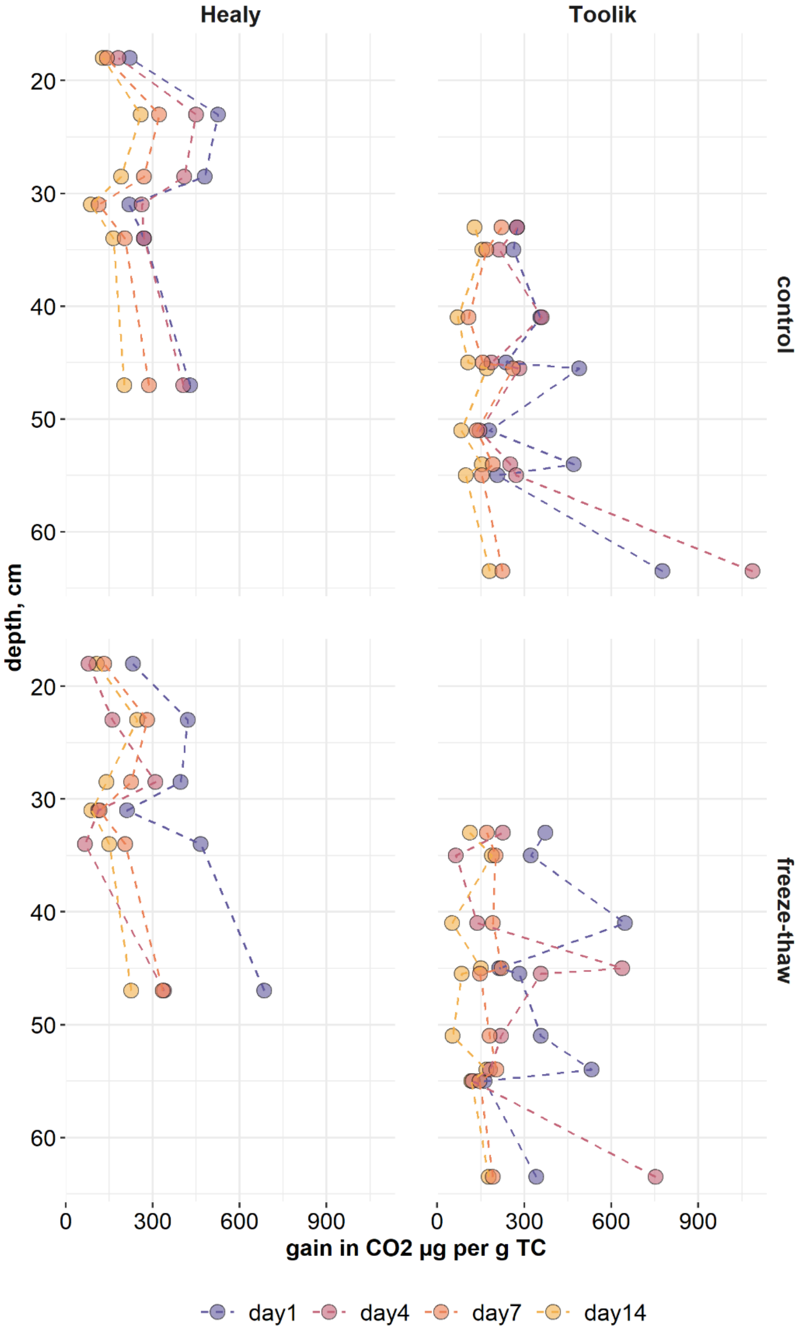

Table C1. Site characteristics for Toolik and Healy (NEON, 2022).

Site	Mean Annual Temperature ˚C	Mean Annual Precipitation (cm)	Slope Gradient	Slope Aspect (°)	NLCD class
Toolik	-9	31.6	~1%	274.10 °	Sedge/ Herbaceous
Healy	-1.3	38.5	~3%	22.57 °	Dwarf Shrub

Table C2. Particle size classes for Healy and Toolik.

Material	Particle Size	Healy %	Toolik %
Upper Mineral	Clay	31 ± 3	25 ± 3
	Fine Silt	31 ± 2	2 ± 0
	Coarse Silt	14 ± 2	9 ± 1
	Fine Sand	5 ± 1	6 ± 1
	Medium Fine Sand	8 ± 0	12 ± 1
	Medium Sand	5 ± 0	15 ± 3
	Medium Coarse Sand	4 ± 1	9 ± 0
	Coarse Sand	2 ± 1	5 ± 1
Lower Mineral	Clay	23 ± 2	25 ± 1
	Fine Silt	27 ± 2	19 ± 0
	Coarse Silt	13 ± 2	8 ± 0
	Fine Sand	7 ± 0	6 ± 1
	Medium Fine Sand	11 ± 1	12 ± 2
	Medium Sand	8 ± 1	14 ± 1
	Medium Coarse Sand	5 ± 1	9 ± 1
	Coarse Sand	5 ± 2	7 ± 2

Clay (< 2 μm), Fine Silt (2 to 20 μm), Coarse Silt (20 to 50 μm), Fine Sand (50 to100 μm), Medium Fine Sand (100 to 250 μm), Medium Sand (250 to 500 μm), Medium Coarse Sand (500 to 1000 μm), Coarse Sand (1000 to 2000 μm)

Table C3: Relative abundances of carbon compound classes within each material grouping before and after freeze-thaw in Healy and Toolik soils, significance 0.05. Statistical comparisons are within site and class between control and freeze-thaw. All values are percentages (%).

	Healy		**Toolik**	
Class	Control	Freeze-Thaw	Control	Freeze-Thaw
Organic				
aliphatic	35.95 ± 6.74	35.01 ± 2.57	33.99 ± 5.69	38.31 ± 1.07
unsaturated/lignin	50.49 ± 5.41	49.09 ± 0.82	48.29 ± 2.84	46.9 ± 1.64
aromatic	10.76 ± 1.2	11.56 ± 0.92	12.73 ± 1.8	10.75 ± 0.02
condensed aromatic	2.8 ± 0.18	4.35 ± 1.2	4.99 ± 1.32	4.04 ± 0.58
Upper mineral				
aliphatic	23.02 ± 4.11	19.19 ± 3.11	24.85 ± 3.39	26.15 ± 0.86
unsaturated/lignin	54.06 ± 3.68	58.4 ± 7.08	52.79 ± 1.43	52.9 ± 3.83
aromatic	15.23 ± 0.97	15.9 ± 1.21	16.04 ± 2.09	14.96 ± 2.54
condensed aromatic	7.68 ± 0.54	6.5 ± 2.75	6.32 ± 1.92	5.99 ± 2.11
Lower mineral				
aliphatic	21.34 ± 3.06	12.29 ± 0.36 *	27.1 ± 0.88	24.02 ± 4.8
unsaturated/lignin	56.79 ± 1.01	63.63 ± 1.3 *	54.15 ± 1.34	54.11 ± 1.53
aromatic	15.37 ± 1.99	17.54 ± 0.52	13.86 ± 1.33	15.59 ± 2.22
condensed aromatic	6.5 ± 0.12	6.55 ± 0.42	4.88 ± 0.85	6.28 ± 1.82

Table C4: Abundances of minerals within each material grouping (measured in the freeze-only control) Healy and Toolik samples. Values are percentages (%).

	Healy	**Toolik**
	abundance (%)	abundance (%)
Upper Mineral		
albite	15.4 ± 1	4.4 ± 0.2
chlorite	6.2 ± 0.6	4.4 ± 0.4
hornblende	1.2 ± 0.4	0 ± 0
kaolinite	4.2 ± 0.5	2.2 ± 0.2
mica	23.2 ± 2	6.2 ± 0.5
microcline	5 ± 0.7	1 ± 0
quartz	44.6 ± 2.1	81.6 ± 0.9
Lower Mineral		
albite	16.3 ± 0.9	4.3 ± 0.7
chlorite	6 ± 0	5 ± 0
hornblende	1.3 ± 0.3	0 ± 0
kaolinite	3 ± 0	2.3 ± 0.3
mica	18.7 ± 1.3	7 ± 1.5
microcline	7 ± 1	1.3 ± 0.3
quartz	48.3 ± 1.2	80.7 ± 1.3